Agenzia Nazionale per le Nuove Tecnologie,
l'Energia e lo Sviluppo Economico Sostenibile

Ministero dello Sviluppo Economico

RICERCA DI SISTEMA ELETTRICO

# Development of a Dynamic Simulator for a LFR DEMO

*S. Bortot, A. Cammi, S. Lorenzi, R. Ponciroli*

Report RdS/2011/49

DEVELOPMENT OF A DYNAMIC SIMULATOR FOR A LFR DEMO

S. Bortot, A. Cammi, S. Lorenzi, R. Ponciroli- POLIMI

Settembre 2011

Report Ricerca di Sistema Elettrico
Accordo di Programma Ministero dello Sviluppo Economico – ENEA
Area: Governo, Gestione e sviluppo del sistema elettrico nazionale
Progetto: Nuovo nucleare da fissione: collaborazioni internazionali e sviluppo competenze in materia nucleare

Responsabile Progetto: Paride Meloni, ENEA

**CIRTEN**

**CONSORZIO INTERUNIVERSITARIO**

**PER LA RICERCA TECNOLOGICA NUCLEARE**

**POLITECNICO DI MILANO**

**DIPARTIMENTO DI ENERGIA, Sezione INGEGNERIA NUCLEARE-CeSNEF**

# Development of a Dynamic Simulator for a LFR DEMO

**AUTORI**

Sara Bortot, Antonio Cammi, Stefano Lorenzi, Roberto Ponciroli

**CERSE-POLIMI RL-1351/2011**

**Milano, 09 Settembre 2011**

*Lavoro svolto in esecuzione della linea progettuale LP3 punto E3 – AdP ENEA MSE del 21/06/07*

*Tema 5.2.5.8 – "Nuovo Nucleare da Fissione"*

*This material has been partially published in:*

*S. Bortot, A. Cammi, S. Lorenzi, R. Ponciroli, "MODELING APPROACHES FOR DYNAMIC ANALYSES OF INNOVARIVE SMRs COMPACT STEAM GENERATORS", In: TRANSACTIONS of the American Nuclear Society, Embedded Topical Meeting of the ANS Winter Meeting "1st Annual ANS SMR 2011 Conference", Washington, DC, USA, October 30 - November 3, 2011.*

*C. Artioli, S. Bortot, A. Cammi, S. Lorenzi, R. Ponciroli, "SAFETY ISSUES AFFECTING THE FEASIBILITY OF AN EARLY HIGH-FLUX LFR TECHNOLOGY DEMONSTRATOR", In: TRANSACTIONS of the American Nuclear Society, ANS Winter Meeting, Washington, DC, USA, October 30 - November 3, 2011.*

*S. Bortot, A. Cammi, S. Lorenzi, "AN ANALYTICAL MODEL FOR THE STUDY OF A SMALL LFR CORE DYNAMICS: DEVELOPMENT AND BENCHMARK", In: Proceedings of the International Conference on Mathematics and Computational Methods applied to Nuclear Science and Engineering (MC 2011), Rio de Janeiro, Brazil, May 8-12, 2011.*

*S. Bortot, A. Cammi, S. Lorenzi, "IMPACT OF LINEAR AND NON-LINEAR KINETICS MODELS ON A SMALL LFR CORE DYNAMICS", In: International Congress on Advances in Nuclear Power Plants (ICAPP2011), Nice, France, May 2-5, 2011.*

*S. Bortot, A. Cammi, C. Artioli, "DYNAMIC PERFORMANCE ASSESSMENT OF MOX AND METALLIC FUEL CORE OPTIONS FOR A GEN-IV LFR DEMONSRATOR", In: Progress in Nuclear Energy, 2011.*

**INDEX**

**EXECUTIVE SUMMARY**

*This document presents the status of development of a dynamic simulator for a Generation IV Lead-cooled Fast Reactor (LFR) demonstrator (DEMO).*

*The development of a zero dimensional, control-oriented model is undertaken. Based upon the European Lead-cooled SYstem (ELSY) DEMO design, the simulator, implemented in MATLAB/SIMULINK®, consists in four essential parts: core, Steam Generator (SG), primary pump, and coolant cold pool.*

*An analytical lumped-parameter model of DEMO core is developed to treat the coupled neutronics and thermal-hydraulics. A non-linear approach is adopted as reference; in addition, two advantageous approximations (linearization and one-neutron-precursor-group treatment of neutron kinetics) are considered; in particular, the study of a linear model is very useful in the perspective of conceiving an adequate control strategy for the reactor.*

*The validation of the reference core model is accomplished through a benchmark analysis with the SAS4A/SASSYS-1 Liquid Metal Reactor Code System, and a very good agreement with the analytical model outcomes is attested.*

*The impact of the above-mentioned approximations is evaluated by investigating and comparing the respective responses to some unprotected transient initiators; moreover, a dynamic performance assessment of MOX and metal as fuel alternative options for DEMO is carried out.*

*For the SG model a moving boundary approach is adopted, which allows to get the physical behavior while satisfying some controller specifications such as simplicity, fast-running characteristics and flexibility, besides assuring coherence with the zero-dimensional core modeling. The SG dynamic behavior is studied by applying some perturbations to the steady-state, acting on both the water (secondary) and the lead (primary) side of the heat exchanger.*

*In conclusion, the complete primary loop model is implemented by assembling the core and the SG models and adding the primary pump and the coolant cold pool.*

*As a major achievement, it can be stated that the free dynamics simulation results are very satisfactory, and they will constitute the basis and provide the means for conceiving a suitable control strategy for the innovative small-size LFR systems under development.*

**NOMENCLATURE**

| | |
|---|---|
| A | Fluid area [$m^2$] |
| $A_n$ | Rate of neutron absorption [$cm^{-3}$ $s^{-1}$] |
| B | Buckling parameter [$cm^{-1}$] |
| Bo | Boiling number [ - ] |
| C | Average specific isobaric heat [J $kg^{-1}$ $K^{-1}$] |
| $c_i$ | $i^{th}$ precursor density [$cm^{-3}$] |
| Co | Convective number [ - ] |
| d | Average density [kg $m^{-3}$] |
| D | Diameter [m] |
| $D_{hyd}$ | Hydraulic diameter [m] |
| $D_{in}$ | Internal tube diameter[m] |
| $D_n$ | Neutron diffusion coefficient [cm] |
| $D_{out}$ | External tube diameter [m] |
| F | Rate of neutron leakage from the active core [$cm^{-3}$ $s^{-1}$] |
| $f_l$ | Coolant volume fraction [ - ] |
| H | Active core height [m] |
| h | Specific enthalpy [J $kg^{-1}$ $K^{-1}$] |
| $h_{chc}$ | Convective heat transfer coefficient [W $m^{-2}$ K] |
| $H_{cl}$ | Cladding-coolant global heat transfer coefficient [W $K^{-1}$] |
| $h_{cr}$ | Control rods differential insertion share [m] |
| K | Turbine admission valve coefficient [m s] |
| k | Multiplication factor [ - ] |
| $K_D$ | Doppler constant [pcm] |
| $K_{fc}$ | Fuel-gap-cladding global heat transfer coefficient [W $K^{-1}$] |
| l | Linear expansion coefficient of cladding steel [$K^{-1}$] |
| L | Tube length [m] |
| M | Mass [kg] |
| $\dot{m}$ | Water mass flow rate [kg $s^{-1}$] |
| MF | Molar fraction [ - ] |
| MM | Molar mass [kg $kmol^{-1}$] |
| n | Neutron density [$cm^{-3}$] |
| N | Atomic density [$cm^{-3}$] |
| Nu | Nusselt number [ - ] |
| p | Porosity [ - ] |

| | |
|---|---|
| P | Tube pressure [bar] |
| Pe | Peclet number [ - ] |
| $p_F$ | Fission probability [ - ] |
| $P_{out}$ | Turbine pressure [bar] |
| $P_p$ | Rate of prompt neutron production by fission [$cm^{-3}$ $s^{-1}$] |
| PP | Pin Pitch [m] |
| $P_r$ | Rate of delayed neutron production by the decay of precursors [$cm^{-3}$ $s^{-1}$] |
| Pr | Prandtl number [ - ] |
| q | Reactor thermal power [MW] |
| Q | SG thermal power [MW] |
| $q''$ | Thermal flux [W $m^{-2}$] |
| $q'''$ | Power density [W $m^{-3}$] |
| R | Active core radius [m] |
| Re | Reynolds number [ - ] |
| $r_{ext}$ | External tube radius [m] |
| $r_{in}$ | Internal tube radius [m] |
| $r_{mean}$ | Mean tube radius [m] |
| S | Rate of neutron production by source [$cm^{-3}$ $s^{-1}$] |
| T | Average temperature [°C] |
| v | Neutron velocity [m $s^{-1}$] |
| $\vec{v}$ | Fluid velocity [m $s^{-1}$] |
| V | Volume [$m^3$] |
| x | Stoichiometric deviation [ - ] |
| y | Plutonium molar fraction [ - ] |
| $\alpha_{CBD}$ | Convective Boiling Dominant coefficient [ - ] |
| $\alpha_D$ | Doppler reactivity feedback coefficient [pcm $K^{-1}$] |
| $\alpha_H$ | Control rod reactivity feedback coefficient [pcm $cm^{-1}$] |
| $\alpha_L$ | Coolant density reactivity feedback coefficient [pcm $K^{-1}$] |
| $\alpha_{NBD}$ | Nucleate Boiling Dominant coefficient[ - ] |
| $\alpha_R$ | Radial expansion reactivity feedback coefficient [pcm $K^{-1}$] |
| $\alpha_{TP}$ | Convective coefficient of two-phase region [ - ] |
| $\alpha_Z$ | Axial expansion reactivity feedback coefficient [pcm $K^{-1}$] |
| β | Total delayed neutron fraction [pcm] |
| $\beta_i$ | $i^{th}$ precursor group delayed-neutron fraction [pcm] |
| Γ | Lead mass flow rate [kg $s^{-1}$] |
| γ | Mean void fraction [ - ] |

| | |
|---|---|
| $\delta\eta_i$ | Variation of the dimensionless precursor density from the steady-state value [ - ] |
| $\delta\psi$ | Variation of the dimensionless neutron density from the steady-state value [ - ] |
| $\eta$ | Void fraction [ - ] |
| $\Lambda$ | Invariant neutron average lifetime [s] |
| $\lambda$ | Thermal conductivity [W $m^{-1}$ $K^{-1}$] |
| $\lambda_d$ | Mean precursor decay constant [$s^{-1}$] |
| $\lambda_{d,i}$ | $i^{th}$ precursor decay constant [$s^{-1}$] |
| $\mu$ | Dynamic viscosity [Pa s] |
| $\nu$ | Average number of neutrons emitted after a fission event [ - ] |
| $\rho$ | Reactivity [pcm] |
| $\Sigma_a$ | Macroscopic neutron absorption cross section [$cm^{-1}$] |
| $\Sigma_f$ | Macroscopic neutron fission cross section [$cm^{-1}$] |
| $\Sigma_s$ | Macroscopic neutron scattering cross section [$cm^{-1}$] |
| $\sigma_s$ | Microscopic neutron scattering cross section [$cm^{-2}$] |
| $\tau_0$ | Core coolant circulation time constant [s] |
| $\tau_{c1}$ | Fuel-cladding-related time constant [s] |
| $\tau_{c2}$ | Cladding-coolant-related time constant [s] |
| $\tau_f$ | Fuel-related time constant [s] |
| $\tau_l$ | Coolant-related time constant [s] |
| $\tau_{pump}$ | Primary coolant pump time constant [s] |
| $\tau_{sg/c}$ | Delay from SG to core [s] |
| $\phi$ | Neutron flux [$cm^{-2}$ $s^{-1}$] |
| $\Phi$ | Dissipation term [W $m^{-3}$] |

**Subscripts**

| | |
|---|---|
| 0 | Steady-state |
| 1 | Sub-cooled region |
| 12 | Interface sub-cooled and two-phase region |
| 2 | Two-phase region |
| 23 | Interface two-phase and superheated region |
| 3 | Superheated region |
| c | Cladding |
| f | Fuel |
| in | Inlet |
| l | Lead coolant |
| out | Outlet |

| | |
|---|---|
| p | Primary side, lead |
| pool | Cold pool |
| s | Secondary side, water |
| sat | Saturation |
| sg | Saturated gas |
| sl | Saturated liquid |
| w | Wall interface |
| wp | Wall interface, primary side |
| ws | Wall interface, secondary side |

# 1. Introduction

The Lead-cooled Fast Reactor (LFR), being one of the six innovative systems selected by the Generation IV International Forum (GIF), is under development worldwide as a very promising fast neutron system to be operated in a closed fuel cycle [1]. In particular, within the 6$^{th}$ and 7$^{th}$ EURATOM Framework Programmes the European LFR community is proposing the ELSY - European Lead-cooled SYstem concept [2], an innovative 600 $MW_e$ pool-type LFR fully complying with the Generation IV goal of sustainability and, in particular, aiming at no net production of Minor Actinides (MAs).

As recognized by the Strategic Research Agenda worked out by the European Sustainable Nuclear Energy Technology Platform (SNETP), LFR complete development requires - as a fundamental intermediate step - the realization of a demonstration plant (DEMO), intended to validate LFR technology as well as the overall system behaviour [3]. Indeed, a demonstration reactor is expected to prove the viability of technology to be implemented in the First-of-a-Kind industrial power plant.

In order to define a first reference configuration of a GEN-IV LFR DEMO, an I-NERI (International Nuclear Energy Research Initiative) agreement between the National Agency for the New Technologies, Energy and Environment (ENEA) and Argonne National Laboratory (ANL) has been signed in 2007. From the Italian side the work is being carried out in the frame of the national R&D programme on "New Nuclear Fission" supported by the Italian Minister of Economic Development (MED) through a general Agreement with ENEA and the Italian University Consortium for the Nuclear Technological Research (CIRTEN).

In such a context, a reference configuration for a 300 $MW_{th}$ pool-type LFR DEMO is being developed and a static neutronics and thermal-hydraulics characterization has been accomplished [4].

Due to the need of investigating reactor responses to power and temperature transients, an approach concerning the simulation of DEMO primary loop dynamics has been developed, in order to provide a helpful tool in this early phase of the reactor pre-design - in which all the system specifications are still considered to be open design parameters - allowing a relatively quick, qualitative analysis of fundamental dynamics and stability aspects that cannot be left aside when refining or even finalizing the system configuration. In fact, reactor dynamics is of primary importance for the study of plant global performances and for the design of an appropriate control system, since it explains the interactions among input and output variables and the nature of the basic dynamic relationships.

An innovative LFR system needs to be studied by adopting a comprehensive approach involving both statics and dynamics. In this perspective, the need of developing a simulation tool able to provide a high level of information about the plant dynamic behavior in order to define a reliable control strategy has been recognized. Therefore, an effort has been spent aimed at deriving a model able to represent the dynamic behavior of the plant while fulfilling the typical control theory requirements. For these reasons, the approach followed is based on a control-oriented perspective: the low number of variables describing the physical system facilitates its coupling with a control system. Moreover, the linearization of the constitutive equations around different working conditions allows to perform stability analyses and to study the robustness of the dynamic system itself on its entire power range; finally, the simulator needs to be fast-running and flexible.

Starting from such requirements, a zero-dimensional simulator for the primary loop has been developed, with a lumped-parameter core model, consisting in a point-wise kinetics description for neutronics and in a single-channel, average-temperature heat transfer model for thermal-hydraulics.
A moving boundary approach for the steam generator modeling has been opted for, as it has been judged to be the most suitable choice in a control-oriented prospective.
To resume, the goals this tools aims at are:

- providing a helpful tool for design purposes and for finalization of the system configuration;
- obtaining fundamental feedbacks on safety and stability, also through a Linear Time-Invariant (LTI) approximation;
- obtaining information about the different candidate core materials dynamic characteristics and performance (e.g., both MOX and metal are envisioned as fuel alternative options [4, 5]);
- studying the system fundamental dynamic aspects through a both qualitative and quantitative transient design-basis analysis by investigating typical scenarios such as Unprotected Loss of Heat Sink (ULOHS), Unprotected Loss of Flow (ULOF) and Unprotected Transient of OverPower (UTOP) events;
- establishing the guidelines for the conception of an appropriate control system thanks to the feedbacks given by the previous point.

## 2. Reference System Description

In this section the reference reactor configuration is briefly described, as it represents the basis for the development of DEMO dynamic simulator.

### 2.1 System Layout

DEMO primary lead loop configuration is shown in Figs. 1 and 2 [6]. The coolant flow from the cold pool enters the core through an open region (there is no core support nor flow distribution structure beneath the core). Once the coolant flow passes through the core, it is collected in a volume (called hot collector) to be distributed to eight parallel pipes. The pipes deliver hot coolant to eight pump/steam generator (SG) modules, where the coolant is pumped first into the volume in the middle of the SG and then flows radially through the heat exchanger (HX). The coolant leaves the SGs at their outer circumference and enters the cold pool from which it returns to the core.
Atop of the hot collector, there is a pool of coolant which is called bypass pool. The coolant temperature in this pool at normal operating conditions is the same as in the cold pool. To keep such a temperature, there is a bypass flow from the cold pool into the bypass pool and then back to the hot collector. Currently, 1 % of the total loop

flow is assumed for the bypass pool flow. The fuel assemblies are supported from the top and the assembly structure above the core extends through the hot collector, bypass pool, and the cover gas region above.

The highest coolant level is achieved in the pump discharge volume located inside the SGs. From this pool, the flow is driven by the hydrostatic pressure of the pool level differences first through the SGs into the cold pool and then through the core into the hot collector. Thus the pressure in the hot collector is the lowest pressure of the system. The hot collector is a liquid-only volume (i.e., there is no cover gas) but it is connected to the bypass pool by means of the bypass flow. As such, the hydrostatic pressure in the hot collector is the same as that in the bypass pool (minus the flow resistance of the bypass flow). Since the flow through the SGs and the core is driven by the hydrostatic pressure differences in the corresponding pools, the liquid surface levels in those pools are defined by the pressure loss in those components. The pressure drop in the SGs defines the difference in levels between the pump discharge volume and the cold pool. The pressure drop in the core defines the differences between the liquid levels in the cold pool and the bypass pool.

The Argon cover gas is assumed to be at 1 atm pressure in all pools.

The pump impeller is located 0.5 m below the cold bypass pool level to provide the required net positive suction head for the pump.

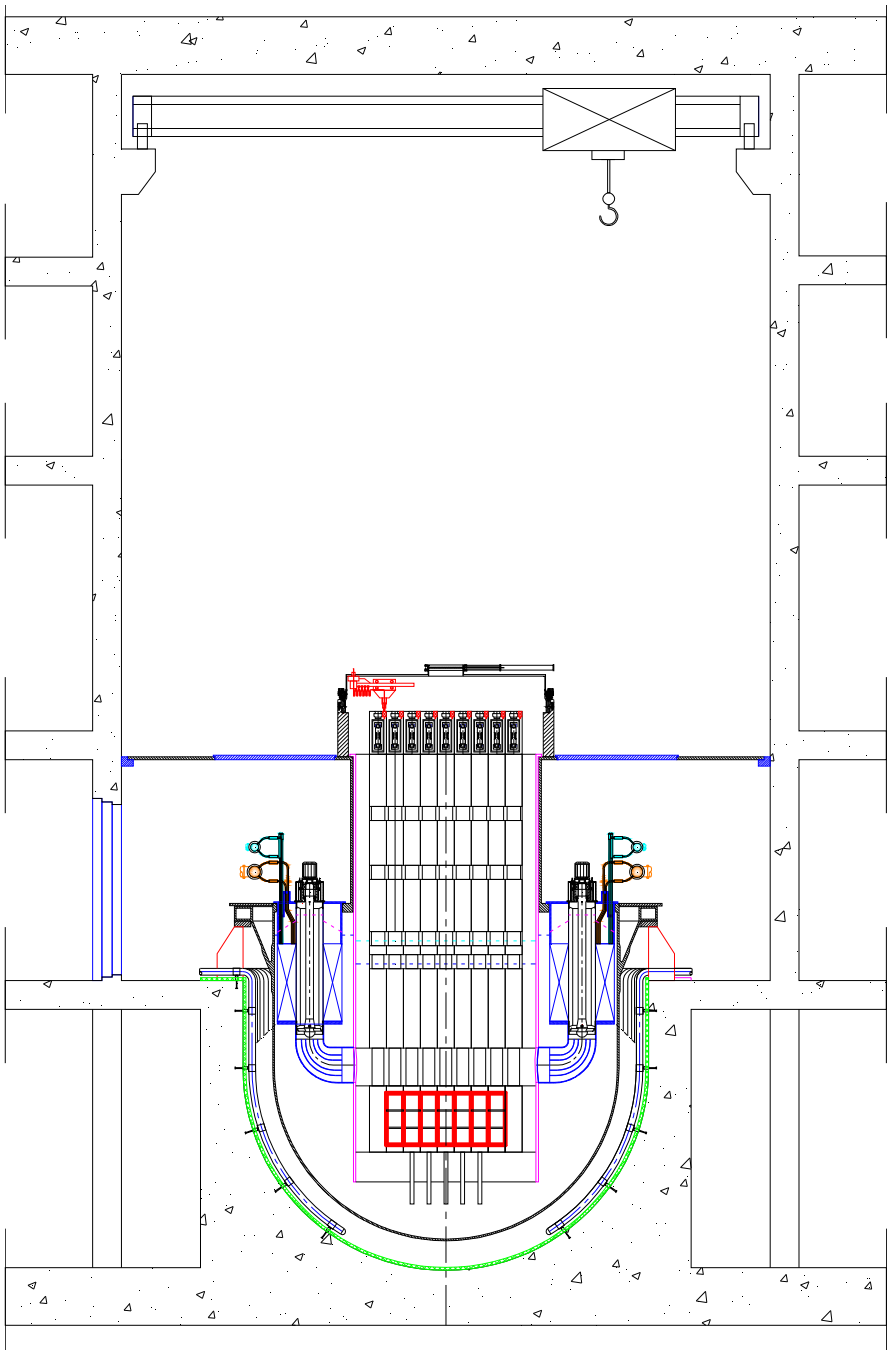

**Figure 1. DEMO reactor block – elevation.**

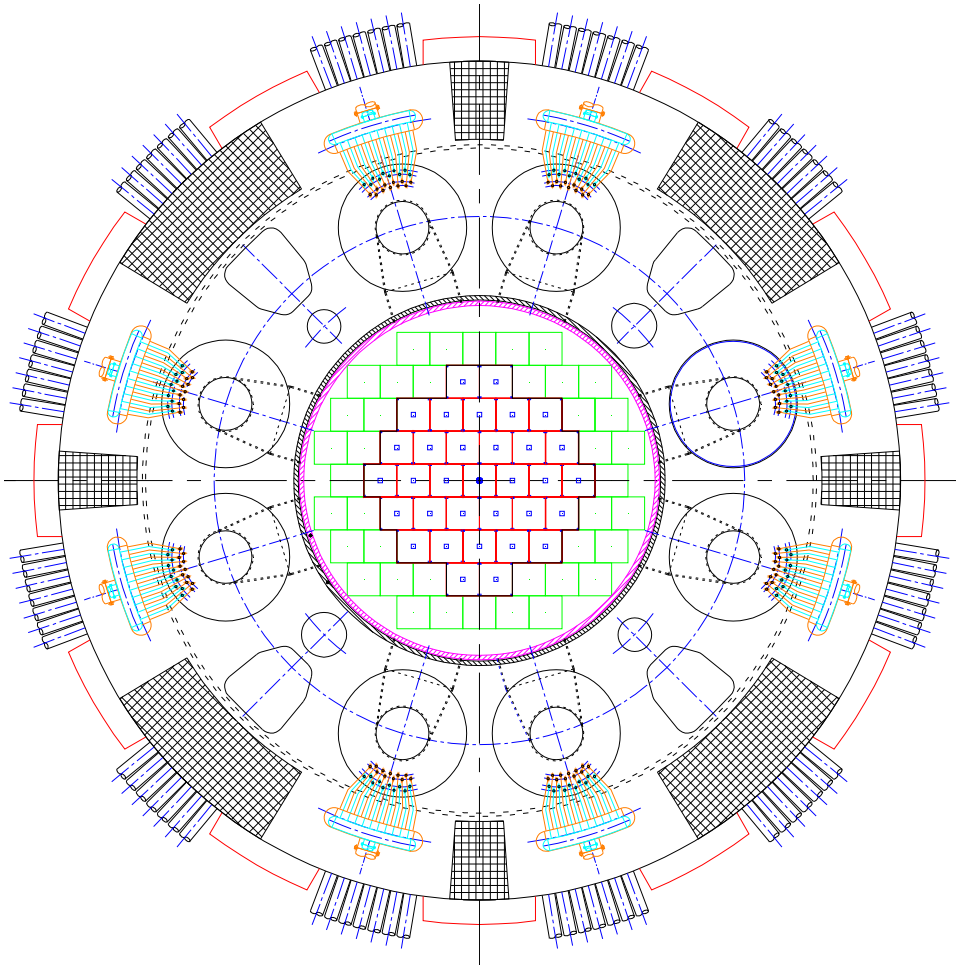

**Figure 2. DEMO reactor block – cross section.**

## 2.2 Components

### 2.2.1 Core

In the current design [4], conventional MOX with Reactor Grade Plutonium (RGP) has been considered as the reference fuel for DEMO, according to the needs of both meeting a reasonably early schedule – as it is the most mature and experience-based fuel form for power reactors in Europe, for which there are several qualified industrial suppliers -, and pursuing the major goal of ELSY representativeness.

Nevertheless, metallic fuel [7] (more precisely, a U-Pu-Zr ternary alloy), for which great experience and database are available in the United States, has been taken into consideration as an alternative option [5] due to the expected superior safety response to operational transients and postulated accidents that metal provides, compared to oxide, might eliminate the practical need for certain safety features required with oxide fuel, such as the capability to withstand core melting scenarios or energetic core disruption.

***MOX-fuelled core option***

In the MOX option [4], DEMO features a 300 $MW_{th}$ core, composed by 24 ductless Fuel Assemblies (FAs) surrounded by dummy assemblies (Fig. 3); in Fig. 4 a 2-D *RZ* representation of the vertical section that yields a useful scheme for the main structural zones is provided. Ensuing from criticality assessment and power flattening, 10 FAs with 29.3 wt.% plutonium fraction constitute the inner zone, and 14 FAs with 32.2 wt.% plutonium fraction compose the outer zone. Hollowed pellets are taken into account in order to achieve a higher linear power and a higher burn-up without undergoing the risk of compromising the pin integrity. As far as FA design is concerned, fuel pins are arranged in a 28×28 square lattice; every FA is provided with four structural uprights at corners connected with the central FMS T91 box voided channel replacing 6×6 central positions.

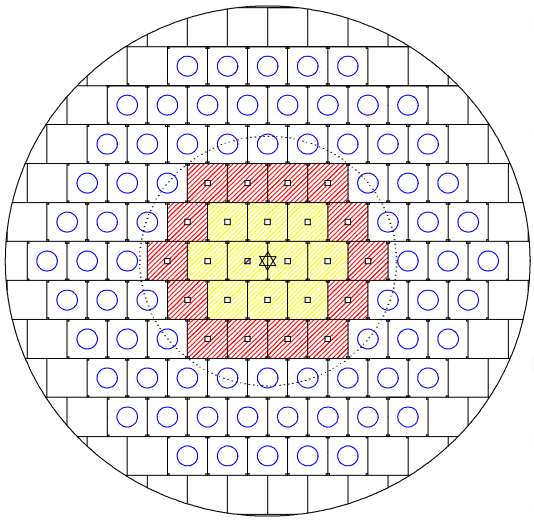

**Figure 3. DEMO core layout.**

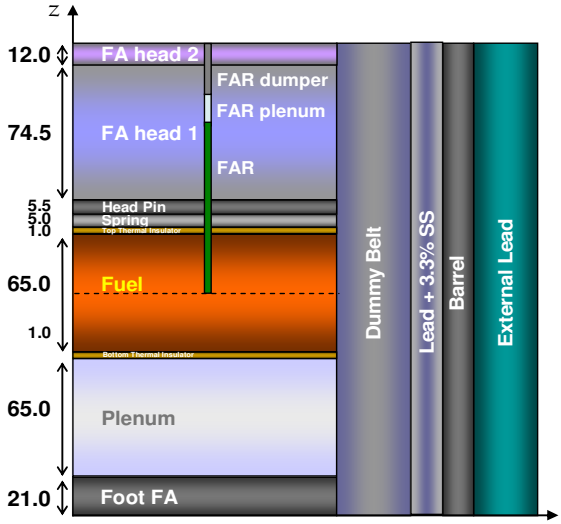


**Figure 4. MOX-fueled DEMO core 2-D *RZ* cylindrical section; dimensions in cm.**

In Tab. I, the main DEMO core specifications are summarized.

**Table I. MOX-fueled core option specifications.**

| Parameter | Value | Units |
|---|---|---|
| Thermal power | 300 | $MW_{th}$ |
| Average coolant outlet temperature | 480 | °C |
| Coolant inlet temperature | 400 | °C |
| Average coolant velocity | 3.0 | m $s^{-1}$ |
| Cladding maximum temperature | 600 | °C |
| Cladding outer diameter | 6.00 | Mm |
| Cladding thickness | 0.34 | Mm |
| Pellet outer diameter | 5.14 | Mm |
| Pellet hole diameter | 1.71 | Mm |
| Fuel column height | 650 | Mm |
| Fuel rod pitch | 8.53 | Mm |
| Number of pins/FA | 744 | - |
| SS box beam inner/outer width | 45.65/48.65 | Mm |
| Number of inner/outer FAs | 10/14 | - |
| Pu fraction inner/outer zone | 29.3/32.2 | wt.% |

In Tab. II DEMO key neutronics performances at Beginning of Cycle (BoC) and End of Cycle (EoC) are resumed.

**Table II. DEMO MOX-fueled neutronic features.**

| Parameter | BoC | EoC | Units |
|---|---|---|---|
| Multiplication factor, $k_{eff}$ | 1.00033 | 1.00093 | - |
| Reactivity, $\rho$ | 33 | 93 | pcm |
| Total peaking factor | 1.43 | 1.40 | - |
| Peak power/FA distribution factor | 1.20 | 1.20 | - |
| Average power density | 327 | 328 | W $cm^{-3}$ |
| Peak total neutron flux, $\varphi$ | 7.27 | 7.54 | $10^{15}$ $cm^{-2}$ $s^{-1}$ |
| Neutron flux fast fraction (E > 0.82 MeV) | 16 | 15 | % |
| Average/peak discharge burn-up | 90 / 130 | | MWd $kg^{-1}$ (HM) |

Two different and independent Control Rod (CR) systems have been envisaged to guarantee the required reliability for reactor shut-down and safety, for which at least 3000 pcm have been requested to be supplied by each absorber set. An innovative system is foreseen both for ELSY and DEMO: a sparse control made by Finger Absorber Rods (FARs) inserted in the center of each FA. This solution permits to regulate locally the power provided by each FA also in relation to the lack of the possibility to vary the mass flow rate in single FAs [4, 5, 8].

Four passive boron carbide ($B_4C$) with 90 at.% enrichment in $^{10}B$ FARs have been foreseen exclusively for SCRAM purposes. Furthermore, a motorized FAR system demanded for cycle reactivity swing control and safe shut-down has been provided. Every remaining FA has been provided with a $B_4C$ (42 at.% enriched in $^{10}B$) FAR so that the required worth (approximately 7000 pcm, i.e. 3000 for back-up SCRAM and 4000 for reactivity swing compensation) was assured. In Fig. 5 a section of the core with control and safety rods is represented; in Fig. 6 the compensation/regulation FAR set insertion curve is depicted.

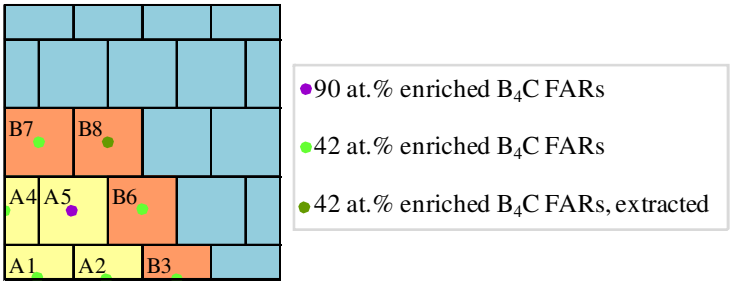


**Figure 5. Core layout with control/regulation and safety FARs positioning in the core.**

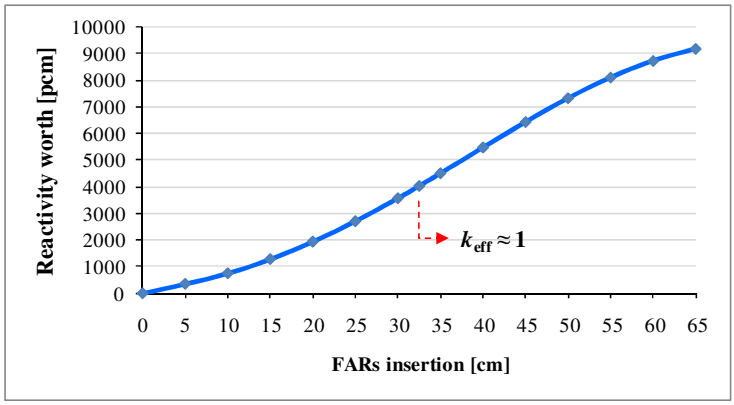


**Figure 6. Regulation/compensation FAR set reactivity insertion curve.**

***Metal-fueled core option***

Based on the MOX-fueled core described above, an analogue design approach has been adopted and an optimization study has been performed to define a core able to accomplish the foremost objective of reaching a high fast neutron flux while meeting all technological constraints.

The fuel element design has been revised in light of the irradiation experience with metallic fuel in Experimental Breeder Reactor (EBR-II), suggesting that a suitable smear density to achieve high burn-up without affecting the pin integrity lies in the range of 75 ÷ 85 %, and the ratio of plenum height to fuel active core height must vary within 1 and 1.5. An innovative particulate metallic fuel form not requiring a sodium bond [7], whose composition is presented in Tab. III, has been envisaged. The neutron spectrum with metal fuel is harder, with an associated smaller Doppler effect, compared to oxide cores, since no moderation from oxygen is present.

**Table III. Metallic fuel composition.**

| Element | Molar fraction (MF) |
|---|---|
| Zirconium | 0.1 |
| Uranium | 0.658 |
| Plutonium | 0.242 |

The resulting metal-fueled DEMO features a 300 $MW_{th}$ core composed by 24 wrapper-less FAs, but with slightly lower plutonium fractions (25.3 wt.% for the inner zone, and 27.9 wt.% for the outer zone) compared to the MOX fuel case. In Fig. 7 the *RZ* core section of the metal-fueled DEMO is provided. The main difference with MOX regards the active length, due to the requirements imposed by the use of metallic fuel instead of MOX.

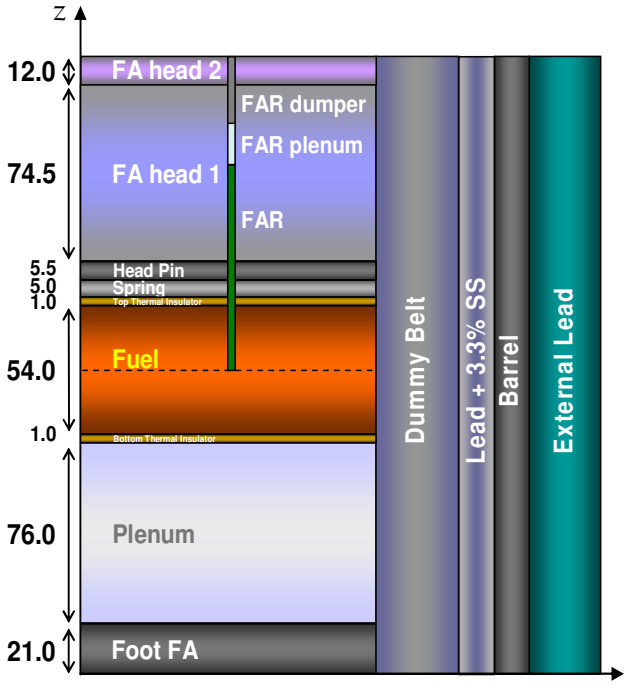


**Figure 7. Metal-fueled DEMO core 2-D *RZ* cylindrical section; dimensions in cm.**

In Tab. IV, the main DEMO metal-fueled core specifications and neutronics performances are summarized.

**Table IV. Metal-fueled core specifications and neutronic performances.**

| **Specification** | **Value** | | **Units** |
|---|---|---|---|
| Thermal power | 300 | | $MW_{th}$ |
| Average coolant outlet temperature | 480 | | °C |
| Coolant inlet temperature | 400 | | °C |
| Average coolant velocity | 3 | | m $s^{-1}$ |
| Cladding maximum temperature | 600 | | °C |
| Cladding outer diameter | 6.00 | | mm |
| Cladding thickness | 0.34 | | mm |
| Fuel porosity | 25 | | % |
| Fuel outer diameter | 4.59 | | mm |
| Fuel column height | 540 | | mm |
| Gas plenum height | 760 | | mm |
| Fuel rod pitch | 8.53 | | mm |
| Num. of pins/FA | 744 | | - |
| SS box in/out width | 45.65/48.65 | | mm |
| Num. of in/out FAs | 10/14 | | - |
| Pu in/out fraction | 25.7/27.9 | | wt.% |
| **Performance** | **BoC** | **EoC** | **Units** |
| $k_{eff}$ | 1.00025 | 0.99844 | - |
| Reactivity, $\rho$ | 25 | - 156 | pcm |
| Total peaking factor | 1.41 | 1.42 | - |
| Power/FA distribution | 1.20 | 1.20 | - |
| Average power density | 365 | 364 | W $cm^{-3}$ |
| Peak tot neutron flux, $\varphi$ | $7.37 \cdot 10^{15}$ | $7.80 \cdot 10^{15}$ | $cm^{-2}$ $s^{-1}$ |
| Fast flux (E>0.82 MeV) | 17 | 16 | % |
| Average / Peak Discharge burn-up | 80 / 112 | | MWd $kg^{-1}$ (HM) |

### 2.2.2 Steam Generator Block

For the preconceptual design of DEMO, the ELSY SG configuration has been borrowed [6]. In ELSY, SGs and main coolant pumps are part of eight removable integrated modules (Figs. 8 and 9). Such innovative SGs offer several advantages in terms of cost, safety, reactor operability, and lead flow path simplicity.

The SG tube bundle (Fig. 9) is composed by a stack of spiral tubes arranged in the bottom-closed, annular space formed by the perforated outer and inner shells of the SG itself. The inlet and outlet ends of each tube are connected to the feed water and steam headers, respectively, both above the reactor roof (Fig. 10).

An axial-flow primary pump, located inside the inner shell, provides the head required to force the coolant to flow radially from the inner to the outer perforated shrouds through the SG spirals tubes. Therefore, the hot primary coolant enters the pump-SG assembly from the bottom and flows radially through the SG spiral tubes arranged at different vertical levels. This ensures that the coolant flows over the SG bundles even in the event of reduction of the primary coolant level in case of leakage from the reactor vessel.

The installation of SGs inside the reactor vessel is a major challenge of a LFR design which includes the need of a sensitive and reliable leak detection system and of a reliable depressurization and isolation system. In ELSY and therefore DEMO careful attention has been given to the issue of mitigating the consequences of the SG tube rupture accident to reduce the risk of pressurization of the primary boundary; to this end, innovative provisions have been conceived which make the primary system more tolerant of the SG tube rupture event [6].

The installation of the pump impeller at an immersion depth of a few meters in lead ensures a realistic net positive suction head and consequently a short pump shaft is sufficient to connect the pump impeller to the pump

motor located on the reactor roof. No supporting bearing in lead is necessary. The location of the pump shaft and impeller inside the SG inner shell makes the SG and associated primary pump almost a single unit and contributes to the compactness of the primary system.

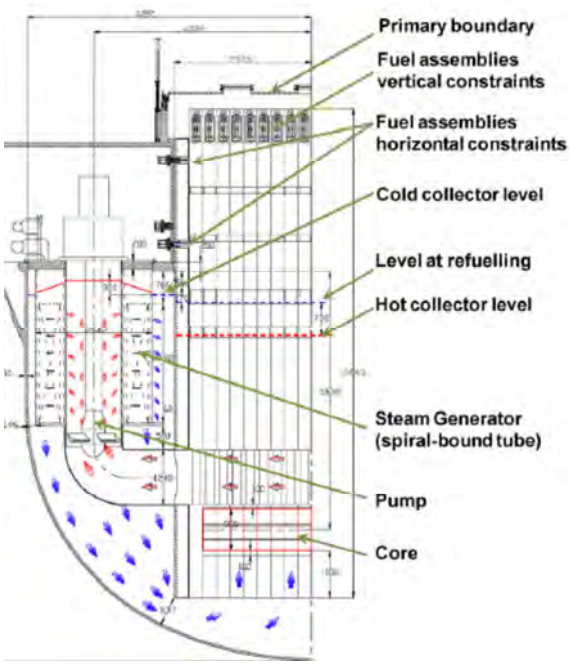


**Figure 8. ELSY SG/primary pump arrangement.**

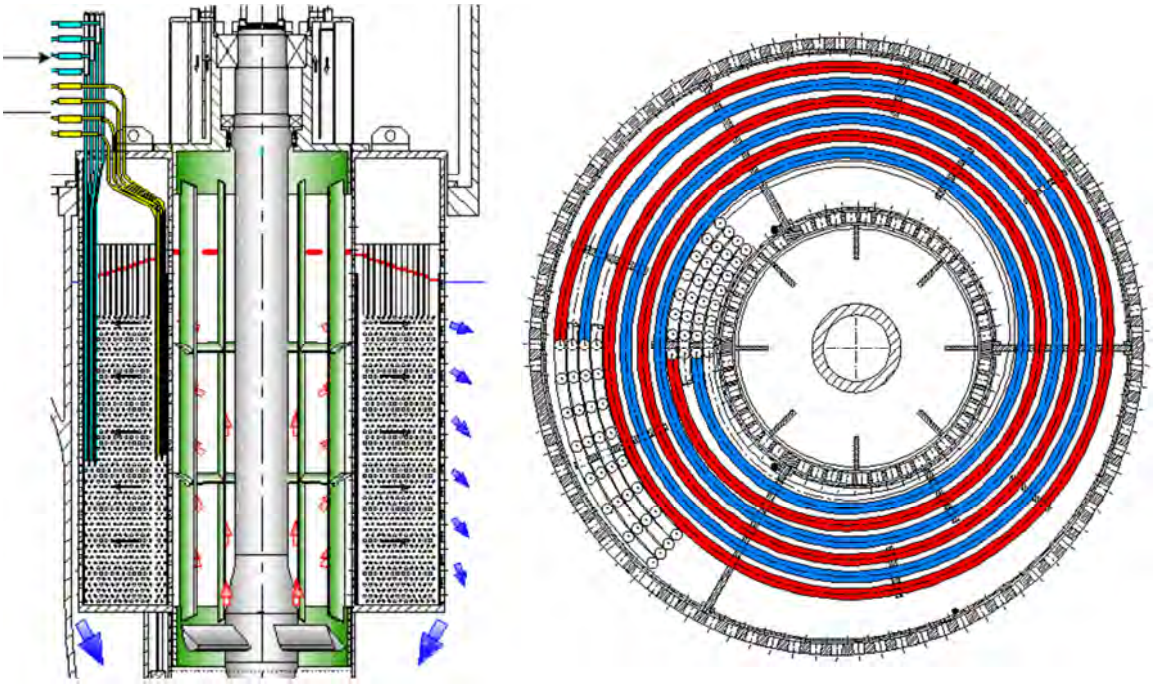

**Figure 9. Steam generator and primary pump unit (left); spiral wound SG tube layer (right).**

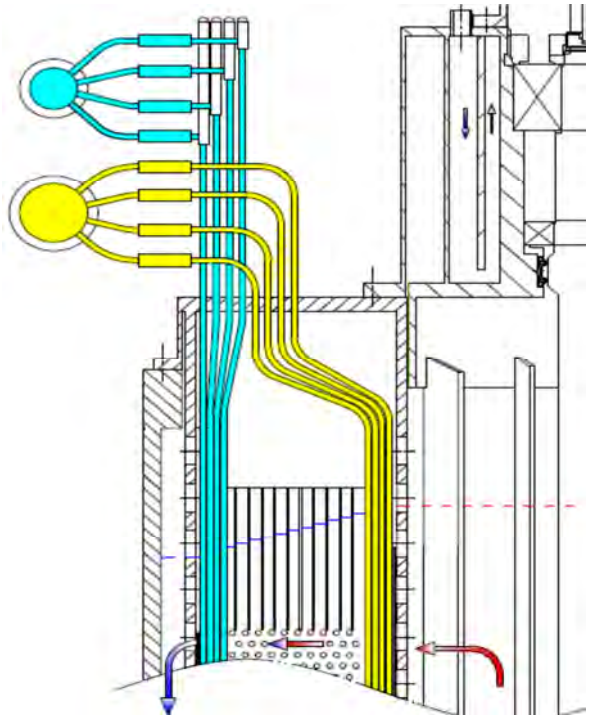

**Figure 10. Steam generator collectors arrangement.**

Redundant, diverse Decay Heat Removal (DHR) capability is provided with:

- steam condensers on the steam loops, DHR1 (Fig. 11);
- direct reactor cooling loops with innovative lead-water dip coolers using storage water at ambient pressure, DHR2-DRC (Fig. 12);
- a Reactor Vessel Air Cooling System (RVACS).

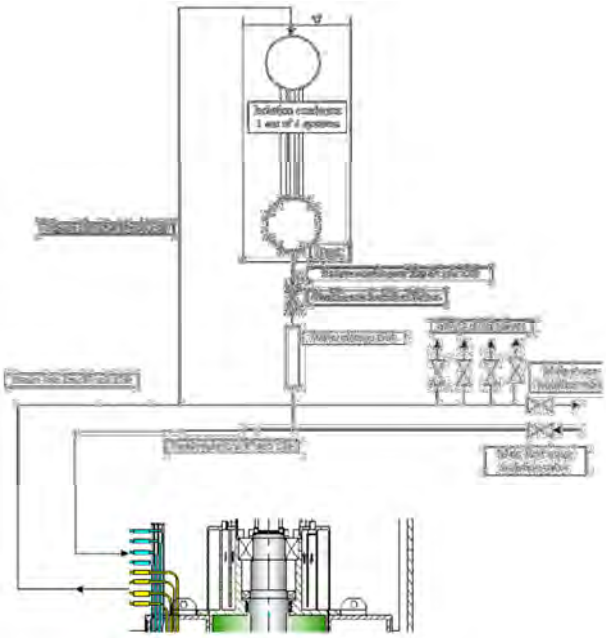

**Figure 11. DHR1 connected to SG (1 out of 4).**

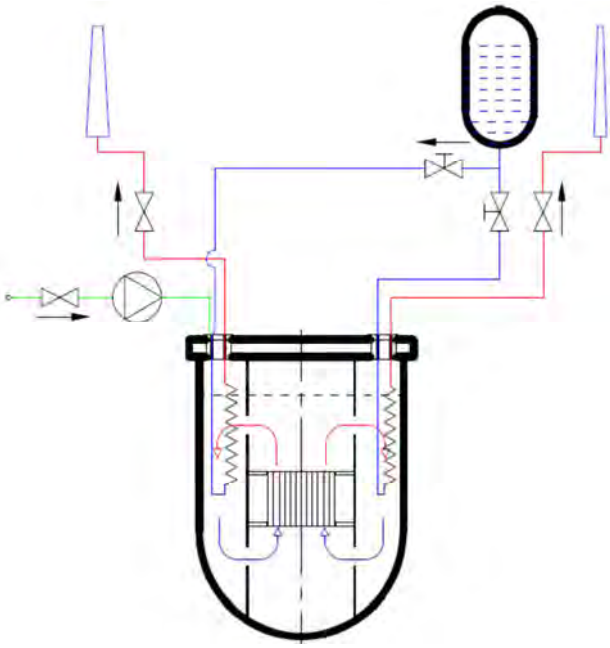

**Figure 12. DRC W-DHR (right-side) and WA-DHR loops.**

The Direct Reactor Cooling (DRC) system is equipped with coolers immersed in the primary system. Stringent safety and reliability requirements of the DRC system are achieved by redundancy and diversification. The DRC system is made of four loops: two loops operating with water (the W-DHR loops) and the remaining loops with water and/or air (the WADHR loops). Each W-DHR loop is made of a cooling water storage tank, a water-lead dip cooler, interconnecting piping, and steam vent piping to discharge steam to the atmosphere.

Many advantages are obtained from this configuration:

- compactness;
- reduced number of tubes;
- resistance to thermal loads;
- elimination of the risk of failure of the water and steam collectors inside the primary boundary by installing them outside the reactor vessel;
- any leaking tube is promptly isolated with check valves on each tube close to the steam header and of a Venturi nozzle close to the feedwater header;
- risk of potentially disruptive pressure surges within the reactor vessel prevented by design features that are fully passive and are actuated by pressurization in the SG bundle ensuring that the flow of any feedwater-steam primary coolant mixture be re-directed upwards.

The innovative reactor primary pumps layout improves several safety-related aspects, such as a moderate volume of the hot collector and a large volume of the cold collector in which DHR coolers are immersed. This favors natural circulation and eliminates the interference between hot coolant streaming from the core and cold coolant from the outlet of the DHR coolers.

Furthermore the free-level of the cold collector, in normal operation, is higher than the free-level of the hot collector, thanks to the pump installation in the hot leg. This, in case of primary pump coast-down, favors a mild

transition from forced to natural circulation of the coolant and hence ensures adequate heat removal from the core during a transient.

### 2.2.3 Pool

The adoption of a pool-type reactor configuration and the installation inside the reactor vessel of a new-design, short-height SGs with integrated mechanical pumps have been the main provisions to fulfill the design goal of compactness.

The reactor vessel is shaped as a cylinder with hemispherical bottom head and flat roof. The lead free surface level is kept sufficiently below the roof to allow for a gentle thermal gradient between the vessel in contact with lead and the colder roof. The reactor vessel is not supported directly by the roof as in most LFR designs, but by a forged Y-piece, the outer leg of which is supported by the ring beam anchored to the reactor pit with the inner leg supporting the roof.

The latter is made of an annular thick plate with penetrations for the dip components and of a large-diameter central up-stand that accommodates the core structures above, including the upper heads of fuel elements.

The safety vessel is anchored in the reactor pit and protected, reactor-side, by a thermal insulation and kept cold by the reactor concrete cooling system. The cold collector is located in the annular space between the reactor vessel and the cylindrical inner vessel. The gas plenum above the lead free level is filled with Argon.

A peculiar, innovative solution of DEMO is the cylindrical inner vessel provided with ducts branching out from its lower part, each duct feeding hot lead to one SG. The cylindrical inner vessel provides also for the lateral restraint of the core, but in contrast to previous solutions, it is not connected to a core support plate.

# 3. Primary Loop Model

The primary loop model, composed by core, steam generators, primary pump and pool is developed by assembling the single components models, as described in the following sections.

## 3.1 Core Model

A lumped-parameter model, reckoning with all the main feedbacks following a reactivity change in the core, has been developed to treat both neutronics and thermal-hydraulics (T/H). The reference analytical core model has been developed through first-principle equations: it employs a zero-dimensional approach for the coupled kinetics (six delayed neutron precursor groups formulation) and T/H, with continuous reactivity feedback due to temperature effects.

Hence it is composed by three main blocks: kinetics, thermal-hydraulics and reactivity, depicted in Fig. 13. Firstly, the reactor neutronics behavior is described by employing a point-wise approximation; afterwards, the thermal exchange is analyzed thorough heat transfer equations considering core-averaged temperatures; finally, the feedback contributions due to temperature effects and expansions are accounted by a linear relation. In particular, the last block connects the T/H output (temperatures) with the kinetics input (reactivity). In this way it easy to obtain a close loop system, that considers the several influences of the physics involved.

The input variables chosen to manipulate the model are:

- lead inlet temperature, $T_{in}$;
- lead mass flow rate, $\Gamma$;
- control rod (CR) insertion length, represented by the height, $h_{cr}$.

The first two variables depend on the thermal exchange occurring in the SG, even if in the first stage of this work they are treated as inputs, while the CR height is always an user-programmed input variable.

The state variables that have been considered are:

- neutron population, $n$;
- precursor densities for the six groups, $c_i$;
- fuel temperature, $T_f$;
- cladding temperature, $T_c$;
- average lead temperature, $T_l$.

The output variables are, in addition to the state ones mentioned above:

- reactor thermal power, $q$;
- lead outlet temperature, $T_{out}$;
- reactivity $\rho$ with its components.

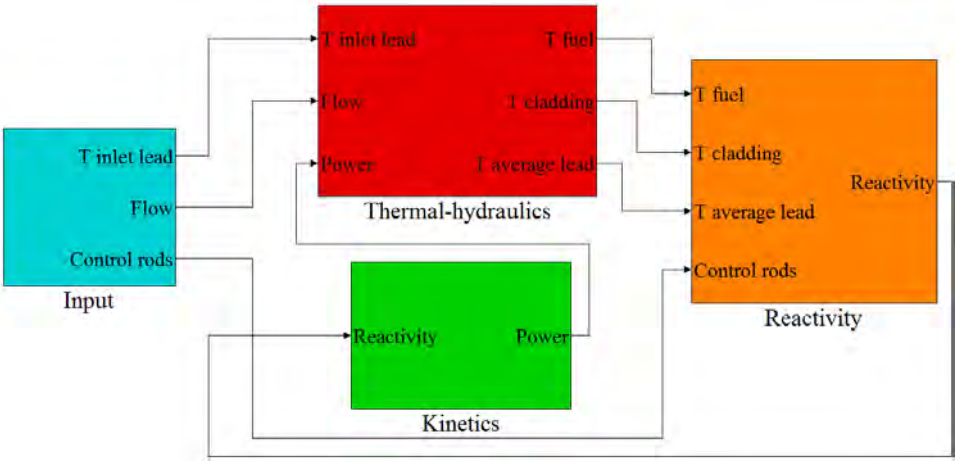


**Figure 13. Core model with blocks and variables.**

### 3.1.1 Non-linear reference model

#### *3.1.1.1 Analytical formulation*

A simplified block-scheme of DEMO core has been adopted, assuming it to consist only of the active core, disregarding both upper and lower plena. The T/H sub-system has been described by single-channel conservation equations, whose representative fuel, cladding and coolant temperatures have been determined through an energy balance over the average pin surrounded by coolant; in these conservation equations reactor power is an input variable retrieved from neutron kinetics, coherently with the approximation of accounting only the total power generated by fission, thus neglecting the contribution of decay heat. The so-calculated T/H parameters have been finally employed to insert the reactivity feedbacks into the neutronics equations.

The reference model in this work is non-linear, zero-dimensional with six precursor groups kinetics. A benchmark analysis with the widely recognized SAS4A/SASSYS-1 Liquid Metal Reactor Code System [9] has been carried out with the purpose of providing verification for the analytical outcomes and indicating how the latter relate to more realistic one-dimensional calculations before proceeding with dynamics analyses.

The three main blocks of the model will be discussed in the following sections.

***Kinetics***

A point-wise kinetics approximation with a six delayed neutron precursor groups formulation is used to develop the neutronics block. The principal hypotheses for this model regard the neutron flux, which is assumed to be not dependent on space, and its energy spectrum, which is considered independent of neutron level. Thus, the core is treated as a lumped source of neutrons, with population and flux related by a constant of proportionality (single energy group), in which the total power is generated only by fission events, neglecting the contribution of decay heat. In addition, neutron and precursor densities are considered separable in time and space, such an assumption being valid if the system is approaching the critical state and if there are no large localized perturbations.

Despite the simplicity of this model, a separation between the behavior of prompt and delayed neutron is necessary. This purpose can be reached by introducing the fraction of delayed neutrons $\beta$, and the six precursor groups represented by $c_i$ with their respective fractions $\beta_i$ and time constants $\lambda_i$.

The equations used to describe kinetics behavior can be retrieved with long calculations from diffusion equation and Fick's law. In this context the system equations are obtained just with a simple balance regarding the neutron life cycle.

The neutron density variation may be expressed as:

$$\frac{dn}{dt} = P_p + P_r - A_n - F + S \tag{1}$$

Where:

- $dn/dt$ is the time variation of neutron population;
- $P_p$ is the rate of prompt neutron production by fission;
- $P_r$ is the rate of delayed neutron production by the decay of precursors;
- $A_n$ is the rate of neutron absorption by non-fissile materials, $(n, \gamma)$ capture or, generally, absorption without release of neutrons;
- $F$ is the rate of neutron leakage from the active core;
- $S$ is the rate of neutron production by an external source. This term is crucial in the reactor start-up but it is typically negligible during full power operation.

Prompt neutron production is obtained as the number of prompt neutrons emitted per fission ($\nu\cdot(1-\beta)$) multiplied by the number of fissions occurred ($\Sigma_f\cdot\varphi=\Sigma_f\cdot n\cdot v$). Delayed neutron production can be related to the precursor decay constants multiplied by their densities and summated over all the six groups ($\Sigma\lambda_i\cdot c_i$).

The leakage term is retrieved from diffusion theory and is proportional to neutron flux ($D_n\cdot B^2\cdot n\cdot v$), while absorptions are connected to the probability of absorption reactions ($\Sigma_a\cdot n\cdot v$).

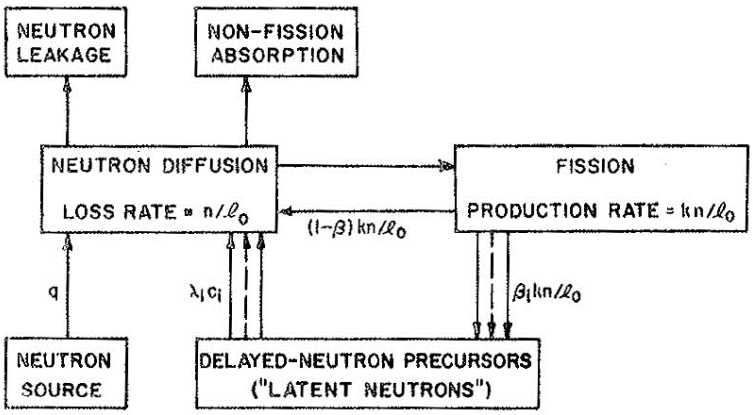


**Figure 14. Simplified neutron cycle.**

Therefore Eq. (1) can be written as:

$$\frac{dn}{dt} = \nu(1-\beta)\Sigma_f nv + \sum_{i=1}^{6} \lambda_{d,i} c_i - \Sigma_a nv - DB^2 nv \quad (2)$$

After some algebraic calculations, the following seven equations are obtained:

$$\frac{dn(t)}{dt} = \frac{\rho(t)-\beta}{\Lambda} n(t) + \sum_{i=1}^{6} \lambda_{d,i} c_i(t) \quad (3)$$

$$\frac{dc_i(t)}{dt} = \frac{\beta_i}{\Lambda} n(t) - \lambda_{d,i} c_i(t) \quad (4)$$

Equations (3) and (4) represent seven Ordinary Differential Equations (ODEs): Eq. (3) is a non-linear equation for neutron density (due to the product between reactivity and neutron density, both state variables) and Eqs. (4) are six linear equations for precursor densities. The main drawback of this model is the impossibility to describe a spatial dependence of the neutron population behavior, since the relationship between the latter and thermal power leads to the impossibility to map the thermal power density within the core.

***Thermal-hydraulics***

Thermal-hydraulics is treated by introducing an average-heat-exchange single-node model and adopting a zero-dimensional approach, coherently with the adoption of the point kinetics approximation.

Three main zones involved in thermal exchange are identified in the core, whose temperatures are significant from a safety point of view. In addition to the fuel and coolant regions, it is necessary to include the cladding temperature into the model: this improvement is due to the constraining problem of steel corrosion in a lead environment that obliges to keep under control this key parameter during transients. In particular cladding temperature must not exceed 550°C in operational transients, while in accidental transients the overtaking of this limit is allowed only for a short time, of the order of half an hour. In Fig. 15 the heat exchange between the involved zone is represented.

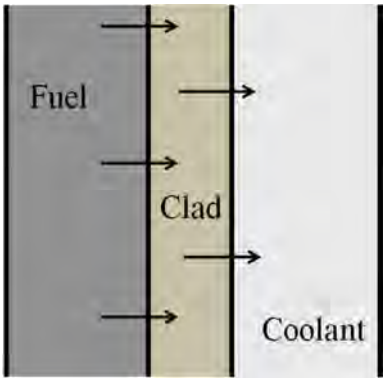


**Figure 15. The three zones considered for the T/H model.**

The main assumptions of the model are:

- the characteristic temperatures are written as mean values over the entire core, allowing to evaluate the average conditions of the different channels;
- lead is considered single phase, thanks to its high boiling point (1750 °C);
- thermal resistances are taken constant and calculated at nominal power;
- axial conduction is neglected since the axial temperature gradient is smaller than the radial one: this effect is due to the geometry of the fuel pins, where the *L/D* (length over diameter) ratio is much greater than 10.

For each zone an ODE represents the energy balance as follows:

$$M_f C_f \frac{dT_f(t)}{dt} = q(t) - k_{fc}\left[T_f(t) - T_c(t)\right] \tag{5}$$

$$M_c C_c \frac{dT_c(t)}{dt} = k_{fc}\left[T_f(t) - T_c(t)\right] - h_{cl}[T_c(t) - T_l(t)] \tag{6}$$

$$M_l C_l \frac{dT_l(t)}{dt} = h_{cl}[T_c(t) - T_l(t)] - 2\Gamma C_l[T_l(t) - T_{in}(t)] \tag{7}$$

where:

$$T_l = \frac{T_{in} + T_{out}}{2} \tag{8}$$

It is important to observe that lead temperature is calculated as the arithmetical mean between the core inlet and outlet temperatures.

The conductive thermal exchange coefficient between fuel and cladding ($k_{fc}$) and convective coefficient between cladding and coolant ($h_{cl}$) are determined by using a separate, multi-zone fuel pin model which takes the temperature distribution from the fuel centerline to the cladding surface into account. Calculations are performed in correspondence with the average nominal temperatures and the parameters obtained are kept constant throughout the dynamic analyses.

The fission power generated within the fuel is taken from the neutron kinetics equations according to Eq. (9), where the subscript 0 indicates steady-state values, and is treated as an input for the heat transfer dynamic model:

$$n(t)/n_0 = q(t)/q_0 \tag{9}$$

***Reactivity***

In the previous sections, the kinetics influence on T/H through the thermal power has been underlined. In order to develop a model with feedbacks, it is necessary to introduce a time-dependent reactivity function with the T/H

influence on it. In fact, during a reactivity variation (e.g., extraction of control rods) some feedback effects occur to balance the reactivity insertion.

In this work, a linear relation for reactivity effects is adopted. Actually it is a time and temperature dependence since reactivity feedback coefficients change with temperature and thus with time. Instead, the linear expression is characterized by constant coefficients, (both in time and temperature), calculated as average values.

In the present work only those reactivity effects which are relevant during the time interval of the typical plant transients analyzed (of the order of a tenth minutes) are accounted for, namely: Doppler (fuel temperature dependent), coolant density (i.e. temperature), core radial and axial expansions. All this phenomena can be traced back to a variation of characteristic temperatures, and through an associated feedback coefficient the ensuing reactivity variation can be calculated.

It is clear that the Doppler coefficient ($\alpha_D$) has to be associated with fuel temperature, as well as the coolant density feedback is led by lead temperature. Coherently with the assumption of closed gap between fuel and cladding at both BoC and EoC, the axial expansion is expressed as a function of the cladding temperature variation. Withal, the radial expansion coefficient is associated with the coolant inlet temperature, since it governs the expansion of the continuous lattice formed by the FA foots [8].

In the non-linear model, the reactivity expression is:

$$\rho(t) = \alpha_D\left[T_f(t) - T_{f0}\right] + \alpha_z[T_c(t) - T_{c0}] + \alpha_l[T_l(t) - T_{l0}] + \alpha_r[T_{in}(t) - T_{in0}] + \alpha_h \Delta h_{cr} \tag{10}$$

which in the linear approximation becomes:

$$\delta\rho(t) = \alpha_D \delta T_f + \alpha_z \delta T_C + \alpha_l \delta T_l + \alpha_r \delta T_l + \alpha_h \delta h_{cr} \tag{11}$$

The respective reactivity coefficients have been estimated for both MOX and metal core configurations at BoC and EoC by means of ERANOS deterministic code [10] ver. 2.1 associated with the JEFF-3.1 data library [11], opting for the two classical procedures of using direct calculations for Doppler and density coolant coefficient and perturbation analyses for the expansion-related ones.

*Doppler effect*

The Doppler coefficient can be expressed as the reactivity variation following a fuel temperature variation:

$$\alpha_D = \frac{\partial \rho}{\partial T_f} \tag{12}$$

The Doppler effect is primarily due to changes in cross section values, in particular the neutron capture ones: its broadening peak involves an enhancement of captures on $^{238}$U.

This effect is associated with a fuel temperature increase, which leads to a neutron energy (and thus velocity) raising. As a consequence, a broadening line (Doppler broadening) occurs due to a spectrum-dependent self-shielding reduction, bringing an increase of resonance captures on $^{238}$U and a resultant reactivity decrease. The

self-shielding phenomenon is lower at high energies than at low ones; in fact, the entity of the Doppler effect in fast reactors is less important than in thermal systems.

This has a significant implications for what concerns fuel options. With MOX, the neutron energy spectrum is shifted to lower energy compared to other fuel options such as metals or nitrides, due to the moderating effect of oxygen. A lower energy spectrum leads to an enhancement of the self-shielding phenomenon and therefore to a higher Doppler coefficient. With metallic fuels, a harder spectrum is expected, and consequently a smaller Doppler effect ensues.

Changes in the Doppler coefficient during the fuel cycle (from BoC to EoC) are difficult to forecast since many effects play a role, such as fuel composition change with burn-up (i.e. build-up of FPs and TRU consumption, etc.) and consequent movement of CRs to compensate the reactivity swing over the cycle.

As mentioned before, the Doppler effect depends strongly on temperature:

$$dk = K_D \frac{dT}{T} \tag{13}$$

where $K_D$ is the Doppler constant [pcm].

For a uniform change in fuel temperature from $T_i$ to $T_f$, the Doppler reactivity effect can be calculated as follows:

$$\rho = \int_{T_i}^{T_f} \frac{dk}{dT} dT = \int_{T_i}^{T_f} \left(\frac{K_D}{T}\right) dT = K_D ln\left(T_f / T_i\right) \tag{14}$$

To calculate an average Doppler coefficient, the total reactivity must be divided by the temperature variation:

$$\alpha_D = \frac{\rho}{T_f - T_i} \tag{15}$$

The Doppler reactivity coefficient is always negative and is responsible for a negative feedback that stabilizes the reactor. In a control-oriented view this aspect is very important because its effects on the system are immediate: a control rod action could be too slow to face a sudden power excursion.

In Tab. V, the Doppler coefficients of DEMO are shown for the four cases considered in this work.

**Table V. DEMO Doppler reactivity coefficient values.**

| | MOX BOC | MOX EOC | MET BOC | MET EOC |
|---|---|---|---|---|
| Initial T [°C] | 1200 | | 700 | |
| Final T [°C] | 1300 | | 750 | |
| ΔT [°C] | 100 | | 50 | |
| $K_D$ [pcm] | -237 | -256 | -138 | -151 |
| $\alpha_D$ [pcm °C$^{-1}$] | -0.15 | -0.17 | -0.14 | -0.15 |

As expected, the MOX fuel option is characterized by a higher Doppler coefficient than the metal one, for the reasons mentioned above.

*Coolant density effect*

The reactivity feedback of coolant density can be evaluated as the reactivity change following a coolant temperature variation:

$$\alpha_l = \frac{\partial \rho}{\partial T_l} \tag{16}$$

The coolant-related reactivity effect is due to the concourse of many contributors, so it is not possible to establish *a priori* which one is predominant and if the coefficient is always negative or not.

In order to figure out the physical mechanism, the following expression for $k_{eff}$ must be considered:

$$k_{eff} = \frac{\nu\Sigma_f}{\Sigma_a^{fuel} + \Sigma_c^{lead} + F} = \frac{\nu\Sigma_f}{\Sigma_{\mathrm{f}}^{\mathrm{fuel}} + \Sigma_c^{fuel} + \Sigma_c^{lead} + F} \tag{17}$$

Regarding fuel, the main contributions to the coolant density coefficient variation are:

- $\nu$, average number of neutrons emitted after a fission event;
- $\Sigma_a^{fuel} = \Sigma_f^{fuel} + \Sigma_c^{fuel}$, captures and fissions occurring in the fuel.

Coolant plays a role for what concerns:

- $F$, neutron leakage term;
- $\Sigma_c^{lead}$, captures occurring in lead.

The main physical phenomenon following a coolant density decrease is a spectral hardening due to a minor moderation by lead. It implies effects mostly on fuel, for which the dominant one is the increase of fission probability $p_F$:

$$\mathrm{p_F} = \frac{\Sigma_{\mathrm{f}}\phi}{\Sigma_{\mathrm{a}}^{\mathrm{tot}}\phi + \mathrm{F}} = \frac{\Sigma_{\mathrm{f}}\phi}{\Sigma_{\mathrm{f}}\phi + \Sigma_{\mathrm{c}}^{\mathrm{fuel}}\phi + \Sigma_{\mathrm{c}}^{\mathrm{mat}}\phi + \mathrm{F}} \tag{18}$$

The predominant contributions to the coolant effect are due to even isotopes – among which $^{238}$U plays a major role (even-even isotope) – because of their fission cross section high sensitivity to spectral hardening (threshold reactions), despite their modest absolute contribution to the total fissions.

Since fission and capture rates depend on neutron flux, the major contribution appears in the inner core zone, decreasing toward the border of the active core, to become almost null in the external zone.

A second effect, less important but not negligible, always regarding fuel, is the increase of $\nu$. Also this effect gives a positive contribution to reactivity.

As to coolant, a significant relative increase in leakage probability is observed after a reduction of coolant density. In diffusion theory, leakage can be written as:

$$F = D\nabla^2\phi = \frac{1}{3\Sigma_{\mathrm{s}}}\nabla^2\phi = \frac{1}{3N_l\sigma_s}\nabla^2\phi \tag{19}$$

In particular the system is more transparent after a density reduction, so that neutrons can escape more efficiently because of a macroscopic absorption cross section global diminution. This is determined by a decrease of both material density (lack of coolant) and microscopic absorption cross section: neutrons interact with less atoms in the core and less efficiently as well, in absolute terms. It is interesting to note from Eq. (19) that the leakage term is strongly dependent on the spatial coordinate through the flux gradient: in the inner zone of the reactor, the gradient is low and the contribution to leakage is minimum; otherwise in peripheral zones the derivative is high and leakages are relevant.

A last effect that must be taken into account is a decrease of captures in lead, due to the change in the absorption cross section, leading to a small reactivity increase.

In DEMO, the dominant contribution is represented by the leakage term, whereas the positive ones are less important due to the small dimensions of the reactor. For the calculation of the coolant density coefficient the entire system is considered (active core with reflector); the reactivity coefficient remains negative even when considering only the active zone. In larger reactors, such as ELSY, the coefficient is positive when considering a density reduction only in the active zone, and slightly negative if the calculations are performed on the entire core [8].

For the coefficient determination, a density decrease of 5 % is taken into account, and is calculated as follows:

$$\left.\frac{\partial k}{\partial T}\right|_l = \frac{\partial k}{\partial(\delta d_l/d_l)}\frac{\partial(\delta d_l/d_l)}{\partial T} \tag{20}$$

The resulting values are collected in Tab. VI.

**Table VI. DEMO coolant density reactivity coefficients.**

| $\alpha_c$ [pcm $K^{-1}$] | MOX BOC | MOX EOC | MET BOC | MET EOC |
|---|---|---|---|---|
| Core + reflector | -1.2267 | -1.1995 | -1.3108 | -1.3903 |
| Core | -0.1763 | -0.2047 | -0.2158 | -0.2544 |
| Active zone | -0.6702 | -0.6475 | -0.7383 | -0.7906 |

*Axial and radial expansions*

Elementary perturbations are now introduced in order to figure the radial and axial expansion reactivity coefficients out through a "partial derivative" approach. Such a method is based on the main hypothesis of superposition principle validity and on the assumption that the system responds linearly within the interval defined by the reference and the perturbed configurations. The following elementary perturbations are applied:

- core radial extension by scaling all radial dimensions, with nominal densities (variation: + 2.5 %);
- core axial extension by scaling all axial dimensions, with nominal densities (variation: + 5 %);
- fuel density reduction (variation: - 5 %);
- steel density reduction (variation: - 5 %);
- absorber density reduction (variation: - 10 %).

The elementary coefficients obtained are combined to compute the axial and radial reactivity coefficients which are described in the following sections.

*Radial expansion*

The radial expansion coefficient can be calculated as the reactivity variation following an inlet temperature variation of the coolant as follows:

$$\alpha_r = \partial\rho\partial T_{in} = \frac{1}{k}\frac{\partial k}{\partial T_{in}} \tag{21}$$

DEMO system design does not foresee the presence of diagrids for FA support and positioning, to guarantee an easy replacement of all the internals during the plant life. To compensate the diagrid removal, a reinforcement of the FA foot and head is necessary to create a continuous-contact lattice with the adjacent assemblies, guaranteeing a correct positioning of FAs [6, 8]. Hence the traditional reactivity effect due to the radial expansion of the diagrid can be calculated thanks to the introduction of the hooping of the FA feet. This way, an enhancement of the coolant inlet temperature makes the FA feet structure expand leading to a global radial expansion.

The elementary coefficients can be properly combined in order to obtain the equivalent effect by radial expansion of the core, according to:

$$\left.\frac{k}{T}\right|_r = \frac{\partial k}{\partial\left(\frac{\delta R}{R}\right)}\frac{\partial\left(\frac{\delta R}{R}\right)}{\partial T} + \sum_{mat}\left(\frac{\partial k}{\partial\left(\frac{\delta d_i}{d_i}\right)}\frac{\partial\left(\frac{\delta d_i}{d_i}\right)}{\partial\left(\frac{\delta R}{R}\right)}\frac{\partial\left(\frac{\delta R}{R}\right)}{\partial T}\right) + \frac{\partial k}{\partial\left(\frac{\delta d_l}{d_l}\right)}\frac{\partial\left(\frac{\delta d_l}{d_l}\right)}{\partial\left(\frac{\delta R}{R}\right)}\frac{\partial\left(\frac{\delta R}{R}\right)}{\partial T} \tag{22}$$

where the first term represents the radial expansion of the entire core, by scaling all the radial dimensions with nominal densities. In this way an expansion of structural materials is considered even if it actually does not represent a real scenario: fuel, cladding and absorber masses cannot change following the considered core expansion. So the second term corrects the overestimation of the densities present in the first term. This correction is proportional to: expansion entity $\partial(\delta R/R)/\partial T$, density variation of materials following the expansion $\partial(\delta d_i/d_i)/\partial(\delta R/R)$ and reactivity change after density correction $\partial k/\partial(\delta d_i/d_i)$.

Ensuing from this correction, the space vacated has to be filled by coolant. The third term expresses the correction of the first one, because it considers that during an expansion, liquid lead behaves differently from solid materials. The space created after the expansion is taken up entirely by the coolant (not by structural materials); the lead density is therefore recalculated by taking the presence of extra lead into account.

The radius variation following an increase of coolant inlet temperature is due to the linear expansion coefficient of T91 steel (FA feet structural material):

$$\partial\left(\delta R/_R\right) = l_c(T_{in})\partial T \tag{23}$$

The density variation of solid materials, following a radius variation is given by:

$$\partial d_i = \partial\left(\frac{M_i}{V_i}\right) = -M_i\frac{\partial V_i}{V_i^2} \approx -d_i\frac{\partial V_i}{V_i} \tag{24}$$

Volume per cent variation of each structural material was obtained by scaling all the radial dimension by the same amount. For this reason the volume variation of materials is equal to the total volume variation of the core, which is equal to twice the radius variation. These considerations lead to the following expression:

$$\partial d_i = -d_i 2\frac{\partial R}{R} \tag{25}$$

Different calculations are made for coolant, where a mass change has to be considered:

$$\partial d_l = \partial\left(\frac{M_l}{V_l}\right) = \frac{V_l\partial M_l - M_l\partial V_l}{V_l^2} \approx \frac{\partial M_l}{V_l} - d_l\frac{\partial V_l}{V_l} \tag{26}$$

The first term refers to lead mass taking up the space created by the expansion:

$$\frac{\partial M_l}{V_l} = d_l\frac{\partial V}{V_l} = d_l\frac{\partial V}{f_l V} = d_l\frac{1}{f_l}2\frac{\partial R}{R} \tag{27}$$

The second term is the same of solid materials and thus the lead density variation is:

$$\partial d_l = -2d_l\left(1-\frac{1}{f_l}\right)\frac{\partial R}{R} \tag{28}$$

Combining all the terms, the final expression for radial expansion is:

$$\left.\frac{\partial k}{\partial T}\right|_r = l_c(T_l)\left\{\frac{\partial k}{\partial\left(\frac{\delta R}{R}\right)} - 2\left[\frac{\partial k}{\partial\left(\frac{\delta d_f}{d_f}\right)} + \frac{\partial k}{\partial\left(\frac{\delta d_{abs}}{d_{abs}}\right)} + \frac{\partial k}{\partial\left(\frac{\delta d_{steel}}{d_{steel}}\right)} + \left(1-\frac{1}{f_l}\right)\frac{\partial k}{\partial\left(\frac{\delta\rho_l}{\rho_l}\right)}\right]\right\} \tag{29}$$

As already said in the previous section, it is necessary to specify where the expansion takes place (i.e., core, reflector, active zone). In Tab. VII the resulting coefficients are shown.

**Table VII. DEMO radial expansion reactivity coefficients.**

| $\alpha_R$ [pcm $K^{-1}$] | MOX BOC | MOX EOC | MET BOC | MET EOC |
|---|---|---|---|---|
| Core + reflector | -0.7741 | -0.7144 | -0.8117 | -0.8045 |
| Core | -0.8627 | -0.8023 | -0.9028 | -0.8999 |
| Active zone | -0.9413 | -0.8727 | -0.9860 | -0.9853 |

*Axial expansion*

The axial expansion coefficient can be calculated according to:

$$\alpha_z = \frac{\partial \rho}{\partial T_c} \tag{30}$$

Therefore $\alpha_Z$ represents the reactivity change following a cladding temperature variation. Similarly to radial expansion, the coefficient is calculated by combining elementary perturbations:

$$\left.\frac{\partial k}{\partial T}\right|_z = \frac{\partial k}{\partial \left(\frac{\delta H}{H}\right)} \frac{\partial \left(\frac{\delta H}{H}\right)}{\partial T} + \sum_{mat} \left( \frac{\partial k}{\partial \left(\frac{\delta d_i}{d_i}\right)} \frac{\partial \left(\frac{\delta d_i}{d_i}\right)}{\partial \left(\frac{\delta H}{H}\right)} \frac{\partial \left(\frac{\delta H}{H}\right)}{\partial T} \right) + \frac{\partial \mathrm{k}}{\partial \mathrm{h_{cr}}} \frac{\partial \mathrm{h_{cr}}}{\partial \mathrm{T}} \tag{31}$$

The first term refers to the reactivity variation following a pure geometric increase of axial dimensions with nominal densities. The second terms regards the correction to the density of solid materials (i.e., fuel and cladding) in order to keep their masses constant. Unlike the previous case, lead density do not change and so no correction is needed. Lead intrinsic expansion due to coolant temperature variation is accounted through the density coefficient.

A height core variation following a cladding temperature change can be estimated through an integral-averaged linear expansion coefficient of T91 clad steel, between inlet and outlet cladding temperatures:

$$\frac{\partial \left(\frac{\delta H}{H}\right)}{\partial T} = \frac{1}{T_{c,out} - T_{c,in}} \int_{T_{c,in}}^{T_{c,out}} l_c\,(T) dT \tag{32}$$

Density variations of solid materials are similar to the radial case described in Eq. (29), but in this case a variation of the core axial dimension corresponds to an equal volume variation:

$$\partial d_i = -d_i \frac{\partial H}{H} \tag{33}$$

There is no correction for lead since its density do not vary after an axial expansion.

The last term represents the reactivity contribution due to the differential expansion of FARs with respect to the active core, due to the instantaneous dilation of both the hot leg and the core. In fact, in DEMO FARs are placed in a voided square tube at the center of each FA. Since FARs and FAs are hung at the top of the reactor vessel, they both are subject to expansion with a change in coolant temperature at the core outlet; therefore, the control rod expansion feedback is determined by the differential movement between FARs and the rest of the FA. As a conservative assumption, it is postulated that the void in which FARs are located provides perfect thermal insulation, so that their expansion can be neglected. On the contrary the FA elongation provides the maximum

value of the differential expansion between fuel and absorbers, resulting in the largest positive reactivity insertion, as expressed by:

$$dh_{cr} = dh_{hot-leg} + dh_{core} \tag{34}$$

where the first term is calculated as:

$$dh_{hot-leg} = h(T_{out}) l_c(T_{out}) dT \tag{35}$$

The axial expansion coefficient is evaluated for the linked case, i.e. when dilation is assumed to be driven by the cladding:

$$dh_{core} = \left( \int_{L_{FARs}}^{Z_{fuel}} l_c(T) dL \right) dT \tag{36}$$

After simple algebraic calculations, the axial expansion coefficient can be calculated according to:

$$\left.\frac{\partial k}{\partial T}\right|_z = \frac{1}{T_{c,out} - T_{c,in}} \int_{T_{c,in}}^{T_{c,out}} l_c(T) dT \left[ \frac{\partial k}{\partial \left(\frac{\delta H}{H}\right)} - \left( \frac{\partial k}{\partial \left(\frac{\delta d_f}{d_f}\right)} + \frac{\partial k}{\partial \left(\frac{\delta d_{steel}}{d_{steel}}\right)} \right) \right] + \frac{\partial k}{\partial h_{in}} \frac{\partial h_{in}}{\partial T} \tag{37}$$

Numerical results are shown in Tab. VIII.

**Table VIII. DEMO axial expansion reactivity coefficients.**

| | MOX BOC | MOX EOC | MET BOC | MET EOC |
|---|---|---|---|---|
| $\alpha_Z$ [pcm K$^{-1}$] | -0.0429 | -0.2374 | -0.1055 | -0.2430 |

#### *3.1.1.2 Code implementation*

The model described above has been handled by using the MATLAB/SIMULINK® tool, a software that allows to solve numerically non-linear Ordinary Differential Equations (ODEs), and that constitutes a reliable instrument for studying the control of dynamics systems.

SIMULINK® provides an interactive graphical environment and a customizable set of block libraries that permit to design, simulate, implement, and test a number of time-varying systems. The program alllows to implement block diagrams in which the principal parts or functions are represented by blocks connected by lines which highlight the relationships among them and provide a visual representation of the physical behavior of the system.

Two examples of model implementation in SIMULINK® are presented in Figs. 16 and 17, refer to DEMO neutron kinetics subsystem and T/H subsystem respectively.

For a control-oriented approach, SIMULINK® is one of the most spread tools for simplicity and reliability: the variables of interest are highlighted in order to handle the system easily and to focus on the influence on state variables and outputs.

SIMULINK® is integrated with MATLAB®, providing straightforward access to an extensive range of tools that allow to develop algorithms, to analyze and visualize simulations, and to define signal, parameter and test data. This is very useful for the purpose of this work, since it allows the immediate use of linear analysis tools. SIMULINK® main key features are represented by:

- Extensive and expandable libraries of predefined blocks;
- Interactive graphical editor for assembling and managing intuitive block diagrams;
- Ability to manage complex designs by segmenting models into hierarchies of design components;
- Model analysis and diagnostics tools to ensure model consistency and identify modeling errors.

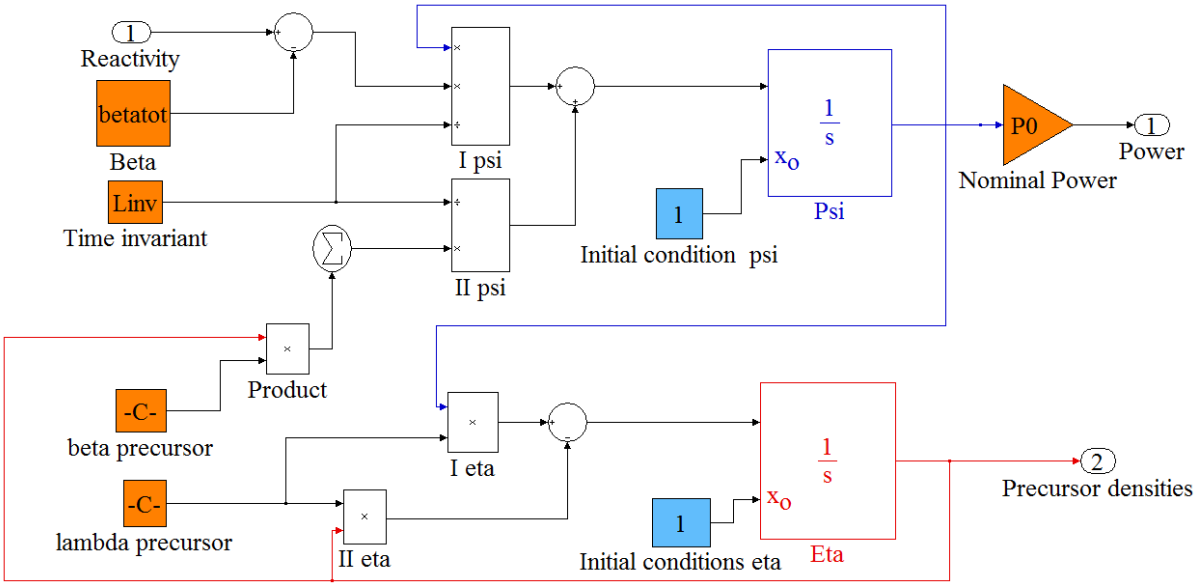


**Figure 16. SIMULINK® model of the neutron kinetics subsystem.**

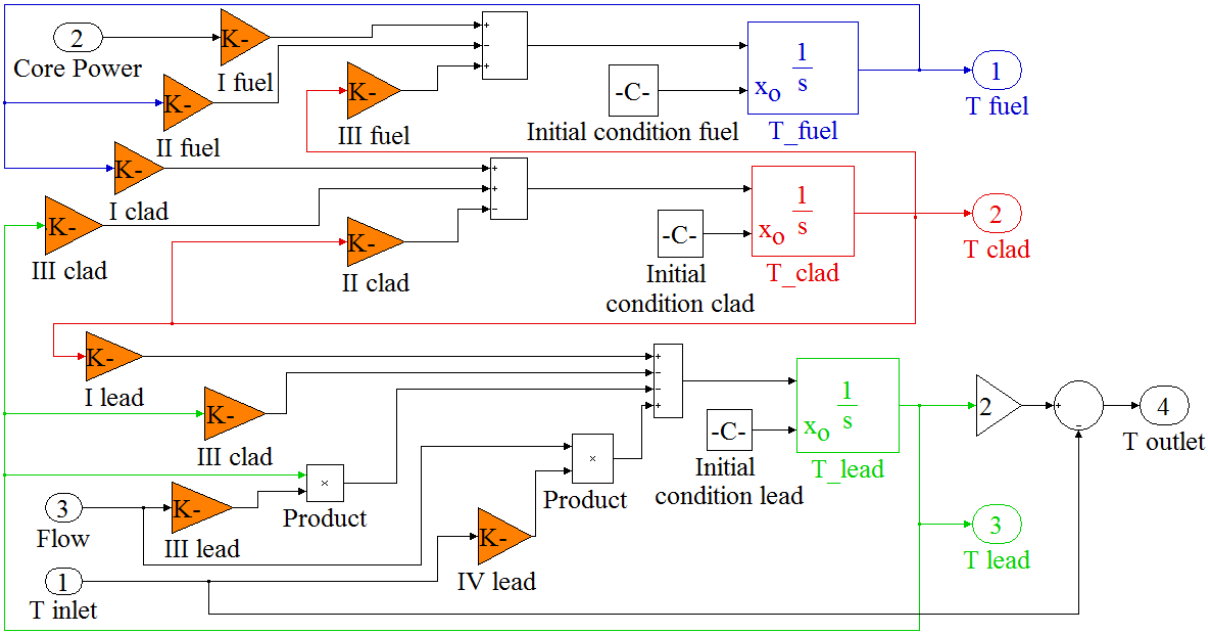


**Figure 17. SIMULINK® model of the thermal-hydraulics subsystem.**

### *3.1.1.3 Parameters and correlations*

*Lead correlations*

In this section, physical properties and correlations implemented for lead are provided. Data are taken from a specific report on HLMCs technology [12]. The temperatures in the following correlations are expressed in Kelvin.

Solid lead is similar to the majority of metals with a Face Centered Cube (FCC) crystal structure. It features a melting temperature of 327.5 °C at atmospheric pressure. Following melting, it exhibits a volume increase of about 3.6 - 3.8 %, whereas the boiling temperature reaches the value of 1743 °C, always at normal pressure.

For molten lead density, a linear relation with temperature, showing a very good agreement with experimental data, is used in this work:

$$d_l = 11367 - 1.1944 \cdot T \tag{38}$$

On the contrary, a large dispersion in data of specific heat capacity at constant pressure are present in literature. The best first estimate of this key parameter can be found according to:

$$C_l = 162.9 - 3.022 \cdot 10^{-2} \cdot T + 8.341 \cdot 10^{-6} \cdot T^2 \tag{39}$$

This parabolic correlation, typical for HLMCs, matches very well experimental data in the range between the melting temperature and 1000 °C, so that its use is suitable for the model purposes.

An Arrhenius-type dependence is chosen to represent the dynamic viscosity of lead as a function of temperature:

$$\mu_l = 4.55 \cdot 10^{-4} exp(1069/T) \quad (40)$$

Similarly to heat capacity, experimental data of molten lead thermal conductivity show a large dispersion, even showing different trends with temperature. Trying to find a physically-based compromise, the following linear correlation is recommended temperatures ranging from the lead melting temperature to 1050 °C:

$$\lambda_l = 9.2 + 0.011 \cdot T \quad (41)$$

Heat transfer in liquid metal coolants is strikingly different from heat transfer in ordinary nuclear coolants such as water and gas, primarily due to their higher thermal conductivity.

The main consequence of this physical property is that liquid metals – among which lead – absorb heat mostly by conduction, even under turbulent conditions. This is not the case of non-metallic coolants, for which the major contribution to heat exchange is due to convection.

The weight of conduction compared with convection can be estimated by the Peclet number, which summarizes the importance of turbulent mixing with respect to heat transfer by conduction in the turbulent zone. The Peclet number is found as the product of Reynolds and Prandtl numbers: the first is a pointer of the flow turbulence; the latter is inversely proportional to thermal conductivity. For Peclet numbers lower than 100, heat transfer is governed mainly by conduction. For Peclet numbers of about 1000, heat conduction and turbulent mixing are equally important. Only for Peclet numbers higher than 50000 the turbulent mixing clearly prevails.

The temperature distribution within a coolant channel containing a liquid metal resembles the temperature distribution in a solid conductor. Thus, temperature varies more slowly and linearly across a channel with liquid metal than with non-metallic coolant.

The heat transfer coefficient for liquid metals has been studied extensively in recent years and several correlations for the calculation of the Nusselt number have been proposed.

For square rod bundles, such as the ones foreseen for DEMO, the only available experimental data are provided by Zhukov [13, 14]. The lack of information and is explainable by the fact that HLMC fast reactors have always been built with triangular bundles and there are no prototypes with a square lattice. Nevertheless, some Computational Fluid Dynamics (CFD) simulations confirm the validity of Zhukov's correlation, recommending it for a square arrangement [15]. Furthermore, compared with other metal liquid correlations such as Lyon-Martinelli [16] and Dwyer [17], Zhukov's correlation is the most conservative.

The correlation is a function of the pitch-to-diameter ratio (*PP/D*) and of the Peclet number:

$$Nu = 7.75\frac{PP}{D} - 14\left(\frac{PP}{D}\right)^{-5} + 0.007Pe^{(0.64+0.246PP/D)} \quad (42)$$

Equation (42) is valid with $10 \leq Pe \leq 2500$ and $1.2 \leq PP/D \leq 1.5$, but the experimentally covered range is only $60 \leq Pe \leq 2000$ and $1.25 \leq PP/D \leq 1.46$.

The coefficient of the Peclet term is chosen without considering grid spacers to be incorporated in DEMO. The presence of grid spacers influence the Nusselt number, making it locally increase significantly (in

correspondence with the grid). Although the Nusselt number strongly depends on the axial coordinate, it has been kept constant in the simulations.

In Tab. IX, the numeric values of the lead-related parameters employed in this work are summarized. All of these parameters are kept constant during transient simulations. The nominal average lead temperature (440 °C) is taken as the reference temperature for the calculation of physical properties through the correlations discussed above.

**Table IX. Lead properties used in simulations.**

| Parameter | MOX option | METAL option | Units |
|---|---|---|---|
| Mass flow rate, $\Gamma$ | 25757 | | kg $s^{-1}$ |
| Density, $d_l$ | 10515 | | kg $m^{-3}$ |
| Mass, $M_l$ | 5429 | 4511 | kg |
| Specific heat capacity, $C_l$ | 145.6 | | J $kg^{-1}$ $K^{-1}$ |
| Viscosity, $\mu_l$ | 0.002037 | | Pa s |
| Thermal conductivity, $\lambda_l$ | 17.04 | | W $m^{-1}$ $K^{-1}$ |
| Convective heat coefficient, $h_{chc,l}$ | 45034 | | W $m^{-2}$ $K^{-1}$ |

*Cladding correlations*

For cladding, the ferritic-martensitic steel (FMS) T91 is the candidate material. Physical properties and correlations are taken from a specific report on HLMCs technology [12].

T91 density is calculated using the following correlation:

$$d_c = 7799 - 0.201 \cdot T - 1.102 \cdot 10^{-4} \cdot T^2 \quad (43)$$

The isobaric heat capacity of T91 monotonically increases with temperature in the range of 550÷1300 °C. The following correlation features a good agreement with experimental data in the same range:

$$C_c = -3.979 \cdot 10^{-9} \cdot T^4 + 1.151 \cdot 10^{-5} \cdot T^3 - 1.103 \cdot 10^{-2} \cdot T^2 + 4.677 \cdot T - 244.0 \quad (44)$$

Thermal conductivity is a parameter very sensitive to microstructure and steel composition; for this reason there are significant differences between the values present in literature. The following correlation tries to obtain the best fit of the available data:

$$\lambda_c = 17.94 + 0.0251 \cdot T - 1.45 \cdot 10^{-5} \cdot T^2 \quad (45)$$

In Tab. X the numeric values of the cladding-related parameters employed in this work are summarized. All of these parameters are kept constant during transient simulations. The steady-state cladding temperatures (retrieved from simple heat exchange calculations) are taken as the reference temperatures to be inserted into the correlations presented above.

**Table X. Cladding parameters used in simulations.**

| Parameter | MOX option | METAL option | Units |
|---|---|---|---|
| Convective thermal exchange clad-lead, $H_{cl}$ | $9.85 \cdot 10^6$ | $8.19 \cdot 10^6$ | W $K^{-1}$ |
| Steady-state temperature, $T_{c0}$ | 470.4 | 476.7 | °C |
| Density[1], $d_c$ | 7731 | | kg $m^{-3}$ |
| Mass, $M_c$ | 5429 | 4511 | kg |
| Specific heat capacity, $C_c$ | 650.9 | 656 | J $kg^{-1}$ $K^{-1}$ |
| Thermal conductivity, $\lambda_c$ | 28.59 | 28.61 | W $m^{-1}$ $K^{-1}$ |

*Fuel correlations: MOX*

Correlations for MOX fuels are very spread in literature and a useful review is taken into account as a reference [18]. MOX fuel contains between $PuO_2$ blended with natural or depleted uranium dioxide. $PuO_2$ replaces the enriched fraction of $^{235}U$ in classic $UO_2$ fuels. The solid solutions formed by uranium and plutonium may be regarded as an almost ideal system. For this reason, the Kopp-Neumann rule [19] can be used to determine some properties (density and heat capacity) of the solid by combining the contributions of each constituent in proportion to its molar fraction.

For what concerns fuel density, a slight difference between uranium and plutonium is considered, in addition to pellet porosity (usually 5 %). The hypostoichiometric correction, due to an oxygen-to-metal ratio of 1.97, is disregarded. The following correlation is therefore used to determine MOX density:

$$d_{f,TD} = d_{f,TD}(273) \cdot (9.9672 \cdot 10^{-1} + 1.179 \cdot 10^{-5} \cdot T - 2.429 \cdot 10^{-9} \cdot T^2 + 1.219 \cdot 10^{-12} \cdot T^3)^{-3} , \quad (46)$$

where $d_{f,TD}(273)$ is the density at 273 K, depending on the plutonium molar fraction $y$ in the MOX:

$$d_{f,TD}(273) = 10970 + 490 \cdot y \quad (47)$$

Practical density is obtained by applying a correction for porosity $p$:

$$d_f = d_{f,TD} \cdot (1 - p) \quad (48)$$

For isobaric heat capacity, a linear correlation for both uranium and plutonium is found; its general formulation is:

$$C_f = c_1 + 2c_2 t + 3c_3 t^2 + 4c_4 t^3 + 5c_5 t^4 - c_6 t^{-2} \quad (49)$$

where t= T/1000, with constants listed in Tab. XI.

[1] Calculated at 20°C.

**Table XI. Constants used in the heat capacity correlation.**

| Constant | $UO_2$ | $PuO_2$ | Units |
|---|---|---|---|
| $c_1$ | 193.238 | 311.7866 | J $kg^{-1} \cdot K^{-1}$ |
| $c_2$ | 162.8647 | 19.629 | J $kg^{-1} \cdot K^{-2}$ |
| $c_3$ | -104.0014 | -0.752 | J $kg^{-1} \cdot K^{-3}$ |
| $c_4$ | 29.2056 | 0 | J $kg^{-1} \cdot K^{-4}$ |
| $c_5$ | -1.9507 | 0 | J $kg^{-1} \cdot K^{-5}$ |
| $c_6$ | 2.6441 | 7.0131 | J·K $kg^{-1}$ |

Using the Kopp-Neumann rule, the isobaric heat capacity of MOX results:

$$C_f^{MOX} = (1-y)C_f^{UO_2} + yC_f^{PuO_2} \tag{50}$$

Thermal conductivity is a property that does not follow the law of mixtures. Experimental data show that the thermal conductivity of MOX fuels is lower than that of uranium oxides, even if the decrease is not appreciable for enrichments up to 15 %.

In the available correlations MOX with 5 % porosity is considered and a hypostoichiometric correction is applied by means of a stoichiometric deviation *x* (in the considered fuel *x* is equal to 0.03):

$$\lambda_f = \frac{1}{A + B \cdot t} + \frac{6400}{t^{5/2}} exp^{-16.35/t} \tag{51}$$

Where

$$A' = 2.85x + 0.035$$

$$B' = -0.715x + 0.286 \tag{52}$$

$$t = T/1000$$

The correlation covers the range of 400 ÷ 2800 °C and is valid for $x < 0.05$.

*Fuel correlations: metallic fuel*

Correlations used for metallic fuel are based on confidential information about the experimental campaigns carried out at EBR-II [20, 21, 22], due to the lack of data available in the open literature.

Density is regarded as a constant parameter (no correlations available), and a smear density of 75 % is considered.

For thermal conductivity, the correlation used is the following:

$$\lambda_f = [A'' + (B'' + C'' \cdot T)T]\frac{1-p}{1+1.7p} \tag{53}$$

where $p$ is porosity and

$$A'' = 17.5\left[\frac{(1 - 2.23 \cdot MF_{Zr})}{(1 + 1.61 \cdot MF_{Zr})} - 2.62 \cdot MF_{Pu}\right]$$

$$B'' = 1.54 \cdot 10^{-2}\left[\frac{(1 + 0.061 \cdot MF_{Zr})}{(1 + 1.61 \cdot MF_{Zr})} + 0.9 \cdot MF_{Pu}\right] \tag{54}$$

$$C'' = 9.38 \cdot 10^{-6}(1 - 2.7 \cdot MF_{Pu})$$

with *MF* indicating molar fraction of each element constituting the metallic alloy.

Isobaric heat capacity is retrieved from the following correlation, where *MM* indicates molar mass of fuel:

$$\begin{cases} C_f = 19.34 + 0.0266 \cdot \dfrac{T}{MM} & T < 873\ K \\ C_f = 162 & 873\ K < T < 923\ K \\ C_f = 8.752 + 0.026 \cdot \dfrac{T}{MM} & T > 923\ K \end{cases} \tag{55}$$

In Tab. XII, the numerical values of the fuel-related parameters employed in this work are summarized. All of these parameters are kept constant during transient simulations. The steady-state fuel temperatures (retrieved from simple heat exchange calculations) are taken as the reference temperatures to be inserted into the correlations presented above.

**Table XII. Fuel parameters used in simulations.**

| Parameter | MOX option | METAL option | Units |
|---|---|---|---|
| Convective heat coefficient for gap, $h_{chc,g}$ | 16717 | -[2] | W m$^{-2}$ K$^{-1}$ |
| Conductive thermal exchange fuel-cladding, $K_{fc}$ | $2.44 \cdot 10^5$ | $1.19 \cdot 10^6$ | W K$^{-1}$ |
| Steady-state temperature, $T_{f0}$ | 1699 | 728.4 | °C |
| Nominal density, $d_f$ | 10480 | 15730 | kg m$^{-3}$ |
| Mass, $M_f$ | 2132 | 2529 | kg |
| Specific heat capacity, $C_f$ | 375.5 | 155.6 | J kg$^{-1}$ K$^{-1}$ |
| Thermal conductivity, $\lambda_f$ | 1.844 | 10.72 | W m$^{-1}$ K$^{-1}$ |

In Tab. XIII the simulation time constants are listed.

[2] No gap is expected in the metallic fuel option.

**Table XIII. Time constants used in simulations.**

| Parameter | MOX option | METAL option | Units |
|---|---|---|---|
| Fuel time constant, $\tau_f$ | 3.252 | 0.3302 | s |
| Fuel to clad time constant, $\tau_{c1}$ | 1.446 | 0.248 | s |
| Clad to coolant time constant, $\tau_{c2}$ | 0.03583 | 0.03612 | s |
| Coolant time constant, $\tau_l$ | 0.08023 | | s |
| Loop coolant time constant, $\tau_0$ | 0.2108 | 0.1751 | s |

Table XIV summarizes the kinetic and feedback parameters used in simulations.

**Table XIV. Kinetic parameters and reactivity coefficients.**

| | MOX | | MET | | Units |
|---|---|---|---|---|---|
| | *Boc* | *Eoc* | *Boc* | *Eoc* | |
| $\beta$ | 319 | 323 | 332 | 337 | pcm |
| $\Lambda$ | 8.0659 | 8.4980 | 6.8771 | 7.0777 | $10^{-7}$ s |
| $\lambda_d$ | 0.081958 | 0.081901 | 0.084529 | 0.08438 | s |
| $\beta_1$ | 6.142 | 6.224 | 6.174 | 6.273 | pcm |
| $\beta_2$ | 71.40 | 72.33 | 71.80 | 72.77 | pcm |
| $\beta_3$ | 34.86 | 35.34 | 36.31 | 36.87 | pcm |
| $\beta_4$ | 114.1 | 115.5 | 120.1 | 121.9 | pcm |
| $\beta_5$ | 69.92 | 70.75 | 73.53 | 74.70 | pcm |
| $\beta_6$ | 22.68 | 22.89 | 24.55 | 24.87 | pcm |
| $\lambda_{d,1}$ | 0.0125 | 0.0125 | 0.0125 | 0.0125 | s |
| $\lambda_{d,2}$ | 0.0292 | 0.0292 | 0.0293 | 0.0292 | s |
| $\lambda_{d,3}$ | 0.0895 | 0.0895 | 0.0905 | 0.0905 | s |
| $\lambda_{d,4}$ | 0.2575 | 0.2573 | 0.2609 | 0.2607 | s |
| $\lambda_{d,5}$ | 0.6037 | 0.6025 | 0.6227 | 0.6215 | s |
| $\lambda_{d,6}$ | 2.6688 | 2.6661 | 2.7047 | 2.7024 | s |
| $\alpha_D$ | -0.15 | -0.17 | -0.14 | -0.15 | pcm $K^{-1}$ |
| $\alpha_C$ | -1.2267 | -1.995 | -1.3180 | -1.3903 | pcm $K^{-1}$ |
| $\alpha_R$ | -0.7741 | -0.7144 | -0.8117 | -0.8045 | pcm $K^{-1}$ |
| $\alpha_Z$ | -0.0429 | -0.2374 | -0.1055 | -0.2430 | pcm $K^{-1}$ |

#### *3.1.1.4 Validation with SAS4A/SASSYS-1 Code System*

The SAS4A and SASSYS-1 computer codes were developed at Argonne National Laboratory (ANL) for thermal, hydraulic, and neutronic analysis of power and flow transients in liquid-metal-cooled nuclear reactors.

The SAS4A code is conceived to analyze severe core disruption accidents with coolant boiling, fuel melting and relocation. The SASSYS-1 code is a tool for margin assessment in design basis accident (DBA) analysis and for consequence assessment in beyond-design-basis accident (BDBA) analysis.

The SAS4A code contains detailed, deterministic models of transient thermal, hydraulic, neutronic, and mechanical phenomena to describe the response of the reactor core, its coolant, fuel elements and structural members to operational and accident conditions.

In addition, SASSYS-1 has the capability to provide a detailed thermal-hydraulic simulation of the primary and secondary coolant circuits and the balance-of-plant steam/water circuit, including component models for heat exchangers, pumps, valves, turbines, condensers, and thermal-hydraulic models of pipes and plena. SASSYS-1 also contains a plant protection and control system modeling capability, which provides digital representations of reactor, pump, valve controllers and their response to input signal changes.

***Code structure basis***

*Geometry*

In the SAS4A/SASSYS-1 core models, the basic geometric element is a fuel pin, its cladding, the associated coolant and structure, with the structure field representing wire wraps, grid plates, and/or hex cans; the term "channel" is used to denote collectively this basic element of fuel, cladding, coolant and structure.

A single SAS4A/SASSYS-1 channel may therefore represent either one pin, or a large number of pins in many subassemblies. In either case, the elementary unit from a code structure and data management stand-point is an individual channel.

Usually, a channel is used to represent an average pin in a fuel subassembly or a group of similar subassemblies. A channel can also be used to represent a blanket assembly or a control rod channel, and the hottest pin in a subassembly can be represented instead of the average pin. Different channels can be used to account for radial and azimuthal power variations within the core, as well as variations in coolant flow orificing and fuel burn-up.

A number of axial zones are used to represent a single channel. One zone represents the fuel-pin section, including the core, axial blankets, and gas plenum; other zones represent reflector regions above and below the pin section (see Fig. 18)

Figure 19 shows the axial mesh structure used for a channel. The coolant and structure nodes run the whole length of the channel. The coolant nodes are staggered with respect to the fuel, cladding, reflector, and structure nodes. Using coolant temperatures defined at the axial boundaries between cladding and structure nodes make easier to calculate accurate coolant temperatures.

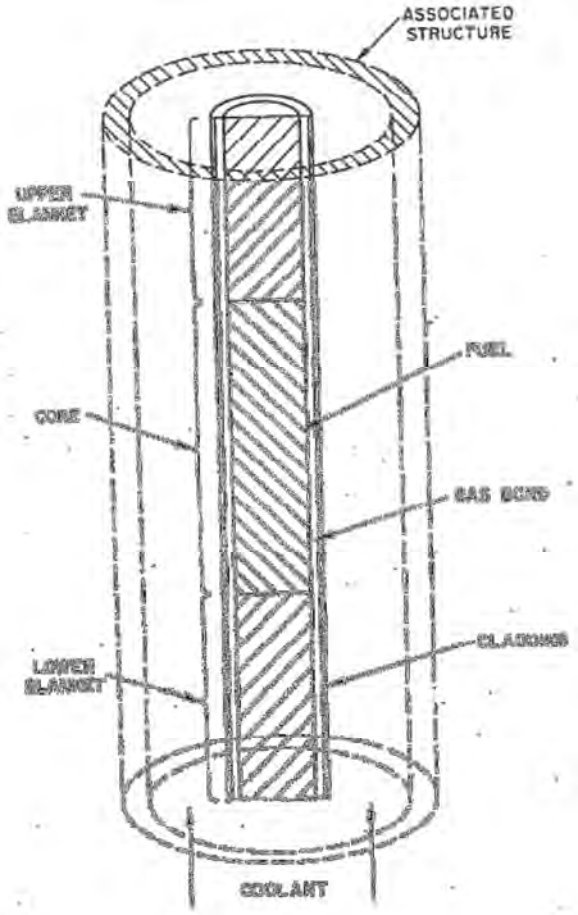


**Figure 18. SAS4A/SASSYS-1 channel schematic representation.**

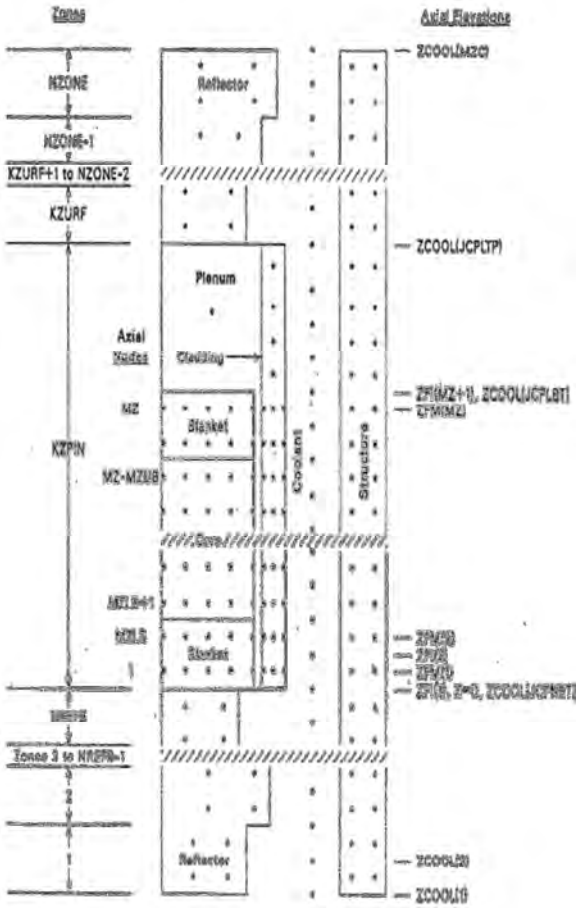


**Figure 19. Schematic of SASSYS-1/SAS4A channel discretization.**

*Neutronics*

The purpose of the SAS4A/SASSYS-1 reactor point kinetics, decay heat and reactivity feedback models is to provide an estimate of the reactor power level to be used in the prediction of energy deposition in the fuel. Reactor material temperature changes and relocations determine the reactivity, which in turn determines the reactor power level and the rate of heating of the reactor materials.

In the SAS4A/SASSYS-1 a time-independent reactor power spatial shape is assumed, along with a space-independent (point) reactor kinetics model; furthermore, different channels can have different decay heat curves.

First-order perturbation theory is used to predict reactivity feedback effects associated with material density changes. Fuel temperature (Doppler) effects are calculated by assuming a logarithmic dependence on the local absolute temperature ratio, with a linearly-dependent variation of the local Doppler coefficient on the coolant void fraction.

The fundamental basis for the assumptions of a time-independent power distribution, point kinetics and first-order perturbation theory is the underlying supposition that the reactor neutron flux distribution is invariant in time. This means that in a transient simulation, the effect of changes in the reactor environment (geometry,

dimensions, temperature and density distributions) on the neutron flux shape are neglected. This significantly reduces the complexity and computational expense of the overall neutronics model, with some loss of accuracy.

*Reactivity feedback*

The net reactivity is the sum of eight components:

$$\delta k(t) = \delta k_p(t) + \delta k_D(t) + \delta k_d(t) + \delta k_c(t) + \delta k_{rc}(t) + \delta k_{cr}(t) + \delta k_{fu}(t) + \delta k_{cl}(t) \quad (56)$$

with:

- $\delta k_p$ = user-programmed reactivity (related to control rods movement);
- $\delta k_D$ = fuel Doppler feedback reactivity. The Doppler constant ($\alpha$) is specified as an input quantity at any axial location in a subassembly. An axial-dependent Doppler worth is defined for each channel for flooded and voided conditions;
- $\delta k_d$ = fuel and cladding axial expansion feedback reactivity. A simple axial expansion reactivity model is available, sufficient for low burn-ups and based on axial distribution of fuel and cladding density reactivity coefficients, and defined in terms of \$ $kg^{-1}$;
- $\delta k_c$ = coolant density or voiding feedback reactivity. It is assumed to be a linear function of the density variation from the original conditions, and is defined at each axial location along the whole coolant channel in the core in terms of \$ $kg^{-1}$;
- $\delta k_{rc}$ = core radial expansion feedback reactivity. A core radial growth is determined by the expansion of the lower support structure (assumed to be proportional to the rise in the subassembly inlet temperature above its initial steady-state value). An option is included in the code to use the inlet plenum wall temperature instead of the coolant inlet temperature, so as to account for time delays in the heating of the lower grid support structure and of structure at the above core load pads, when existing;
- $\delta k_{cr}$ = control rod drive expansion feedback reactivity. The control rod drives is assumed to be washed by the outlet coolant from the core; thermal expansion of the drives due to a rise in core outlet temperature causes the control rods to be inserted further into the core, providing a negative reactivity component;
- $\delta k_{fu}$ = fuel relocation feedback reactivity. It is calculated as the product of the input material reactivity worth and the change in the axial material mass distribution since the initial steady-state condition;
- $\delta k_{cl}$ = cladding relocation feedback reactivity. It is calculated as the product of the input material reactivity worth and the change in the axial material mass distribution since the initial steady-state condition.

*Thermal-hydraulics*

The core assembly thermal-hydraulics treatment includes the calculation of fuel, cladding, coolant and structure temperatures, as well as coolant flow rates and pressure distributions. Although SASSYS-1 and SAS4A are mainly transient codes, both steady-state and transient temperatures and coolant pressures are calculated, the former being simply obtained from the transient equations after dropping all time derivatives: results are obtained rapidly from a direct solution based on conservation of energy and use of spatial finite differencing.

***Core model implementation***

The SAS4A/SASSYS-1 model of DEMO incorporates three core channels. The first one is the so-called average channel, which is included to represent the general core behavior during transients; its design parameters (such as pin dimensions, coolant areas, etc.) are based on a single FA, and an independent parallel channel hypothesis (i.e., no cross-flow of coolant between FAs) is assumed. Assembly power and flow rate are calculated as core-averaged values, whereas the respective axial power profile is obtained by averaging the ones of each FA, previously retrieved by means of ERANOS. Furthermore, fuel, coolant, and cladding reactivity feedback coefficients are provided for each axial node along the fuel pin height through perturbation calculations.

In the case of MOX fuel, transient simulations are preceded by fuel deformation calculations, in which fuel axial and radial growth, along with other fuel behavior characteristics such as void and crack formation, are determined for a given history of steady-state irradiation. For metal, it is assumed that the fuel is expanded inside the cladding such that the gap is closed for both the BoC and EoC cases.

The second channel modeled represents the hot channel, which is intended for calculation of the peak core temperatures during transients, being the most power producing assembly. Its geometry, as well as power profile and reactivity coefficients, are assumed to be identical to the core average channel, whereas, in the case of oxide fuel, the actual fuel pellet geometry at the start of the transient is different, due to the higher power level impacting the above mentioned fuel deformation calculations.

The third channel represents the dummy (reflector/shielding) assemblies located around the active core, whose modeling main purpose is to accurately account for the coolant reactivity feedback they are responsible for. Reflector assemblies are simply modeled as a 86 % coolant and 14 % structure mix, so as to conserve such volume fractions and to correctly predict the respective reactivity feedback.

In addition to coolant, cladding, and fuel reactivity effects, two additional feedbacks are considered for the entire core (as opposed to the other feedbacks which are modeled individually for each channel): core radial expansion and control rod driveline elongation. The former is reproduced as a combination of the expansion of FA bottoms and the assumed load pad-like structure located just above the active core. The modeling of control rod driveline displacement is based on an elongation of the structure positioned above the core linear with temperature. The control rod expansion feedback is represented by a negative dilation (contraction) of the FA portion located above the core (hot leg): whether a coolant outlet temperature increase occurs, the expanding FAs are modeled by contracting FARs, so that the relative displacement is preserved.

***Results***

The non-linear core model is solved using the MATLAB/SIMULINK® tool and validated with the reference SAS4A/SASSYS-1 calculations.

Three simulations of simple, core-wise transients are carried out: a 20 pcm (corresponding to approximately 0.06 $) reactivity step introduction (Unprotected Transient of OverPower, UTOP), a 20 K inlet temperature positive step change (reproducing an Unprotected Loss Of Heat Sink – ULOHS - accident scenario), and a coolant flow rate reduction manually specified as a function of time (*i.e.*, simplified Unprotectd Loss Of Flow - ULOF - event, in which the pump driving head has been modeled to exponentially decay with an 8 s pump coast-down half-time) are simulated at BoC and EoC for both MOX and metallic fuel cores. The comparison of integral quantities

such as reactivity and power is provided in the following sections, since they give overall indication of the analytical method performance, compared with the reference SAS4A/SASSYS-1 calculations.

Results concerning temperatures are not compared due to the fact that SAS4A/SASSYS-1 provides peak values for each channel, and a comparison with core-averaged values would not be consistent and meaningful for the aim of this work.

*UTOP simulation*

The dynamic responses of the MOX and metal-fuelled DEMO cores to a stepwise reactivity insertion of 20 pcm, corresponding to approximately 0.06 $ (Figs. from 20 to 23), are investigated at both BoC and EoC.

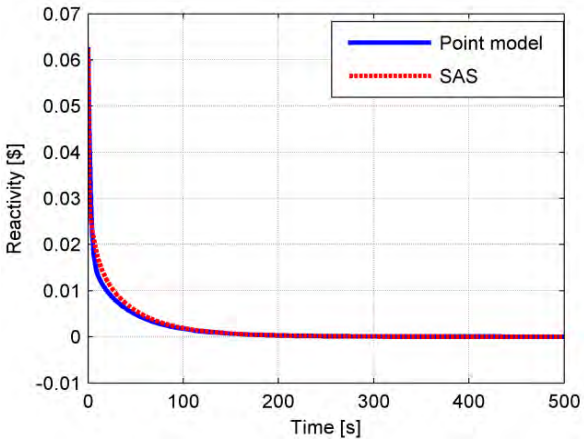


**Figure 20. Reactivity function following a 20 pcm reactivity insertion for MOX BoC.**

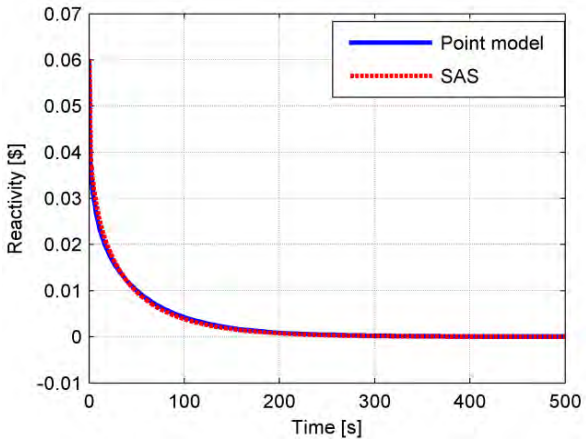


**Figure 22. Reactivity function following a 20 pcm reactivity insertion for MET BoC.**

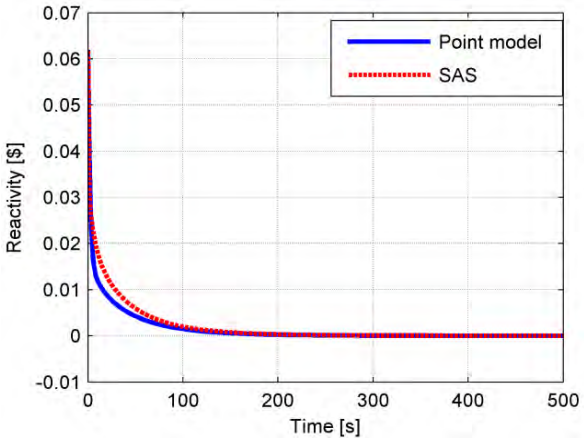


**Figure 21. Reactivity function following a 20 pcm reactivity insertion for MOX EoC.**

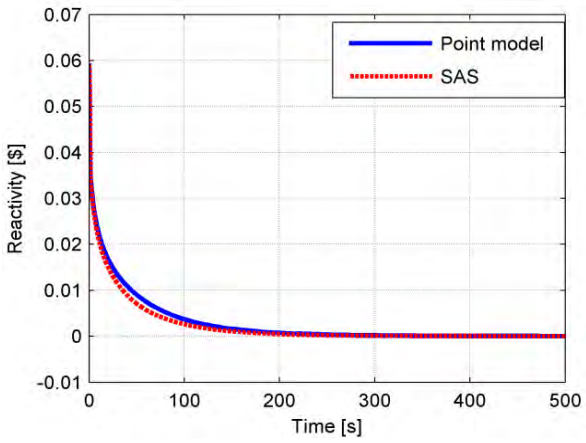


**Figure 23. Reactivity function following a 20 pcm reactivity insertion for MET EoC.**

The analytical model reproduces the results obtained by SAS4A/SASSYS-1 very satisfactorily, in particular at BoC the reactivity curves being almost completely overlapped: in the case of MOX fuel, reactivity tends

asymptotically to zero with a little smoother slope in SAS4A/SASSYS-1, whereas the opposite situation is found for metallic fuel, in which the analytical point model predicts a slower achievement of the steady-state.

As Figs. from 24 to 27 highlight, the expected response is observed, i.e. the initial instantaneous power rise (prompt jump), whose time characteristic and amplitude are essentially determined by the prompt neutron lifetime.

The normalized power curves exhibit slightly greater discrepancies, though still of the order of some per cents: in fact, at the end of the transient the power results increased by approximately 7.2 % (MOX BoC), 6.4 % (MOX EoC), 14.4 % (metal BoC) and 12.8 % (metal EoC) with respect to the steady-state values, the discrepancies with SAS4A/SASSYS-1 being under one per cent for BoC and up to 2.3 % for EoC.

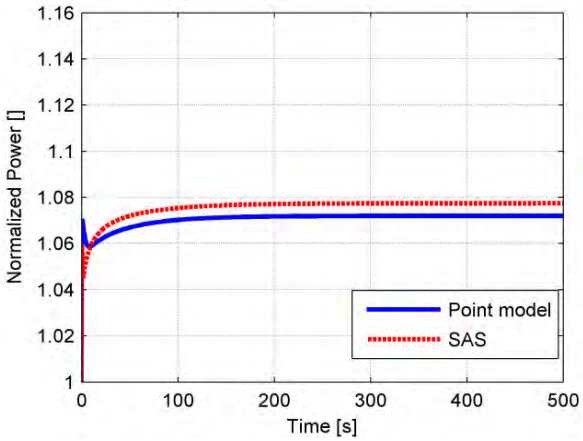


**Figure 24. Normalized power following a 20 pcm reactivity insertion for MOX BoC.**

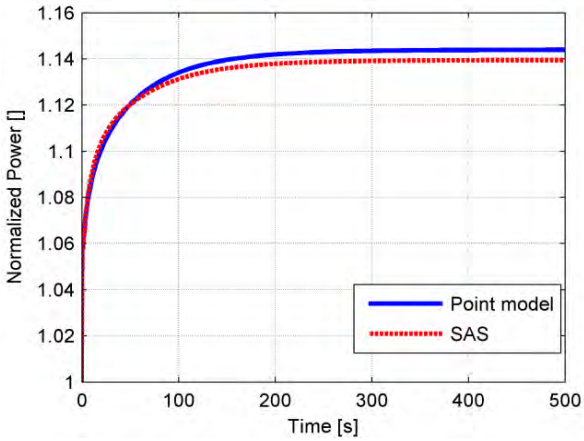


**Figure 26. Normalized power following a 20 pcm reactivity insertion for MET BoC.**

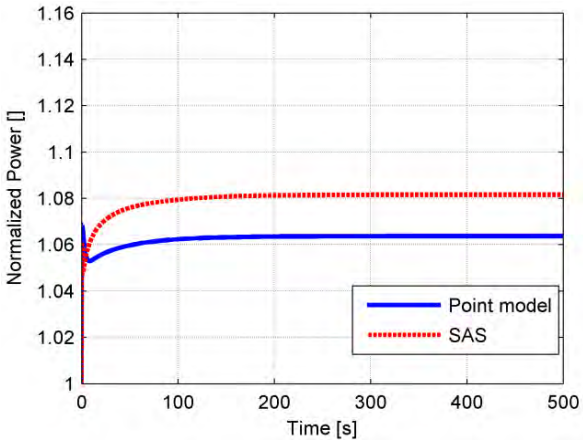


**Figure 25. Normalized power following a 20 pcm reactivity insertion for MOX EoC.**

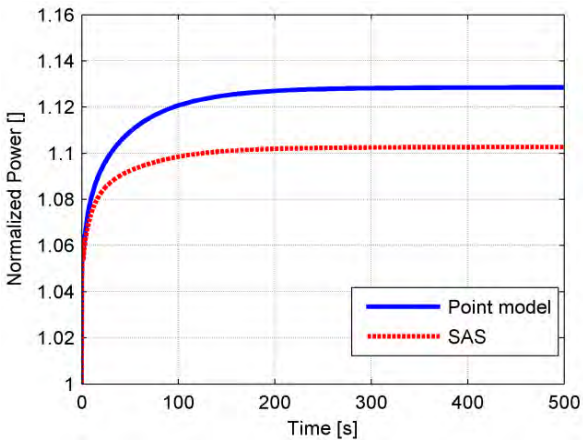


**Figure 27. Normalized power following a 20 pcm reactivity insertion for MET BoC.**

In the case of MOX fuel, a difference is found just after the prompt jump: the reactivity decrease due to feedback brings about a minor as well as slower diminution of power, which anyway settles at a lower value than the one foreseen by SAS4A/SASSYS-1. The differences on the sudden decrease after the initial peak may be due to the

fact that in SAS the Doppler reactivity feedback, that is responsible for the power diminution, has an axial distribution whereas in the analytical model it is constant all over the core. Coherently with the reactivity trend, the analytical model overestimates the power rise in the case of metallic fuel, the transient developments being analogous though.

The UTOP scenario is investigated for different reactivity stepwise insertions, and results confirm a satisfactory agreement with SAS4A/SASSYS-1. For example, after a 5 pcm reactivity insertion, the reactor power undergoes an enhancement by 1.8 % (MOX BoC), 1.6 % (MOX EoC), 3.6 % (metal BoC) and 3.2 % (metal EoC) with respect to the steady-state values, the discrepancies with SAS4A/SASSYS-1 being under one per cent.

Table XV resumes the new steady-state power levels provided by SAS and by the analytical model in both cases of 5 and 20 pcm reactivity insertion.

**Table XV. SAS and analytical model results in UTOP simulations.**

| UTOP | 5 pcm simulation | | | 20 pcm simulation | | |
|---|---|---|---|---|---|---|
| | SAS | Analytical model | Discrepancy[3] | SAS | Analytical model | Discrepancy[8] |
| MOX BoC | 306 | 305.4 | - 0.20 % | 323.21 | 321.6 | - 0.5 % |
| MOX EoC | 306.38 | 304 | - 0.52 % | 324.45 | 319.2 | - 1.62 % |
| MET BoC | 310.43 | 310.8 | + 0.12 % | 341.85 | 343.2 | + 0.40 % |
| MET EoC | 307.68 | 309.6 | + 0.62 % | 330.79 | 338.4 | + 2.30 % |

*ULOHS simulation*

The core inlet temperature is enhanced by 20 K to simulate a ULOHS event, leading to an insertion of negative reactivity (Figs. from 28 to 31) due to radial expansion and lead density feedbacks. Because of the negative reactivity injection brought by higher lead temperatures, the core power undergoes a prompt decrease in the first part of the transient (Figs. from 32 to 35), as far as the contribution of Doppler (due to the fuel average temperature reduction) starts balancing the effects of lead temperature on reactivity, along with the axial expansion (due to the increased cladding temperature). A similar general trend is observed for the reactivity function resulting from the two models, even if a more negative peak is noticed in the analytical model case compared with SAS4A/SASSYS-1 for both MOX (difference of 0.05 $, i.e. 16 pcm) and metal (less evident, of the order of 0.02 $, approximately 6 pcm). Just after the sudden decrease, reactivity increases again showing first a rapid rise, in particular for MOX fuel, and then a slower slope due to the opposing contribution of the axial contraction effect (MOX BoC), finally reinstating criticality.

[3] Calculated as per cent relative error made by the analytical model, considering SAS as the reference.

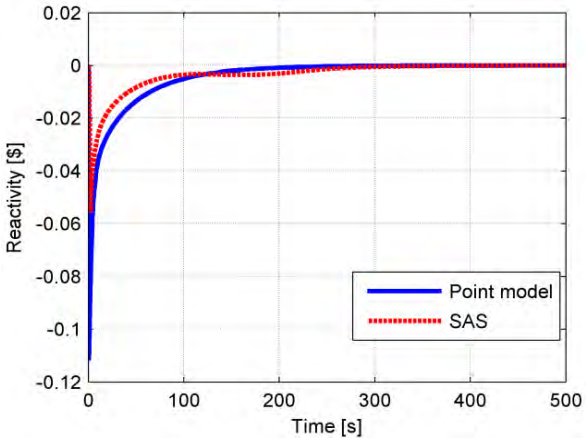


**Figure 28. Reactivity function following a 20 K inlet temperature enhancement for MOX BoC.**

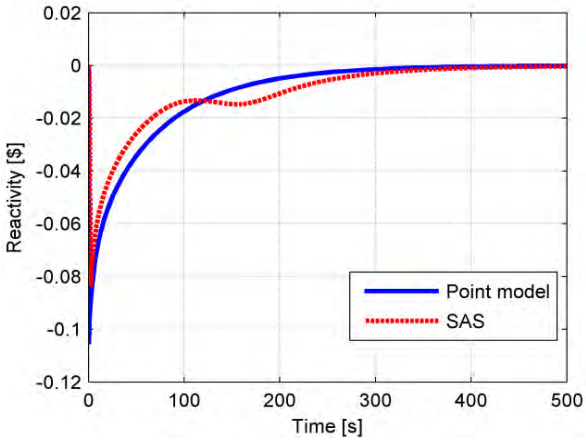


**Figure 29. Reactivity function following a 20 K inlet temperature enhancement for MET BoC.**

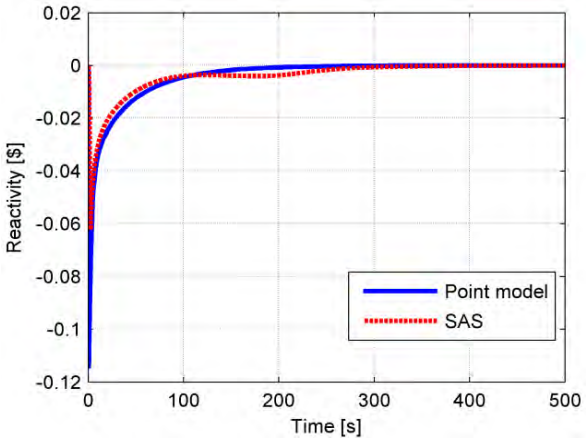


**Figure 30. Reactivity function following a 20 K inlet temperature enhancement for MOX EoC.**

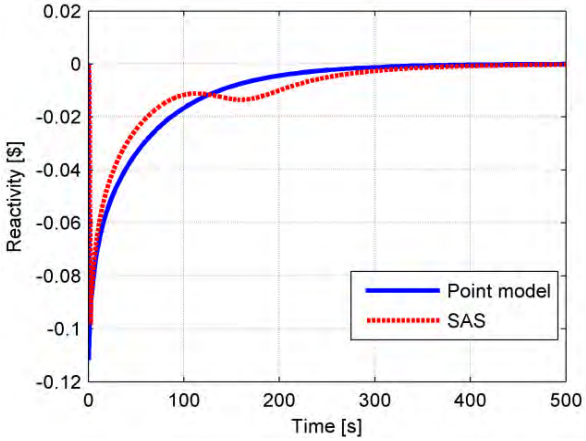


**Figure 31. Reactivity function following a 20 K inlet temperature enhancement for MET EoC.**

Differently from SAS4A/SASSYS-1, the first order linearized expression for reactivity implemented in the simplified model produces a monotonic enhancement, which appears to be a kind of fit of the oscillatory function provided by the one-dimensional non-linear model. Indeed, the respective curves are almost overlapped: for MOX discrepancies are negligible, whereas for metal they appear a little more important.

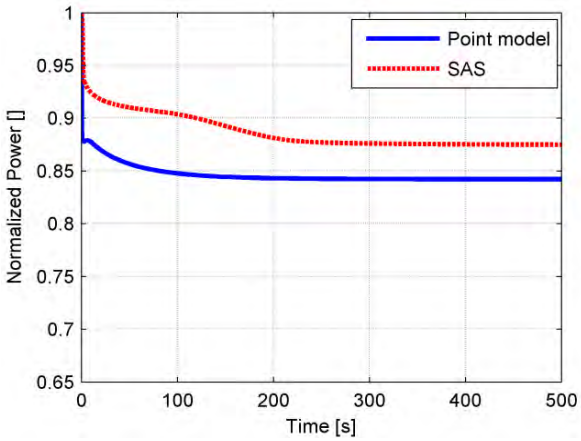


**Figure 32. Normalized power following a 20 K inlet temperature enhancement for MOX BoC.**

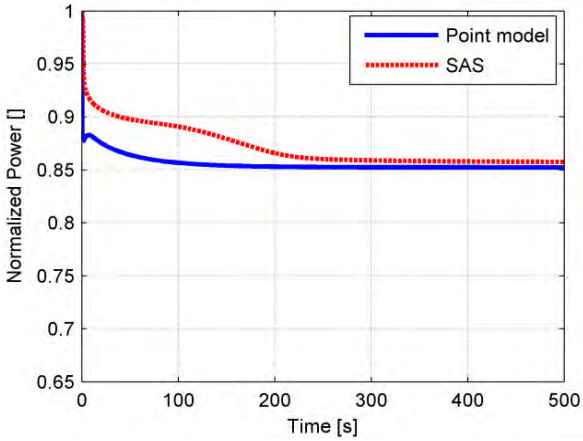


**Figure 33. Normalized power following a 20 K inlet temperature enhancement for MOX EoC.**

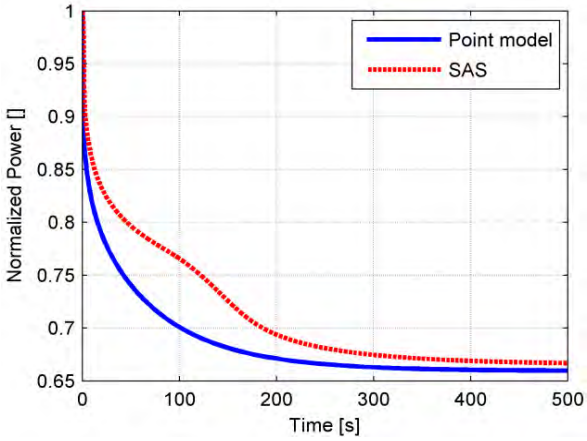


**Figure 34. Normalized power following a 20 K inlet temperature enhancement for MET BoC.**

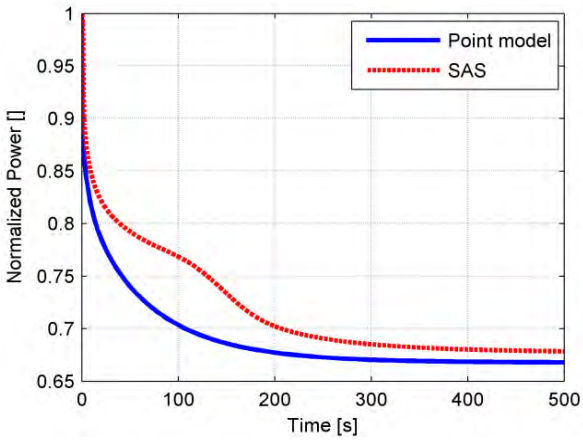


**Figure 35. Normalized power following a 20 K inlet temperature enhancement for MET EoC.**

The normalized power curves exhibit discrepancies directly depending on the different reactivity trends mentioned above, the power level resulting always slightly underestimated by the analytical model. In the case of MOX, the prompt power decrease is followed by a modest spike increase, after which the function tends to its asymptotic value; SAS4A/SASSYS-1 results show an analogous behavior, but more delayed in time. After the transient, the power is decreased by approximately 15.8 % (MOX BoC) and 14.8 % (MOX EoC) compared to the steady-state values, the discrepancies with SAS4A/SASSYS-1 being larger at BoC than at EoC. In the case of metal, quite significant differences (of the order of 8 %) are found in the intermediate part of the transient, as expected, but the asymptotic figures turn out to be consistent: the power settles at approximately 65.9 % (metal BoC) and 66.8 % (metal EoC) of its nominal value, the respective discrepancies with SAS4A/SASSYS-1 being up to 1.4 %.

The ULOHS scenario is investigated for different coolant inlet temperature stepwise increases, and results confirm a satisfactory agreement with SAS4A/SASSYS-1. For example, after a 5 K temperature enhancement,

the reactor power undergoes a decrease by 3.9 % (MOX BoC), 3.7 % (MOX EoC), 8.5 % (metal BoC) and 8.3 % (metal EoC) with respect to the steady-state values, the discrepancies with SAS4A/SASSYS-1 resulting under one per cent. As seen in the UTOP simulations above, discrepancies between SAS and the analytical model are very small in the case of small variations from the steady-state. For the purpose the model is expected to achieve, this is very satisfactory since small variations are typical situations considered in a control-oriented view.

Table XVI resumes the new steady-state power levels provided by SAS and by the analytical model in both cases of 5 °C and 20 °C inlet temperature enhancement.

**Table XVI. SAS and analytical model results in ULOHS simulations.**

| ULOHS | 5 K simulation | | | 20 K simulation | | |
|---|---|---|---|---|---|---|
| | SAS | Point model | Discrepancy[8] | SAS | Point model | Discrepancy[8] |
| MOX BoC | 290.27 | 288.15 | - 0.73 % | 262.36 | 252.63 | - 3.71 % |
| MOX EoC | 288.89 | 288.93 | + 0.01 | 257.11 | 255.66 | - 0.57 % |
| MET BoC | 274.8 | 274.44 | - 0.13 % | 199.59 | 197.88 | - 0.86 % |
| MET EoC | 275.7 | 275.07 | - 0.23 % | 203.12 | 200.34 | - 1.37 % |

*ULOF simulation*

A simplified ULOF event is simulated by specifying the core mass flow rate as a function of time, the pump driving head being modeled to exponentially decay with an 8 s coast-down half-time.

As an immediate effect, the coolant average temperature undergoes an increase, making the cladding temperature rise analogously. The respective feedbacks involved concur to bring about an insertion of negative reactivity (depicted in Figs. from 36 to 39), which makes the core power be subject to a steep decrease in the first part of the transient (Figs. from 40 to 43), as far as the contribution of Doppler starts balancing the negative reactivity effects, along with the axial re-contraction due to the decreasing cladding temperature, and the positive contribution of the lead density effect, finally reinstating criticality.

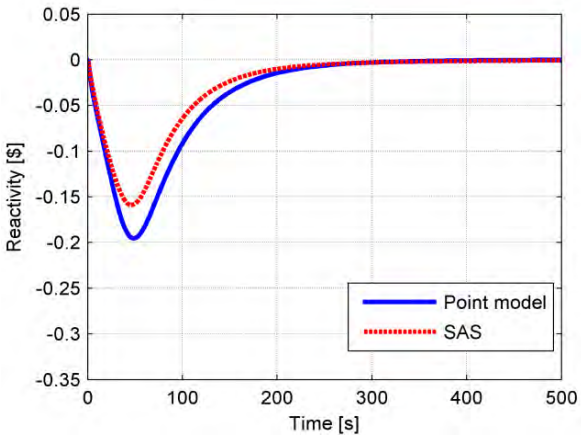


**Figure 36. Reactivity function following a mass flow rate reduction for MOX BoC.**

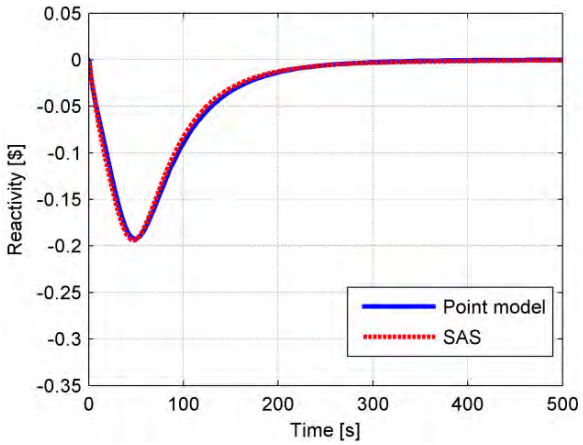


**Figure 37. Reactivity function following a mass flow rate reduction for MOX EoC.**

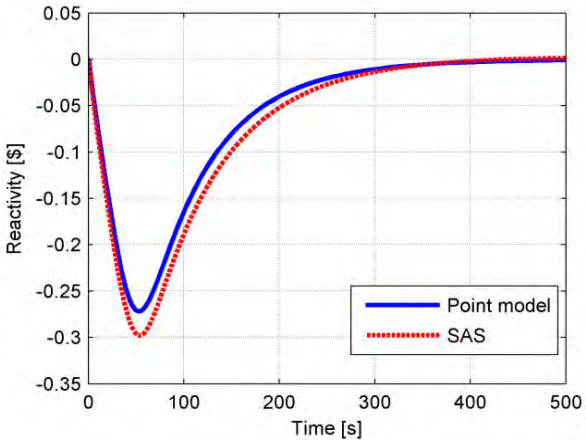


**Figure 38. Reactivity function following a mass flow rate reduction for MET BoC.**

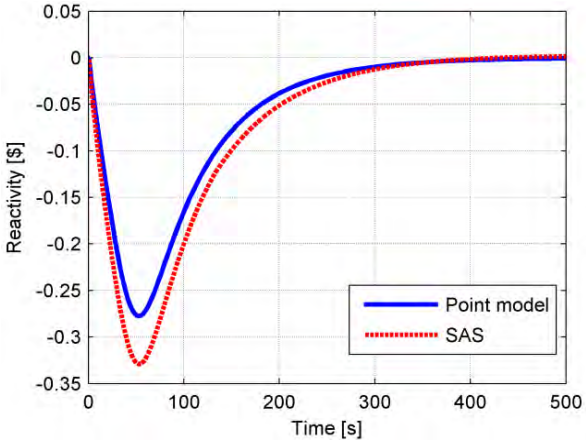


**Figure 39. Reactivity function following a mass flow rate reduction for MET EoC.**

A very good agreement is found between the analytical model and SAS4A/SASSYS-1 results, in particular for MOX at EoC, where reactivity curves are almost perfectly overlapped. Some discrepancies are present in the other cases, despite the analogous trends during the transient: the point model provides a more negative reactivity variation for MOX at BoC (by approximately 0.04 $, corresponding to 14 pcm), and a less consistent diminution for metal at both BoC and EoC (by approximately 0.03 $, 10 pcm, and 0.05 $, 18 pcm).

The normalized power curves exhibit some discrepancies as well: the power level results underestimated in the worst situation by approximately 20 % (BoC) by the analytical model in the case of MOX; the same trend is found also at EoC, even if the difference between SAS and the analytical model are less important. On the contrary, the analytical model overestimates the results up to a dozen per cents in the simulations with metallic fuel. It must be recalled that such a severe accidental transient, typically studied within safety analyses, is not among the main targets of a control-oriented model; anyway, results show that the simple analytical point model developed is quite satisfactory even in this kind of scenario.

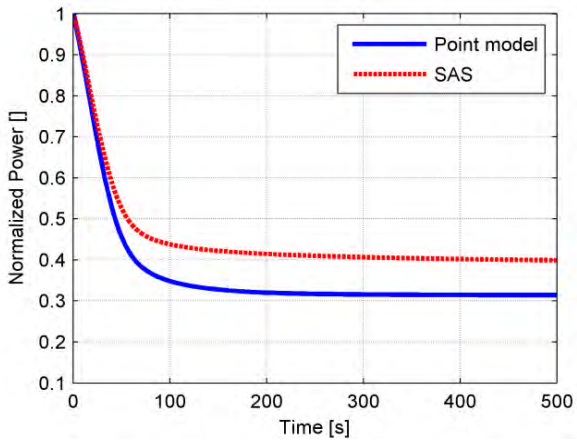


**Figure 40. Normalized power following a mass flow rate reduction for MOX BoC.**

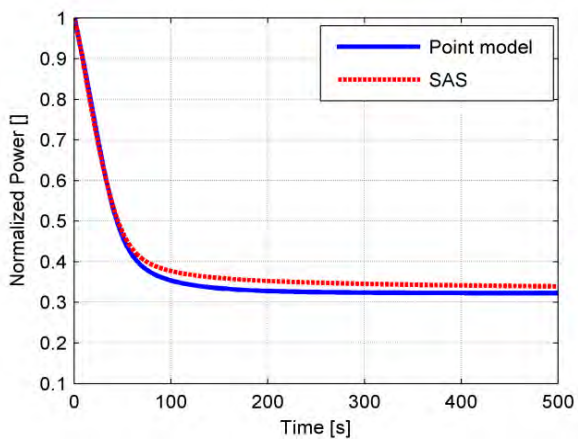


**Figure 41. Normalized power following a mass flow rate reduction for MOX EoC.**

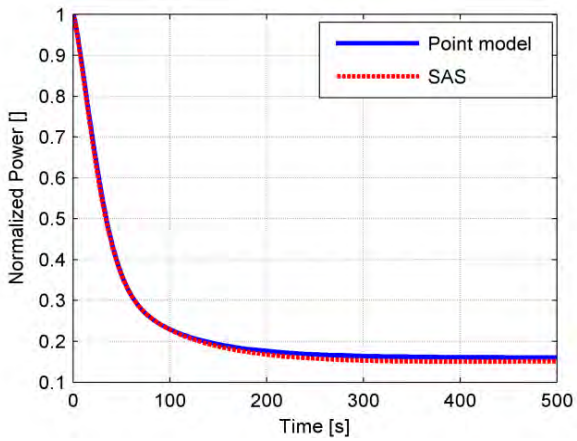


**Figure 42. Normalized power following a mass flow rate reduction for MET BoC.**

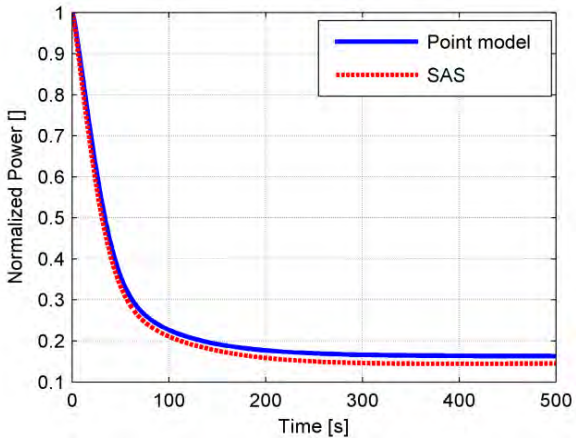


**Figure 43. Normalized power following a mass flow rate reduction for MOX EoC.**

Table XVII resumes the new steady-state power levels provided by SAS and by the analytical model after ULOF simulations.

**Table XVII. SAS and analytical model results in ULOF simulations.**

| ULOF | Pump 8 s decay time | | |
|---|---|---|---|
| | SAS | Analytical model | Discrepancy |
| MOX BoC | 119.65 | 94.17 | - 21.3 % |
| MOX EoC | 101.70 | 96.69 | - 4.93 % |
| MET BoC | 45.31 | 48 | + 5.93 % |
| MET EoC | 43.44 | 48.84 | + 12.42 % |

#### *3.1.1.5 Sensitivity analysis*

A sensitivity analysis has been performed in order to evaluate the impact of material physical properties and of the calculation of reactivity coefficients on the on the simulation parameters and the system dynamics performance.

Different correlations to define the properties of MOX and metallic fuel, as well as T91 FMS and lead, have been examined. In Tab. XVIII the per cent variations of power due to a 1 % variation of each parameter have been collected referring to the UTOP and ULOHS scenarios discussed above (20 pcm and 20 K cases).

**Table XVIII. Sensitivity analysis on material physical properties.**

| Physical parameters | UTOP | | ULOHS | |
|---|---|---|---|---|
| | MOX | METAL | MOX | METAL |
| Pin outer diameter | 0.004135 | 0.001393 | - 0.011550 | - 0.005709 |
| Cladding thickness | - 0.001033 | - 0.002229 | 0.002886 | 0.009108 |
| Active height | 0.042310 | 0.032330 | - 0.118100 | - 0.132100 |
| Pin number | 0.041430 | 0.027640 | - 0.115700 | - 0.112900 |
| Pin pitch | - 0.000696 | - 0.003770 | 0.001944 | 0.015400 |
| Average coolant temperature | 3.243000 | 6.572000 | 4.121000 | 11.31000 |
| Inlet coolant temperature | - 1.385000 | - 2.621000 | - 2.220000 | - 7.257000 |
| Outlet coolant temperature | - 1.863000 | - 3.947000 | - 1.844000 | - 3.806000 |
| Coolant density | $5.014 \cdot 10^{-9}$ | $4.674 \cdot 10^{-8}$ | $7.359 \cdot 10^{-9}$ | $- 8.819 \cdot 10^{-7}$ |
| Coolant specific heat capacity | $5.014 \cdot 10^{-9}$ | $4.674 \cdot 10^{-8}$ | $7.359 \cdot 10^{-9}$ | $- 8.819 \cdot 10^{-7}$ |
| Coolant thermal conductivity | 0.000452 | 0.002446 | - 0.001261 | - 0.009995 |
| Coolant viscosity | 0 | $- 2.319 \cdot 10^{-13}$ | $- 6.750 \cdot 10^{-14}$ | $1.336 \cdot 10^{-12}$ |
| Clad density | $4.287 \cdot 10^{-9}$ | $2.585 \cdot 10^{-8}$ | $1.608 \cdot 10^{-8}$ | $- 9.282 \cdot 10^{-7}$ |
| Clad specific heat capacity | $4.287 \cdot 10^{-9}$ | $2.585 \cdot 10^{-8}$ | $1.608 \cdot 10^{-8}$ | $- 9.282 \cdot 10^{-7}$ |
| Clad thermal conductivity | 0.000569 | 0.002076 | - 0.001591 | - 0.008482 |
| Fuel density | 6.117·10-7 | 5.635·10-7 | - 2.285·10-6 | - 9.700·10-6 |
| Fuel practical density | 0 | 5.635·10-7 | 0 | - 9.700·10-6 |
| Fuel specific heat capacity | 1.678·10-7 | 5.635·10-7 | - 6.967·10-7 | - 9.700·10-6 |
| Fuel thermal conductivity | 0.037150 | 0.023100 | - 0.103700 | - 0.094370 |
| Pu fraction | 1.112·10-8 | - 0.016170 | - 4.620·10-8 | 0.066050 |
| Fuel internal diameter | -1.374·10-7 | 0 | 5.717·10-7 | 0 |
| Power | 0.958800 | 0.972000 | 1.115000 | 1.114000 |
| Gap thickness | - 0.000116 | 0 | 0.000311 | 0 |
| Gap height | 0.003155 | 0 | - 0.008809 | 0 |

In Tabs. XIX and XX the results showing the power per cent variation corresponding to a unitary per cent perturbation of reactivity coefficients are collected with reference to the UTOP and ULOHS simulations, respectively.

**Table XIX. Sensitivity analysis on reactivity coefficients (UTOP scenario).**

| Coefficient | MOX BOC | MOX EOC | METAL BOC | METAL EOC |
|---|---|---|---|---|
| $\alpha_D$ | - 0.046740 | - 0.041790 | - 0.041450 | - 0.035890 |
| $\alpha_L$ | - 0.011830 | - 0.009132 | - 0.047260 | - 0.040510 |
| $\alpha_R$ | - 0.007473 | - 0.005443 | - 0.029310 | - 0.023470 |
| $\alpha_Z$ | - 0.000730 | - 0.003187 | - 0.007312 | - 0.013600 |

**Table XX. Sensitivity analysis on reactivity coefficients (ULOHS scenario).**

| Coefficient | MOX BOC | MOX EOC | METAL BOC | METAL EOC |
|---|---|---|---|---|
| $\alpha_D$ | 0.117800 | 0.108400 | 0.139000 | 0.127600 |
| $\alpha_L$ | - 0.071610 | - 0.063040 | - 0.091120 | - 0.089560 |
| $\alpha_R$ | - 0.045220 | - 0.037570 | - 0.056510 | - 0.051900 |
| $\alpha_Z$ | - 0.001627 | - 0.008499 | 0.006928 | 0.012640 |

### 3.1.2 One-precursor-group approximation

A one precursor group approximation is employed to build a second approximate model from the reference non-linear one. The purpose is to simplify the kinetics model, since the equation system can be reduced from seven to two equations, one for neutron density and one for the average behavior of precursors.

Firstly, it is necessary to define two parameters. The one group delayed neutron fraction, $\beta$, can be defined as:

$$\beta = \sum_{i=1}^{6} \beta_i \tag{57}$$

The determination of the one group decay constant $\lambda$ is more problematic, since there is not a unique expression but the approximation depends strongly on the entity of the reactivity insertion. In fact $\lambda$ is calculated from the inhour equation, which can be approximated in different ways according to reactor period ($T$) and inserted reactivity ($\rho$). The inhour equation takes $\lambda$, $\rho$ e $T$ into account as follows:

$$\rho = \frac{\Lambda}{T} + \sum_{i=1}^{6} \frac{\beta_i}{1 + \lambda_{d,i} T} \tag{58}$$

In the considered case, a small reactivity approximation is chosen, far from the condition of prompt critical state. After this consideration, the relation for the one group decay constant can be written as:

$$\frac{1}{\lambda_d} = \frac{1}{\beta} \sum_{1}^{6} \frac{\beta_i}{\lambda_{d,i}} \tag{59}$$

For both small and very large reactivity variations the approximation brings goods results compared with the six groups reference model. The main differences lay in an intermediate zone, near to the prompt critical state. The equation for neutron density $n(t)$ has two exponential terms, one increasing and one decreasing. The absence of an intermediate term leads to a faster dynamics in the one group approximation than in the six groups case, with an underestimation of the time necessary to reach the new steady state.

***Results***

The impact of the one neutron precursor group approximation is evaluated by assessing the limits of the latter model predictions, which is compared to the reference one (non-linear, six precursor groups) for increasing perturbations. In particular, the system behavior following unprotected transient initiators such as ULOHS - simulated by coolant inlet temperature enhancements -, and UTOP - induced by direct reactivity insertions led by a control rod withdrawal -, is investigated. Furthermore, a SCRAM scenario is studied.

*ULOHS scenario*

The latter ULOHS scenario (20 K temperature rise) is further investigated by employing the one-group approximation for the non-linear neutron kinetics. Also in this case results show a very good agreement upon steady-state figures (discrepancies of the order of some per mils), but quite significant differences in the first half (approximately up to 200 s) of the transient: for example, at the very beginning the simplified model generally underestimates the power variation (Fig. 44) quite evidently, the largest discrepancies being of the order of 8 $MW_{th}$ (MOX, BoC), and then slightly overestimates it (by approximately 1 $MW_{th}$ for both metal and MOX at BoC and EoC) just before it settles at its final values. As far as temperatures are concerned (Fig. 45), an analogous situation is found: discrepancies at the beginning of the transients are of the order of some 3 ÷ 5 K for cladding and of some 10 ÷ 15 K for fuel, while being roughly ten times smaller towards the steady-state.

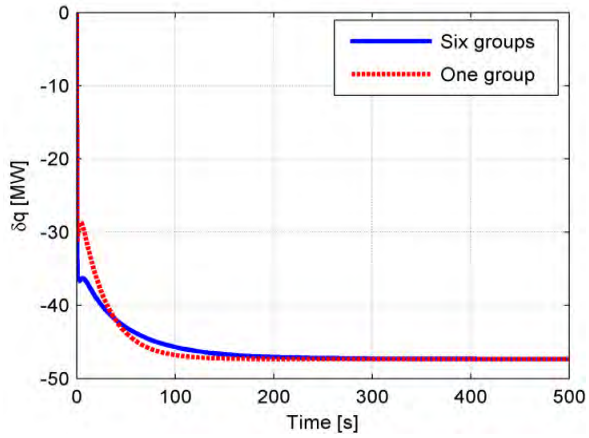


**Figure 44. Power variation following a 20 K enhancement of coolant inlet temperature (MOX, BoC).**

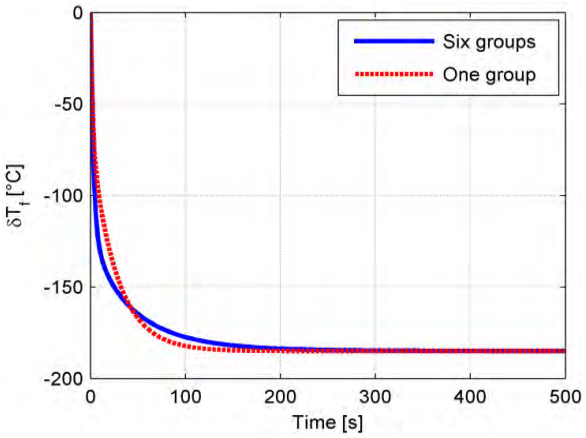


**Figure 45. Fuel temperature variation following a 20 K enhancement of coolant inlet temperature (MOX, BoC).**

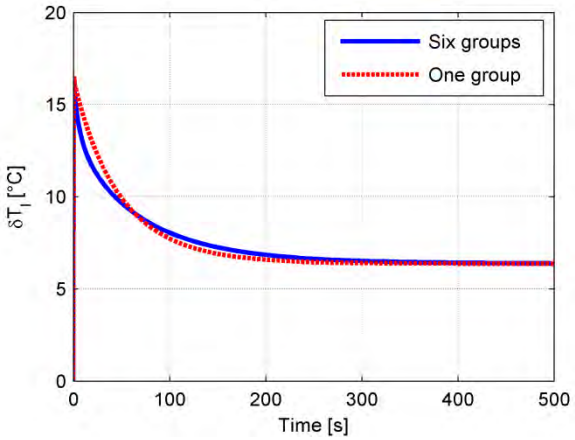


**Figure 46. Lead average temp. variation following a 20 K enhancement of coolant inlet temperature (Met, BoC).**

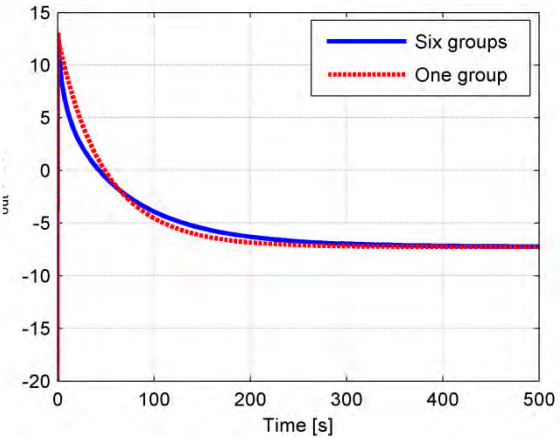


**Figure 47. Outlet temperature variation following a 20 K enhancement of coolant inlet temperature (Met, BoC).**

As evident from Figs. 46 and 47, when employing the one-group approximation for neutron precursors, the model yields a kind of "amplified" dynamics: the respective output functions exhibit analogous trends compared to the reference ones, but usually characterized by greater derivatives, as their emphasized variations indicate, resulting conservative at the very beginning of the transient, and slightly less conservative just before reaching the steady-state. The one-group approximation underestimates the time to reach the new steady-state values since in such an approximation five time exponential terms are neglected in the neutron population expression.

*UTOP scenario*

The UTOP scenario initiated by a 20 pcm reactivity insertion is in turn examined to compare once more the six-group non-linear point kinetics treatment with its one-group approximation. Results show a very good agreement upon steady-state figures (discrepancies of the order of some per mils), but quite significant differences in the first half (approximately up to 200 s) of the transient.

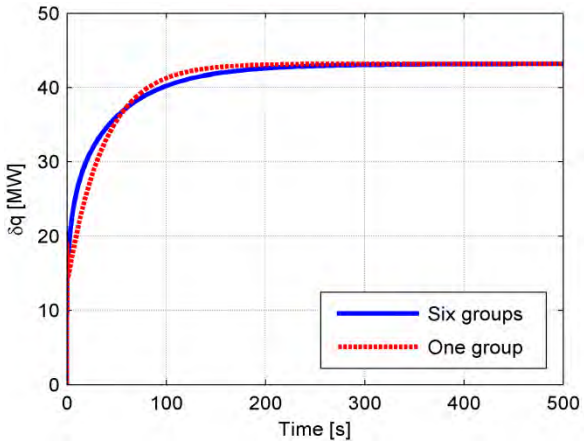


**Figure 48. Power variation following a 20 pcm reactivity insertion (Met, BoC).**

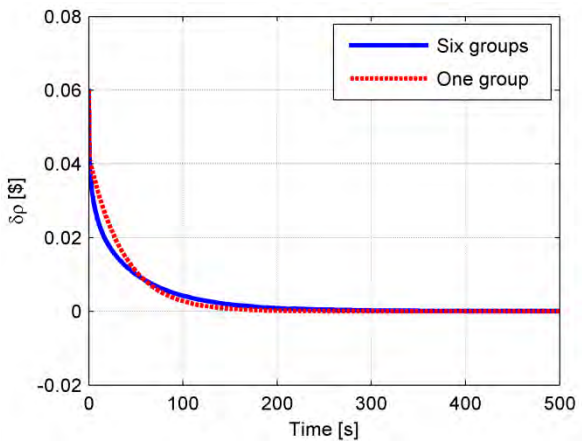


**Figure 49. Reactivity variation following a 20 pcm reactivity insertion (Met, BoC).**

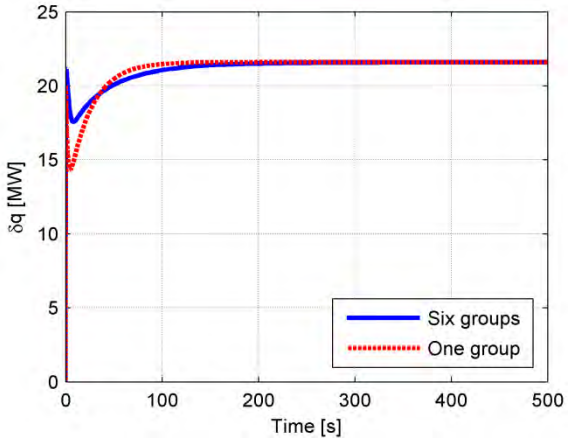


**Figure 50. Power variation following a 20 pcm reactivity insertion (MOX, BoC).**

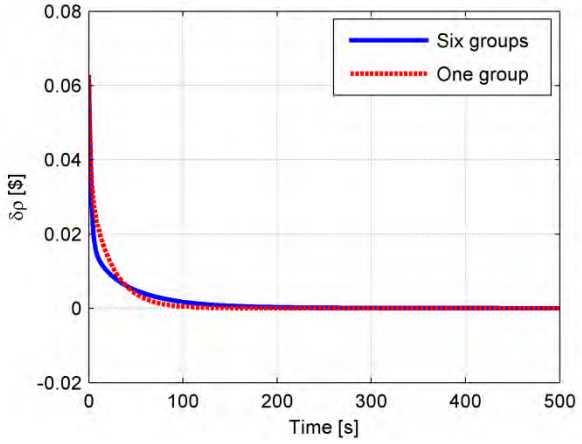


**Figure 51.1 Reactivity variation following a 20 pcm reactivity insertion (MOX, BoC).**

As in the ULOHS situation, the simplified model generally underestimates the power variation (Figs. from 48 to 51) quite evidently in the first 100 seconds, the largest discrepancies being of the order of 6 $MW_{th}$ (metal, BoC), and then slightly overestimates it (by less than 1 $MW_{th}$ for both metal and MOX at BoC and EoC) just before it settles at the new steady-state, whose achievement is anticipated by some seconds indeed. Nevertheless, results attest again a kind of "amplified" dynamics brought by the one-group approximation and a time-to-steady state underestimation, as clarified above.

***SCRAM simulation***

As a final point, a SCRAM simulation is carried out with the focal purpose of assessing the suitability of the one-group approximation of neutron kinetics in such a scenario, for which a proper comprehension of the system dynamics and its characteristic time response constitutes a fundamental safety-related concern.

The emergency FAR system is simulated to be activated by inserting 4800 pcm (*i.e.*, some 15 $) of negative reactivity, and handled with the non-linear reference model, given the magnitude of the perturbation, certainly not properly manageable by a linearized one.

As predictable, the system shuts itself down immediately after the stepwise perturbation, with time characteristics and amplitudes essentially determined by the prompt neutron lifetimes and the delayed neutron fractions involved. The one-group-approximated model provides a reasonably accurate representation of the average system dynamics; however, at the beginning of the transient it underestimates the reactivity decrease to some extent, so that the zero-power condition is reached with some delay compared with the reference results.

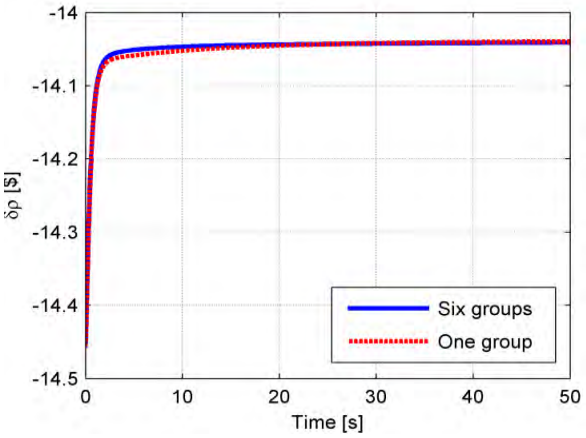


**Figure 52. Reactivity variation following a - 4800 pcm insertion (metal, BoC).**

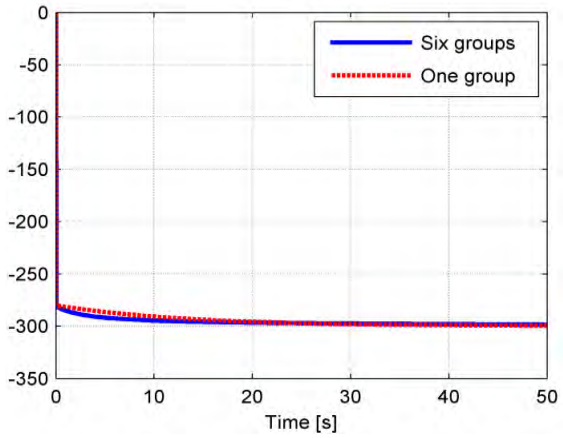


**Figure 53. Power variation following a - 4800 pcm insertion (metal, BoC).**

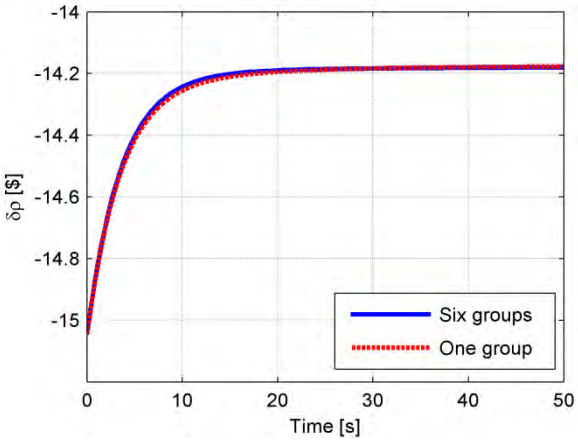


**Figure 53. Reactivity variation following a - 4800 pcm insertion (MOX, BoC).**

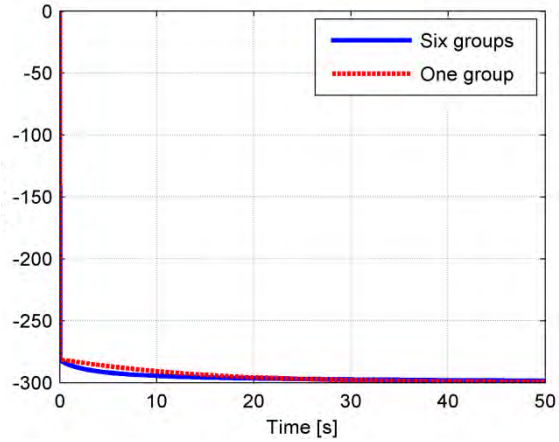


**Figure 54. Power variation following a - 4800 pcm insertion (MOX, BoC).**

Nevertheless, it can be stated that the combination of each precursor group exponential decay is well reproduced by its fictitious one-group representation, which actually grasps the weight-averaged behavior.

### 3.1.3 Linear approximation

Linearization consists in the approximation of a non-linear system through a linear system, based on the assumption that the system is almost linear within a certain range of operation. The need to linearize the model comes from the handiness of linear analysis tools allowing to:

- display and analyze dynamic behaviors of a model;
- verify the system stability;
- express a physical model in terms of transfer function, state space model, or zero-pole-gain model;
- determine the response of a model to arbitrary input signals.

For these reasons, the reference non-linear model is linearized around the equilibrium operating points (e.g., at nominal power) to achieve a simple, quick and accurate analysis of the system dynamic behavior.

***Method***

*Linear kinetics*

As far as kinetics is concerned, the linearization involves only Eq. (3) because of the presence of the product $\rho(t) \cdot n(t)$ between two state variables. After the linearization around the stationary configuration point, neutron and precursor densities are normalized in order to unloose the problem from the initial values; in such a way a model easy to handle and adaptable to various operating points can be obtained.

Firstly, a variational formulation for the following variables is introduced:

$$n(t) = n_0 + \delta n(t)$$

$$c_i(t) = c_{i0} + \delta c(t)$$
$$\rho(t) = \rho_0 + \delta\rho(t) \quad (60)$$

After some algebraic calculations, the equation system becomes:

$$\frac{d}{dt}\delta n(t) = \frac{\rho_0 - \beta}{\Lambda}\delta n(t) + \sum_{i=1}^{6}\lambda_{d,i}\delta c_i + \frac{n_0}{\Lambda}\delta\rho(t) + \frac{\delta\rho(t)\delta n(t)}{\Lambda} \quad (61)$$

$$\frac{d}{dt}\delta c_i(t) = \frac{\beta_i}{\Lambda}\delta n(t) - \lambda_{d,i}\delta c_i \quad (62)$$

The out-and-out linear approximation can be accomplished by neglecting the last term in Eq. (11). In fact, if it is possible to consider only small reactivity insertions, this second-order term can be ignored. In the simulation section, the impact of this approximation on results for small and large reactivity variations is evaluated.
Normalization permits to define two new variables:

$$\psi(t) = \frac{n(t)}{n_0} \qquad \eta_i(t) = \frac{c_i(t)}{c_{i0}} \quad (63)$$

Using the steady-state condition:

$$c_{i0} = \frac{\beta_i}{\lambda_i\Lambda}n_0 \quad (64)$$

the final linearized system of equations is obtained:

$$\frac{d}{dt}\delta\psi(t) = -\frac{\beta}{\Lambda}\delta\psi(t) + \sum_{i=1}^{6}\frac{\beta_i}{\Lambda}\delta\eta_i + \frac{\delta\rho(t)}{\Lambda} \quad (65)$$

$$\frac{d}{dt}\delta\eta_i(t) = \lambda_{d,i}\delta\psi(t) - \lambda_{d,i}\delta\eta_i \quad (66)$$

Equations (65) and (66) represent a system of seven ODEs, referring to the deviation from the operating point. For $t \leq 0$ the system is considered at steady state; the initial conditions are:

$$\delta\psi(0) = 0 \qquad \delta\eta(0) = 0 \quad (67)$$

*Linear thermal-hydraulics*

The T/H block has to be linearized since in Eq. (7) two non-linear terms are present (i.e., the product between mass flow rate and average lead temperature, and between mass flow rate and lead inlet temperature). The affected variables can be written as:

$$T_f(t) = T_{f0} + \delta T_f(t)$$

$$T_c(t) = T_{c0} + \delta T_c(t)$$

$$T_l(t) = T_{l0} + \delta T_l(t)$$

$$\Gamma(t) = \Gamma_0 + \delta\Gamma(t) \tag{68}$$

$$q(t) = q_0 + \delta q(t)$$

The introduction of characteristic time constants can be useful, both to simplify the management of variables from an algebraic point of view, and to have reference values for what concerns heat exchange:

$$\tau_f = \frac{M_f C_f}{k_{fc}}$$

$$\tau_{c1} = \frac{M_c C_c}{k_{fc}}$$

$$\tau_{c2} = \frac{M_c C_c}{h_{cl}} \tag{69}$$

$$\tau_l = \frac{M_l C_l}{h_{cl}}$$

$$\tau_0 = \frac{M_l}{\Gamma}$$

The first four temporal parameters represent the time constants of the thermal exchange occurring between two zones, whereas $\tau_0$ indicates the coolant circulation time in the core loop.

Finally, the following equations are found:

$$\frac{d\delta T_f(t)}{dt} = -\frac{1}{\tau_f}\delta T_f(t) + \frac{1}{\tau_f}\delta T_c(t) + \frac{1}{M_f C_f}\delta q(t) \tag{70}$$

$$\frac{d\delta T_c(t)}{dt} = \frac{1}{\tau_{c1}}\delta T_f(t) - \left(\frac{1}{\tau_{c1}} + \frac{1}{\tau_{c2}}\right)\delta T_c(t) + \frac{1}{\tau_{c2}}\delta T_l(t) \tag{71}$$

$$\frac{d\delta T_l(t)}{dt} = \frac{1}{\tau_l}\delta T_c(t) - \left(\frac{1}{\tau_l} + \frac{2}{\tau_0}\right)\delta T_l(t) + \frac{2}{\tau_0}\delta T_{in}(t) - \frac{2}{M_l}\delta\Gamma(t)\delta T_l(t) + \frac{2}{M_l}\delta\Gamma(t)\delta T_{in}(t) - \frac{2}{M_l}(T_{l0} - T_{in0})\delta\Gamma(t) \tag{72}$$

The linearization is performed again by neglecting the second-order terms, (i.e., products between coolant temperatures and mass flow rate). It is important to observe that this approximation will lead to several discrepancies if a large mass flow rate variation is considered, as in the Unprotected Loss of Flow (ULOF) case. With the following relation between thermal power and neutron density:

$$\delta q(t) = q_0\delta\psi(t) \tag{73}$$

the definitive equations describing the T/H behavior of the system are found:

$$\frac{d\delta T_f(t)}{dt} = -\frac{1}{\tau_f}\delta T_f(t) + \frac{1}{\tau_f}\delta T_c(t) + \frac{q_0}{M_f C_f}\delta\psi(t) \tag{74}$$

$$\frac{d\delta T_c(t)}{dt} = \frac{1}{\tau_{c1}}\delta T_f(t) - \left(\frac{1}{\tau_{c1}} + \frac{1}{\tau_{c2}}\right)\delta T_c(t) + \frac{1}{\tau_{c2}}\delta T_l(t) \tag{75}$$

$$\frac{d\delta T_l(t)}{dt} = \frac{1}{\tau_l}\delta T_c(t) - \left(\frac{1}{\tau_l} + \frac{2}{\tau_0}\right)\delta T_l(t) + \frac{2}{\tau_0}\delta T_{in}(t) - \frac{2}{M_l}(T_{l0} - T_{in0})\delta\Gamma(t) \tag{76}$$

***Model implementation***

For a linear model, the use of SIMULINK® is not necessary thanks to the possibility to study the system directly in MATLAB®. In fact, the set of linearized equations can be handled in terms of state vector ($\underline{X}$), input vector ($\underline{U}$), output vector ($\underline{Y}$), corresponding matrices ($\underline{\underline{A}}$, $\underline{\underline{B}}$ and $\underline{\underline{C}}$, respectively) and feedthrough matrix ($\underline{\underline{D}}$), leading to the following state space representation:

$$\begin{cases} \dot{\underline{X}} = \underline{\underline{A}}\,\underline{X} + \underline{\underline{B}}\,\underline{U} \\ \underline{Y} = \underline{\underline{C}}\,\underline{X} + \underline{\underline{D}}\,\underline{U} \end{cases} \tag{77}$$

The ten state variables are the variations from the respective steady-state values of: fuel temperature ($\delta T_f$), cladding temperature ($\delta T_c$), average coolant temperature ($\delta T_l$), neutron density ($\delta\psi$) and six groups neutron precursor densities ($\delta\eta_i$):

$$\underline{X} = \begin{bmatrix} \delta\psi \\ \delta\eta_1 \\ \delta\eta_2 \\ \delta\eta_3 \\ \delta\eta_4 \\ \delta\eta_5 \\ \delta\eta_6 \\ \delta T_f \\ \delta T_c \\ \delta T_l \end{bmatrix} \tag{78}$$

The twelve output variables considered are the variations from the respective steady-state values of: thermal power ($\delta q$), precursor densities ($\delta\eta_i$), temperatures - fuel ($\delta T_f$), cladding ($\delta T_c$), average coolant ($\delta T_l$), and outlet coolant ($\delta T_{out}$ ) - and reactivity ($\delta\rho$):

$$\underline{Y} = \begin{bmatrix} \delta q \\ \delta\eta_1 \\ \delta\eta_2 \\ \delta\eta_3 \\ \delta\eta_4 \\ \delta\eta_5 \\ \delta\eta_6 \\ \delta T_f \\ \delta T_c \\ \delta T_l \\ \delta T_{out} \\ \delta\rho \end{bmatrix} \tag{79}$$

In order to obtain information from the model, three variables are taken into account as inputs: variations of CRs insertion share ($\delta h_{cr}$), inlet coolant temperature ($\delta T_{in}$) and coolant mass flow rate ($\delta\Gamma$). The latter are perturbed to simulate different scenarios, such as UTOP, ULOHS and ULOF, respectively The resulting input vector is:

$$\underline{U} = \begin{bmatrix} \delta h_{cr} \\ \delta T_{in} \\ \delta\Gamma \end{bmatrix} \tag{80}$$

The MIMO (Multi Input – Multi Output) system described by Eqs. (77) is directly simulated in MATLAB®, once the four matrices are obtained:

$$\underline{\underline{A}} = \begin{bmatrix} -\frac{\beta}{\Lambda} & \frac{\beta_1}{\Lambda} & \frac{\beta_2}{\Lambda} & \frac{\beta_3}{\Lambda} & \frac{\beta_4}{\Lambda} & \frac{\beta_5}{\Lambda} & \frac{\beta_6}{\Lambda} & \frac{\alpha_D}{\Lambda} & \frac{\alpha_Z}{\Lambda} & \frac{\alpha_L+\alpha_R}{\Lambda} \\ \lambda_{d,1} & -\lambda_{d,1} & 0 & 0 & 0 & 0 & 0 & 0 & 0 & 0 \\ \lambda_{d,2} & 0 & -\lambda_{d,2} & 0 & 0 & 0 & 0 & 0 & 0 & 0 \\ \lambda_{d,3} & 0 & 0 & -\lambda_{d,3} & 0 & 0 & 0 & 0 & 0 & 0 \\ \lambda_{d,4} & 0 & 0 & 0 & -\lambda_{d,4} & 0 & 0 & 0 & 0 & 0 \\ \lambda_{d,5} & 0 & 0 & 0 & 0 & -\lambda_{d,5} & 0 & 0 & 0 & 0 \\ \lambda_{d,6} & 0 & 0 & 0 & 0 & 0 & -\lambda_{d,6} & 0 & 0 & 0 \\ \frac{q}{M_f C_f} & 0 & 0 & 0 & 0 & 0 & 0 & -\frac{1}{\tau_f} & \frac{1}{\tau_f} & 0 \\ 0 & 0 & 0 & 0 & 0 & 0 & 0 & \frac{1}{\tau_{c1}} & -\left(\frac{1}{\tau_{c1}}+\frac{1}{\tau_{c2}}\right) & \frac{1}{\tau_{c2}} \\ 0 & 0 & 0 & 0 & 0 & 0 & 0 & 0 & \frac{1}{\tau_l} & -\left(\frac{1}{\tau_l}+\frac{2}{\tau_0}\right) \end{bmatrix} \tag{81}$$

$$\underline{\underline{B}} = \begin{bmatrix} \frac{\alpha_H}{\Lambda} & 0 & 0 \\ 0 & 0 & 0 \\ 0 & 0 & 0 \\ 0 & 0 & 0 \\ 0 & 0 & 0 \\ 0 & 0 & 0 \\ 0 & 0 & 0 \\ 0 & 0 & 0 \\ 0 & 0 & 0 \\ 0 & \frac{2}{\tau_0} & -\frac{2}{M_l}(T_{l0}-T_{in0}) \end{bmatrix} \tag{82}$$

$$\underline{\underline{C}} = \begin{bmatrix} q_0 & 0 & 0 & 0 & 0 & 0 & 0 & 0 & 0 & 0 \\ 0 & 1 & 0 & 0 & 0 & 0 & 0 & 0 & 0 & 0 \\ 0 & 0 & 1 & 0 & 0 & 0 & 0 & 0 & 0 & 0 \\ 0 & 0 & 0 & 1 & 0 & 0 & 0 & 0 & 0 & 0 \\ 0 & 0 & 0 & 0 & 1 & 0 & 0 & 0 & 0 & 0 \\ 0 & 0 & 0 & 0 & 0 & 1 & 0 & 0 & 0 & 0 \\ 0 & 0 & 0 & 0 & 0 & 0 & 1 & 0 & 0 & 0 \\ 0 & 0 & 0 & 0 & 0 & 0 & 0 & 1 & 0 & 0 \\ 0 & 0 & 0 & 0 & 0 & 0 & 0 & 0 & 1 & 0 \\ 0 & 0 & 0 & 0 & 0 & 0 & 0 & 0 & 0 & 1 \\ 0 & 0 & 0 & 0 & 0 & 0 & 0 & 0 & 0 & 2 \\ 0 & 0 & 0 & 0 & 0 & 0 & 0 & \alpha_D & \alpha_Z & \alpha_L+\alpha_R \end{bmatrix} \tag{83}$$

$$\underline{\underline{D}} = \begin{bmatrix} 0 & 0 & 0 \\ 0 & 0 & 0 \\ 0 & 0 & 0 \\ 0 & 0 & 0 \\ 0 & 0 & 0 \\ 0 & 0 & 0 \\ 0 & 0 & 0 \\ 0 & 0 & 0 \\ 0 & 0 & 0 \\ 0 & 0 & 0 \\ 0 & -1 & 0 \\ \alpha_H & 0 & 0 \end{bmatrix} \tag{84}$$

***Results***

The impact of the system linearization is evaluated by analyzing several simple core-wise ULOHS, UTOP, and ULOF scenarios. In particular, the latter are simulated by imposing respectively small and consistent perturbations on input variables. In particular the results concerning a 5 and 20 K coolant inlet temperature enhancement for a simplified ULHOS simulation, and a 20 and 170 pcm reactivity insertion for a UTOP are presented and discussed referring to both the MOX- and metal-fueled cores at BoC and EoC. Analogously, the ULOF transient is studied by imposing mass flow rate reductions by 100, 1000 and 5000 kg $s^{-1}$.

*ULOHS scenario*

The dynamic responses of the MOX and metal-fuelled DEMO cores to a stepwise inlet temperature increase by 5 and 20 K is first considered. As depicted in Figs. 55 and 56 respectively, the new steady-states reached after the transients are exactly coincident in the case of small perturbations (5 K temperature enhancement), whereas very slight discrepancies (far smaller than 1 %) are present after a more consistent disturbance (20 K variation).

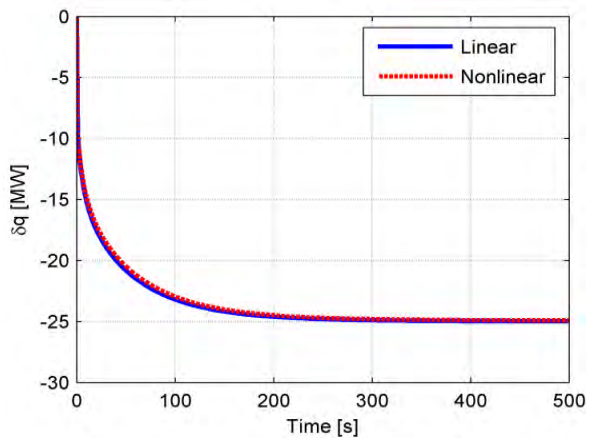


**Figure 55. Thermal power variation following a 5 K enhancement of coolant inlet temperature (met EoC).**

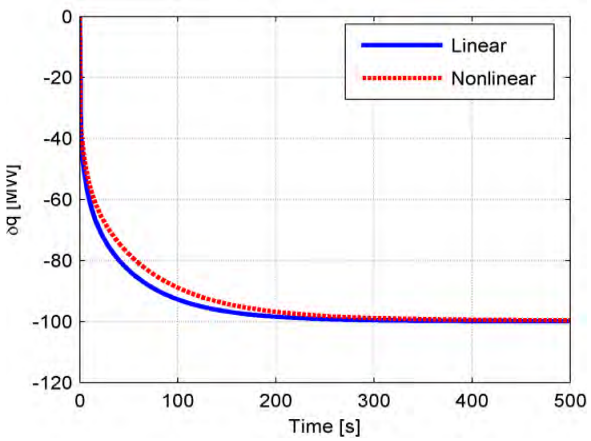


**Figure 56. Thermal power variation following a 20 K enhancement of coolant inlet temperature (met EoC).**

As shown in the case of power - assumed as an example of integral output variable of fundamental interest -, the impact of linearization is revisable during the transient development, rather than on steady-state figures. In fact, when small disturbances are applied, reactivity, power, temperature and neutron precursors linear and non-linear curves are almost entirely overlapped; conversely, when bigger perturbations are imposed, discrepancies are found at the beginning of the transients, on the basis of which it is evident how the linearized model underestimates power and temperatures (e.g. in Figs. 57 and 58), whose variation appear steeper, besides neutron precursor concentrations.

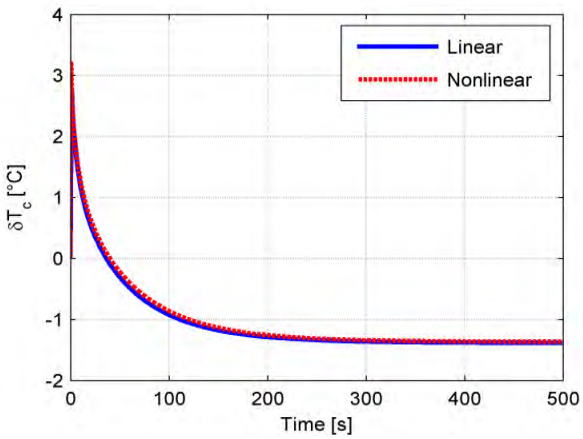


**Figure 57. Cladding temperature variation following a 5 K enhancement of coolant inlet temperature (met, EoC).**

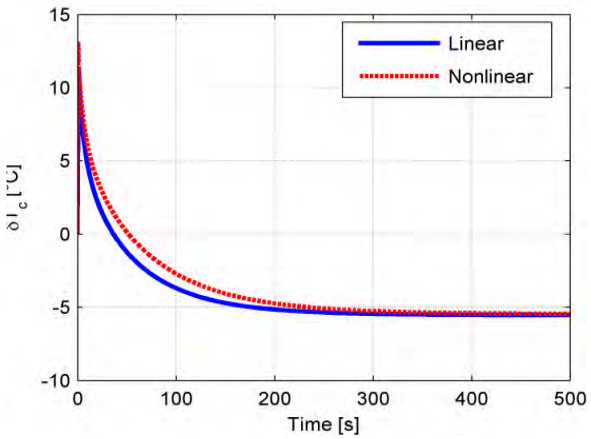


**Figure 58. Clad temperature variation following a 20 K enhancement of coolant inlet temperature (met, EoC).**

On the contrary, reactivity is slightly overestimated during the transient (Figs. 59 and 60). Anyway, discrepancies in the results are not very significant, in particular concerning the new steady-state characteristics (Tabs. XXI and XXII), mainly due to the fact that both disturbances lie in the range of the so-called small perturbations in absolute terms, being the corresponding reactivity variation of the maximum order of 0.1 $. This means that the term neglected during the linearization, i.e. $\delta\rho\delta n$, does not heavily influence the new steady-state results in ULOHS transient simulations for both 5 °C and 20 °C coolant inlet temperature enhancements, as clearly confirmed by the results. Nevertheless, it is pointed out that the linear model generally provides less conservative results.

A 20 K variation of the coolant inlet temperature, that in LWRs may be regarded as a significant perturbation though not so extraordinary, in a pool-type LFR system represents a very large disturbance, considering the thermal inertia of the pool. In this view, the linear model appears to be a suitable means to study such a kind of transients, since expected perturbations on this input parameter (coolant inlet temperature) lay in the range of small perturbations.

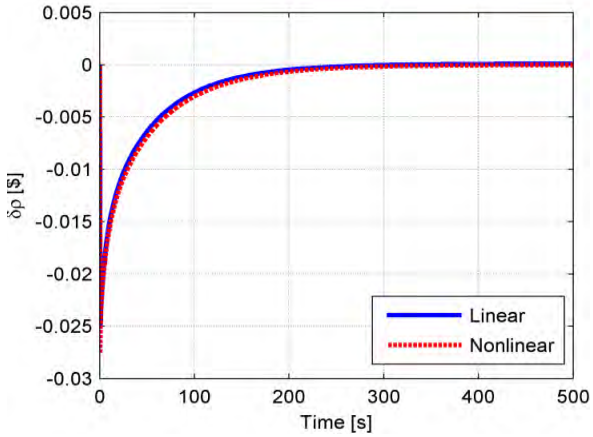


**Figure 59. Reactivity variation following a 5 K enhancement of coolant inlet temperature (met, EoC).**

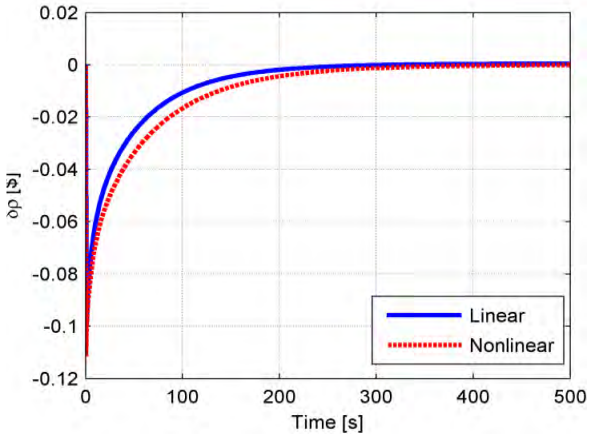


**Figure 60. Reactivity variation following a 20 K enhancement of coolant inlet temperature (met, EoC).**

**Table XXI. Variation of power and temperatures at the end of the transient for 5 °C ULOHS.**

| ULOHS 5°C | Variation of characteristic variables from their steady-state values at the end of the transient | | | | | | | |
|---|---|---|---|---|---|---|---|---|
| | Linear | | | | Non-linear | | | |
| | MOX BoC | MOX EoC | Met BoC | Met EoC | MOX BoC | MOX EoC | Met BoC | Met EoC |
| Power [$MW_{th}$] | - 11.85 | - 11.09 | - 25.64 | - 24.99 | - 11.84 | - 11.08 | - 25.55 | - 24.92 |
| Fuel T. [°C] | - 46.28 | - 43.00 | - 23.06 | - 22.35 | - 46.26 | - 42.98 | - 22.96 | - 22.27 |
| Clad T. [°C] | 2.218 | 2.396 | - 1.551 | - 1.385 | 2.219 | 2.398 | - 1.529 | - 1.368 |
| Lead T. [°C] | 3.421 | 3.522 | 1.582 | 1.668 | 3.421 | 3.522 | 1.593 | 1.677 |
| Outlet T. [°C] | 1.841 | 2.043 | - 1.837 | - 1.664 | 1.842 | 2.045 | - 1.814 | - 1.646 |

**Table XXII. Variation of power and temperatures at the end of the transient for 20 °C ULOHS.**

| ULOHS 20°C | Variation of characteristic variables from their steady-state values at the end of the transient | | | | | | | |
|---|---|---|---|---|---|---|---|---|
| | Linear | | | | Non-linear | | | |
| | MOX BoC | MOX EoC | Met BoC | Met EoC | MOX BoC | MOX EoC | Met BoC | Met EoC |
| Power [$MW_{th}$] | - 47.38 | - 44.35 | - 102.6 | - 99.96 | - 47.36 | - 44.34 | - 102.1 | - 99.66 |
| Fuel T. [°C] | - 185.1 | - 172 | - 92.25 | - 89.41 | - 185 | - 172 | - 91.79 | - 89.07 |
| Clad T. [°C] | 8.873 | 9.586 | - 6.203 | - 5.54 | 8.878 | 9.588 | - 6.096 | - 5.463 |
| Lead T. [°C] | 13.68 | 14.09 | 6.327 | 6.673 | 13.68 | 14.09 | 6.382 | 6.713 |
| Outlet T. [°C] | 7.365 | 8.174 | - 7.347 | - 6.655 | 7.37 | 8.176 | - 7.236 | - 6.575 |

*UTOP scenario*

The UTOP scenario simulation confirms the outcomes of the previous analysis: two disturbances are investigated and quite consistent discrepancies between the reference non-linear model and the simplified linearized one are found concerning the transient development following a consistent stepwise reactivity insertion (170 pcm, corresponding to approximately 0.5 $); on the contrary, curves representing dynamic responses to a small perturbation (*i.e.*, 20 pcm, about 0.06 $) exhibit an almost perfect mutual agreement. In both cases, steady-state figures differ for some per mils, at most.

The power variations induced by a 20 and 170 pcm reactivity insertion are depicted in the following Figures for MOX and metal at EoC, assumed as examples.

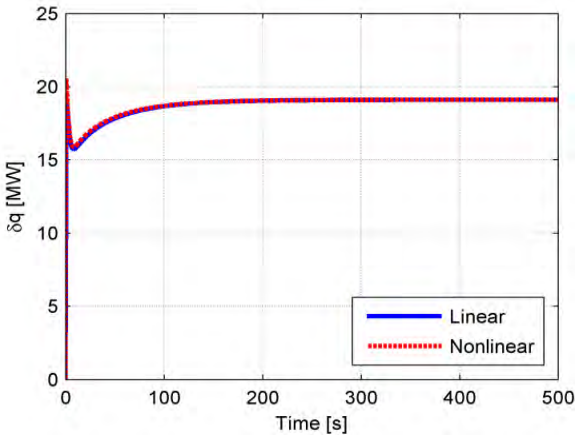


**Figure 61. Power variation following a 20 pcm reactivity insertion (MOX, EoC).**

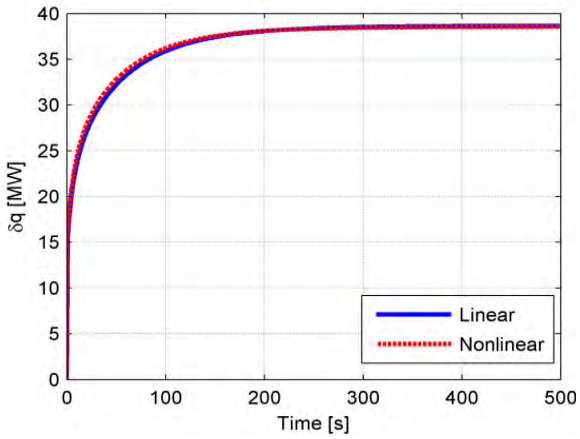


**Figure 62. Power variation following a 20 pcm reactivity insertion (met, EoC).**

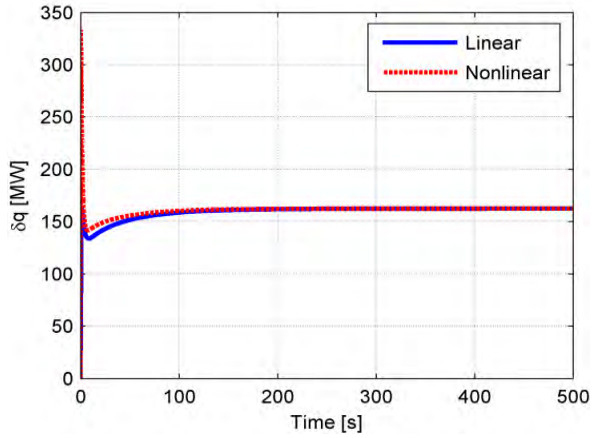


**Figure 63. Power variation following a 170 pcm reactivity insertion (MOX, EoC).**

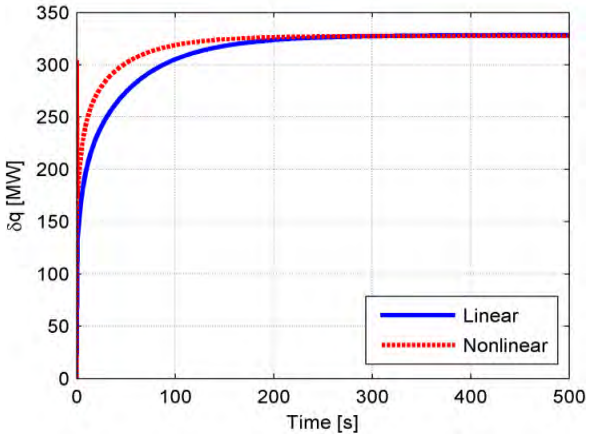


**Figure 64. Power variation following a 170 pcm reactivity insertion (met, EoC).**

It appears very clearly how small perturbations induce transients that the linearized model is perfectly able to reproduce, the largest discrepancies reaching a maximum of 5 % (corresponding to about 1 $MW_t$) in the case of MOX fuel. On the contrary, the non-conservativeness of the simplified model results critical following the insertion of 0.5 $: the power spike subsequent to such a perturbation has an amplitude of approximately 330 $MW_{th}$, which is underestimated by the double of its amount (165 $MW_{th}$) when linearizing the equations. An equivalent situation is found in the case of metal, where discrepancies are of the order of 120 $MW_{th}$. Therefore, the linear model turns out to be not able to properly describe the system dynamics, since qualitative trends are reproduced, but without quantitative consistency during the transient development, which undergoes a slight delay as well. The reason can be found in the lack of the second-order term $\delta\rho\delta n$, neglected during the linearization. In fact, the major discrepancies are found at the beginning when, thanks to the neutron prompt

jump, the quantity $\delta\rho\delta n$ reaches its highest value in the transient. As a consequence, temperature rises are always slower and less consistent, reaching their asymptotic values a bit later than in the reference case as well.

Discrepancies during transients are of the greatest order of 15 K for cladding temperatures, and of 60 K for fuel temperatures (metal, BoC), both corresponding to some 25 %. As far as neutron precursors are concerned, their concentrations result slightly underestimated by the linearized model, as described in the previous section (ULOHS simulation).

Anyway, the linear steady-state results are very close to the non-linear ones, as shown in Tabs. XXIII and XXIV, confirming that the terms neglected with linearization determine some differences only during the transient simulation without affecting the final results.

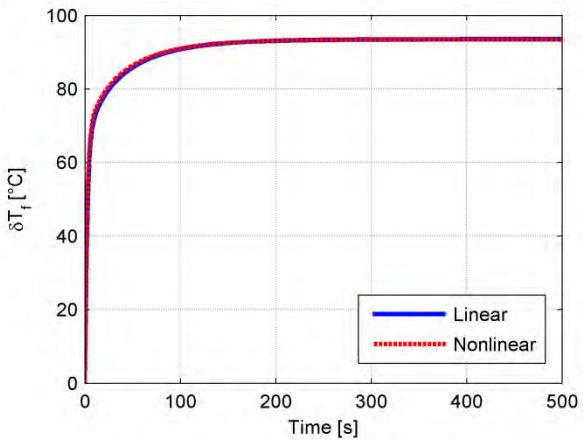


**Figure 65. Fuel temperature variation following a 20 pcm step reactivity insertion (MOX, BoC).**

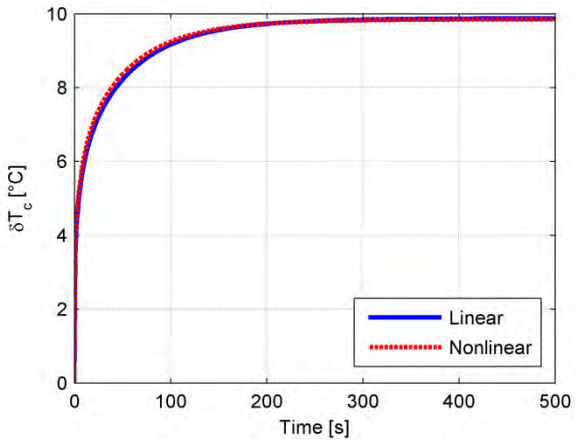


**Figure 66. Cladding temperature variation following a 20 pcm reactivity insertion (met, EoC).**

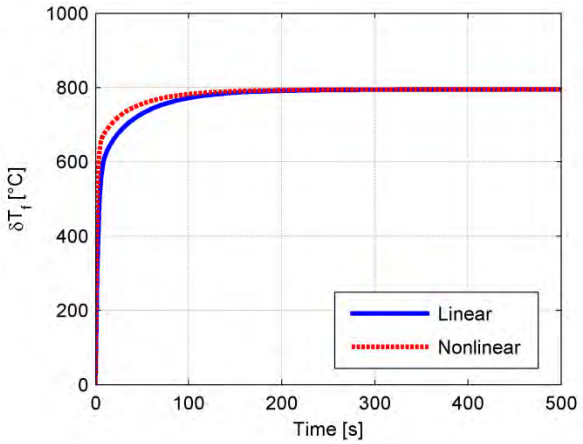


**Figure 67. Fuel temperature variation following a 170 pcm step reactivity insertion (MOX, BoC).**

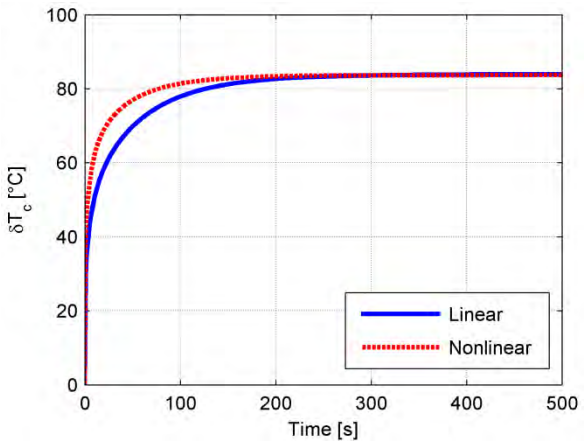


**Figure 68. Cladding temperature variation following a 170 pcm reactivity insertion (met, EoC).**

**Table XXIII. Variation of power and temperatures at the end of the transient for 5 pcm UTOP.**

| UTOP 5 pcm | Variation of characteristic variables from their steady-state values at the end of the transient | | | | | | | |
|---|---|---|---|---|---|---|---|---|
| | Linear | | | | Non-linear | | | |
| | MOX BoC | MOX EoC | Met BoC | Met EoC | MOX BoC | MOX EoC | Met BoC | Met EoC |
| Power [MWt] | 5.4 | 4.776 | 10.83 | 9.657 | 5.398 | 4.78 | 10.79 | 9.638 |
| Fuel T. [°C] | 23.38 | 20.68 | 11.85 | 10.57 | 23.37 | 20.69 | 11.81 | 10.55 |
| Clad T. [°C] | 1.268 | 1.122 | 2.766 | 2.467 | 1.268 | 1.122 | 2.757 | 2.462 |
| Lead T. [°C] | 0.72 | 0.6368 | 1.444 | 1.288 | 0.7197 | 0.6373 | 1.439 | 1.285 |
| Outlet T. [°C] | 1.44 | 1.274 | 2.887 | 2.575 | 1.439 | 1.275 | 2.877 | 2.57 |

**Table XXIV. Variation of power and temperatures at the end of the transient for 170 pcm UTOP.**

| UTOP 170 pcm | Variation of characteristic variables from their steady-state values at the end of the transient | | | | | | | |
|---|---|---|---|---|---|---|---|---|
| | Linear | | | | Non–linear | | | |
| | MOX BoC | MOX EoC | Met BoC | Met EoC | MOX BoC | MOX EoC | Met BoC | Met EoC |
| Power [MWt] | 183.6 | 162.4 | 368.1 | 328.3 | 183.5 | 162.4 | 367 | 327.6 |
| Fuel T. [°C] | 794.8 | 703 | 402.9 | 359.4 | 794.6 | 703 | 401.7 | 358.6 |
| Clad T. [°C] | 43.11 | 38.13 | 94.06 | 83.89 | 43.1 | 38.13 | 93.77 | 83.7 |
| Lead T. [°C] | 24.48 | 21.65 | 49.08 | 43.78 | 24.47 | 21.65 | 48.93 | 43.68 |
| Outlet T. [°C] | 48.96 | 43.3 | 98.16 | 87.55 | 48.94 | 43.3 | 97.86 | 87.36 |

Despite the fact that 0.5 $ is a great insertion of reactivity, it is useful to remind that this quantity corresponds only to 170 pcm, being the delayed neutron fraction $\beta$ typically small in fast reactors.

*ULOF scenario*

Among accidental transients, a simplified ULOF is ultimately simulated by introducing both a trivial and two major disturbances on the mass flow rate, which is more precisely step-reduced by 100, 1000 and 5000 kg $s^{-1}$.

In the former circumstances the findings of the preceding analyses are attested again, as a very good consistency between the non-linear reference model and its linearized version is obtained pertaining to the final steady-state results, which turn out to be almost exactly coincident (differences of at most some tenths of per cent) in the case of 100 kg $s^{-1}$ mass flow rate reduction, and show definitely negligible discrepancies (the largest being of some 2.6 %) for a - 1000 kg $s^{-1}$ perturbation.

Incongruities emerge concerning both the transient developments and steady-state figures after the application of the most considerable perturbation: as depicted for instance in Fig. 71, power variations differ by approximately 6 % in the case of metallic fuel, up to 13 % for MOX, corresponding to 2.5 and 2.8 $MW_{th}$, respectively. This occurs for each parameter, besides power: discrepancies upon reactivity are limited to 0.01 $, while cladding temperatures, whose increases are the most critical in this kind of scenarios, differ by 0.5 K at most. In addition to the term neglected also in the ULOHS and UTOP cases, *i.e.* $\delta\rho\delta n$, other two terms are disregarded here, involving the mass flow rate. For this reason the worst case to be handled by a linearized model is a large ULOF, in which significant discrepancies are present also in the new steady-state values (Tabs. from XXV to XXVII). The system dynamics responses reveal the non-conservative nature of the linear approximation, which becomes evident once the input parameter alteration exceeds the limits of small perturbations.

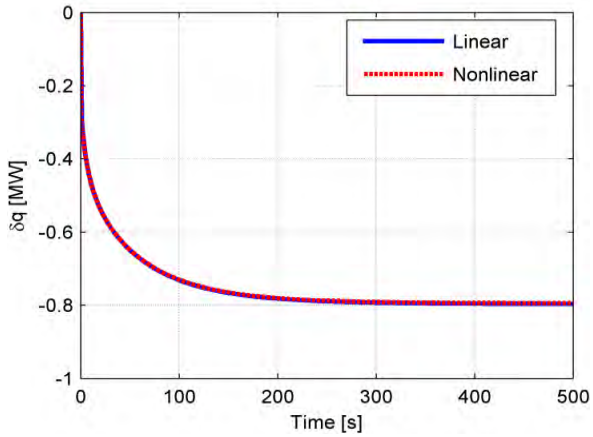


**Figure 69. Power variation following a 100 kg $s^{-1}$ mass flow rate reduction (met, BoC).**

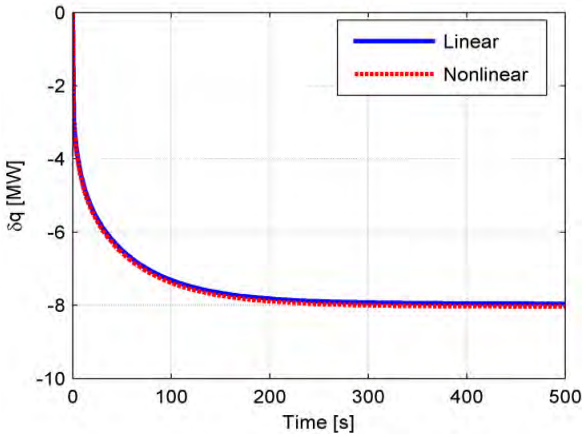


**Figure 70. Power variation following a 1000 kg $s^{-1}$ mass flow rate reduction (met, BoC).**

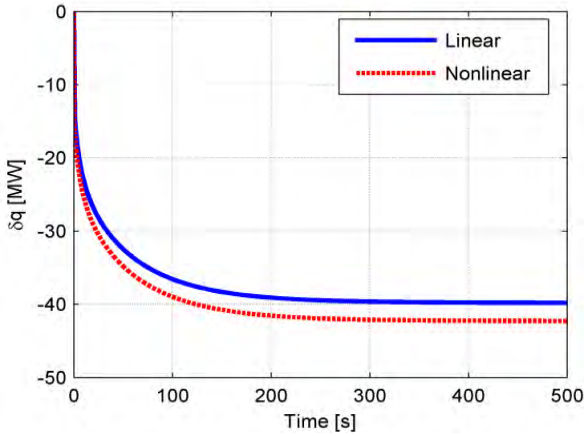


**Figure 71. Power variation following a 5000 kg $s^{-1}$ mass flow rate reduction (met, BoC).**

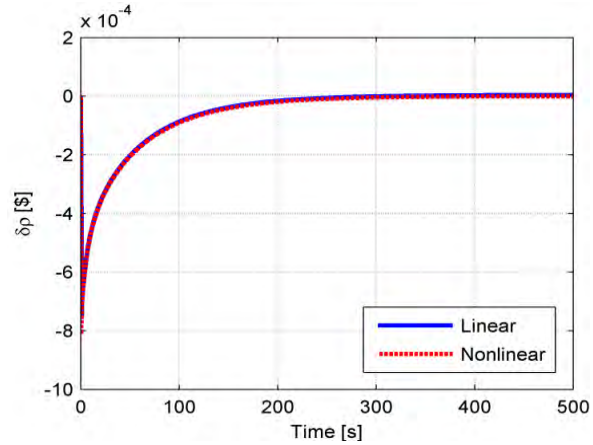


**Figure 72. Reactivity variation following a 100 kg $s^{-1}$ mass flow rate reduction (met, BoC).**

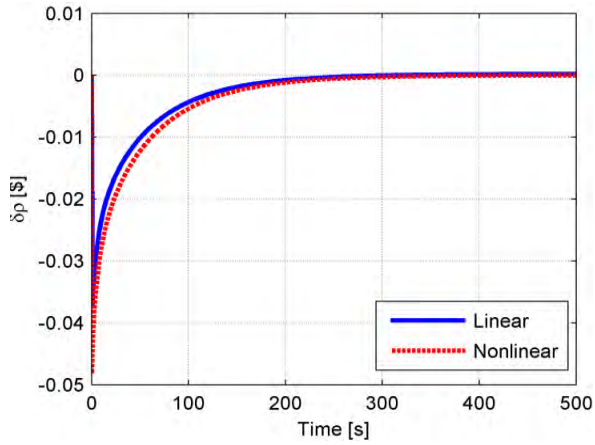


**Figure 73. Reactivity variation following a 5000 kg $s^{-1}$ mass flow rate reduction (met, BoC).**

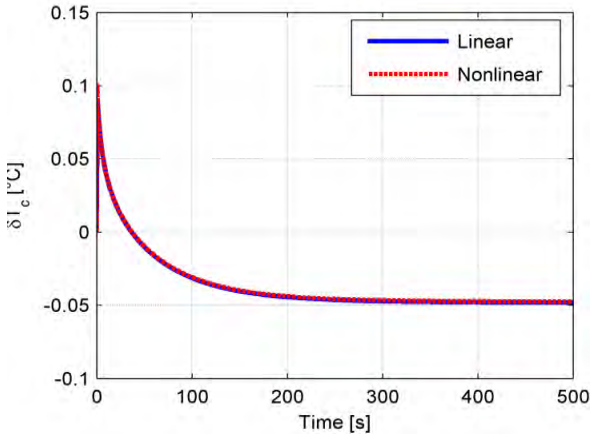


**Figure 74. Clad temperature variation following a 100 kg $s^{-1}$ mass flow rate reduction (met, BoC).**

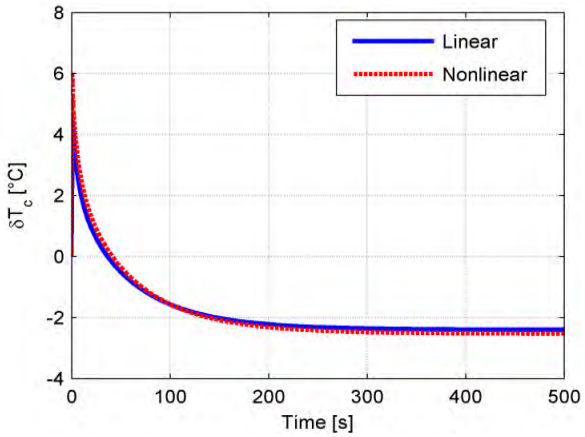


**Figure 75. Clad temperature variation following a 5000 kg $s^{-1}$ mass flow rate reduction (met, BoC).**

**Table XXV. Variation of power and temperatures at the end of the transient for 100 kg $s^{-1}$ ULOF.**

| ULOF 100 kg $s^{-1}$ | Variation of characteristic variables from their steady-state values at the end of the transient | | | | | | | |
|---|---|---|---|---|---|---|---|---|
| | Linear | | | | Non-linear | | | |
| | MOX BoC | MOX EoC | Met BoC | Met EoC | MOX BoC | MOX EoC | Met BoC | Met EoC |
| Power [$MW_{th}$] | - 0.3679 | - 0.3444 | - 0.7963 | - 0.7761 | - 0.3688 | - 0.3414 | - 0.7959 | - 0.7707 |
| Fuel T. [°C] | - 1.437 | - 1.335 | - 0.7163 | - 0.6942 | - 1.441 | - 1.322 | - 0.7114 | - 0.6838 |
| Clad T. [°C] | 0.0689 | 0.07443 | - 0.04816 | - 0.04301 | 0.06911 | 0.07554 | - 0.04787 | - 0.04142 |
| Lead T. [°C] | 0.1062 | 0.1094 | 0.04912 | 0.05181 | 0.1065 | 0.1102 | 0.04937 | 0.05274 |
| Outlet T. [°C] | 0.2125 | 0.2188 | 0.09825 | 0.1036 | 0.2131 | 0.2204 | 0.09873 | 0.1055 |

**Table XXVI. Variation of power and temperatures at the end of the transient for 1000 kg $s^{-1}$ ULOF.**

| ULOF 1000 kg $s^{-1}$ | Variation of characteristic variables from their steady state values at the end of the transient | | | | | | | |
|---|---|---|---|---|---|---|---|---|
| | Linear | | | | Non-linear | | | |
| | MOX BoC | MOX EoC | Met BoC | Met EoC | MOX BoC | MOX EoC | Met BoC | Met EoC |
| **Power [$MW_{th}$]** | - 3.679 | - 3.444 | - 7.963 | - 7.761 | - 3.778 | - 3.536 | - 8.037 | - 7.84 |
| **Fuel T. [°C]** | - 14.37 | - 13.35 | - 7.163 | - 6.942 | - 14.76 | - 13.71 | - 7.22 | - 7.004 |
| **Clad T. [°C]** | 0.689 | 0.7443 | - 0.4816 | - 0.4301 | 0.7081 | 0.7662 | - 0.4811 | - 0.4297 |
| Lead T. [°C] | 1.062 | 1.094 | 0.4912 | 0.5181 | 1.092 | 1.125 | 0.5008 | 0.5281 |
| Outlet T. [°C] | 2.125 | 2.188 | 0.9825 | 1.036 | 2.183 | 2.25 | 1.002 | 1.056 |

**Table XXVII. Variation of power and temperatures at the end of the transient for 5000 kg $s^{-1}$ ULOF.**

| ULOF 5000 kg $s^{-1}$ | Variation of characteristic variables from their steady state values at the end of the transient | | | | | | | |
|---|---|---|---|---|---|---|---|---|
| | Linear | | | | Non-linear | | | |
| | MOX BoC | MOX EoC | Met BoC | Met EoC | MOX BoC | MOX EoC | Met BoC | Met EoC |
| Power [$MW_{th}$] | - 18.4 | - 17.22 | - 39.81 | - 38.81 | - 21.21 | - 19.94 | - 42.3 | - 41.4 |
| Fuel T. [°C] | - 71.87 | - 66.77 | - 35.81 | - 34.71 | - 82.85 | - 77.33 | - 38.02 | - 37.01 |
| Clad T. [°C] | 3.445 | 3.722 | - 2.408 | - 2.151 | 3.974 | 4.312 | - 2.531 | - 2.273 |
| Lead T. [°C] | 5.312 | 5.469 | 2.456 | 2.591 | 6.127 | 6.336 | 2.637 | 2.785 |
| Outlet T. [°C] | 10.62 | 10.94 | 4.912 | 5.181 | 12.25 | 12.67 | 5.274 | 5.571 |

### 3.1.4 Stability analysis

The first advantage ensuing from the model linearization is the possibility to perform comparative analyses on the system open-loop stability. Stability is the property for a linear system to have finite outputs for any bounded inputs. Qualitative insights into the response characteristics of the continuous-time LTI system can be drawn from its representative Transfer Function (TF), which is derived by Laplace-transforming the state-space model in MATLAB®. Indeed, stability is very easy to infer: in order for a linear system to be stable, in fact, all of its poles (namely, roots of the characteristic equation or, equivalently, eigenvalues of the matrix $\underline{\underline{A}}$) must have negative real parts.

As a result of such an investigation, both MOX and metallic fuel systems turn out to be stable at BoC and EoC, since all their poles have strictly negative real part, the dominant ones being at - 0.01217 and - 0.0116 $s^{-1}$ at BoC, and at - 0.01221 and - 0.01172 $s^{-1}$ at EoC, respectively (see Tab. XXVIII).

Moreover, a difference that is worth mentioning is for poles 5 and 7: the first are real in the case of metal-fuelled core and complex conjugates for the MOX-fueled DEMO, and vice versa for the latter (poles 6 are complex for both systems, instead), suggesting an oscillatory behavior during the transients.

**Table XXVIII. System representative transfer function poles.**

| Pole | MOX fuel | | Metal fuel | | Units |
|---|---|---|---|---|---|
| | BoC | EoC | BoC | EoC | |
| $P_1$ | - 0.01217 | - 0.01221 | - 0.0116 | - 0.01172 | $s^{-1}$ |
| $P_2$ | - 0.02341 | - 0.2392 | - 0.01917 | - 0.01917 | $s^{-1}$ |
| $P_3$ | - 0.08296 | - 0.08352 | - 0.07697 | - 0.07767 | $s^{-1}$ |
| $P_4$ | - 0.2421 | - 0.2438 | - 0.1835 | - 0.186 | $s^{-1}$ |
| $P_5$ | 0.4687 + 0.159i | 0.4833 + 0.172i | - 0.5485 | - 0.5497 | $s^{-1}$ |
| $P_6$ | 0.4687 - 0.159i | 0.4833 - 0.172i | - 2.883 + 0.302i | - 2.952 + 0.251i | $s^{-1}$ |
| $P_7$ | - 2.475 | - 2.47 | - 2.883 - 0.302i | - 2.952 - 0.251i | $s^{-1}$ |
| $P_8$ | - 6.259 | - 6.253 | - 8.53 | - 8.417 | $s^{-1}$ |
| $P_9$ | - 44.23 | - 44.23 | - 47.09 | - 47.07 | $s^{-1}$ |
| $P_{10}$ | $-3.955 \cdot 10^3$ | $-3.801 \cdot 10^3$ | $-4.828 \cdot 10^3$ | $-4.762 \cdot 10^3$ | $s^{-1}$ |

In Fig. 76 the pole-zero map of the transfer function between power and coolant inlet is depicted, showing that all pole lay in the left half of the complex plane as well as the zeros. Transfer functions can be calculated and pole-zero maps can be plotted for each output/input pairs; they would feature the same poles shown in Tab. XXVIII but different zeros depending on each single case. In Fig. 77 a zoom around the origin of the axes is shown.

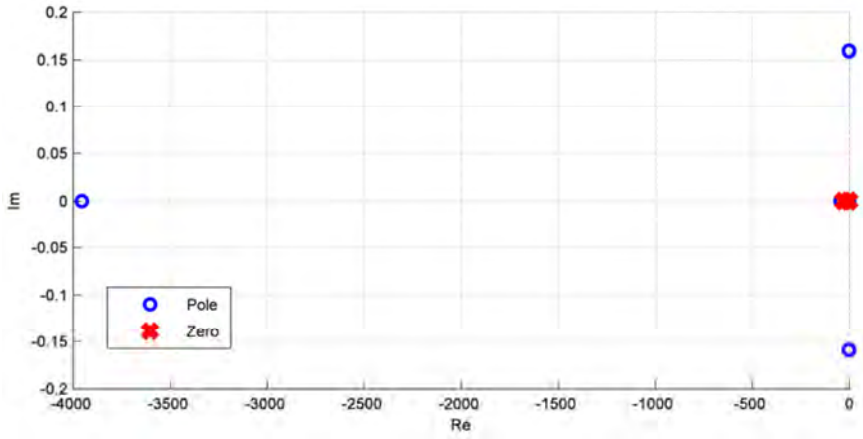


**Figure 76. Pole-zero map of the TF between power (output) and coolant inlet temperature (input).**

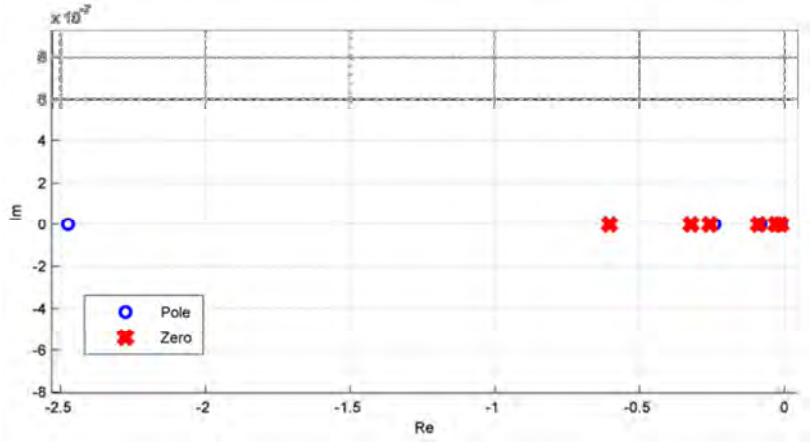


**Figure 77. Zoom-in of Figure 76.**

### 3.1.5 Fuel dynamic performance assessment

Input parameters are perturbed in order to investigate the dynamic behavior of MOX and metallic fuel DEMO cores by means of the linear model, as well as to observe and compare BoC and EoC new equilibrium configurations after the transients.

Three different scenarios are examined separately: the effects of an increase of the lead inlet temperature (+ 5 K compared to its nominal value, namely 673.15 K), of an ideal control rod extraction (corresponding to a reactivity step-insertion of + 5 pcm), and of a mass flow rate reduction (- 100 kg $s^{-1}$ compared to its nominal value, namely 25757 kg $s^{-1}$).

Simulations are started at initial time 0 s and run for 700 s, in order for the asymptotic output values to be reached.

*UTOP scenario*

The dynamic responses of the MOX and metal-fuelled DEMO cores to a stepwise reactivity insertion of 5 pcm (Fig. 78) is investigated at both BoC and EoC.

As Fig. 79 highlights, the expected response is observed, *i.e.* the initial, instantaneous power rise (prompt jump), whose slightly different time characteristic and amplitude between MOX and metallic fuel are essentially determined by the prompt neutron lifetime and the delayed neutron fraction of the respective systems.

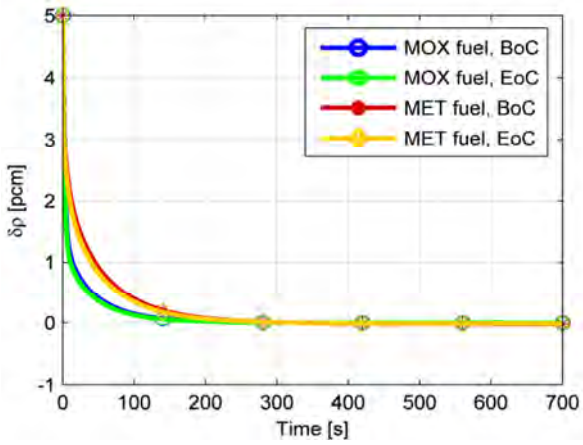


**Figure 78. Core reactivity variation due to an insertion of 5 pcm.**

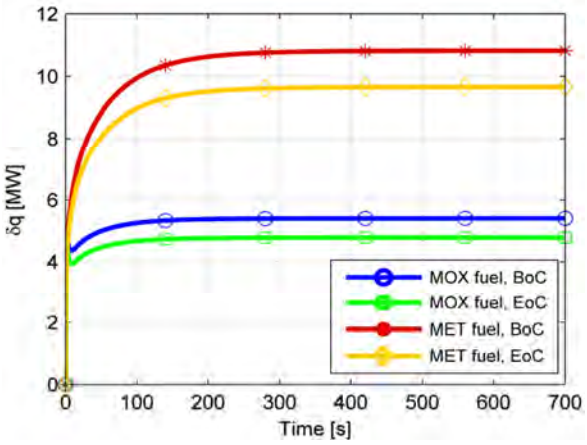


**Figure 79. Core power variation due to an insertion of 5 pcm**.

After the power sudden rise at the very beginning of the transient, fuel and lead temperatures (Figs. 80 and 81) start increasing monotonically (a much steeper trend is observed for MOX fuel), so as to balance the positive reactivity introduced by extracting the ideal control rod. Coherently with the lower Doppler contribution in metallic fuel (Fig. 82), a gentler slope of the power curve is found for the latter, as well as for BoC configurations compared to EoC ones. On the other hand, MOX shows a definite power decrease following the fuel temperature rise due to a higher Doppler contribution to reactivity (Fig. 83); in fact, even if the Doppler coefficient is slightly larger than for metal, the consistent fuel temperature enhancement makes the difference. Since the Doppler effect is the fastest reactivity feedback, a lower Doppler contribution (as expected with metallic fuels) may be problematic for reactivity accidents that cannot be faced only with a too slow action of control rods. Furthermore, MOX fuel has a faster dynamics than metal.

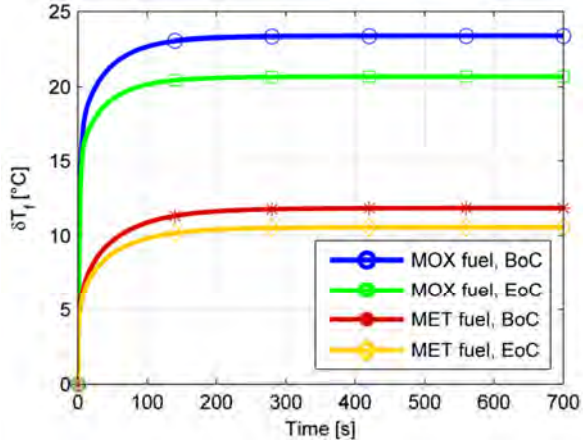


**Figure 80. Fuel temperature variation due to an insertion of 5 pcm.**

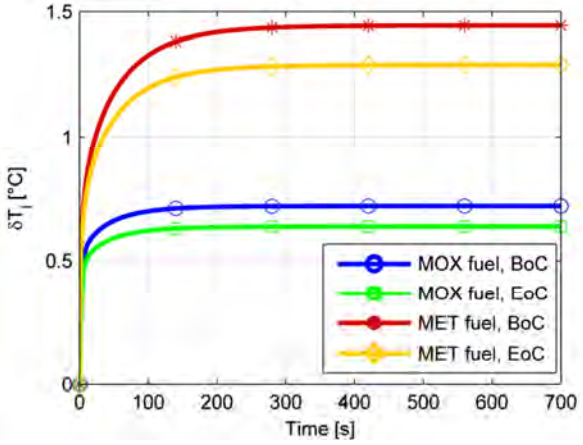


**Figure 81. Coolant average temperature variation due to an insertion of 5 pcm.**

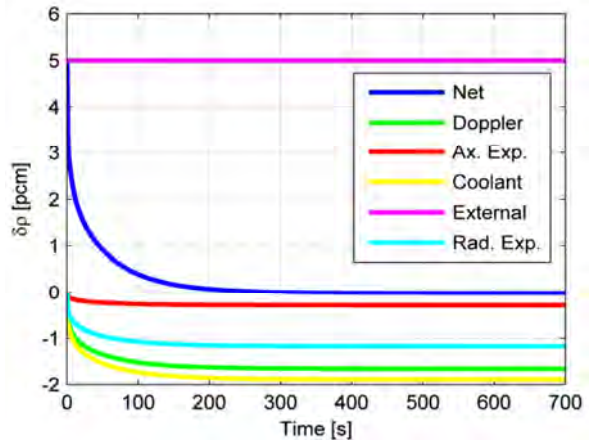


**Figure 82. Reactivity contributors variation due to an insertion of 5 pcm (metal, BoC).**

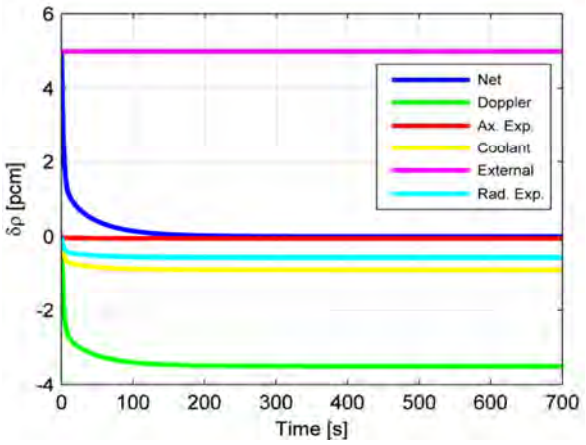


**Figure 83. Reactivity contributors variation due to an insertion of 5 pcm (MOX, BoC).**

As to fuel average temperature variations, a steeper slope is observed again in the case of MOX at both BoC and EoC, which settles at greater relative variations (+ 23.38/+ 20.68 K at BoC/EoC for MOX fuel *vs.* + 11.85/+ 10.57 K at BoC/EoC for metallic fuel) than metal due to its lower thermal conductivity, despite the smaller power enhancement.

A negative reactivity insertion is brought by the cladding temperature increase –which finally sets at + 1.23/+ 1.12 K at BoC/EoC for MOX, and at + 2.77/+ 2.47 K at BoC/EoC for metal. The reactor power finally settles at + 5.4/4.78 $MW_{th}$ for MOX at BoC/EoC and at + 10.83/+ 9.66 for metallic fuel at BoC/EoC.

As evident in Fig. 81, also the average coolant temperature features positive variations of 0.72/0.64 K (MOX fuel, BoC/EoC) and 1.44/1.29 K (metallic fuel, BoC/EoC), and the coolant outlet temperature (Fig. 85) shows an analogous trend but characterized by major (double) amplitude, resulting in total enhancements by 1.44/1.28 K (MOX fuel, BoC/EoC) and 2.89/2.58 K (metallic fuel, BoC/EoC).

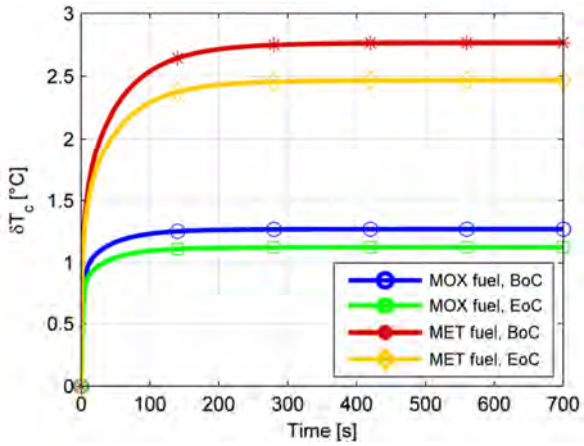


**Figure 84. Cladding temperature variation due to an insertion of 5 pcm.**

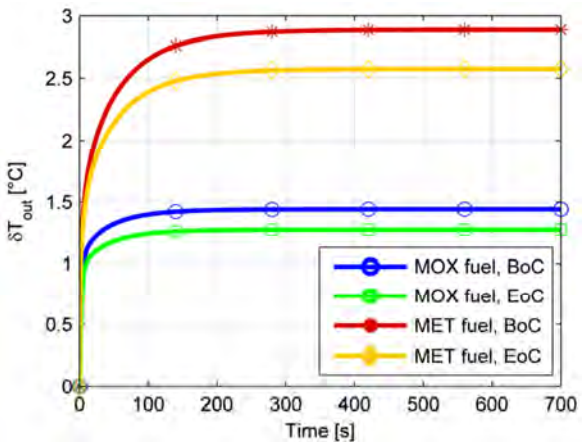


**Figure 85. Coolant outlet temperature variation due to an insertion of 5 pcm.**

*ULOHS scenario*

For a simplified ULOHS simulation, the core inlet temperature is enhanced by 5 K, leading to an insertion of negative reactivity (Fig. 86) due to both the instantaneous radial expansion and the lead density feedbacks, the latter being induced by the coolant average temperature increase (Fig. 87).

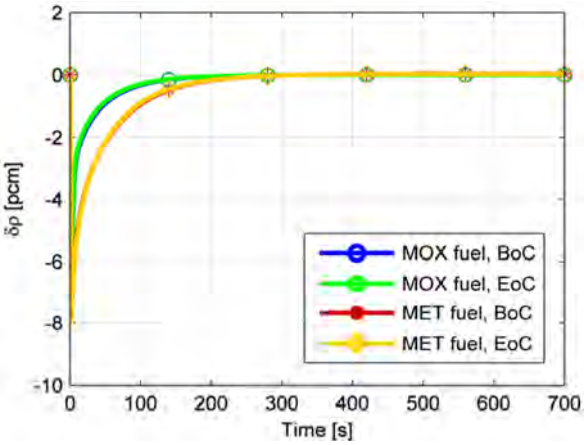


**Figure 86. Core reactivity variation due to an enhancement by 5 K of core inlet temperature.**

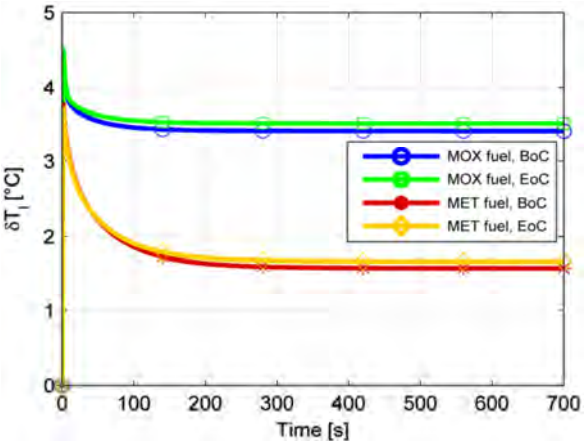


**Fig. 87. Coolant average temperature variation due to an enhancement by 5 K of core inlet temperature.**

Because of the negative reactivity injection brought by higher lead temperatures, the core power undergoes a prompt decrease in the first part of the transient, as far as the contribution of Doppler (due to the fuel average temperature reduction, faster and more consistent for MOX than for metal) starts balancing the effects of lead temperature on reactivity. Figures 88 and 89 highlight the contribution of each reactivity component, showing that only the Doppler effect – significantly stronger in the case of MOX - is accountable for the reactivity rise after the negative peaks caused by both higher coolant temperatures and core axial displacement.

It is interesting to note the difference between the two kinds of fuel: in the case of MOX, its lower thermal conductivity leads to a large fuel temperature decrease and consequently to a high Doppler contribution. On the contrary, in the metallic fuel temperature varies less than in the previous case, and therefore less reactivity is introduced. As in UTOP simulations, the dynamics of MOX is quicker than that of metal, reaching the steady-state in half the time compared with the latter.

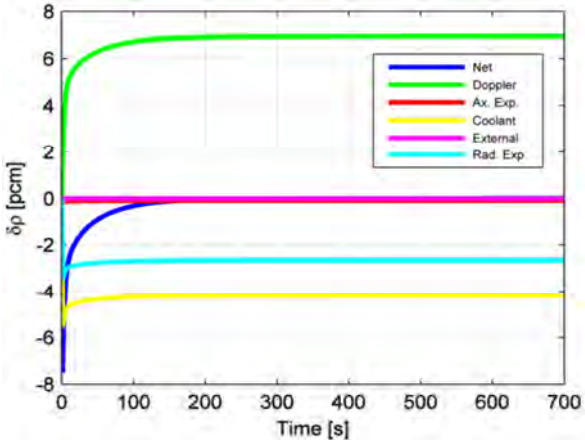


**Figure 88. Reactivity contributors variation due to an enhancement by 5 K of core inlet temperature (MOX BoC).**

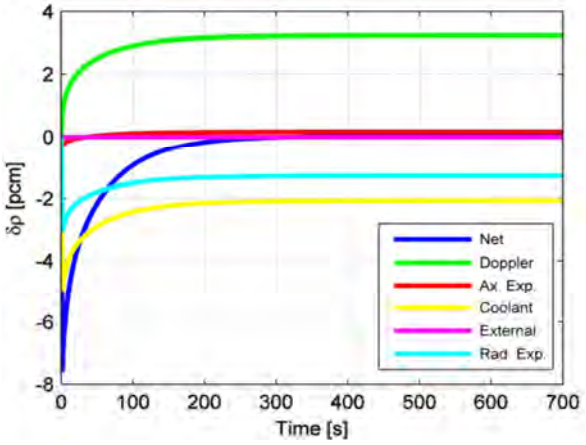


**Figure 289. Reactivity contributors variation due to an enhancement by 5 K of core inlet temperature (Metal BoC).**

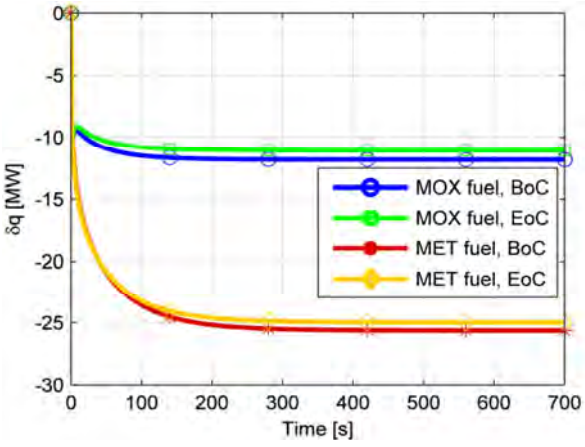


**Figure 90. Core power variation due to an enhancement by 5 K of core inlet temperature.**

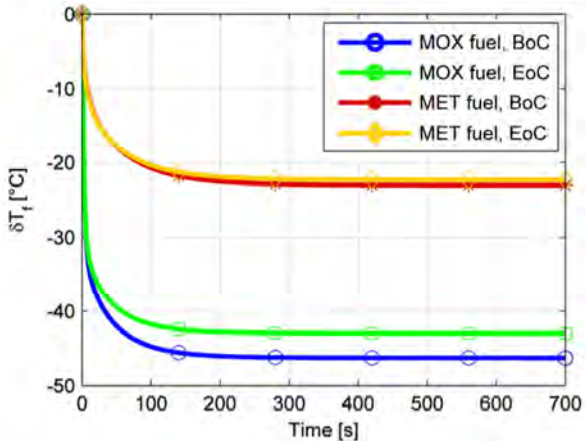


**Figure 91. Fuel temperature variation due to an enhancement by 5 K of core inlet temperature.**

Therefore, the reactor power stabilizes at new equilibrium values, approximately 11.85/11.09 (MOX) and 25.65/25 (metal) $MW_{th}$ lower than the nominal ones at BoC and EoC, respectively.

At the end of the transient, the coolant outlet temperature shows a variation of + 1.84/+ 1.04 K at BoC/EoC for MOX and of – 1.84/- 1.67 K at BoC/EoC for metal, but, in the case of the former, smaller than both the inlet perturbation and the average coolant temperature enhancement (+ 3.42/+ 3.52 K at BoC/EoC), due to the decrease in reactor power. Instead, in the case of metallic fuel the average lead temperature undergoes a slight increase (+ 1.58/+ 1.67 K at BoC/EoC).

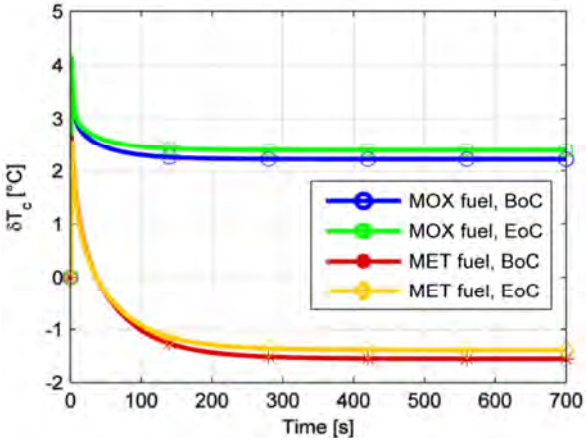


**Figure 92. Cladding temperature variation due to an enhancement by 5 K of core inlet temperature.**

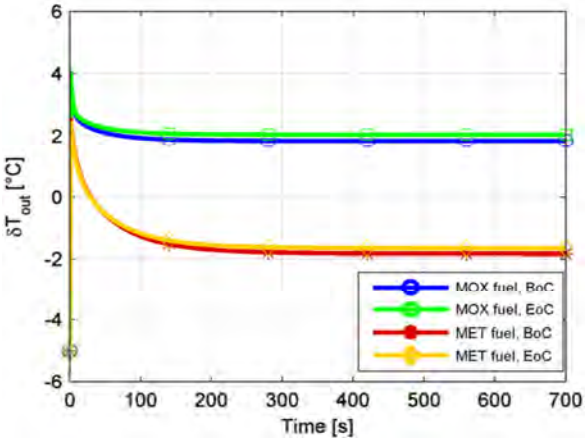


**Figure 393. Coolant outlet temperature variation due to an enhancement by 5 K of core inlet temperature.**

The fuel temperature response is monotonically negative and settles at about – 46.29/- 43 at BoC/EoC for MOX, and at - 23.07/- 22.36 K at BoC/EoC for metal.

As to cladding temperature, after the peaks in the very first part of the transient, it eventually sets at a relative variation of + 2.22/+ 2.40 (BoC/EoC, MOX core) with respect to the steady-state value. Concerning the metal-fuelled core, a better behavior is found, making this fuel alternative quite attractive in the light of the very stringent constraints that T91 temperature is subject to: in fact, after slightly increasing at the very beginning of the transient, the latter decreases by 1.55/1.4 K at BoC/EoC, providing a larger margin against the technological limit of 600 °C.

*ULOF scenario*

The core mass flow rate is reduced by 100 kg $s^{-1}$, which corresponds to a 0.3 % variation from its nominal value. As an immediate effect, the coolant average temperature (Fig. 94) undergoes an increase of approximately 0.075 K, making the cladding temperature rise analogously (Fig. 95).

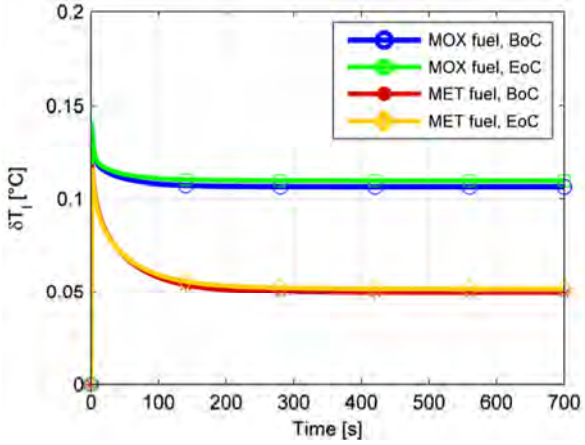


**Figure 94. Coolant average temperature variation due to a reduction by 100 kg $s^{-1}$ of core mass flow rate.**

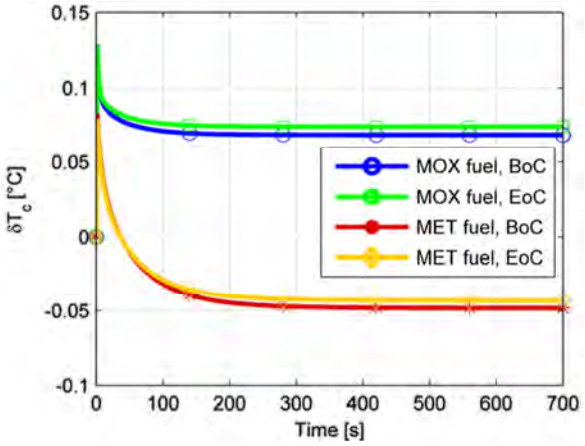


**Figure 95. Cladding temperature variation due to a reduction by 100 kg $s^{-1}$ of core mass flow rate.**

The feedbacks involved in lead and cladding temperature concur to bring about a slight insertion of negative reactivity (Figs. 96 and 97).

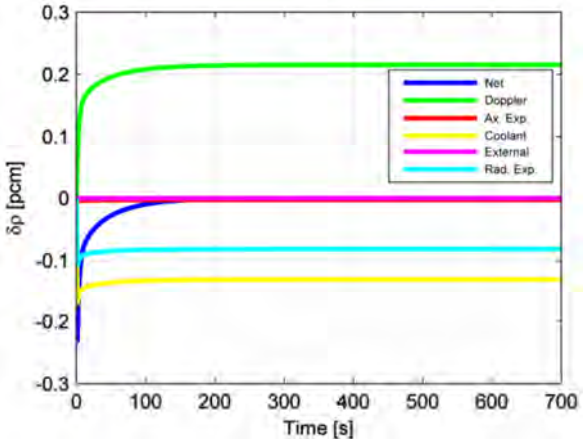


**Figure 96. Reactivity contributors variation due to an a reduction by 100 kg $s^{-1}$ of core mass flow rate (MOX BoC).**

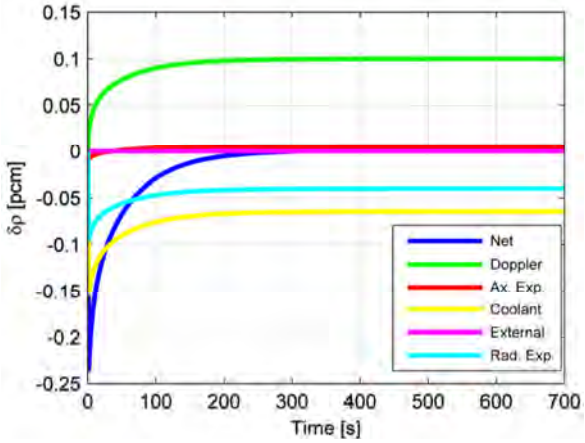


**Figure 97. Reactivity contributors variation due to an a reduction by 100 kg $s^{-1}$ of core mass flow rate (Met BoC).**

Because of the negative reactivity injection, the core power undergoes a steep decrease in the first part of the transient, as far as the contribution of Doppler (due to the fuel average temperature following reduction, faster and more consistent for MOX than for metal starts balancing the negative reactivity effects, finally reinstating criticality. Analogous considerations as for the previous simulations can be made on MOX and metal concerning thermal conductivity, temperatures, Doppler effect and dynamic behavior.

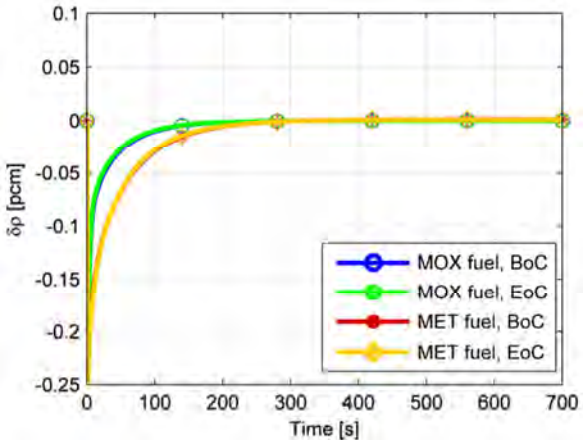


**Figure 98. Core reactivity variation due to a reduction by 100 kg $s^{-1}$ of core mass flow rate.**

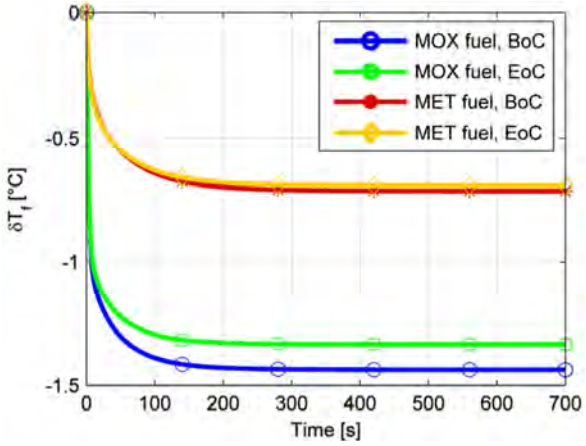


**Figure 99. Fuel temperature variation due to a reduction by 100 kg $s^{-1}$ of core mass flow rate.**

The reactor power stabilizes at new equilibrium values which are approximately 0.37/0.34 (MOX) $MW_{th}$ and 0.80/0.78 (metal) $MW_{th}$ lower than the nominal ones at BoC and EoC, respectively.

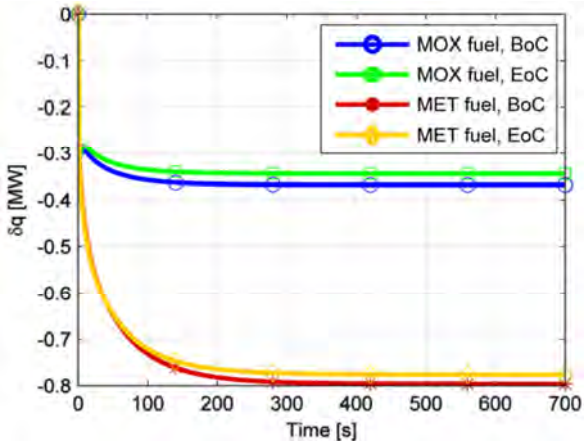


**Figure 100. Core power variation due to a reduction by 100 kg $s^{-1}$ of core mass flow rate.**

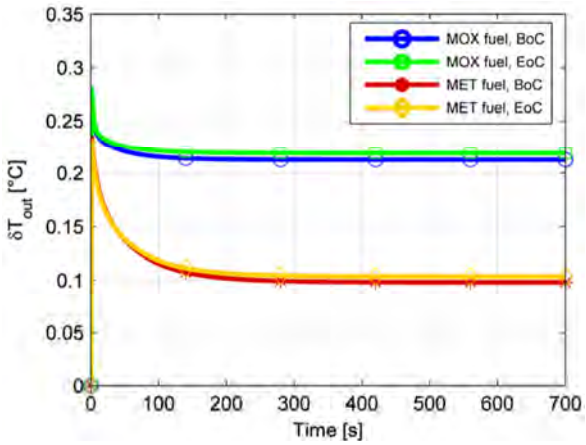


**Figure 101. Coolant outlet temperature variation due to a reduction by 100 kg $s^{-1}$ of core mass flow rate.**

At the end of the transient, the lead outlet temperature shows a variation of + 0.21 K at BoC and EoC for MOX and of + 0.1 K at BoC and EoC for metal - corresponding to twice as much as the enhancement of the average coolant temperature -, due to the reactor power slight decrease. The fuel temperature response is monotonically negative and settles at about – 1.43/- 1.33 at BoC/EoC for MOX, and at - 0.72/- 0.69 K at BoC/EoC for metal. As to the cladding temperature, after the peaks in the very first part of the transient, it eventually sets at a relative variation of + 0.07 (BoC and EoC, MOX core) with respect to the steady state value. Concerning the metal-fuelled core, a better behavior is found: after slightly increasing at the very beginning of the transient, the latter decreases more significantly, the final variation with respect to the steady-state value resulting - 0.05/- 0.04 K at BoC/EoC.

## 3.2 SG Model

In this section the second major component constituting DEMO primary loop is described: as done for the core, the SG model is presented followed by the respective transient simulations.

### 3.2.1 Approach description

As done for the core, the control purpose of the model suggests a straightforward way to describe the SGs. The simplest description of a physical system that also allows to study its free dynamics is the one based on first principle equations. In this perspective, the model is built on mass and energy balances, as follows:

$$\frac{\partial d}{\partial t} + \nabla \cdot (d\,\vec{v}) = 0 \tag{85}$$

$$\frac{\partial dh}{\partial t} + \nabla \cdot (dh\,\vec{v}) = -\nabla \cdot \overrightarrow{q''} - q''' + \frac{DP}{Dt} + \Phi \tag{86}$$

No momentum balance nor pressure drop are taken into account.

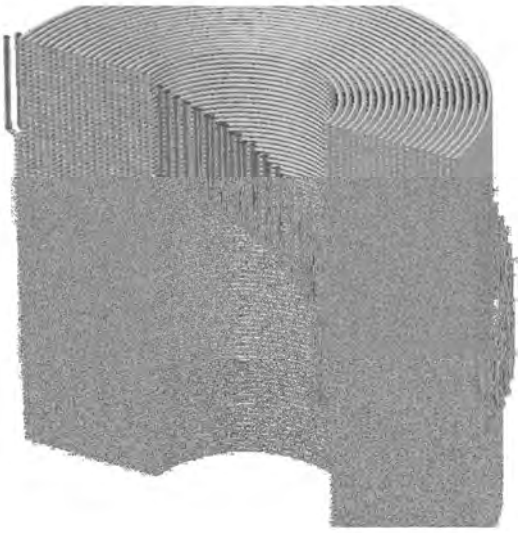

**Figure 102. The geometry of tube bundles of ELSY SG.**

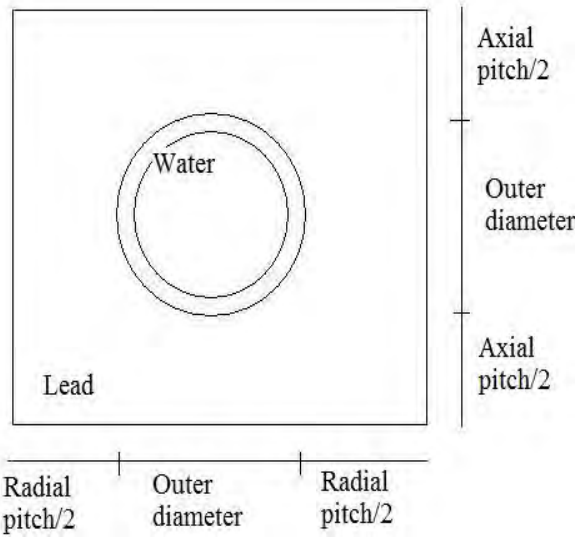


**Figure 103. Simplified geometry adopted in this work.**

It has been chosen to manipulate Eq. (85) to obtain a set of zero-dimensional equations.

Because of the complexity of the real component geometry (Fig. 102), it is necessary to adopt a simplified version (Fig. 103): in particular, the spiral tubes are substituted with concentric tube bundles in a counter-flow heat exchanger configuration.

The problem is approached through a single-channel analysis, in which the behavior of a tube-centered channel in a square pattern has been studied. Furthermore, only one SG has been considered, with a rescaled number of

tubes in order to guarantee a thermal power of 300 $MW_{th}$, instead of eight 37.5 $MW_{th}$ SGs of, which represents the real situation.

A moving boundary approach is the ideal candidate for the model purposes [23]. In this analysis, three spatial regions are considered: the water flowing inside the tube, the lead flowing in the outer region, and the wall constituting the interface between the two fluids.

Three variables are employed to represent three zones along the tube, namely the sub-cooled length $L_1$, the two-phase length $L_2$, and the superheated one $L_3$ (Fig. 104).

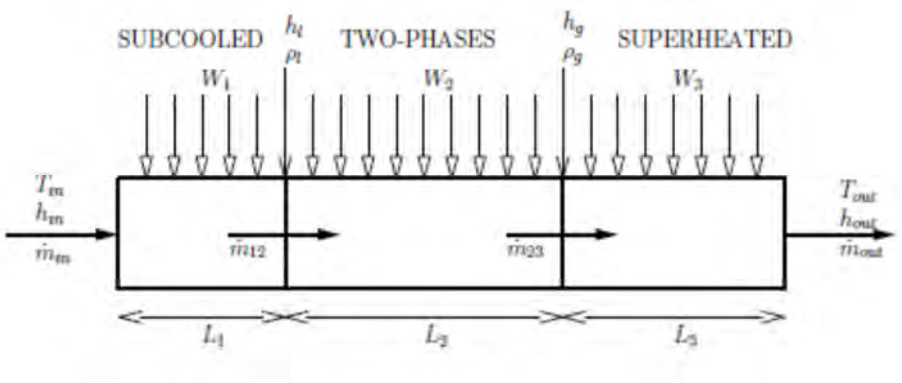


**Figure 104. Schematic representation of the moving boundary approach adopted for the SG model.**

The model is based on the idea of following the heat exchange from lead to water passing through the wall interface represented. This way, a convective heat exchange from the secondary fluid bulk to the internal wall interface is considered in the water region; a conductive heat transfer from the secondary-side wall surface to the primary-side one is modeled; finally, a convective heat exchange is taken into account to calculate the bulk primary coolant temperature.

#### *3.2.1.1 Primary side modeling*

Lead in the SG is a single-phase fluid, thus it is not necessary to consider the mass balance over the different regions. Three energy balance equations are written to describe the lead behavior in the SG, whose form is the same as the one adopted for water in the sub-cooled region:

$$A_p d_{p1} C_{p1}\left[\frac{d}{dt}\left(L_1 T_{p1}\right) - T_{p12}\cdot\frac{dL_1}{dt}\right] = \Gamma C_{p1}\left(T_{p12} - T_{p,out}\right) + \pi D_{out} h_{chc,p1} L_1\left(T_{p1} - T_{wp1}\right) \tag{87}$$

$$A_p d_{p2} C_{p2}\left[\frac{d}{dt}\left(L_2 T_{p2}\right) - T_{p23}\cdot\frac{d}{dt}\left(L_1 + L_2\right) + T_{p12}\cdot\frac{dL_1}{dt}\right] = \Gamma C_{p2}\left(T_{p23} - T_{p12}\right) + \pi D_{out} h_{chc,p2} L_2\left(T_{p2} - T_{wp2}\right) \tag{88}$$

$$A_p d_{p3} C_{p3}\left[\frac{d}{dt}\left(L_3 T_{p3}\right) - T_{p23}\cdot\frac{d}{dt}\left(L_1 + L_2\right)\right] = \Gamma C_{p3}\left(T_{p,in} - T_{p23}\right) + \pi D_{out} h_{chc,p3} L_3\left(T_{p3} - T_{wp3}\right) \tag{89}$$

For the three mean lead temperatures in the respective zones as many closure equations are taken into account:

$$T_{p1} = \frac{T_{p,out} + T_{p12}}{2} \tag{90}$$

$$T_{p2} = \frac{T_{p12} + T_{p23}}{2} \tag{91}$$

$$T_{p3} = \frac{T_{p23} + T_{p,out}}{2} \tag{92}$$

#### *3.2.1.2 Secondary side modeling*

As mentioned above, the secondary fluid undergoes a phase transition while flowing through the SG. For this reason, both mass and energy balances have to be taken into account to describe the water behavior in the model. For a one-dimensional case Eq. (85), representing a mass balance, can be formulated as:

$$\frac{\partial A_s d_s}{\partial t} + \frac{\partial \dot{m}}{\partial z} = 0 \tag{93}$$

The energy balance equation (86) can be simplified by neglecting the axial conduction and by assuming a one dimensional flow as follows:

$$\frac{\partial (A_s d_s h_s - A_s d_s)}{\partial t} + \frac{\partial \dot{m} h_s}{\partial z} = \pi D_s h_{chc,s} (T_{wsi} - T_i) \tag{94}$$

where the heat exchange is taken into account by means of the convective coefficient $h_{chc,s}$ between internal wall and water, calculated by a proper correlation.

In a moving boundary model, a zero-dimensional lumped-parameter analysis is performed by integrating the model equations on the volume they are referred to, and then by applying Leibniz's rule to the PDE:

$$\frac{d}{dt}\int_{z_1}^{z_2} f(z,t)dz = f(z_2,t)\frac{dz_2}{dt} - f(z_1,t)\frac{dz_1}{dt} + \int_{z_1}^{z_2}\frac{\partial f(z,t)}{\partial t}dz \tag{95}$$

In this way, a one-dimensional PDE is changed into an only-time-dependent equation (ODE) that describes the whole behavior of the integration domain.

Generally, the average values of the variables involved, such as density, temperature and specific enthalpy, are derived from the ones evaluated at the interfaces by performing an arithmetical mean.

*Sub-cooled region*

In a SG the sub-cooled region corresponds to the first section of the tube entered by the feedwater. Therefore, the volume considered for this region extends from zero to $L_1$, that is called the sub-cooled length.

By integrating Eq. (87) over the sub-cooled volume as follows:

$$\int_0^{L_1} \frac{\partial A_s d_s}{\partial t} dz + \int_0^{L_1} \frac{\partial \dot{m}}{\partial z} dz = 0 \tag{96}$$

and by applying Leibnitz's rule on the first term and integrating the second term, the following equation for mass is finally obtained:

$$A_s \left[ \frac{d}{dt}(L_1 d_{s1}) - d_{sl} \frac{dL_1}{dt} \right] = \dot{m}_{in} - \dot{m}_{12} \tag{97}$$

where $d_{s1}$ is the mean water density in the sub-cooled region, calculated as:

$$\int_0^{L_1} d \cdot dz = L_1 d_{s1} \tag{98}$$

In a similar way, a zero-dimensional moving boundary energy balance equation can be derived:

$$_s \left[ \frac{d}{dt}(L_1 d_{s1} h_{s1}) - d_{sl} h_{sl} \frac{dL_1}{dt} - L_1 \frac{dP}{dt} \right] = \dot{m}_{in} h_{s,in} - \dot{m}_{12} h_{sl} + \pi D_{in} h_{chc,s1} L_1 (T_{ws1} - T_{s1}) \tag{99}$$

where $L_1 d_{s1} h_{s1}$ comes from:

$$\int_0^{L_1} d \cdot h \cdot dz = L_1 d_{s1} h_{s1} \tag{100}$$

Among the thermal-hydraulic properties, saturated liquid density and enthalpy are obtained, in respect to Gibb's law, by the following constitutive equations, which depend only on pressure:

$$d_{sl} = d_{sl}(P) \tag{101}$$

$$h_{sl} = h_{sl}(P) \tag{102}$$

For the sub-cooled region average density and enthalpy, the constitutive equations depend on pressure and mean temperature:

$$d_{s1} = d(P, T_{s1}) \tag{103}$$

$$h_{s1} = h(P, T_{s1}) \tag{104}$$

$$h_{s,in} = h\left(P, T_{s,in}\right) \tag{105}$$

One closure equation for the sub-cooled region is finally needed:

$$T_{s1} = \frac{T_{s,in} + T_{s2}}{2} \tag{106}$$

*Two-phase region*

The flow in the two-phase region is assumed to be homogeneous at equilibrium conditions, with a mean density expressed by the following closure equation:

$$d_{s2} = \gamma \rho_{sg} + (1 - \gamma)\rho_l \tag{107}$$

where γ is the mean value of void fraction, assumed to be constant in the two phase region, that is from $L_1$ to ($L_1$ + $L_2$):

$$\gamma = (1 + \eta) \cdot (1 - \eta \cdot log(1 + 1/\eta)) \tag{108}$$

and η is the saturated density ratio, defined as:

$$\eta = \frac{d_{sg}}{d_{lg} - d_{sg}} \tag{109}$$

According to this hypothesis and similarly to what done for the sub-cooled region, (i.e. integrating Eqs. (87) and (88) over the two-phase region and then applying Leibnitz's rule) the mass and energy balances in the two-phase region are now represented by the following equations:

$$A_s \left[\frac{d}{dt}(L_2 d_{s2}) + d_{sl}\frac{dL_1}{dt} - d_{sg}\frac{d}{dt}(L_1 + L_2)\right] = \dot{m}_{12} - \dot{m}_{23} \tag{110}$$

$$\begin{aligned} {}_s\left[\frac{d}{dt}\left(L_2\left(\gamma d_{sl}h_{sl} + (1-\gamma)d_{sg}h_{sg}\right)\right) + d_{sl}h_{sl}\frac{dL_1}{dt} - d_{sg}h_{sg}\frac{d}{dt}(L_1 + L_2) - L_2\frac{dP}{dt}\right] \\ = \dot{m}_{12}h_{sl} - \dot{m}_{23}h_{sg} + \pi D_{in}h_{chc,s2}L_2(T_{ws2} - T_{s2}) \end{aligned} \tag{111}$$

Among the thermal-hydraulic properties, saturated steam density and enthalpy with saturation temperature are obtained, in respect to Gibb's law, by the following constitutive equations, depending only on pressure:

$$d_{sg} = d_{sg}(P) \tag{112}$$

$$h_{sg} = h_{sg}(P) \tag{113}$$

$$T_{s2} = T_{sat}(P) \tag{114}$$

*Superheated region*

The superheated region extending from quote ($L_1 + L_2$) to quote $L$, is represented by the usual mass and energy balance equations, obtained by applying an analogous procedure as before:

$$A_s\left[\frac{d}{dt}(L_3 d_{s3}) - d_{sg}\frac{dL_3}{dt}\right] = \dot{m}_{23} - \dot{m}_{out} \tag{115}$$

$$A_s\left[\frac{d}{dt}(L_3 d_{s3} h_{s3}) - d_{sg}h_{sg}\frac{dL_3}{dt} - L_3\frac{dP}{dt}\right] = \dot{m}_{23}h_{sg} - \dot{m}_{out}h_{s,out} + \pi D_{in}h_{chc,s3}L_3(T_{ws3} - T_{s3}) \tag{116}$$

For average density and enthalpy in the superheated region, the constitutive equations depend on pressure and mean temperature:

$$\rho_{s3} = \rho(P, T_{s3}) \tag{117}$$

$$h_{s3} = h(P, T_{s3}) \tag{118}$$

$$h_{s,out} = h\left(P, T_{s,out}\right) \tag{119}$$

One closure equation for this region is necessary regarding the steam outlet temperature:

$$T_{s,out} = 2T_{s3} - T_{s2} \tag{120}$$

and one regards the superheated length, that is well defined from the sub-cooled and two-phase ones:

$$L_3 = L - L_1 - L_2 \tag{121}$$

#### *3.2.1.3 Wall interface modeling*

The description of the wall region is based on an energy balance and in particular two kinds of interfaces have to be considered: axial and radial. The first ones correspond to the boundaries of the different regions defined by the water behavior, whereas the second ones consist in the surfaces the two fluids flow on. The dynamic behavior of the wall is specified by the evolution of its mean temperature. The mean temperature in a region is derived by averaging the respective axial interface values and related to the radial interfaces through the heat conduction equation. The three wall equations for the three region are:

$$d_{w1}A_{w1}C_{w1}\left[\frac{dL_1}{dt}\cdot(T_{w1}-T_{w12})+L_1\frac{dT_{w1}}{dt}\right] = \pi D_{out}h_{chc,p1}L_1\left(T_{p1}-T_{wp1}\right)-\pi D_{in}h_{chc,s1}L_1(T_{ws1}-T_{s1}) \quad (122)$$

$$d_{w2}A_wC_{w2}\left[(T_{w2}-T_{w23})\cdot\frac{d}{dt}(L_1+L_2)+\frac{dL_1}{dt}\cdot(T_{w12}-T_{w2})+L_2\frac{dT_{w2}}{dt}\right] = \pi D_{out}h_{chc,p2}L_2\left(T_{p2}-T_{wp2}\right)-\pi D_{in}h_{chc,s2}L_2(T_{ws2}-T_{s2}) \quad (123)$$

$$d_{w3}A_wC_{w3}\left[(T_{w23}-T_{w3})\cdot\frac{d}{dt}(L_1+L_2)+L_3\frac{dT_{w3}}{dt}\right] = \pi D_{out}h_{chc,p3}L_3\left(T_{p3}-T_{wp3}\right)-\pi D_{in}h_{chc,p3}L_3(T_{ws3}-T_{s3}) \quad (124)$$

Several closure equations are needed to close the set of equation. In fact in this sense, the wall is a sort of closure interface between lead and water sides.

For the external (primary-side lead) and internal (secondary-side water) wall temperatures, the following set of equations is taken into account, based on conductive heat exchange:

$$T_{ws1} = T_{w1} + Q_{s1}/2\pi\lambda_{w1}L_1 ln(r_{in}/r_{mean}) \quad (125)$$

$$T_{wp1} = T_{w1} + Q_{p1}/2\pi\lambda_{w1}L_1 ln(r_{ext}/r_{mean}) \quad (126)$$

$$T_{ws2} = T_{w2} + Q_{s2}/2\pi\lambda_{w2}L_2 ln(r_{in}/r_{mean}) \quad (127)$$

$$T_{wp2} = T_{w2} + Q_{p2}/2\pi\lambda_{w2}L_2 ln(r_{ext}/r_{mean}) \quad (128)$$

$$T_{ws3} = T_{w3} + Q_{s3}/2\pi\lambda_{w3}L_3 ln(r_{in}/r_{mean}) \quad (129)$$

$$T_{wp3} = T_{w3} + Q_{p3}/2\pi\lambda_{w3}L_3 ln(r_{ext}/r_{mean}) \quad (130)$$

where $Q$ is the power exchanged by lead or water in each zone:

$$Q_{p1} = \Gamma C_{p1}\left(T_{p,in}-T_{p23}\right) \quad (131)$$

$$Q_{s1} = \dot{m}_{12}h_{sl} - \dot{m}_{in}h_{s,in} \quad (132)$$

$$Q_{p2} = \Gamma C_{p2}\left(T_{p23}-T_{p12}\right) \quad (133)$$

$$Q_{s2} = \dot{m}_{23}h_{sg} - \dot{m}_{12}h_{sl} \quad (134)$$

$$Q_{p3} = \Gamma C_{p3}\left(T_{p12} - T_{p,out}\right) \tag{135}$$

$$Q_{s3} = \dot{m}_{out} h_{s,out} - \dot{m}_{23} h_{sg} \tag{136}$$

### 3.2.2 Code implementation

The equations proposed for the model are not ready-to-use in SIMULINK® since in this MATLAB® environment it is not possible to manage implicit differential equations. Consequently, for each region it is necessary to make the equations representing a characteristic variable explicit.

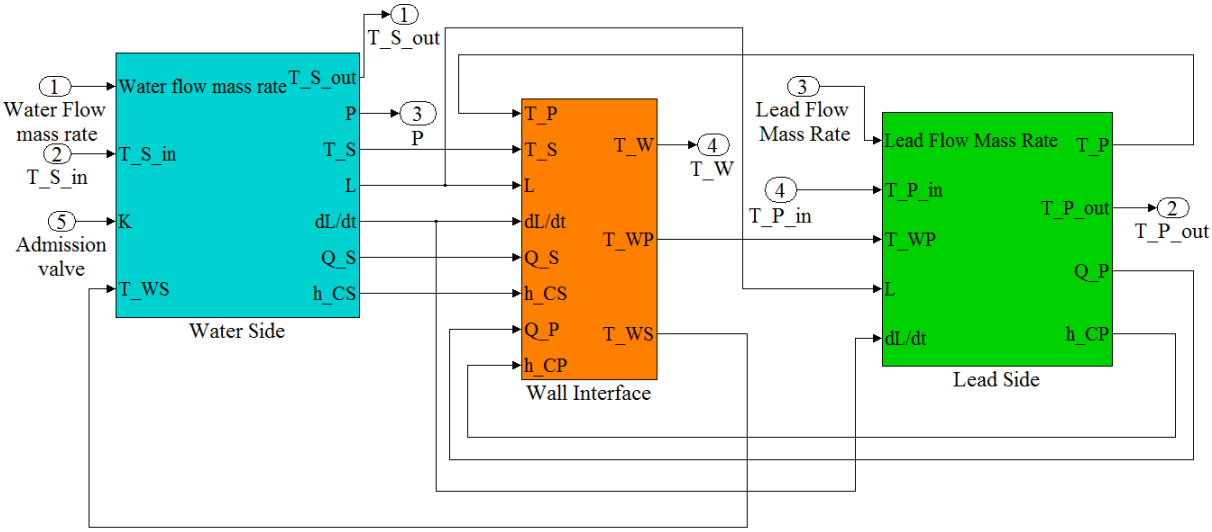


**Figure 105. Coupled-model representation of the SG component: it is possible to notice the different blocks involved, which are referred to the different zones defined (water side, lead side and wall).**

#### *3.2.2.1 Primary side correlations*

Three energy balance equations describe the lead-side behavior in the model. The variables regarded as state variables are the mean lead temperature in each region, defined by the sub-cooled, two-phase and superheated lengths $L_1$, $L_2$ and $L_3$.

The input variables are the lead mass flow rate and inlet temperature. In the primary loop model, the inlet lead temperature will be retrieved from the core block instead.

The output variables, besides the mean lead temperature and outlet lead temperature, are the power exchanged in each zone between lead and wall, and the convective heat transfer coefficient. The three equation implemented in SIMULINK® are the following:

$$\frac{dT_{p1}}{dt} = +\frac{\left(T_{12} - T_{p1}\right)}{L_1}\frac{dL_1}{dt} + \frac{\Gamma}{d_{p1}A_p L_1}\left(T_{12} - T_{p,out}\right) - \frac{\pi D_{out} h_{chc,p1}}{d_{p1}A_p C_{p1}}\left(T_{p1} - T_{wp1}\right) \tag{137}$$

$$\frac{dT_{p2}}{dt} = +\frac{(T_{23}-T_{12})}{L_2}\frac{dL_1}{dt} + \frac{(T_{23}-T_{p2})}{L_2}\frac{dL_2}{dt} + \frac{\Gamma}{d_{p2}A_pL}(T_{23}-T_{12}) - \frac{\pi D_{out}h_{chc,p2}}{d_{p2}A_pC_{p2}}(T_{p2}-T_{wp2}) \quad (138)$$

$$\frac{dT_{p3}}{dt} = -\frac{T_{p3}}{L_3}\frac{dL_3}{dt} - \frac{T_{23}}{L_3}\left(\frac{dL_1}{dt}+\frac{dL_2}{dt}\right) + \frac{2\Gamma}{d_{p3}A_pL}(T_{p,in}-T_{p3}) - \frac{\pi D_{out}h_{chc,p3}}{d_{p3}A_pC_{p3}}(T_{p3}-T_{wp3}) \quad (139)$$

In Fig. 106 the implementation in SIMULINK® of Eq. (137) is depicted.

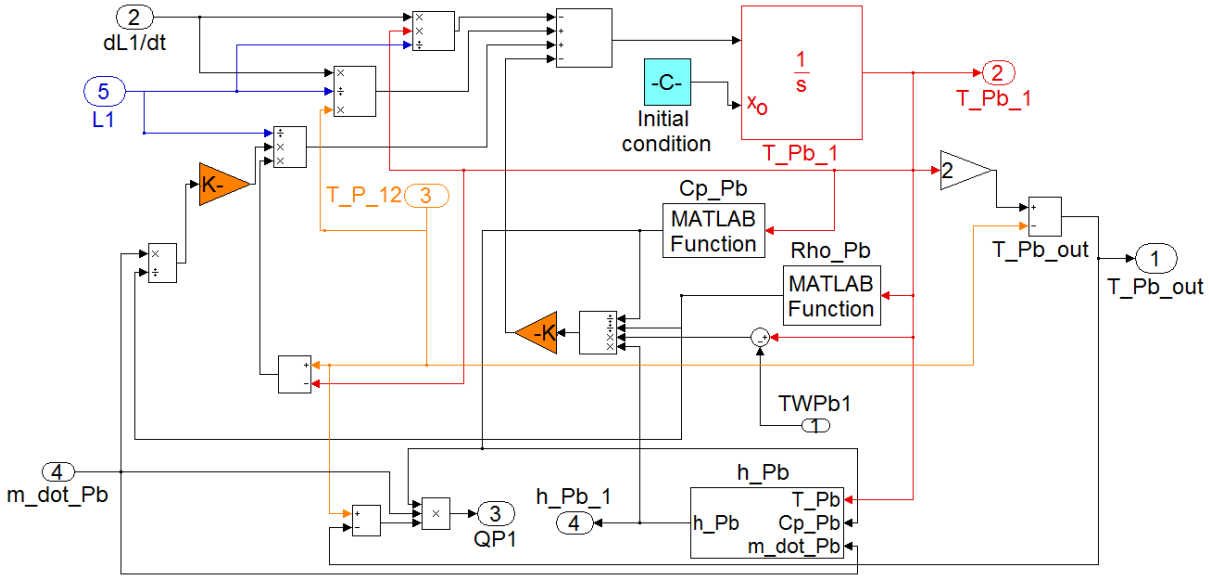


**Figure 106. Implementation in SIMULINK® of the energy balance in region 1 on the primary side.**

The correlations implemented in the SG model for lead density, specific heat capacity, viscosity, and thermal conductivity are the same used for the core model, whereas for the convective heat transfer coefficient a different correlation is needed, since the Zhukov one is valid only for lead flowing through the core. Therefore, the Ibraghimov-Subbotin-Ushakov correlation [24] is chosen to be implemented coherently with the present wall heat flux and hydrodynamic conditions.

$$h_{chc,p} = (4.5 + 0.014Pe^{0.8})\frac{\lambda}{D_{hyd}} \quad (140)$$

### *3.2.2.2 Secondary side correlations*

The equations involved on the water side are six: three mass balances and three energy balances. In order to represent this set of equations, six main variables are taken into account for the implementation in SIMULINK®:

- Sub-cooled length, $L_1$;
- Water mass flow rate at the interface between sub-cooled and two-phase regions, $\dot{m}_{12}$;
- Two-phase length, $L_2$;

- Pressure, $p$;
- Water mass flow rate at the interface between two-phase and superheated regions, $\dot{m}_{23}$;
- Mean steam temperature in superheated region, $T_{s3}$.

These variables represent a sort of "state variable" in for the model in SIMULINK®, being necessary due to the causality nature of the program. The knowledge of the state allows to understand the complete behavior of the system. In this view, the input variables for the water side are represented by:

- Water mass flow rate at the SG inlet, $\dot{m}_{in}$;
- Inlet water temperature, $T_{s,in}$;
- Turbine admission valve flow coefficient, $K$, that permits to change the steam mass flow rate at the SG outlet .

The water block output variables, besides outlet steam temperature and state variables themselves - that are important for the whole system -, are selected depending on the fact that their knowledge is necessary for the other two subsystems; they are:

- Mean water/steam temperature in the three regions, $T_s$;
- Length time derivative, $dL/dt$;
- Power exchanged between water and wall in each region, $Q_s$;
- Convective heat transfer coefficient, $h_{chc,s}$.

From mass and energy balances in the sub-cooled region, sub-cooled length and mass flow rate between the first and second water region are retrieved, respectively:

$$\frac{dL_1}{dt} = -\frac{L_1}{(d_{s1} - \rho_{sl})}\frac{d}{dt}d_{s1} + \frac{\dot{m}_{in} - \dot{m}_{12}}{A_s(d_{s1} - d_{sl})} \tag{141}$$

$$\dot{m}_{12} = \frac{A_s}{h_{sl}}\left[(d_{sl}h_{sl} - d_{s1}h_{s1})\frac{dL_1}{dt} - d_{s1}L_1\frac{dh_{s1}}{dt} - h_{s1}L_1\frac{d}{dt}d_{s1} + L_1\frac{dP}{dt} + \frac{\dot{m}_{in}h_{s,in}}{A_s} + \frac{\pi D_{in}h_{chc,s1}}{A_s}(T_{ws1} - T_{s1})\right] \tag{142}$$

In Fig. 107 the implementation in SIMULINK® of the previous mass balance equation is presented.

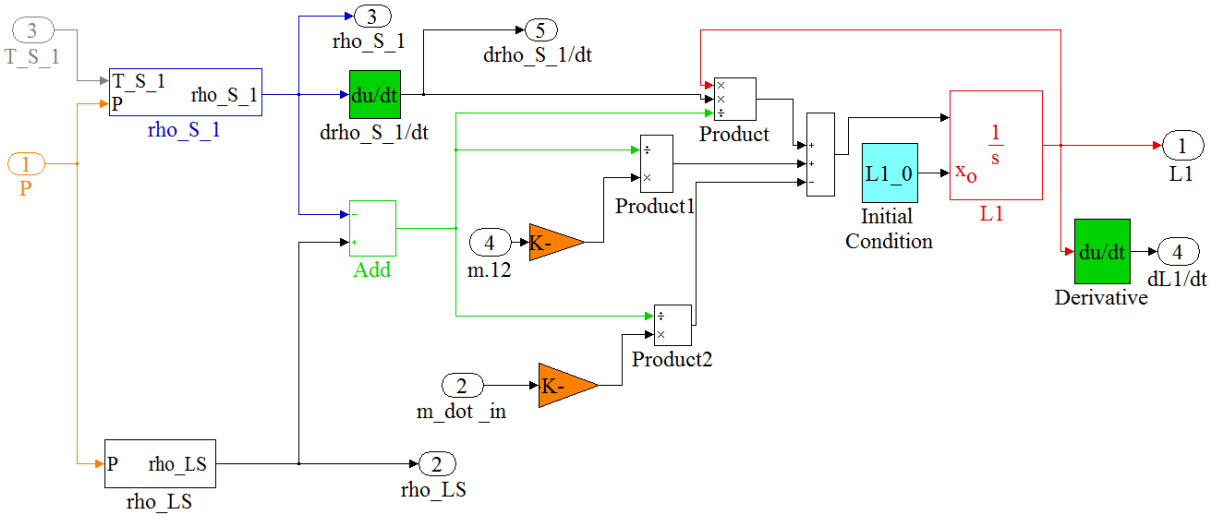


**Figure 107. Implementation in SIMULINK® of the mass balance in the sub-cooled region.**

From mass and energy balances in the two-phase region, two-phase length and tube pressure are obtained respectively:

$$\frac{dL_2}{dt} = -\frac{L_2}{(d_{s2}-d_{sg})}\frac{d}{dt}d_{s2} - \frac{(d_{sl}-d_{sg})}{(d_{s2}-d_{sg})}\frac{dL_1}{dt} + \frac{\dot{m}_{12}-\dot{m}_{23}}{A_s(d_{s2}-d_{sg})} \tag{143}$$

$$\frac{dP}{dt} = \frac{d}{dt}\left[\gamma d_{sg}h_{sg} + (1-\gamma)d_{sl}h_{sl}\right] + \frac{\gamma d_{sg}d_{sg} + (1-\gamma)d_{sl}h_{sl} - d_{sg}h_{sg}}{L_2}\frac{dL_2}{dt} + \frac{d_{sl}h_{sl} - d_{sg}h_{sg}}{L_2}\frac{dL_1}{dt} + \frac{\dot{m}_{23}h_{sg} - \dot{m}_{12}h_{sl}}{A_sL_2} - \frac{\pi D_{in}h_{chc,s2}}{A_s}(T_{ws2} - T_{s2}) \tag{144}$$

Figure 108 shows the SIMULINK® representation of the previous equation.

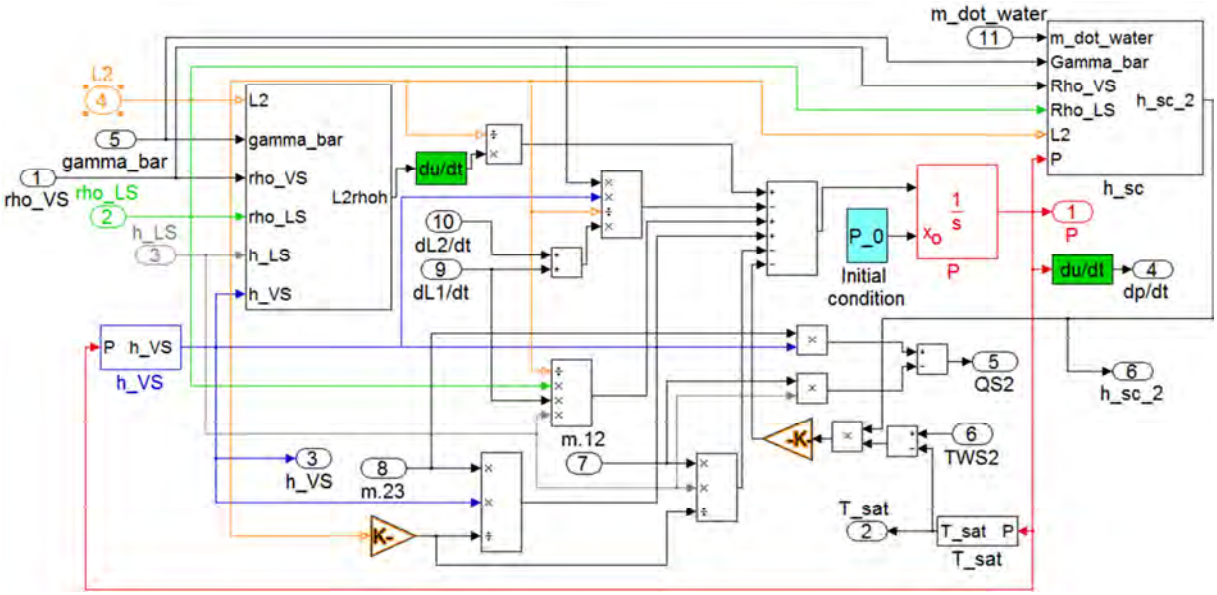


**Figure 108. Implementation in SIMULINK® of the energy balance in the two-phase region.**

From mass and energy balances on the superheated region, flow rate between the second and third water region and mean steam temperature in superheated region are obtained respectively:

$$\dot{m}_{23} = K(P - P_{out}) + A_s\left[L_3\frac{d}{dt}d_{s3} + \left(d_{sg} - d_{s3}\right)\frac{dL_1}{dt} + \left(d_{sg} - d_{s3}\right)\frac{dL_2}{dt}\right] \tag{145}$$

$$T_{s3} = T_{ws3} + \frac{A_s}{\pi D_{in} h_{chc,s3}}\left[\frac{d_{sg}h_{sg} - d_{s3}h_{s3}}{L_3}\left(\frac{dL_1}{dt} + \frac{dL_2}{dt}\right) + d_{s3}\frac{dh_{s3}}{dt} + h_{s3}\frac{d}{dt}d_{s3} - \frac{dP}{dt} + \frac{\dot{m}_{out}h_{s,out} - \dot{m}_{23}h_{sg}}{A_s L_3}\right] \tag{146}$$

For the implementation of water thermodynamic and physical properties the data provided by IAPWS IF97 standard (International Association for the Properties of Water and Steam) are used [25].

A tool available in MATLAB® allowing the use of these data is XSTEAM® for MATLAB, in which thermodynamic and physical properties for water at pressures ranging from 1 bar to 1000 bar, and at temperatures ranging from 0 °C to 2000 °C are collected.

In this way, density, enthalpy, dynamic viscosity, thermal conductivity, and isobaric specific heat capacity are calculated in the model.

The convective heat transfer coefficient between water and tube internal surface is quantitatively evaluated by adopting the Dittus-Boelter correlation in the mono-phase regions (sub-cooled and superheated) according to:

$$h_{chc,s1,s3} = 0.023\frac{\lambda}{D_{in}}Re^{0.8}Pr^{0.4} \tag{147}$$

The Kandlikar correlation [26] is employed in the two-phase region:

$$h_{chc,s2} = 0.023 \frac{k}{D_{in}} Re^{0.8} Pr^{0.4} \alpha_{TP} \tag{148}$$

where $\alpha_{TP}$ is the maximum between $\alpha_{NBD}$ and $\alpha_{CBD}$:

$$\alpha_{NBD} = (1 - x_d)^{0.8} (0.6683 Co^{-0.2} + 1058 Bo^{0.7}) \tag{149}$$

$$\alpha_{CBD} = (1 - x_d)^{0.8} (1.136 Co^{-0.9} + 667.2 Bo^{0.7}) \tag{150}$$

Where $x_d$ is the dryness fraction, Co is the convective number and Bo is the boiling number:

$$Co = \left(\frac{1 - x_d}{x_d}\right)^{0.8} \left(\frac{d_{sg}}{d_{sl}}\right)^{0.5} \tag{151}$$

$$Bo = \frac{q''}{\Gamma (h_{sg} - h_{sl})} \tag{152}$$

#### *3.2.2.3 Wall interface correlations*

Three energy balance equations represent the wall behavior in the model. The variables regarded as state variables are the mean wall temperature in each region, defined by the sub-cooled, two-phase and superheated length $L_1$, $L_2$ and $L_3$.

The three equations implemented in SIMULINK® are the following:

$$\frac{dT_{w1}}{dt} = + \frac{(T_{w12} - T_{w1})}{L_1} \frac{dL_1}{dt} + \frac{\pi D_{out} h_{chc,p1}}{d_{w1} A_w C_{w1}} (T_{p1} - T_{wp1}) + \frac{\pi D_{in} h_{chc,s1}}{d_{w1} A_w C_{w1}} (T_{s1} - T_{ws1}) \tag{153}$$

$$\frac{dT_{w2}}{dt} = + \frac{(T_{w23} - T_{w12})}{L_2} \frac{dL_1}{dt} + \frac{(T_{w23} - T_{w2})}{L_2} \frac{dL_2}{dt} + \frac{\pi D_{out} h_{chc,p2}}{d_w A_w C_{w2}} (T_{p2} - T_{wp2}) + \frac{\pi D_{in} h_{chc,s2}}{d_w A_w C_{w2}} (T_{s2} - T_{ws2}) \tag{154}$$

$$\frac{dT_{w3}}{dt} = - \frac{T_{w3}}{L_3} \frac{dL_3}{dt} - \frac{T_{w23}}{L_3} \left(\frac{dL_1}{dt} + \frac{dL_2}{dt}\right) + \frac{\pi D_{out} h_{chc,p3}}{d_w A_w C_{w3}} (T_{p3} - T_{wp3}) + \frac{\pi D_{in} h_{chc,s3}}{d_w A_w C_{w3}} (T_{s3} - T_{ws3}) \tag{155}$$

Figure 109 shows the SIMULINK® modeling of Eq. (153).

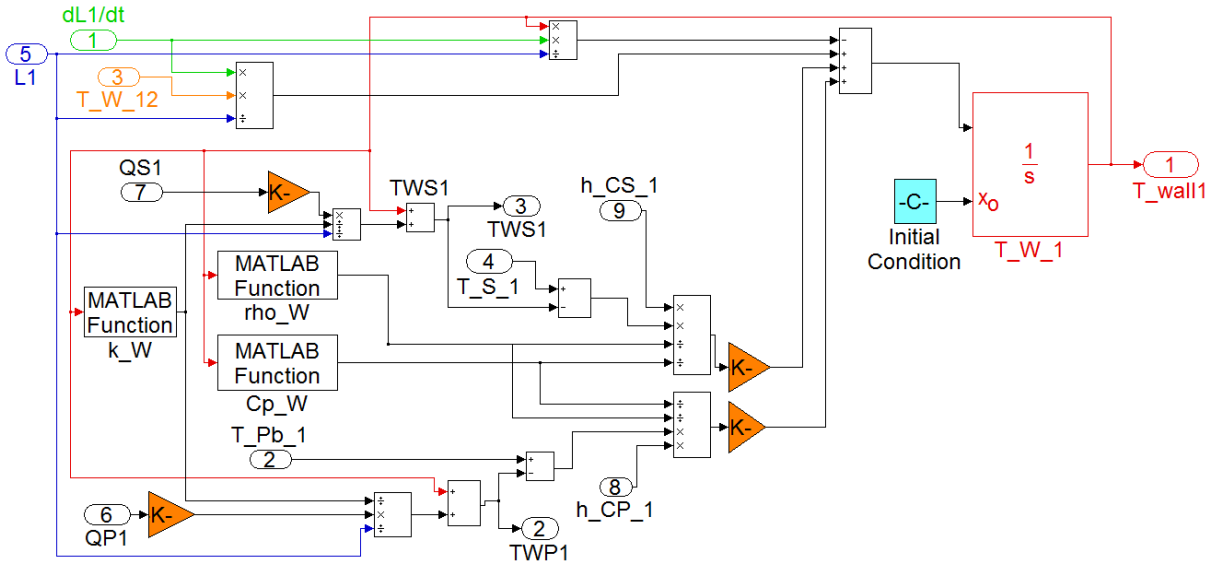


**Figure 109. Implementation in SIMULINK® of the energy balance in region 1 for the wall.**

T91 ferritic-martensitic steel is the wall interface material. The correlations implemented in the SG model for density, specific heat capacity, and viscosity of T91 are the same used for the core model.

### 3.2.3 Simulations

Before connecting the entire primary system, the SG model has been simulated alone to study the dynamic behavior of this single component. Five different scenarios have been simulated, three involving the water side and two the lead one. The secondary-side-driven simulations are:

- Enhancement of feedwater mass flow rate;
- Enhancement of feedwater temperature;
- Variation of turbine admission valve flow coefficient, with consequent depressurization.

The primary-side-driven simulations are:

- Enhancement of lead inlet mass flow rate;
- Enhancement of lead inlet temperature.

Except for the feedwater inlet temperature variation, the above-mentioned scenarios are simulated as step changes imposed at 100 s and run for 200 s, which are sufficient to reach the new steady-state values after the transient development. Differently from the other input variables variations, the feedwater inlet perturbation is simulated as a ramp of 1 °C $s^{-1}$ for 10 s since its derivative is explicitly involved in the model, and a step input does not have a finite derivative.

The geometrical data are taken from the ELSY SG design proposed by Ansaldo [27], opportunely rescaled coherently with DEMO power size (i.e. 300 $MW_{th}$). By changing the number of tubes in the configuration, this goal is easily obtained.

The sub-cooled water entering the tubes has a temperature of 335 °C and a pressure of 188.5 bar. The expected steam outlet temperature is 470 °C at 188.5 bar, since no pressure drop is considered.

On the lead side nominal temperatures are fixed by the core: the SG inlet temperature is the outlet core one (480 °C), while the SG outlet temperature is the inlet core one (400 °C). Atmospheric pressure is considered for the primary side. The main data are resumed in Tab. XXIX.

**Table XXIX. Geometric and thermal-hydraulic data of the SG configuration.**

| **STEAM GENERATOR** | | | |
|---|---|---|---|
| Power [$MW_{th}$] | | 300 | |
| **Water side** | | **Lead side** | |
| Inlet Temp. [°C] | 335 | Inlet Temp. [°C] | 480 |
| Outlet Temp. [°C] | 470 | Outlet Temp. [°C] | 400 |
| Pressure [bar] | 188.5 | Pressure [bar] | 1 |
| Total mass flow rate [kg $s^{-1}$] | 185.56 | Total mass flow rate [kg $s^{-1}$] | 25757 |
| Tubes Number [#] | | 358 | |
| Tube Length [m] | | 55 | |
| Internal diameter [mm] | | 17.22 | |
| External diameter [mm] | | 22.22 | |
| Radial pitch [mm] | | 24 | |
| Axial pitch [mm] | | 24 | |

The steady-state is simulated, and very satisfactory results are found (see Tab. XXX) for what concerns both water and lead outlet temperatures, which achieve the desired reference values of 470 and 400 °C, respectively.

**Table XXX. Nominal steady-state values.**

| **Length** | | **Water temperature** | |
|---|---|---|---|
| Sub-cooled [m] | 7.086 | Sub-cooled [°C] | 347.9 |
| Two-phase [m] | 16.00 | Two-phase [°C] | 360.8 |
| Superheated [m] | 31.91 | Superheated [°C] | 415.4 |
| **Lead temperature** | | Outlet [°C] | 470.0 |
| Superheated [°C] | 463 | Pressure [bar] | 188.5 |
| Two-phase [°C] | 428.6 | **Power exchanged** | |
| Sub-cooled [°C] | 405.6 | Sub-cooled length [kW] | 118.6 |
| Outlet [°C] | 400 | Two-phase length [kW] | 364.2 |
| **Wall temperature** | | Superheated length [kW] | 355.2 |
| Sub-cooled [°C] | 372.7 | Each tube [kW] | 838.0 |
| Two-phase [°C] | 383.9 | Eight SGs [MW] | 300.0 |
| Superheated [°C] | 441.2 | | |

The steady-state physical and thermodynamic properties calculated with the above-mentioned correlations are listed in the Tab. XXXI.

**Table XXXI. Physical and thermodynamic properties at the reference steady-state.**

| | Sub-cooled region | Two-phase region | | | Superheated region |
|---|---|---|---|---|---|
| **LEAD** | | | | | |
| Mean temperature [°C], $T_P$ | 405.6 | 428.6 | | | 463 |
| Density [kg m$^{-3}$], $\rho_P$ | 10556.26 | 10528.79 | | | 10487.75 |
| Isobaric heat capacity [J kg$^{-1}$ K$^{-1}$], $C_p$ | 146.23 | 145.8 | | | 145.17 |
| Convective heat coefficient [W m$^{-2}$ K$^{-1}$], $h_{cp}$ | 11072.24 | 11090.37 | | | 11117.43 |
| **WALL** | | | | | |
| Mean temperature [°C], $T_W$ | 372.7 | 383.9 | | | 441.2 |
| Density [kg m$^{-3}$], $\rho_W$ | 7623.23 | 7619.36 | | | 7599.17 |
| Isobaric heat capacity [J kg$^{-1}$ K$^{-1}$], $C_W$ | 584.23 | 590.51 | | | 628.07 |
| Thermal conductivity [W m$^{-1}$ K$^{-1}$], $k_W$ | 28.10 | 28.17 | | | 28.47 |
| **WATER** | | **L** | **Mean** | **G** | |
| Mean temperature [°C], $T_S$ | 347.9 | 360.8 | | | 415.4 |
| Pressure [bar], $p$ | 188.5 | 188.5 | | | 188.5 |
| Density [kg m$^{-3}$], $\rho_S$ | 602.5 | 523.2 | 259.7 | 147.2 | 83.34 |
| Enthalpy [J kg$^{-1}$], $h_S$ | $1.635 \cdot 10^6$ | $1.77 \cdot 10^6$ | $2.273 \cdot 10^6$ | $2.473 \cdot 10^6$ | $2.938 \cdot 10^6$ |
| Convective heat coefficient [W m$^{-2}$ K$^{-1}$], $h_{CS}$ | $2.6 \cdot 10^4$ | $7.459 \cdot 10^4$ | | | $1.184 \cdot 10^4$ |

*Feedwater mass flow rate variation*

The SG dynamic response to a step enhancement of the feedwater mass flow rate by 10 % (from 185.56 kg s$^{-1}$ to 204.12 kg s$^{-1}$) is investigated.

As a first consequence of this perturbation, the sub-cooled length increases (Fig. 110) because a greater amount of water has to be heated, and consequently more power is exchanged in this zone. The latter phenomenon results in a stronger effect than that immediately brought by the mass flow rate increase, leading to a slightly higher mean temperature of the sub-cooled water (Fig. 111).

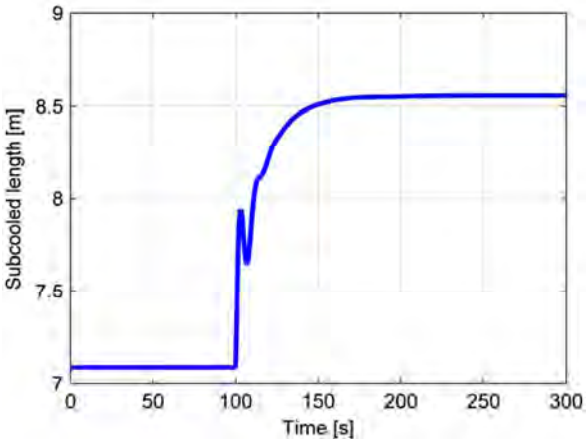


**Figure 110. Sub-cooled length following a 10 % enhancement of feedwater mass flow rate.**

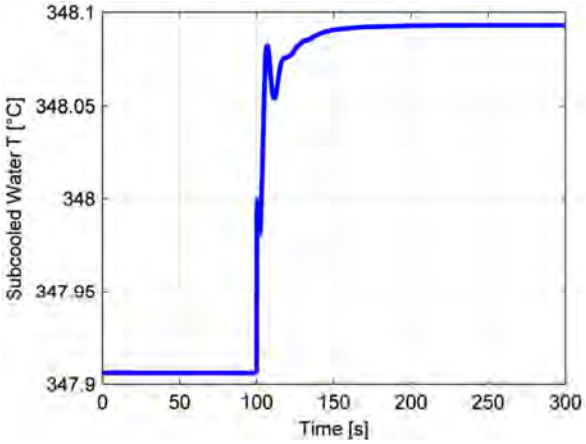


**Figure 111. Mean water temp. in the sub-cooled region following a 10 % enhancement of feedwater mass flow rate.**

The feedwater mass flow rate enhancement has an impact also on the two-phase zone: pressure undergoes an increase (Fig. 112), and consequently the saturation temperature, which exhibits exactly the same trend, eventually resulting in an enhancement of the two-phase length (Fig. 113). It is interesting to note the peculiar

non-minimum-phase behavior of this variable, which shows a sudden decrease at the very beginning of the transient and settles at a higher steady-state value compared to the starting figure.

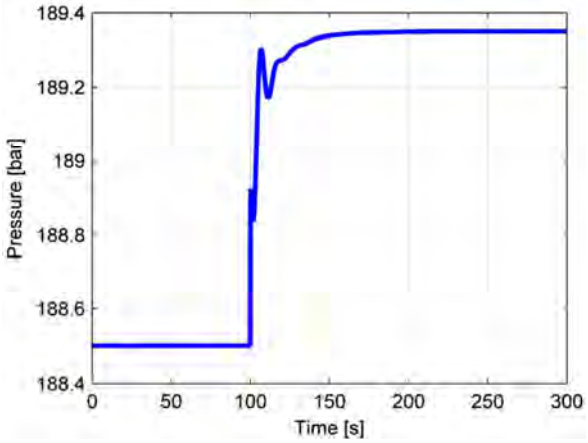


**Figure 112. Pressure in the SG following a 10 % enhancement of feedwater mass flow rate.**

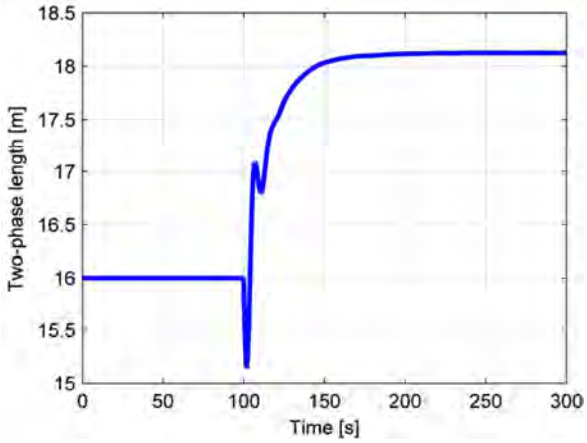


**Figure 113. Two-phase length following a 10 % enhancement of feedwater mass flow rate.**

The main effect of this transient is found in the superheated zone, which results reduced do due to the enlargement of the first two regions. A shorter stretch remains available for superheating the steam (Fig. 114), and a drastic decrease by almost 13 °C occurs in the outlet SG temperature (Fig. 115). These different thermal exchange conditions have direct impact on the primary side: water is colder and therefore the power exchanged in the SG is greater (Fig. 116), bringing to lower lead temperatures in all the three zones of the tubes. The final effect is that the outlet lead temperature is subject to a 5 °C decrease, which is considerable for a heavy liquid metal (Fig. 117).

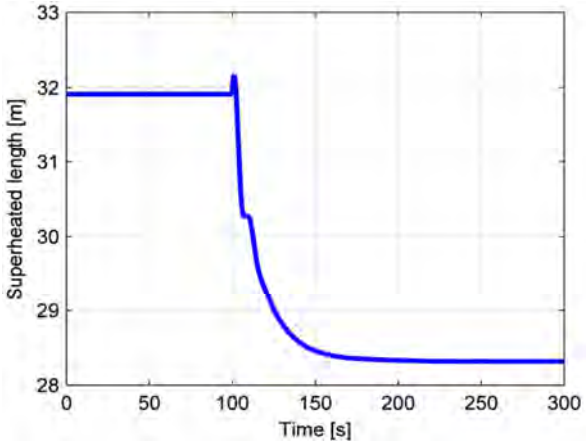


**Figure 114. Superheated length following a 10 % enhancement of feedwater mass flow rate.**

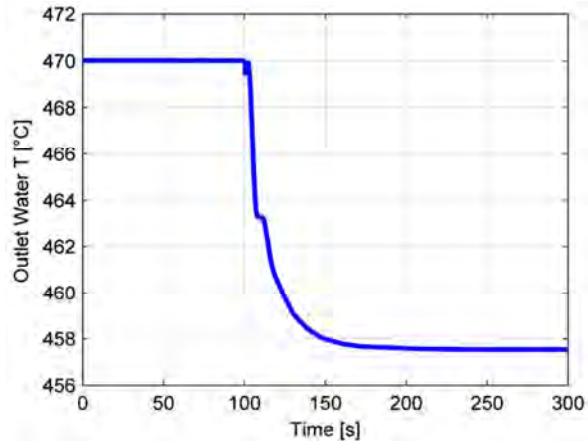


**Figure 115. Outlet steam temperature following a 10 % enhancement of feedwater mass flow rate.**

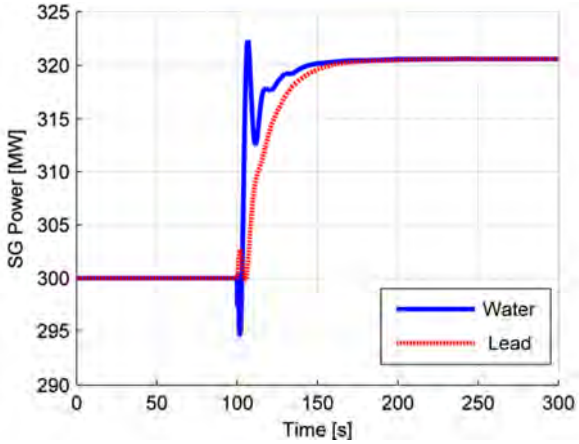


**Figure 116. Thermal power exchanged, both on water and lead sides, following a 10 % enhancement of feedwater mass flow rate.**

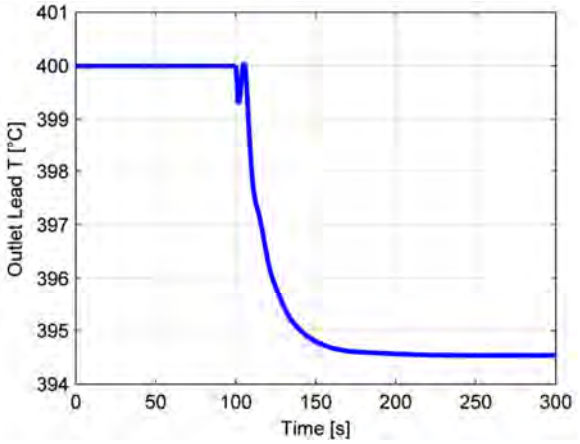


**Figure 117. Outlet lead temperature following a 10 % enhancement of feedwater mass flow rate.**

A non-minimum-phase effect resulting in the two-phase and superheated lengths dynamics is pointed out in Figs. 113 and 14; an analogous behavior, even if less evident, is revisable in the case of outlet water and lead temperatures.

The occurrence of these undershoots is very common in SG models and reveals the presence of zeros in the right-half plane in the transfer function of these variables. This is not a physical behavior, but comes from the nature of the model instead. In fact a non-minimum-phase network is characterized by having more than one path connecting an input to an output [28], as in this case: temperature and length of a specific zone may be changed either by different conditions of the previous or the next region on the same side, or by a modification of the heat exchange conditions on the other side in the same region. For example, the two-phase length on the water side can be influenced either by a change of the inlet water conditions through the sub-cooled zone, or by a different heat exchange with the lead (caused by any change on the primary side). The presence of a non-minimum phase behavior causes a complication in conceiving the control strategy, since there is not an univocal way to act on the involved controlled variable. Furthermore in these kinds of models, the initial behavior at the very beginning of the transient shows a trend opposite to the one immediately subsequent the final steady-state value is reached with.

In Tab. XXXII, the final steady-state results are summarized for the main variables.

**Table XXXII. Final steady-state values after a 10 % enhancement of feedwater mass flow rate.**

| Length | |
|---|---|
| Sub-cooled [m] | 8.557 |
| Two-phase [m] | 18.13 |
| Superheated [m] | 28.32 |
| **Lead temperature** | |
| Superheated [°C] | 462.5 |
| Two-phase [°C] | 426.0 |
| Sub-cooled [°C] | 400.8 |
| Outlet [°C] | 394.5 |
| **Wall temperature** | |
| Sub-cooled [°C] | 370.2 |
| Two-phase [°C] | 383.1 |
| Superheated [°C] | 437.1 |

| Water temperature | |
|---|---|
| Sub-cooled [°C] | 348.1 |
| Two-phase [°C] | 361.2 |
| Superheated [°C] | 409.4 |
| Outlet [°C] | 457.5 |
| Pressure [bar] | 189.4 |
| **Power exchanged** | |
| Sub-cooled length [kW] | 132.9 |
| Two-phase length [kW] | 396.1 |
| Superheated length [kW] | 366.6 |
| Each tube [kW] | 895.6 |
| Eight SGs [MW] | 320.6 |

*Feedwater temperature variation*

The feedwater inlet temperature is enhanced by 10 °C (from 335°C to 345°C) with a ramp input of 1°C $s^{-1}$, leading to an immediate increase of the mean sub-cooled water temperature (Fig. 118) and to a decrease of the sub-cooled length (Fig. 119) due to the reduced difference between inlet temperature and saturation temperature. Since a higher inlet temperature does not affect the pressure in the SG, this variable and the related saturation temperature do not change their final values, as well as the two-phase length, even if some oscillations are present before reaching the end of transient.

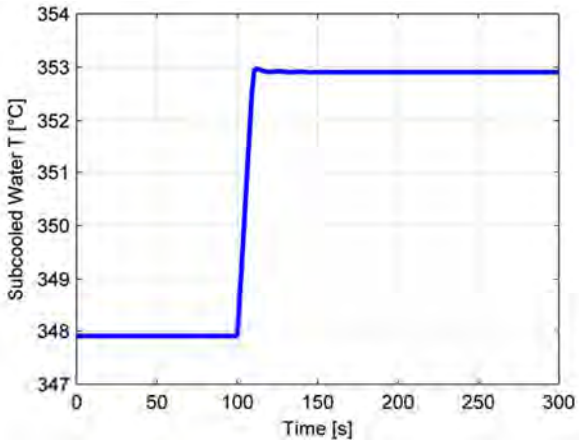


**Figure 118. Mean water temp in sub-cooled region following an enhancement by 10 K of feedwater inlet temp.**

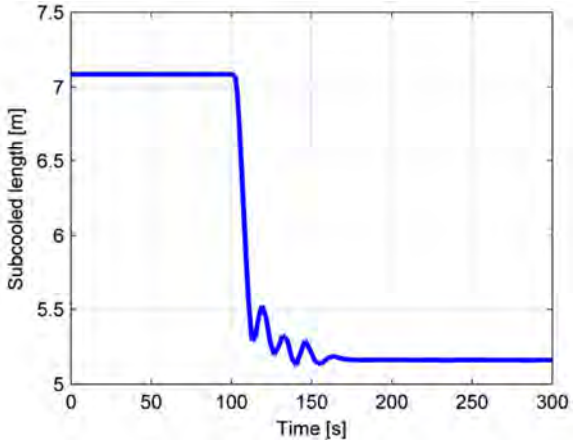


**Figure 119. Sub-cooled length following an enhancement by 10 K of feedwater inlet temperature.**

A shorter sub-cooled length, together with an almost unvaried two-phase tract leaves more space available for the superheated zone, which therefore increases its length (Fig. 120), making a greater power be exchanged in this zone and leading to a higher outlet steam temperature (Fig. 121).

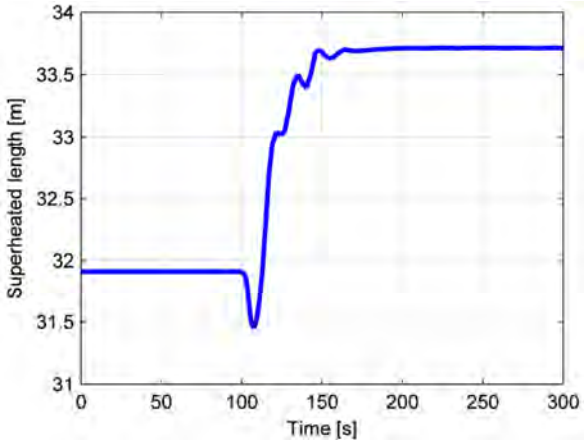


**Figure 120. Superheated length following an enhancement by 10 K of feedwater inlet temperature.**

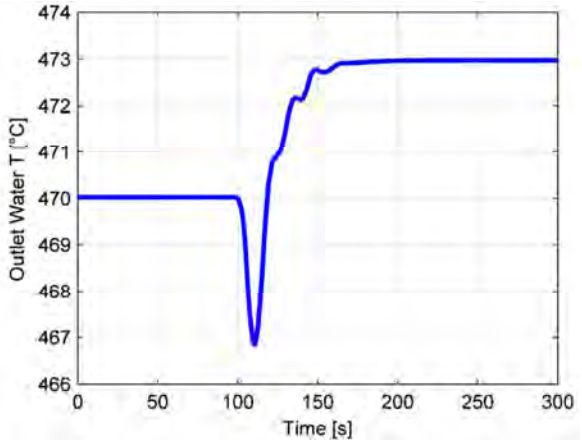


**Figure 121. Outlet steam temperature following an enhancement by 10 K of feedwater inlet temperature.**

The primary fluid responds to the different water conditions (and so heat exchange) by changing its temperature: in the first zone, that corresponds to the superheated zone on the water side, lead slightly decreases its temperature, due to the enhanced thermal power exchange.

Conversely, in the last region it flows through, corresponding to the first water length, the power exchanged is reduced because of the reduced difference between water inlet temperature and saturation temperature. For this reason, lead outlet temperature (Fig. 122) undergoes an increase owing to a globally worse heat exchange in the SG (Fig. 123).

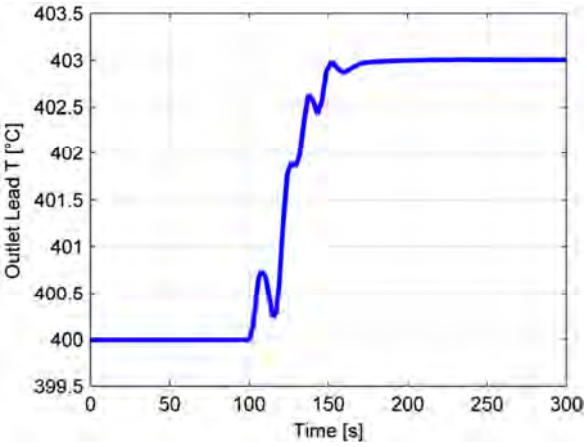


**Figure 122. Outlet lead temperature following an enhancement by 10 K of feedwater inlet temperature.**

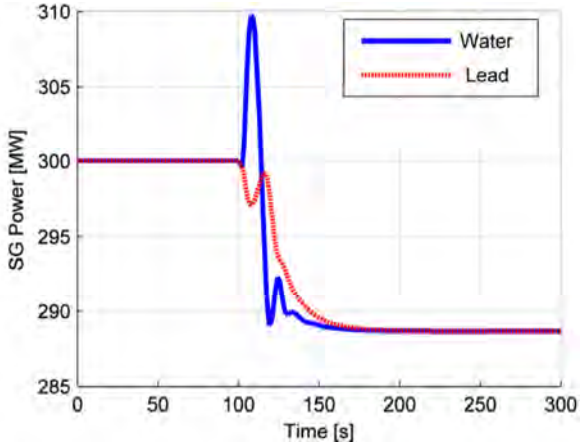


**Figure 123. Thermal power exchange, on both water and lead sides, following an enhancement by 10 K of feedwater inlet temperature.**

Also in this case, non-minimum phase phenomena are present, in particular in the water-related variables for the reasons mentioned above.

In Tab. XXXIII the final steady-state results are summarized for the main variables.

**Table XXXIII. Steady-state values after an enhancement by 10 K of feedwater inlet temperature.**

| Length | | Water temperature | |
|---|---|---|---|
| Sub-cooled [m] | 5.160 | Sub-cooled [°C] | 352.9 |
| Two-phase [m] | 16.12 | Two-phase [°C] | 360.8 |
| Superheated [m] | 33.72 | Superheated [°C] | 416.9 |
| **Lead temperature** | | Outlet [°C] | 473.0 |
| Superheated [°C] | 462.7 | Pressure [bar] | 188.5 |
| Two-phase [°C] | 428.1 | **Power exchanged** | |
| Sub-cooled [°C] | 406.9 | Sub-cooled length [kW] | 81.63 |
| Outlet [°C] | 403.0 | Two-phase length [kW] | 364.2 |
| **Wall temperature** | | Superheated length [kW] | 360.5 |
| Sub-cooled [°C] | 375.7 | Each tube [kW] | 806.4 |
| Two-phase [°C] | 383.7 | Eight SGs [MW] | 288.7 |
| Superheated [°C] | 441.8 | | |

*Turbine admission valve flow coefficient variation*

The coefficient is enhanced by 10 % in order to simulate the opening of this valve to follow the load, for instance. With this action, an enhancement of the steam outlet temperature, and thus a better quality of the steam entering the turbine, is expected.

Following the stepwise increase of the turbine admission valve, pressure in the SG tube decreases as an immediate consequence (Fig. 124).

After depressurization, the saturation temperature decreases with the same trend (Fig. 125) and, because of the reduced difference between inlet and two-phase temperature, a shorter sub-cooled length is achieved (Fig. 126).

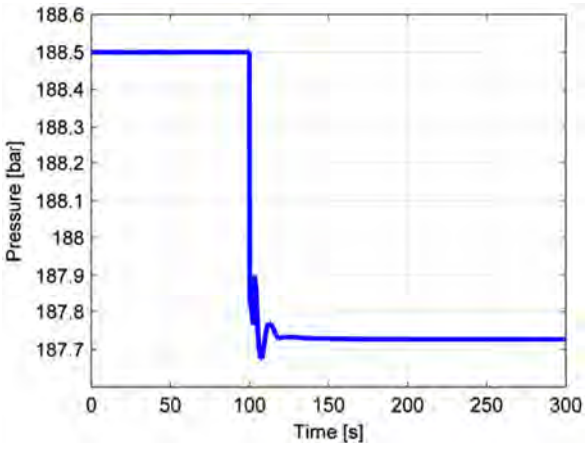


**Figure 124. Pressure in the SG following a 10 % enhancement of turbine admission valve coefficient.**

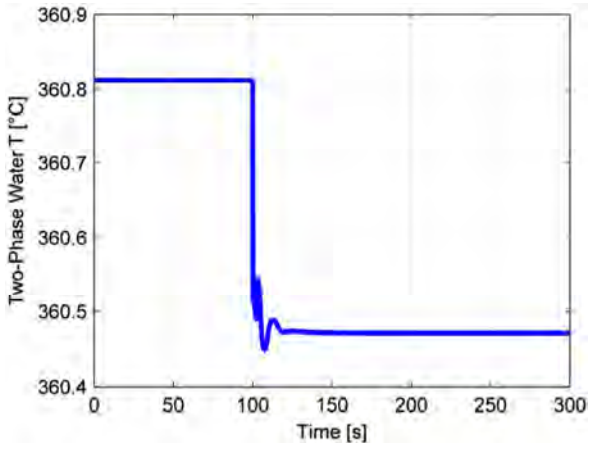


**Figure 125. Saturated water temperature following a 10 % enhancement of turbine admission valve coefficient.**

Small perturbations and deviations occur in the two-phase and superheated lengths (Figs. 127 and 128), but the main consequence of depressurization is the increase of steam outlet temperature, even if at a smaller pressure (Fig. 129).

On the whole, the power exchanged in the SG increases (Fig. 130). Lead is subject to the different heat exchange condition and decreases its outlet temperature (Fig. 131) because of the lower temperature of water in both the sub-cooled and the two-phase regions.

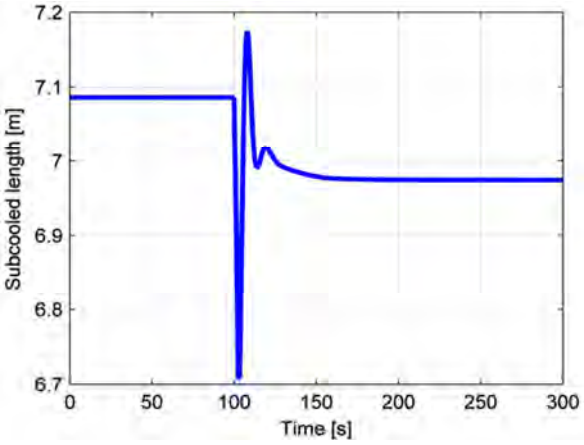


**Figure 126. Sub-cooled length following a 10 % enhancement of turbine admission valve coefficient.**

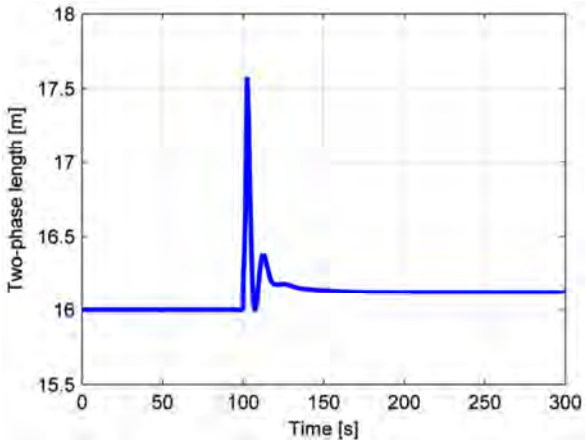


**Figure 127. Two-phase length following a 10 % enhancement of turbine admission valve coefficient.**

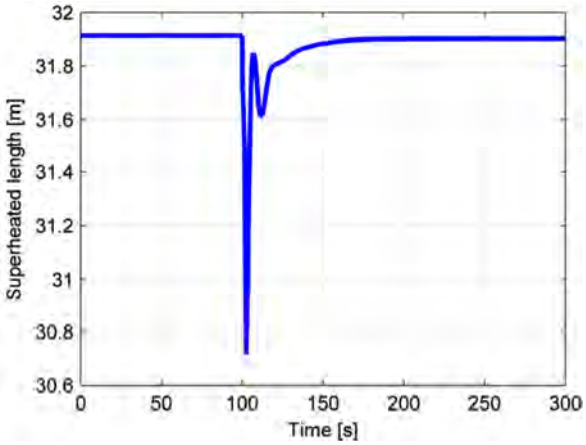


**Figure 128. Superheated length following a 10 % enhancement of turbine admission valve coefficient.**

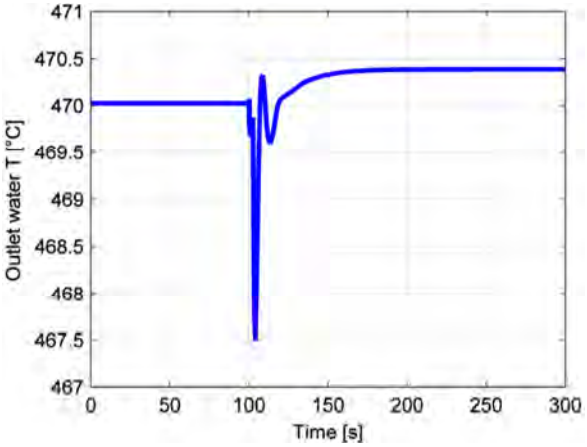


**Figure 129. Steam outlet temperature following a 10 % enhancement of turbine admission valve coefficient.**

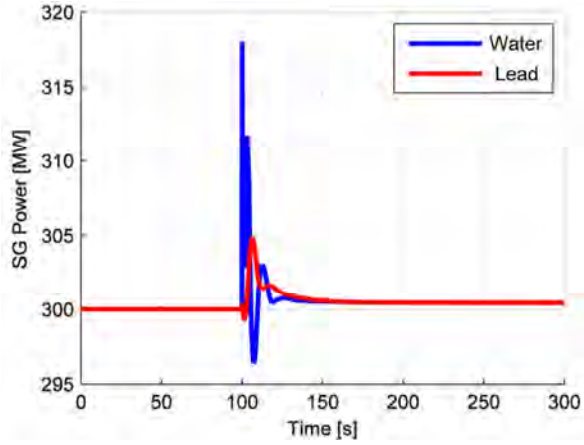


**Figure 130. Thermal power exchanged, on both water and lead sides, following a 10 % enhancement of turbine admission valve coefficient.**

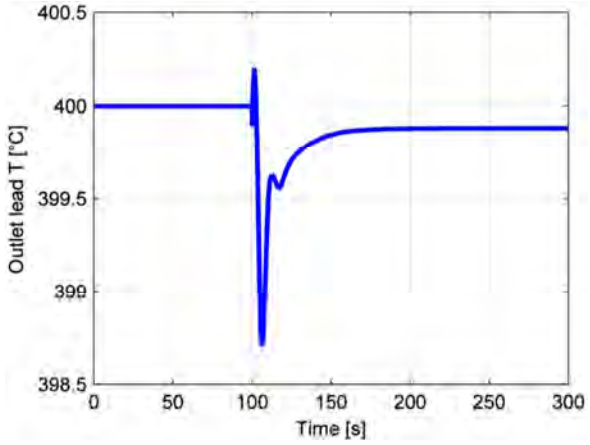


**Figure 131. Lead outlet temperature following a 10 % enhancement of turbine admission valve coefficient.**

In Tab. XXXIV, the final steady-state results are summarized for the main variables.

**Table XXXIV. Final steady-state values after a 10 % enhancement of turbine admission valve coefficient.**

| **Length** | |
|---|---|
| Sub-cooled [m] | 6.974 |
| Two-phase [m] | 16.12 |
| Superheated [m] | 31.90 |
| **Lead temperature** | |
| Superheated [°C] | 463.0 |
| Two-phase [°C] | 428.5 |
| Sub-cooled [°C] | 405.4 |
| Outlet [°C] | 399.9 |
| **Wall temperature** | |
| Sub-cooled [°C] | 372.5 |
| Two-phase [°C] | 383.6 |
| Superheated [°C] | 441.3 |

| **Water temperature** | |
|---|---|
| Sub-cooled [°C] | 347.7 |
| Two-phase [°C] | 360.5 |
| Superheated [°C] | 415.4 |
| Outlet [°C] | 470.4 |
| Pressure [bar] | 187.7 |
| **Power exchange** | |
| Sub-cooled length [kW] | 116.7 |
| Two-phase length [kW] | 367.9 |
| Superheated length [kW] | 354.7 |
| Each tube [kW] | 839.3 |
| Eight SGs [MW] | 300.5 |

*Lead inlet mass flow rate*

The SG dynamic response to a stepwise enhancement of the lead inlet mass flow rate by 10 % (equivalent to 2575.7 kg $s^{-1}$) is investigated.

A greater amount of lead has to be heated and, as an immediate effect, the coolant temperature raises, in particular at the SG outlet (Fig. 132). As a consequence of the primary fluid higher temperature, the heat exchange is improved (Fig. 133). On the water side, this change leads to a decrease in the sub-cooled and two-phase lengths (Figs. 134 and 135), and therefore to an increase of the superheated one (Fig. 136).

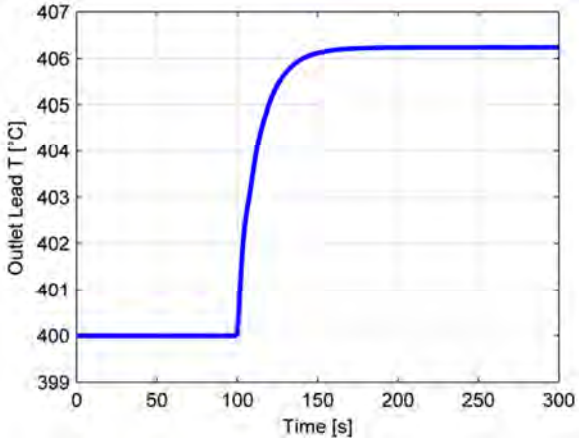


**Figure 132. Outlet lead temperature following a 10 % enhancement of lead inlet mass flow rate.**

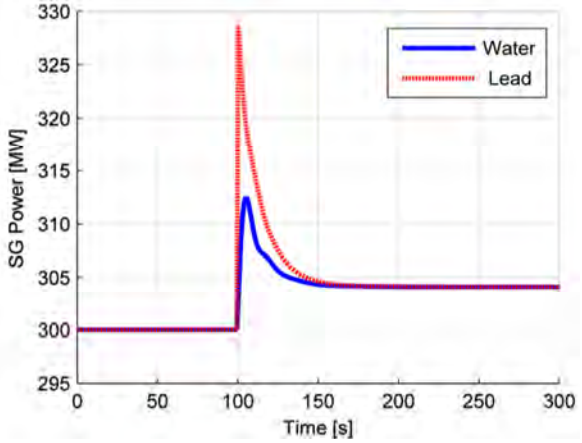


**Figure 133. Thermal power exchanged, on both water and lead sides, following a 10 % enhancement of lead inlet mass flow rate.**

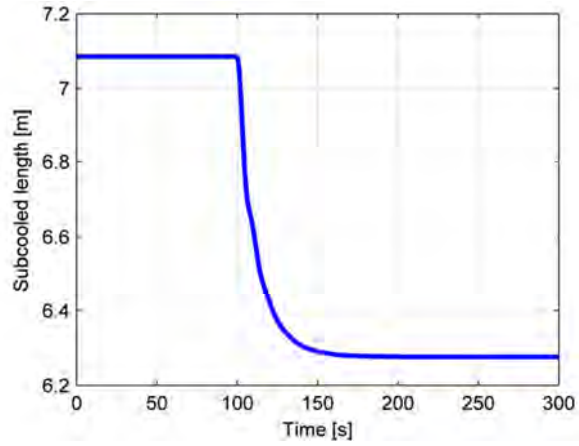


**Figure 134. Sub-cooled length following a 10 % enhancement of lead inlet mass flow rate.**

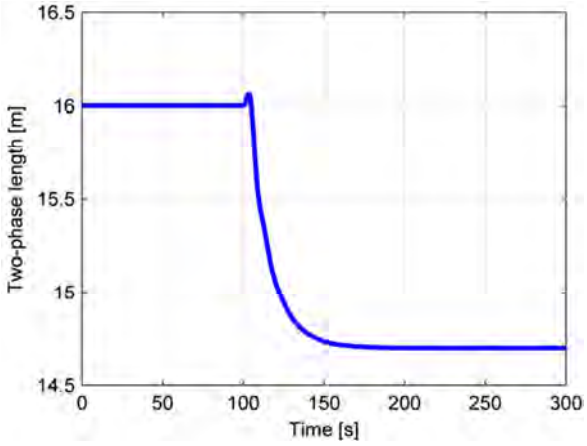


**Figure 135. Two-phase length following a 10 % enhancement of lead inlet mass flow rate.**

Except for some transient variations, sub-cooled and saturated water temperatures and pressures do not change their values. On the contrary, the superheated length enhancement brings a significant increase of the outlet steam temperature (Fig. 137).

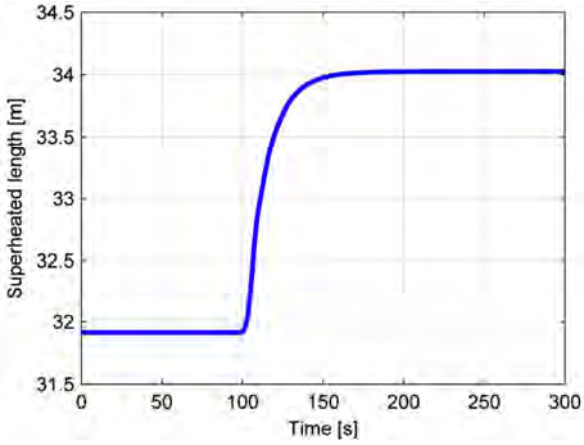


**Figure 136. Sub-cooled length following a 10 % enhancement of lead inlet mass flow rate.**

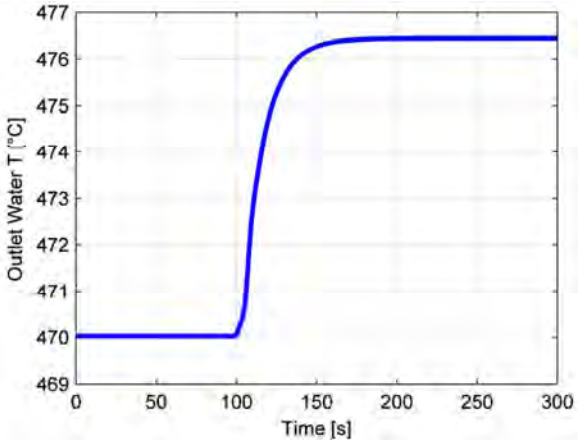


**Figure 137. Steam outlet temperature following a 10 % enhancement of lead inlet mass flow rate.**

In this transient scenario, induced by a change in lead conditions, the non-minimum phase behavior is not present, with the exception of a very small overshoot in the two-phase length.

In Tab. XXXV the final steady-state results are summarized for the main variables.

**Table XXXV. Final steady-state values after a 10 % enhancement of lead inlet mass flow rate.**

| **Length** | |
|---|---|
| Sub-cooled [m] | 6.276 |
| Two-phase [m] | 14.70 |
| Superheated [m] | 34.03 |
| **Lead temperature** | |
| Superheated [°C] | 464.0 |
| Two-phase [°C] | 432.3 |
| Sub-cooled [°C] | 411.4 |
| Outlet [°C] | 406.2 |
| **Wall temperature** | |
| Sub-cooled [°C] | 375.8 |
| Two-phase [°C] | 385.8 |
| Superheated [°C] | 443.9 |

| **Water temperature** | |
|---|---|
| Sub-cooled [°C] | 347.9 |
| Two-phase [°C] | 360.8 |
| Superheated [°C] | 418.6 |
| Outlet [°C] | 476.4 |
| Pressure [bar] | 188.5 |
| **Power exchanged** | |
| Sub-cooled length [kW] | 118.6 |
| Two-phase length [kW] | 364.2 |
| Superheated length [kW] | 366.7 |
| Each tube [kW] | 849.5 |
| Eight SGs [MW] | 304.1 |

*Lead inlet temperature*

The lead inlet temperature is enhanced by 10 K (from 480 °C to 490 °C), leading to an immediate mean lead temperature increase in all the regions and in particular in the outlet one (Fig. 138).

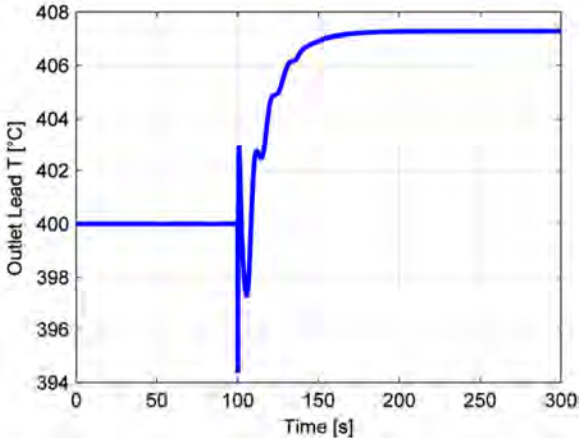


**Figure 138. Lead outlet temperature following an enhancement by 10 K of lead inlet temperature.**

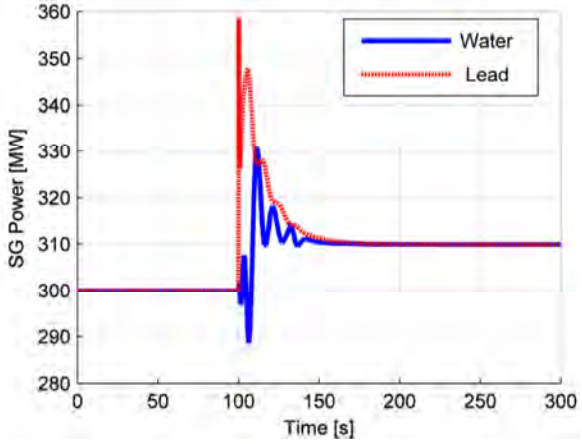


**Figure 139. Thermal power exchanged, on both water and lead sides, following an enhancement by 10 K of lead inlet temperature.**

The improved heat exchange, due to higher primary fluid temperatures, leads to an increase of the power exchanged in the SG (Fig. 139) and thus to a shortening of the sub-cooled and two-phase lengths (Figs. 140 and 141). In this way, a larger region is available for superheating (Fig. 142) and an increase of the steam outlet temperature occurs (Fig. 143). Since a variation on the lead side does not affect pressure inside the SG tubes, no pressure variations are present on the secondary side, and consequently the mean water temperatures in the sub-cooled and two-phase regions, as well as the power exchanged in these zone, remain constant except for some transient oscillations.

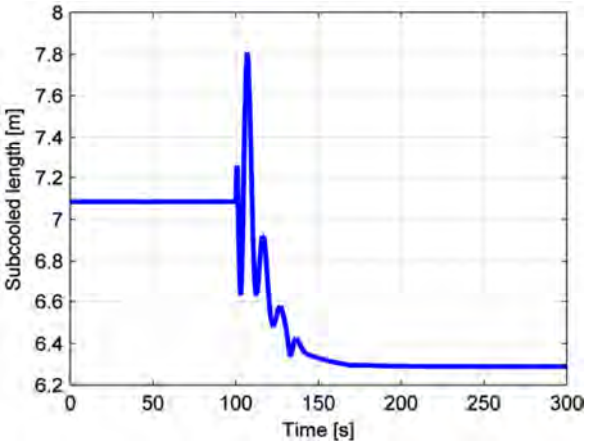


**Figure 140. Sub-cooled length following an enhancement by 10 K of lead inlet temperature.**

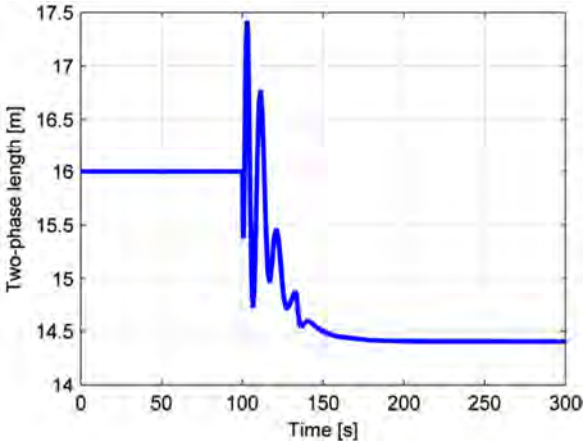


**Figure 141. Two-phase length following an enhancement by 10 K of lead inlet temperature.**

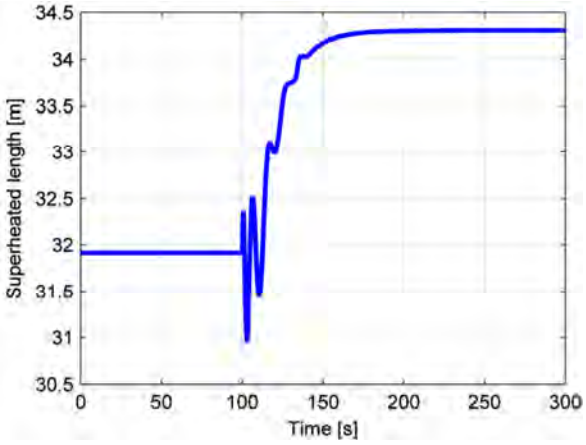


**Figure 142. Superheated length following an enhancement by 10 K of lead inlet temperature.**

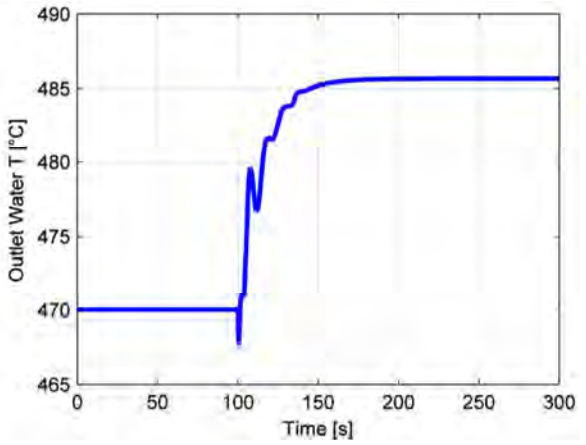


**Figure 143. Steam outlet temperature following an enhancement by 10 K of lead inlet temperature.**

Several undershoots and overshoots are present in this simulation, due to the sudden change in inlet lead temperature (stepwise change of 10 °C, which is a large value for a liquid metal).

In Tab. XXXVI the final steady-state results are summarized for the main variables.

**Table XXXVI. Final steady-state values after an enhancement by 10 K of lead inlet temperature.**

| **Length** | |
|---|---|
| Sub-cooled [m] | 6.289 |
| Two-phase [m] | 14.41 |
| Superheated [m] | 34.30 |
| **Lead temperature** | |
| Superheated [°C] | 471.7 |
| Two-phase [°C] | 435.9 |
| Sub-cooled [°C] | 412.9 |
| Outlet [°C] | 407.3 |
| **Wall temperature** | |
| Sub-cooled [°C] | 375.8 |
| Two-phase [°C] | 386.3 |
| Superheated [°C] | 449.8 |

| **Water temperature** | |
|---|---|
| Sub-cooled [°C] | 347.9 |
| Two-phase [°C] | 360.8 |
| Superheated [°C] | 423.2 |
| Outlet [°C] | 485.7 |
| Pressure [bar] | 188.5 |
| **Power exchanged** | |
| Sub-cooled length [kW] | 118.6 |
| Two-phase length [kW] | 364.2 |
| Superheated length [kW] | 382.8 |
| Each tube [kW] | 865.6 |
| Eight SGs [MW] | 309.9 |

## 3.3 Pump Model

For predicting a flow transient through the primary loop, the equation for the primary pump flow rate ($\Gamma$) change in time is given by:

$$\frac{d\Gamma}{dt} = \frac{\Gamma_{ref} - \Gamma}{\tau_{pump}} \tag{156}$$

where $\Gamma_{ref}$ is the set point of the primary coolant pump flow rate and $\tau_{pump}$ is the respective time constant.

## 3.4 Pool Model

The presence of the pool in the reactor configuration is responsible for a very large thermal inertia. The coolant mass flow rate leaving the SGs is only a small fraction of the entire amount of lead present inside the reactor vessel. With this conceptual design, an enhancement of the core outlet temperature do not influence the core inlet temperature directly, due to the mixing with the pool colder lead.
Such an effect on the system time response is taken into account by adopting the following energy balance:

$$\frac{dT_{pool}}{dt} = \frac{\Gamma\left(T_{out\ SG} - T_{pool}\right)}{M} \tag{157}$$

The parameter denoted by *M* refers to the whole lead mass contained in the external vessel since, thanks to the coolant high thermal conductivity, a higher temperature mass flow rate flowing into the external vessel is perceived in the whole system.

## 3.5 Hot and Cold Legs Model

A drawback of any zero-dimensional approach consists in the incapacity to catch transport phenomena, in particular the time needed by lead to flow from the SG outlet to the core inlet. This is a key aspect in a control-oriented view, because it determines the characteristic time constants of the system free dynamics. Anyway, this effect can be simulated by introducing suitable time delays to take into account the different time intervals needed by lead to flow into its loops (from core outlet to SG inlet, and from SG outlet to core inlet).

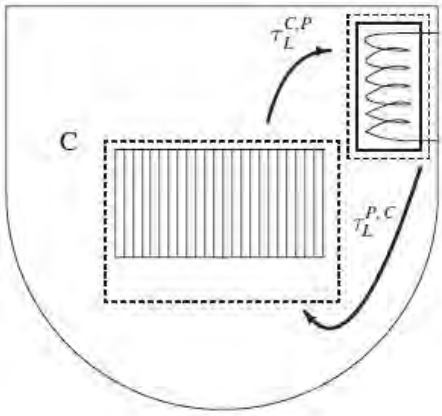


**Figure 144. Simplified view of the primary loop and its main the components. In particular, the time delays implemented to consider the transport effects are graphically represented.**

In the evaluation of the delay due to the lead motion, only a fraction of the entire lead mass is credited in the calculation for the cold and hot legs respective delays. In the former, the coolant inside the pool is decreased by the amount of lead above the SG midplane; in the latter only the coolant present in the hot collector and leg is accounted for.

The general expression for the time delay is:

$$\tau = \frac{M_{lead}}{\Gamma_{SG}} \tag{158}$$

It is important to notice the difference with the energy balance performed on the pool, in which the entire lead mass is involved in the thermal exchange, being consequently affected by the entrance of a hotter or colder lead mass flow rate.

## 3.6 Loop Model

A primary loop model, composed by core, steam generators, primary pump and pool is developed by assembling the two previous models (core and SG) and by implementing the new components description (pump and pool).
For the core model, the only input that can be handled is the user-programmed reactivity, managed by control rods. In the core model described previously, lead inlet temperature and coolant mass flow rate are input variables as well, but in the closed loop they turn into variables retrieved from the pool and pump blocks, respectively. The latter is positioned between core outlet and SG inlet; a delay due to the time needed by the lead to cover the hot leg length is necessarily considered.
The inputs for the SG model are reduced to two: now the primary side input variables, constituted by lead mass flow rate and temperature, are retrieved from pump and core model output, respectively. At the outlet of the SG, a block is added to simulate the presence of the pool, which reveals to be an essential element to determine the proper dynamics of the primary loop. In addition, another delay is considered to reckon the time needed by lead to cover the distance from the SG outlet to the core inlet. In Fig. 145 the MATLAB/SIMULINK® block representation of the primary loop model is proposed.

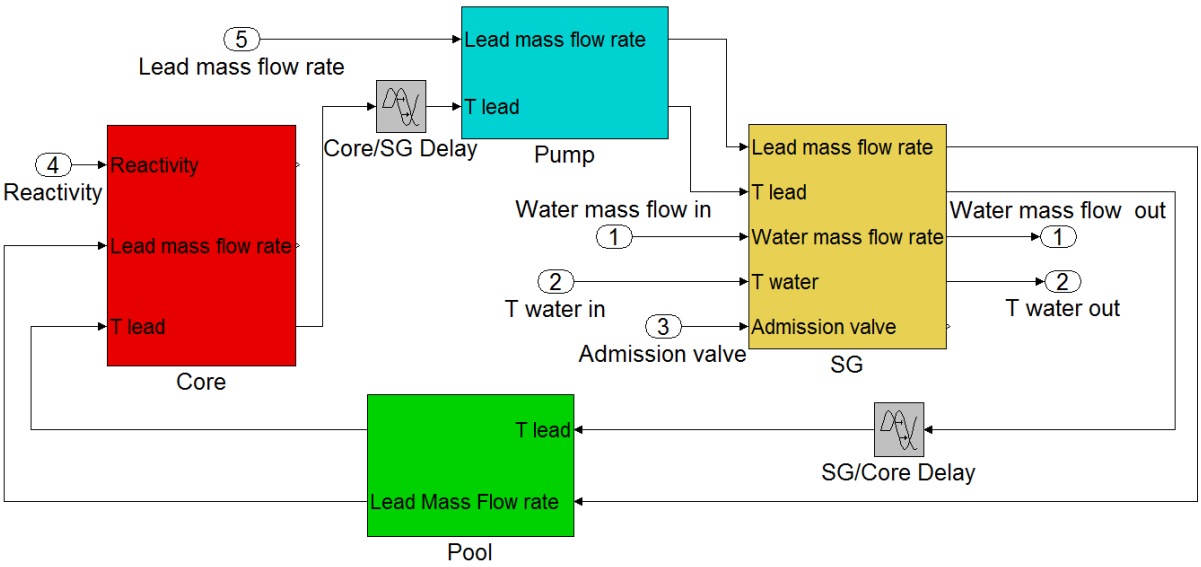


**Figure 145. Primary loop model representation.**

## 4. Simulations and Results

Five different scenarios are simulated in order to obtain information about the whole system behavior in a control-oriented view. Two transients are initiated by acting on the secondary water side: enhancements of feedwater mass flow rate and temperature are considered.

A third scenario is performed on the SG side: the turbine admission valve is simulated to be opened, with consequent depressurization.

A fourth transient is initiated by acting on the pump block so as to modify the reference lead mass flow rate.

The last simulation is performed on the core sub-system and consists in a reactivity insertion due to a control rod set withdrawal.

Except for the inlet feedwater temperature variation, all the above-mentioned scenarios are simulated as step changes at time 500 s and are run for 1500 s, as a longer time is needed to reach the steady-state than in the case of core and SG alone , due to the delay and thermal inertia of the pool. The feedwater inlet temperature variation is simulated as a ramp of 1 °C $s^{-1}$ for ten seconds since its derivative is directly implemented in the model and problems would occur in solving the respective equations (a step input does not have a finite derivative).

The simulation parameters regarding both core and SG are summarized in Tabs. from IX to XIV and Tabs. from XXIX to XXXI, respectively. In addition, the following Table shows the simulation parameters of pool and pump, and the calculated time delays.

**Table XXXVII. Parameters inserted into the primary loop model.**

| Parameters | | Units |
|---|---|---|
| Lead mass in the pool | 2.7816E6 | kg |
| Pump time constant | 4 | s |
| SG-core delay (pool delay) | 67.5 | s |
| Core-SG delay (hot leg delay) | 5.17 | s |

*Water flow rate variation*

The first input variable perturbed is the water flow rate at the SG inlet, which undergoes a 10 % stepwise enhancement. A negative coolant density reactivity coefficient is considered in this simulation.

The transient is influenced by the presence of the pool and the respective delay: in fact, for the first 70 s the only component is affected by the perturbation is the SG and its dynamics is very similar to that presented and discussed concerning the stand-alone simulation. After 70 s the core inlet temperature starts decreasing and the relative dynamics, driven by the negative coolant density and radial expansion feedbacks, leads to a new core outlet temperature that gives a feedback on the SG inlet temperature in turn. In this second part of the transient SG and core are strongly coupled with reciprocal feedbacks. After 1500 s from the initial step, the steady-state is reached.

As already described, the first consequence of a water mass flow rate enhancement is an increase of the sub-cooled and two-phase lengths and temperatures, besides an increase of pressure in the SG, as described in Figs. from 146 to 149.

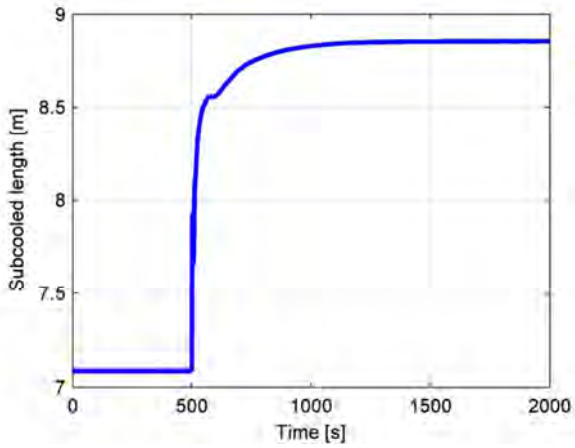


**Figure 146. Sub-cooled length variation in the SG following a 10 % enhancement of water mass flow rate.**

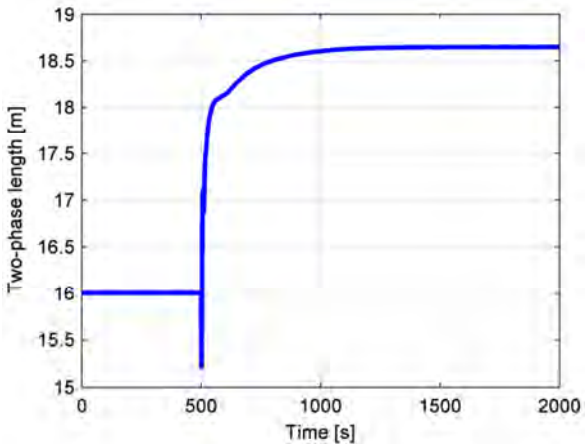


**Figure 147. Two-phase length variation in the SG following a 10 % enhancement of water mass flow rate.**

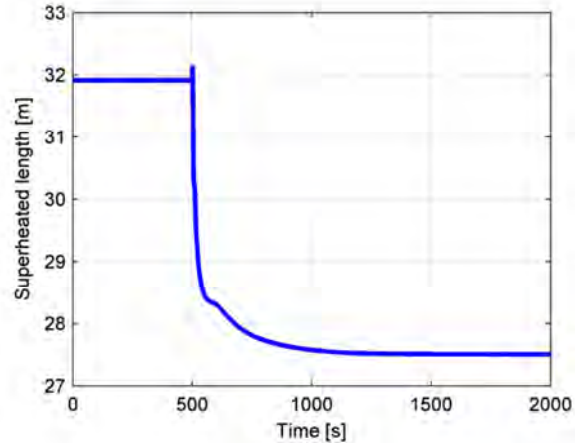


**Figure 148. Superheated length variation in the SG following a 10 % enhancement of water mass flow rate.**

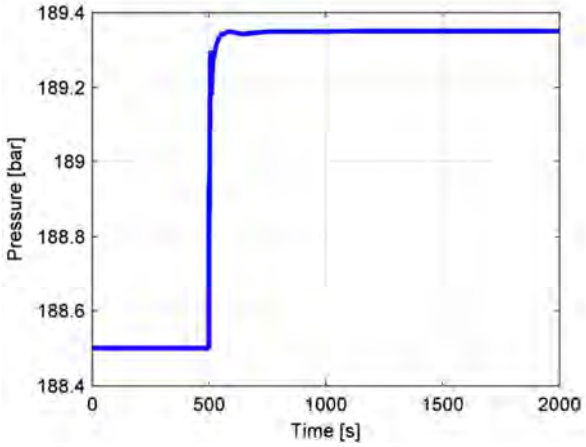


**Figure 149. SG pressure variation in the SG following a 10 % enhancement of water mass flow rate.**

As a result of the subsequently reduced superheated length, a lower steam temperature at the SG outlet of SG is found (Fig. 150), in conjunction with a similar decrease of the primary coolant SG outlet temperature due to the different heat exchange conditions, as Fig. 151 depicts.

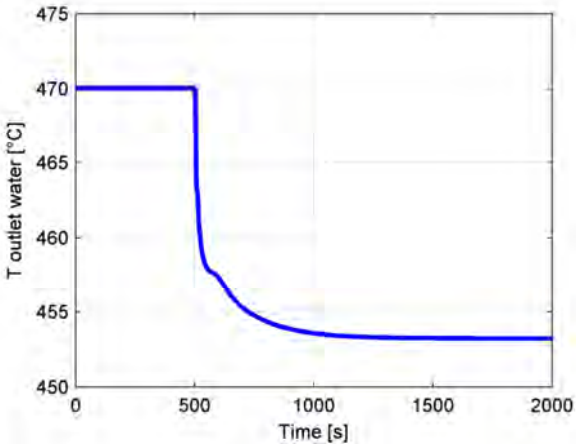


**Figure 150. Steam outlet temperature variation in the SG following a 10 % enhancement of water mass flow rate.**

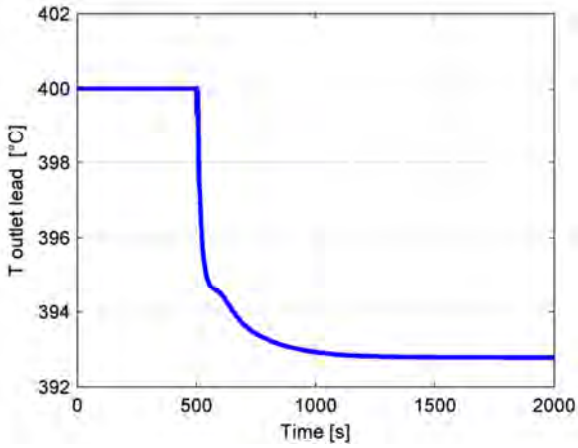


**Figure 151. Lead SG outlet temperature variation following a 10 % enhancement of water mass flow rate.**

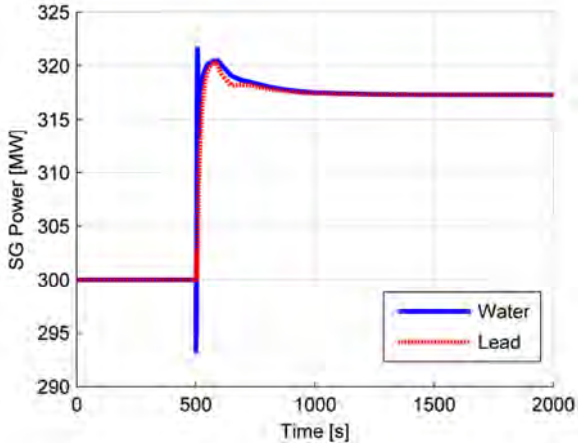


**Figure 152. SG power variation following a 10 % enhancement of water mass flow rate.**

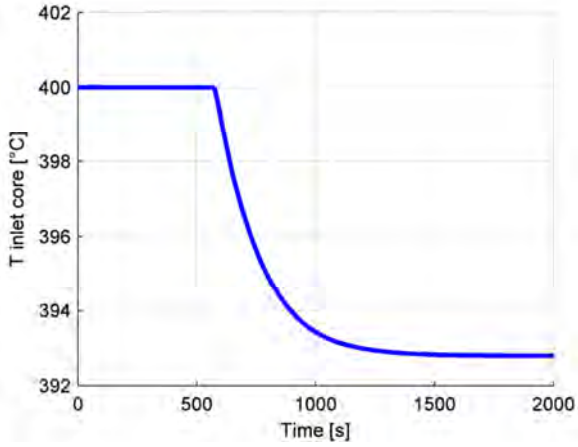


**Figure 153. Coolant core inlet temp. variation following a 10 % water enhancement of water mass flow rate.**

In fact, even though a lower steam temperature is obtained, the increase of water mass flow rate leads to an enhancement of the power globally exchanged in the SG (Fig. 152), eventually bringing to a colder lead temperature, since the primary mass flow rate is kept constant. The effect of having coupled the SG with the core is evident after 70 s, when a gentler slope in the parameters decrease (for water and lead temperatures, and superheated length) or increase (sub-cooled and two-phase lengths) is observed. The primary coolant at the SG outlet is then mixed with the hotter lead contained in the pool, inducing a lower core inlet temperature (Fig. 153), delayed and moderated (see Fig. 150 for the comparison). After 70 s a colder lead begins to flow into the core: an insertion of positive reactivity due to both the radial and coolant density negative feedback coefficients (Figs. 154 and 155) occurs, bringing an enhancement of power (Fig. 156) and fuel temperature (Fig. 157), whose increase counterbalances the positive reactivity insertion thanks to the Doppler effect.

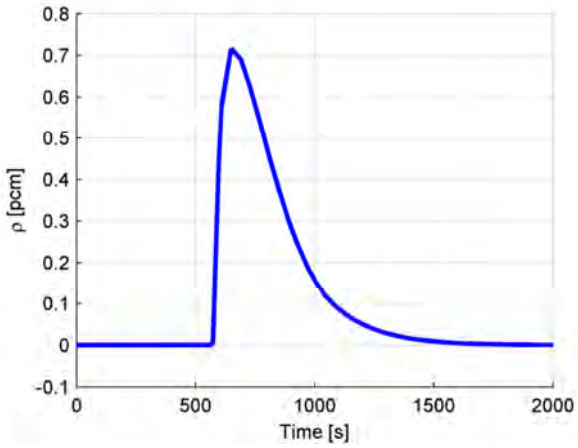


**Figure 154. Reactivity global variation following a 10 % enhancement of water mass flow rate.**

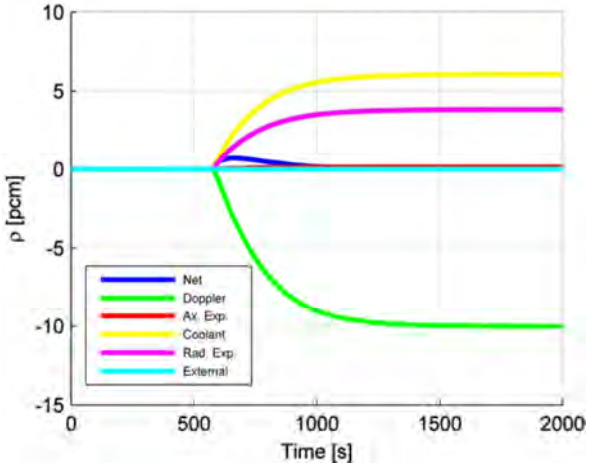


**Figure 155. Reactivity components variation following a 10 % enhancement of water mass flow rate.**

Nevertheless, the outlet lead temperature undergoes a decrease, even if smaller than the inlet perturbation, and consequently colder lead is delivered to the SG. This explains the different slope in the second part of the transient: the behavior of the SG subject to a decrease of the primary coolant inlet temperature is characterized by a decrease of power, that compensates for the increase of the exchanged power due to the water mass flow rate enhancement . A decrease of both water and lead temperatures, and superheated length are then combined with the behavior brought the initial perturbation but with different rapidity of transient.

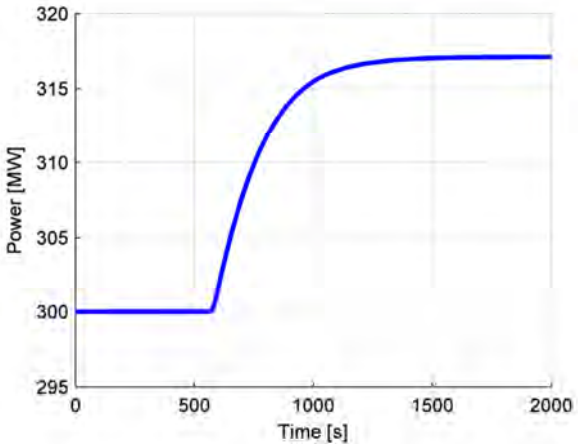


**Figure 156. Core power variation following a 10 % enhancement of water mass flow rate.**

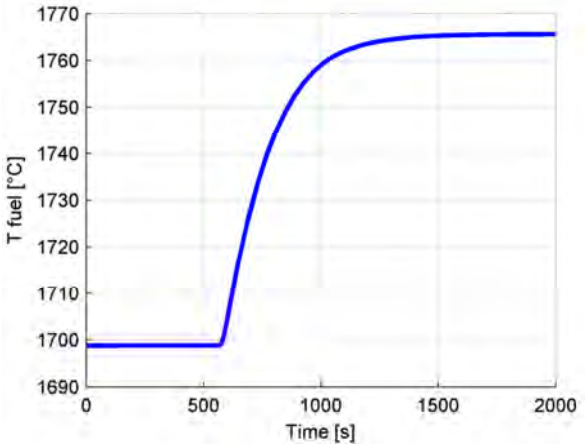


**Figure 157. Fuel temperature variation following a 10 % enhancement of water mass flow rate.**

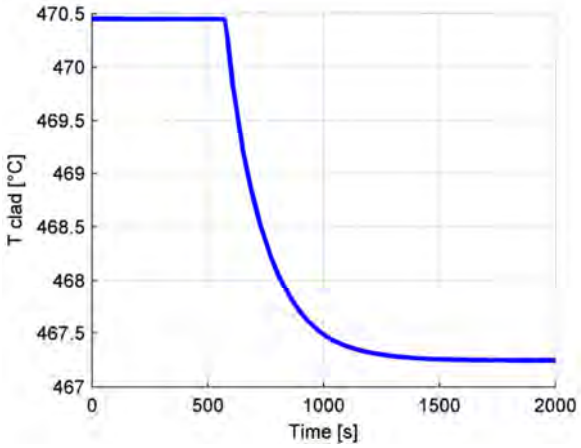


**Figure 158. Cladding temperature variation following a 10 % enhancement of water mass flow rate.**

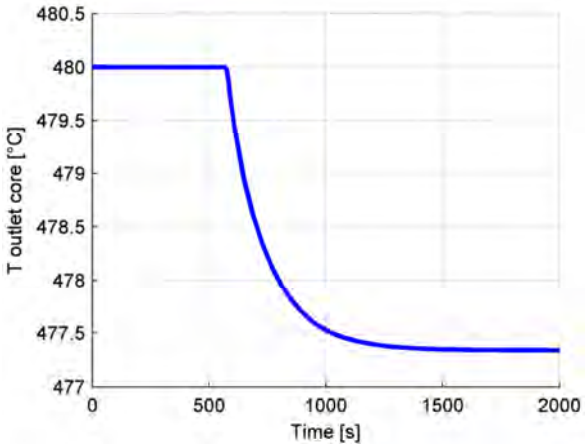


**Figure 159. Coolant core outlet temperature variation following a 10 % enhancement of water mass flow rate.**

Table XXXVIII resumes the main plant parameters at the end of the transient.

**Table XXXVIII. Results after water mass flow rate positive variation.**

| **Water mass flow variation: + 18.56 kg $s^{-1}$** | | | |
|---|---|---|---|
| **Core** | | Variation | % Variation |
| Power [MW] | 317.1 | +17.1 | +5.7 % |
| Fuel temperature [°C] | 1766 | +67 | +3.79 % |
| Cladding temperature [°C] | 467.2 | -3.2 | -0.68 % |
| Coolant in temperature [°C] | 392.8 | -7.2 | -1.8 % |
| Mean coolant temperature [°C] | 435.1 | -4.9 | -1.11 % |
| Coolant out temperature [°C] | 477.3 | -3.7 | -0.77 % |
| **Steam generator** | | | |
| Sub-cooled length [m] | 8.854 | 1.768 | +24.95 % |
| Two-phase length [m] | 18.65 | 2.65 | +16.56 % |
| Superheated length [m] | 27.50 | -4.41 | -13.82 % |
| *Lead temperature* | | | |
| Inlet [°C] | 477.3 | -3.7 | -0.77 % |
| Superheated region [°C] | 460.2 | -2.8 | -0.60 % |
| Two-phase region [°C] | 424.3 | -4.3 | -1 % |
| Sub-cooled region [°C] | 399.1 | -6.5 | -1.6 % |
| Outlet [°C] | 392.8 | -7.2 | -1.8 % |
| *Wall temperature* | | | |
| Sub-cooled region [°C] | 369.5 | -3.2 | -0.86 % |
| Two-phase region [°C] | 382.5 | -1.4 | -0.36 % |
| Superheated region [°C] | 434.8 | -6.4 | -1.45 % |
| *Water temperature* | | | |
| Inlet [°C] | 335.0 | 0 | 0 % |
| Sub-cooled region [°C] | 348.1 | +0.2 | +0.06 % |
| Two-phase region [°C] | 361.2 | +0.4 | +0.11 % |
| Superheated region [°C] | 407.2 | -8.2 | +1.97 % |
| Water outlet temperature [°C] | 453.2 | -16.8 | -3.57 % |
| Pressure [bar] | 189.3 | 0.9 | +0.45 % |

*Inlet water temperature variation*

A 1 °C $s^{-1}$ ramp is imposed for 10 s, obtaining a final 10 °C total enhancement of the feedwater temperature at the SG inlet.

Also in this scenario the presence of the pool causes the transient to be determined by the superposition of two different dynamic behaviors: the first, similar to that of the stand-alone SG simulation, and the second affected by the feedback of the core, mainly due to the primary coolant temperature variation. Two thousand seconds are required also in this case to reach the new steady-state values.

After the feedwater inlet temperature enhancement , the sub-cooled length decreases (Fig. 160). As shown in Fig. 163, pressure, neglecting some numerical oscillations, does not exhibit any change following this perturbation, while a longer superheated zone is obtained (Fig. 162), as well as a slightly reduced two-phase length (Fig. 161).

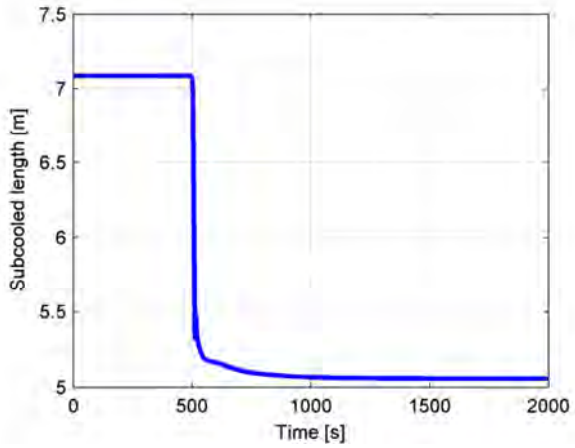


**Figure 160. Sub-cooled length variation in the SG following a 10 °C enhancement of water inlet temperature.**

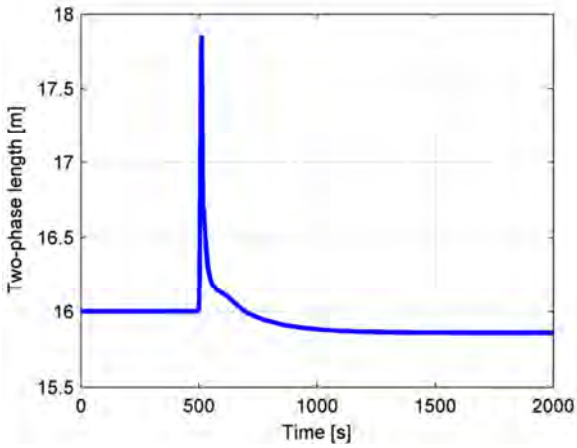


**Figure 161. Two-phase length variation in the SG following a 10 °C enhancement of water inlet temperature.**

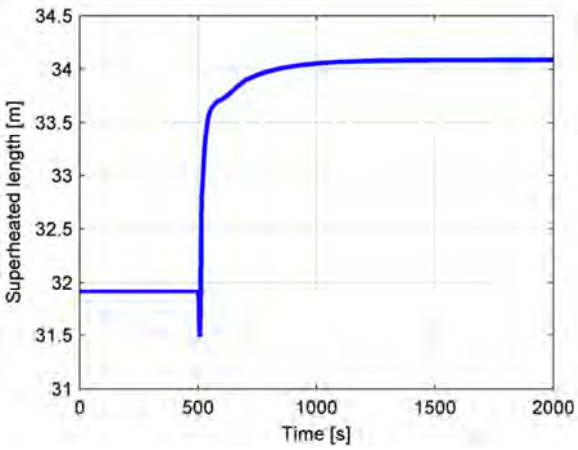


**Figure 162. Superheated length variation in the SG following a 10 °C enhancement of water inlet temperature.**

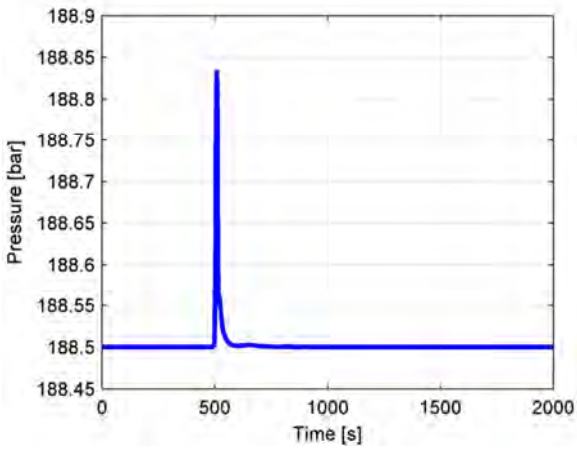


**Figure 163. SG pressure variation in the SG following a 10 °C enhancement of water inlet temperature.**

As a consequence of a higher inlet temperature, also a higher outlet steam temperature is reached, but by a minor amount (Fig. 164). This is due to the reduced temperature gap between primary and secondary fluids, which

causes the heat exchange worsening, noticeable in the higher outlet lead temperature depicted in Fig. 165 and in the SG power decrease in Fig. 166.

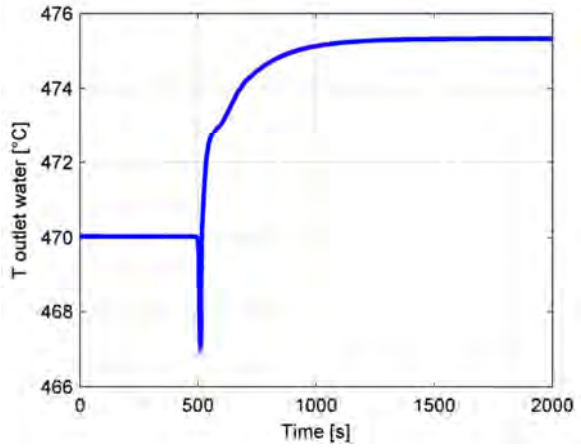


**Figure 164. Steam outlet temperature variation in the SG following a 10 °C enhancement of water inlet temperature.**

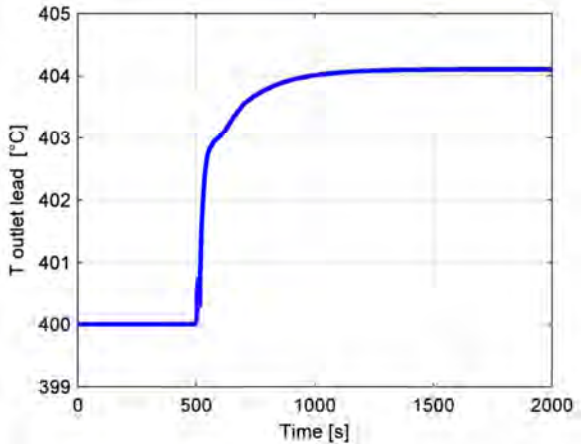


**Figure 165. Lead SG outlet temperature variation following a 10 °C enhancement of water inlet temperature.**

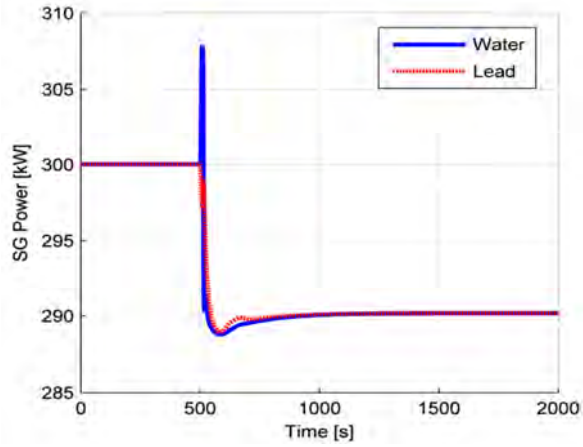


**Figure 166. SG power variation following a 10 °C enhancement of water inlet temperature.**

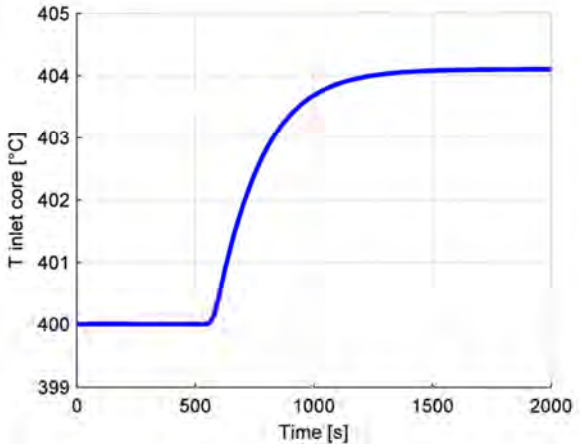


**Figure 167. Coolant core inlet temperature variation following a 10 °C enhancement of water inlet temperature.**

As in the previous case, the delaying and gentling action of the pool on the lead core inlet temperature is observed. After covering the distance from the SG outlet to the core inlet, the hotter lead enters the active core (Fig. 167), bringing a negative reactivity insertion, as shown in Fig. 168, primarily due to the radial and coolant density coefficients depicted in Fig. 169. Also in this case these coefficients are the main contributors to the reactivity variation in the system following a change in the SG conditions.

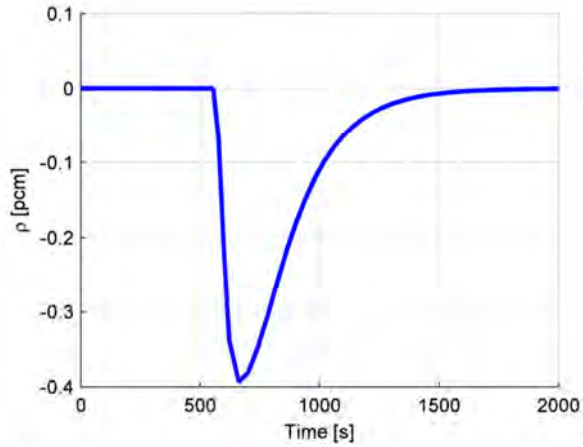


**Figure 168. Reactivity global variation following a 10 °C enhancement of water inlet temperature.**

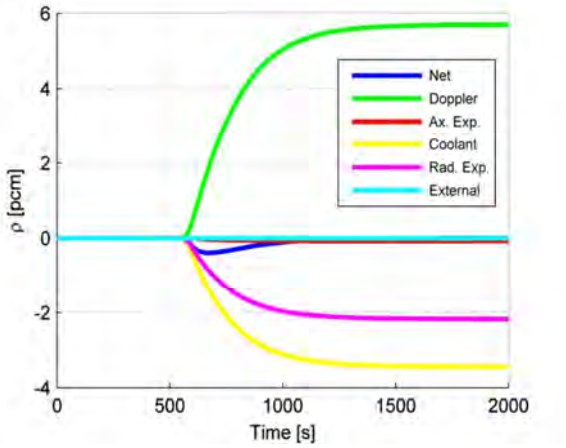


**Figure 169. Reactivity components variation following a 10 °C enhancement of water inlet temperature.**

Following the negative reactivity insertion, the core power decreases (Fig. 170) until the Doppler effect, due to the decreasing fuel temperature (Fig. 171), counterbalances the previous reactivity decrease with a positive contribution, finally reinstating criticality, as shown in Fig. 169.

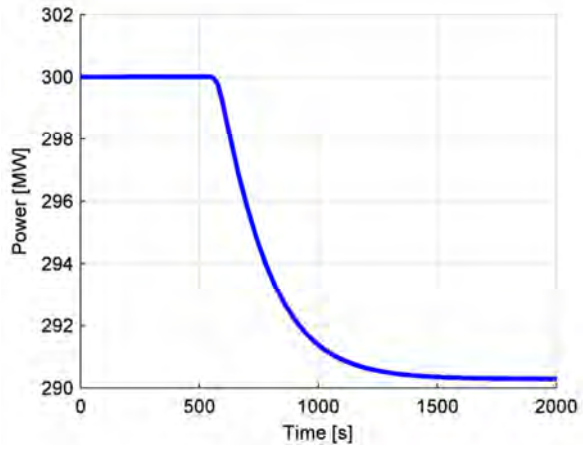


**Figure 170. Core power variation following a 10 °C enhancement of water inlet temperature.**

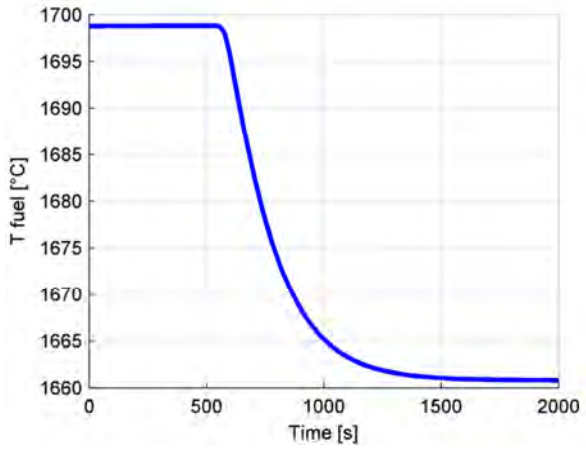


**Figure 171. Fuel temperature variation following a 10 °C enhancement of water inlet temperature.**

As a consequence of the reduced thermal power generated within the core, the coolant temperature at the core outlet shows a minor enhancement compared with the one at the core inlet (Fig. 172), but still accountable for the feedback at the SG inlet, which initiates the second part of the transient.

The lead temperature rise at the SG inlet explains the small increase of power after 570 s (Fig. 166). Actually, a temperature enhancement on the SG primary side leads to an increase of the exchanged power, that meanwhile entails an increase of both steam and lead temperatures, but with a slower dynamics which overlays the trend given from the increase of water temperature.

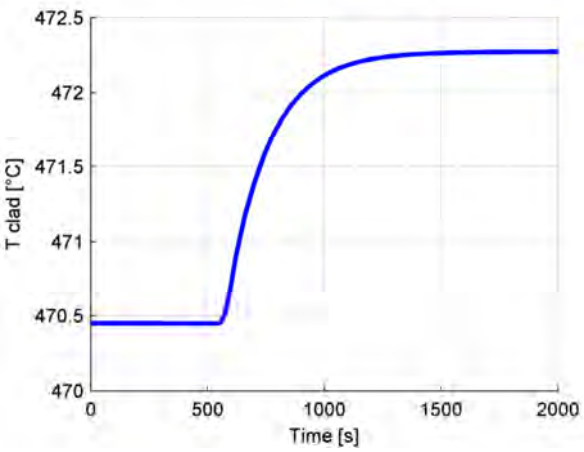


**Figure 172. Cladding temperature variation following a 10 °C enhancement of water inlet temperature.**

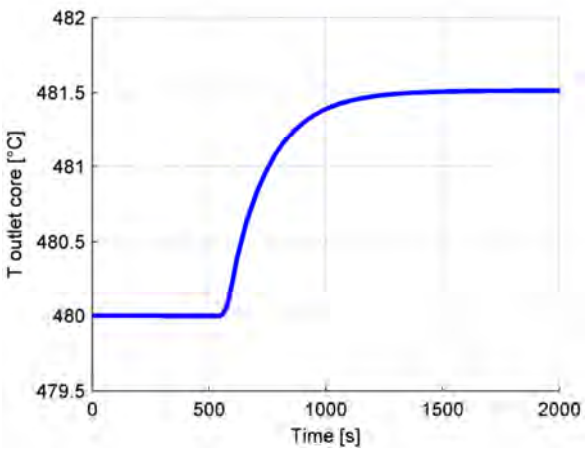


**Figure 173. Coolant core outlet temperature variation following a 10 °C enhancement of water inlet temperature.**

Table XXXIX resumes the main plant values at the end of the transient.

**Table XXXIX. Results after feedwater temperature positive variation.**

| **Feedwater temperature: +10 °C** | | | |
|---|---|---|---|
| **Core** | | Variation | % Variation |
| Power [MW] | 290.3 | -9.7 | -3.23 % |
| Fuel temperature [°C] | 1661 | -38 | -2.24 % |
| Cladding temperature [°C] | 472.3 | +1.9 | +0.40 % |
| Coolant in temperature [°C] | 404.1 | +4.1 | +1.03 % |
| Mean coolant temperature [°C] | 442.8 | +2.8 | +0.64 % |
| Coolant out temperature [°C] | 481.5 | +1.5 | +0.31 % |
| **Steam generator** | | | |
| Sub-cooled length [m] | 5.057 | -2.029 | -28.63 % |
| Two-phase length [m] | 15.86 | -0.14 | -0.88 % |
| Superheated length [m] | 34.09 | +2.18 | +6.83 % |
| *Lead temperature* | | | |
| Inlet [°C] | 481.5 | +1.5 | +0.31 % |
| Superheated region [°C] | 464.1 | +1.1 | +0.24 % |
| Two-phase region [°C] | 429.2 | +0.6 | +0.14 % |
| Sub-cooled region [°C] | 408.0 | +2.4 | +0.59 % |
| Outlet [°C] | 404.1 | +4.1 | +1.03 % |
| *Wall temperature* | | | |
| Sub-cooled region [°C] | 376.2 | +3.5 | +0.94 % |
| Two-phase region [°C] | 384.1 | +0.2 | +0.05 % |
| Superheated region [°C] | 443.1 | +1.9 | +0.43 % |
| *Water temperature* | | | |
| Inlet [°C] | 345.0 | +10 | +2.98 % |
| Sub-cooled region [°C] | 352.9 | +5 | +1.44 % |
| Two-phase region [°C] | 360.8 | 0 | 0 % |
| Superheated region [°C] | 418.1 | +2.7 | +0.65 % |
| Water outlet temperature [°C] | 475.3 | +5.3 | +1.13 % |
| Pressure [bar] | 188.5 | 0 | 0 % |

*Turbine admission valve coefficient variation*

In order to study the system behavior following a change on the electrical request, a 10 % enhancement of the turbine admission valve flow coefficient is performed.

Once again the transient is influenced by the presence of the pool and the respective delay. Also in this case, the simulation starts with a direct perturbation on the SG: in particular the simulated opening of the turbine admission valve leads to a depressurization of the system. The dynamics is very close to the one seen in the stand-alone simulation for the first 70 seconds, whereas after the core inlet temperature starts decreasing and the relative dynamics leads to a new coolant core outlet temperature, a feedback on the SG is given by a reduced lead inlet temperature. In this second part of the transient SG and core are tightly coupled with reciprocal feedbacks. After 1500 s from the initial step, the steady-state is reached.

The first consequence of a step increase of the turbine admission valve coefficient is the almost instantaneous decrease of pressure in the SG tube (Fig. 174). After depressurization, the saturation temperature decreases with the same trend and, because of the closer gap between inlet and two-phase temperature, a shorter sub-cooled length ensues (Fig. 175), associated with a slight increase of the two-phase region and a very faint decrease of the superheated zone, described in Fig. 176 and 177, respectively.

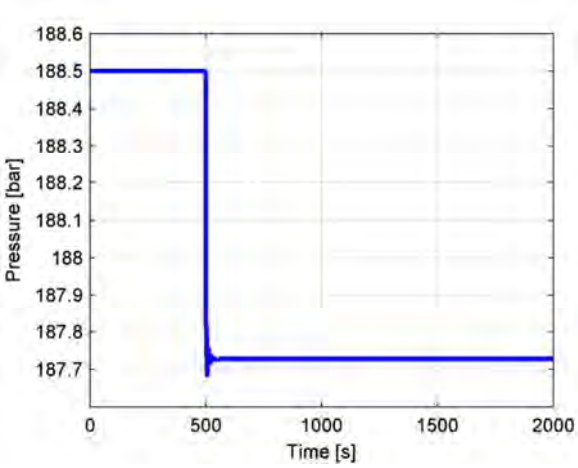


**Figure 174. Pressure variation in the SG following a 10 % enhancement of turbine admission valve coefficient.**

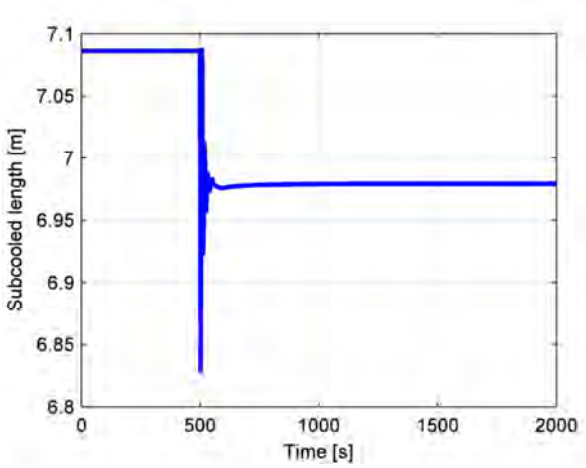


**Figure 175. Sub-cooled length variation in the SG following a 10 % enhancement of turbine admission valve coefficient.**

The main consequence of depressurization is an increase of the outlet steam temperature (Fig. 179), even though at lower pressure. On the whole, lead is subject to different heat exchange conditions, and consequently decreases its outlet temperature, as described in Fig. 178, since the lower water temperatures in the sub-cooled and two-phase regions favor a greater power transfer from the primary fluid to the secondary one. No significant effects are provided by the core feedback, probably due to the slight perturbation applied.

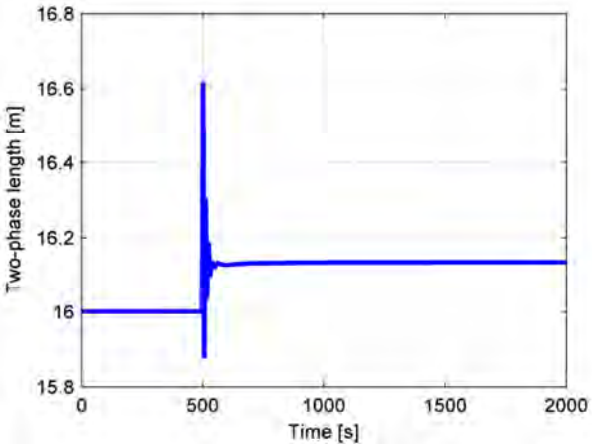


**Figure 176. Two-phase length variation in the SG following a 10 % enhancement of turbine admission valve coefficient.**

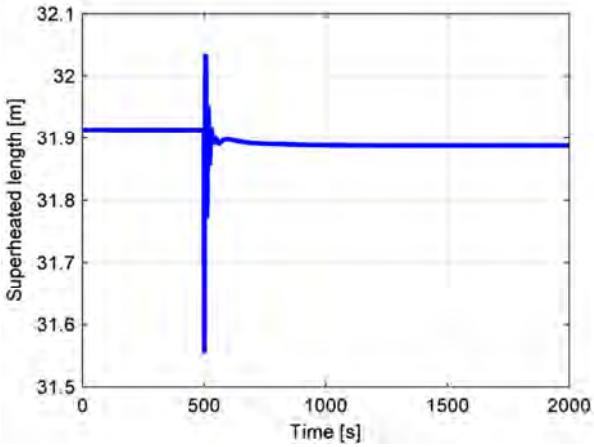


**Figure 177. Superheated length variation in the SG following a 10 % enhancement of turbine admission valve coefficient.**

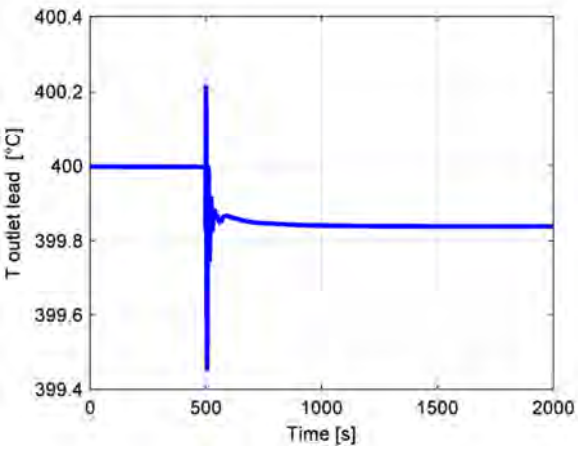


**Figure 178. Lead SG outlet temp. variation following a 10 % enhancement of turbine admission valve coefficient.**

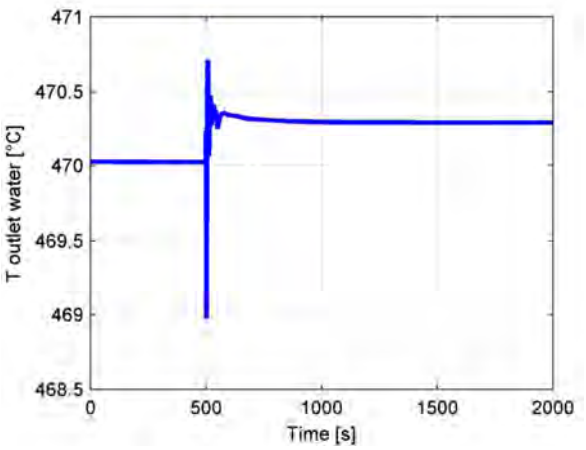


**Figure 179. Steam outlet temp variation in the SG following a 10 % enhancement of turbine admission valve coefficient.**

The core perceives the change in the SG conditions simply as a decrease of inlet coolant temperature (Fig. 180), and its response is typical of this kind of scenarios: a positive reactivity insertion occurs due to both coolant and expansion coefficients, as depicted in Figs. 181 and 182.

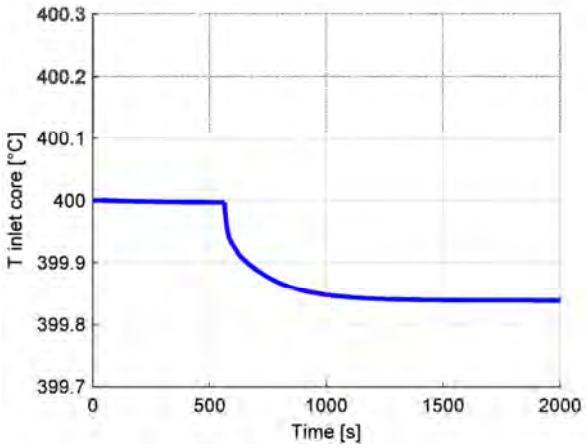


**Figure 180. Coolant core inlet temp. variation following a 10 % enhancement of turbine admission valve coefficient.**

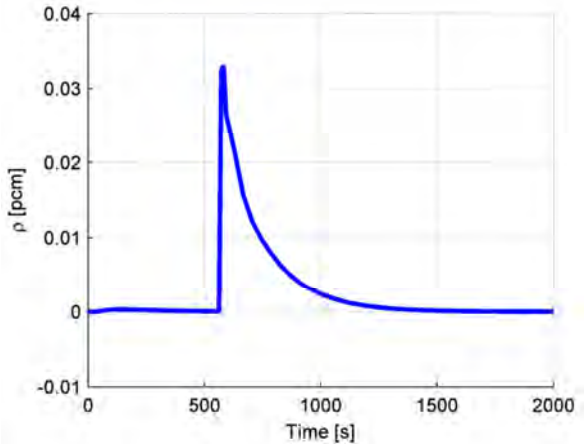


**Figure 181. Global reactivity variation following a 10 % enhancement of turbine admission valve coefficient.**

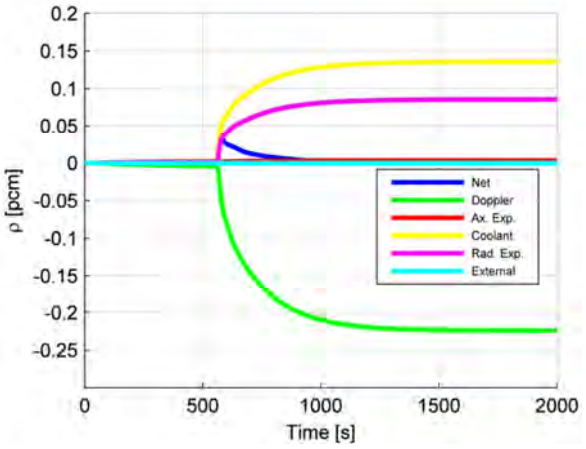


**Figure 182. Reactivity components variation following a 10 % enhancement of turbine admission valve coefficient.**

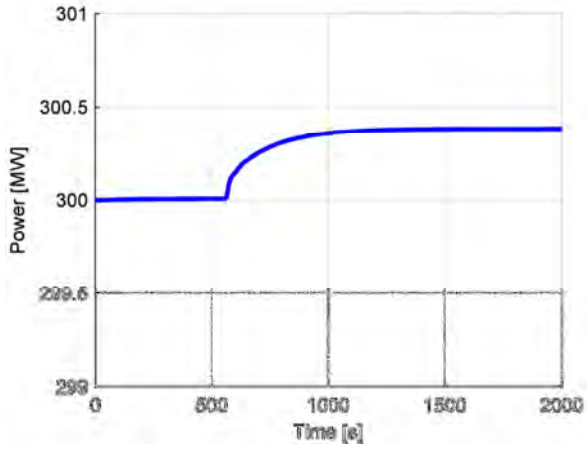


**Figure 183. Core power variation following a 10 % enhancement of turbine admission valve coefficient.**

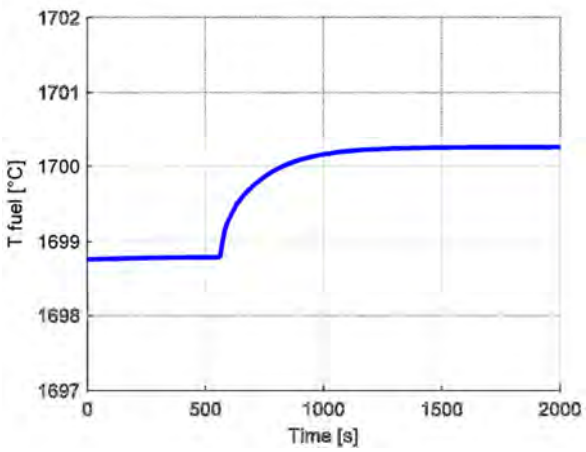


**Figure 184. Fuel temperature variation following a 10 % enhancement of turbine admission valve coefficient.**

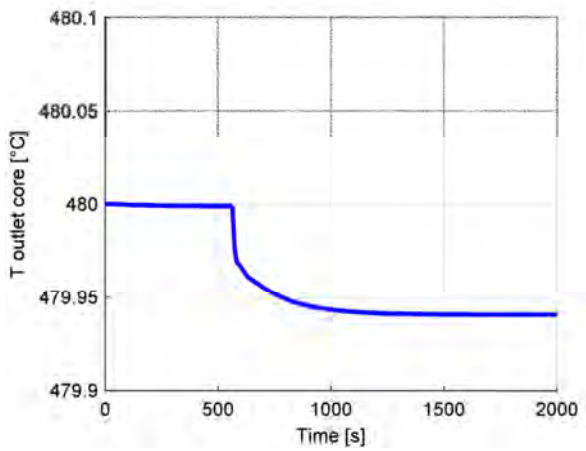


**Figure 185. Coolant outlet temperature variation following a 10 % enhancement of turbine admission valve coefficient.**

The ensuing power increase (Fig. 183) is stabilized by the Doppler effect brought by the concurrent increase of fuel temperature, shown in Fig. 184. Subsequently, a decrease of the lead core outlet temperature is expected (Fig. 185). Anyway, this last variation does not affect the SG behavior in an appreciable way.
Table XL resumes the main plant variables at the end of the transient.

**Table XL. Results after variation of turbine admission valve coefficient.**

| **Coefficient of turbine admission: +10%** | | | |
|---|---|---|---|
| **Core** | | Variation | % Variation |
| Power [MW] | 300.4 | +0.4 | +0.13 % |
| Fuel temperature [°C] | 1700 | +1 | +0.06 % |
| Cladding temperature [°C] | 470.4 | 0 | 0 % |
| Coolant in temperature [°C] | 399.8 | -0.2 | -0.05 % |
| Mean coolant temperature [°C] | 439.9 | -0.1 | -0.02 % |
| Coolant out temperature [°C] | 479.9 | -0.1 | -0.02 % |
| **Steam generator** | | | |
| Sub-cooled length [m] | 6.979 | -0.107 | -1.51 % |
| Two-phase length [m] | 16.13 | +0.13 | +0.81 % |
| Superheated length [m] | 31.89 | -0.02 | --0.06 % |
| *Lead temperature* | | | |
| Inlet [°C] | 479.9 | -0.1 | -0.02 % |
| Superheated region [°C] | 463.0 | 0 | 0 % |
| Two-phase region [°C] | 428.5 | -0.1 | -0.2 % |
| Sub-cooled region [°C] | 405.4 | -0.2 | -0.05 % |
| Outlet [°C] | 399.8 | -0.2 | -0.05 % |
| *Wall temperature* | | | |
| Sub-cooled region [°C] | 372.5 | -0.2 | -0.05 % |
| Two-phase region [°C] | 383.6 | -0.3 | -0.08 % |
| Superheated region [°C] | 441.2 | 0 | 0 % |
| *Water temperature* | | | |
| Inlet [°C] | 335.0 | 0 | 0 % |
| Sub-cooled region [°C] | 347.7 | -0.2 | -0.06 % |
| Two-phase region [°C] | 360.5 | -0.3 | -0.08 % |
| Superheated region [°C] | 415.4 | 0 | 0 % |
| Water outlet temperature [°C] | 470.3 | +0.3 | +0.07 % |
| Pressure [bar] | 187.7 | -0.8 | -0.42 % |

*Lead mass flow rate variation*

The following figures refer to a 10 % stepwise enhancement of lead mass flow rate in the primary loop.
This simulation is quite different from the previous two, since it does not regard the secondary side of the SG and the perturbation involves both sub-systems at the same time: differently from the water-side simulations, in which perturbations act first on the SG and then on the core, a change in the lead mass flow rate affects simultaneously both core and SG. In addition, the feedback due to both a higher lead temperature at the SG outlet(due to the flow enhancement) and a colder coolant at the core outlet have to be considered. The steady-state is reached after two thousand seconds.
For what concerns the SG, an enhancement of lead mass flow rate leads to a raise of lead temperatures, in particular at the SG outlet (Fig. 186). As a consequence of the higher temperature of the primary fluid, the heat exchange is improved, causing a sudden (but temporary) enhancement of the exchanged power, as shown in Fig. 187.

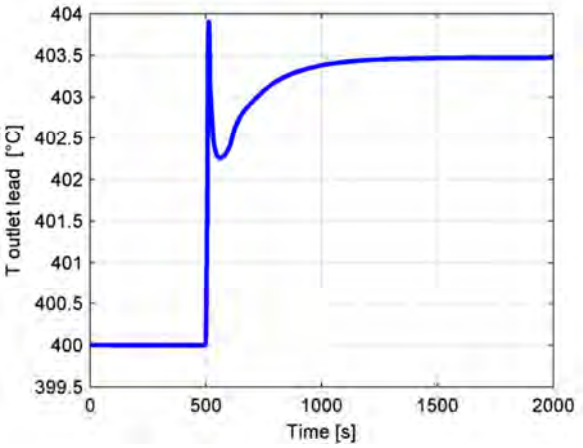


**Figure 186. Lead SG outlet temperature variation following a 10 % enhancement of lead mass flow rate.**

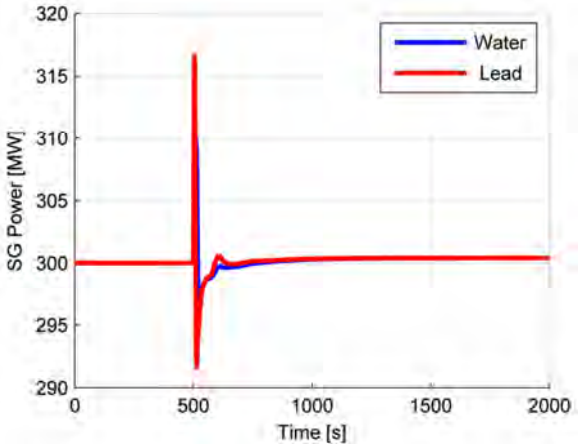


**Figure 187. SG power variation following a 10 % enhancement of lead mass flow rate.**

On the water side, this change leads to a decrease in the sub-cooled and two-phase lengths (Figs. 188 and 189), and to a consequent increase of the superheated region and of the steam outlet temperature, as described respectively in Figs. 190 and 192; pressure (Fig. 191) does not change since in the present model it does not result affected by changes on the lead side. This is the trend expected for a stand-alone SG simulation, but the system is now coupled with the core: at the same time of the flow perturbation colder coolant coming from the core outlet starts entering the SG as well because of the enhancement of lead mass flow rate through the core.

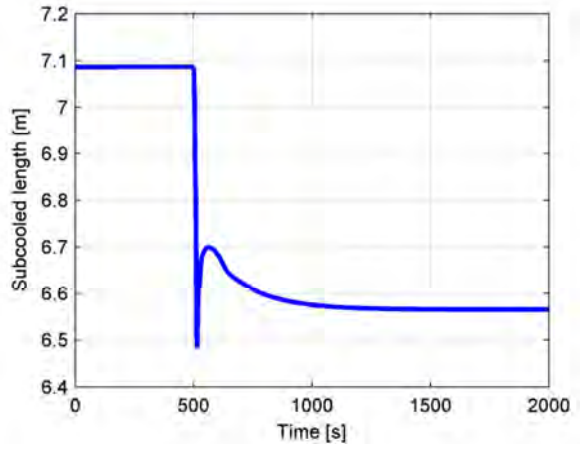


**Figure 188. Sub-cooled length variation in the SG following a 10 % enhancement of lead mass flow rate.**

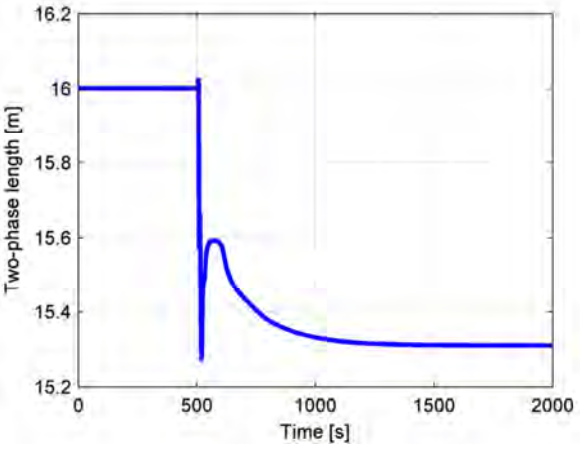


**Figure 189. Two-phase length variation in the SG following a 10 % enhancement of lead mass flow rate.**

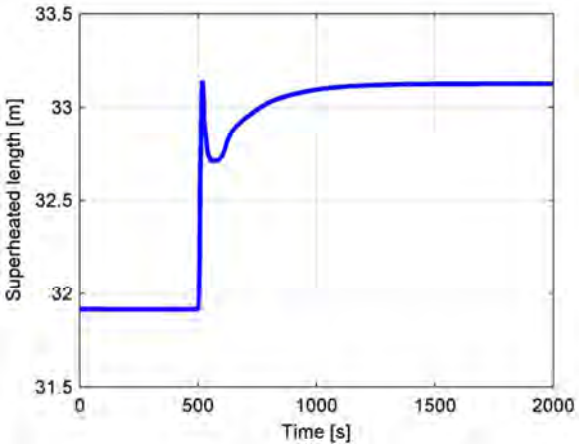


**Figure 190. Superheated length variation in the SG following a 10 % enhancement of lead mass flow rate.**

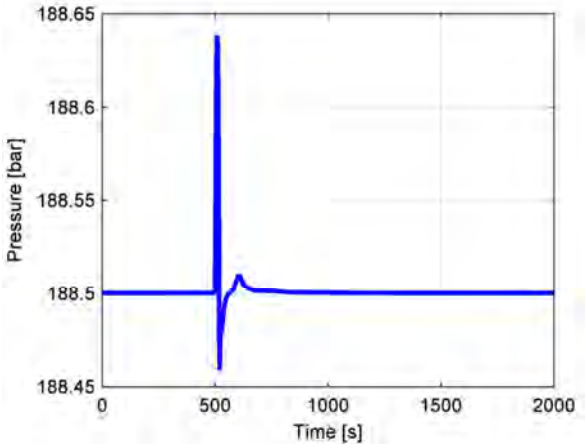


**Figure 191. Pressure variation in the SG following a 10 % enhancement of lead mass flow rate.**

Because of the superposition of these two perturbations – an enhancement of lead mass flow rate and a contemporary decrease of its temperature at the SG inlet – greater oscillations characterize the first seconds of the transient. Furthermore, these variations act in a mutually opposite way on the SG.

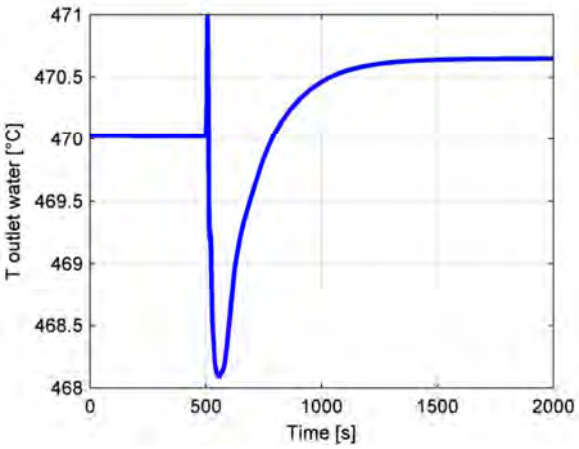


**Figure 192. Steam outlet temp. variation in the SG following a 10 % enhancement of lead mass flow rate.**

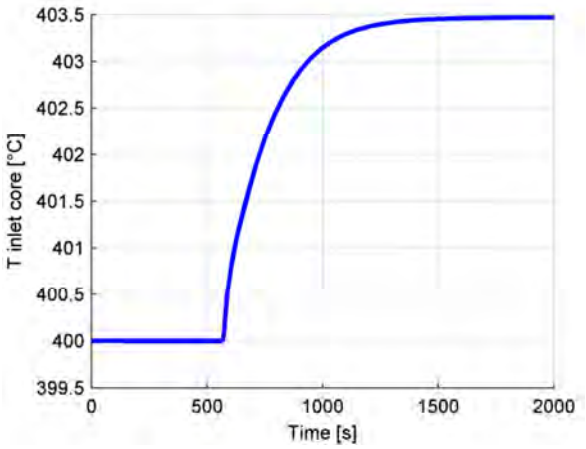


**Figure 193. Coolant core inlet temperature variation following a 10 % enhancement of lead mass flow rate.**

Concerning the core, the situation is similar even though the perturbation due to the hotter inlet coolant temperature is delayed and smoothed by the presence of the pool, whose effects can be clearly seen in Fig. 193. After the flow step, the first effect is a sudden reduction of the average and outlet coolant temperatures (Fig. 194), due to the excess of coolant mass flow rate flowing through the core. A similar behavior is noticeable for the cladding temperature (Fig. 195), which is accountable, together with the reduced coolant temperature, for a positive reactivity insertion (Fig. 196), primarily due to the negative coolant density, and radial and axial

expansion coefficients (Fig. 197). Following this reactivity insertion, the power and consequently the fuel temperature increase, causing a prompt reactivity decrease due to the Doppler effect.

These are the phenomena occurring in the first part of the transient, before any feedback is given by the SG.

After 70 s, a hotter coolant begins to flow into the core, providing the immediate decrease of reactivity (coolant density, radial and axial expansion feedbacks), which combines with the negative effect of Doppler. In this way, a slow but significant inversion of trend is found in the core power and fuel temperature, while coolant and clad temperature exhibit a steeper rise, with consequent stabilizing effect on reactivity, which returns to zero. In conclusion, it is evident that even for the core both the transient response and steady state are the result of a compromise between two opposite trends; in particular the behavior induced by the lead mass flow rate enhancement is strongly scaled down by the increase of the core inlet temperature due to the SG feedback.

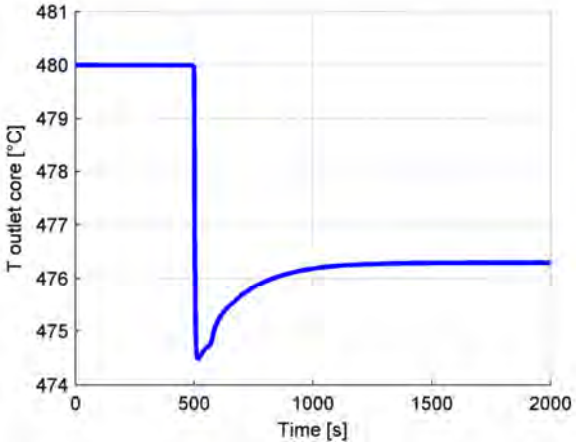


**Figure 194. Coolant core outlet temperature variation following a 10 % enhancement of lead mass flow rate.**

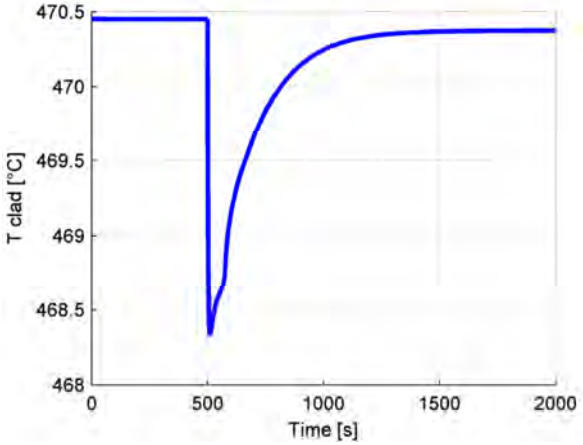


**Figure 195. Cladding temperature variation following a 10 % enhancement of lead mass flow rate.**

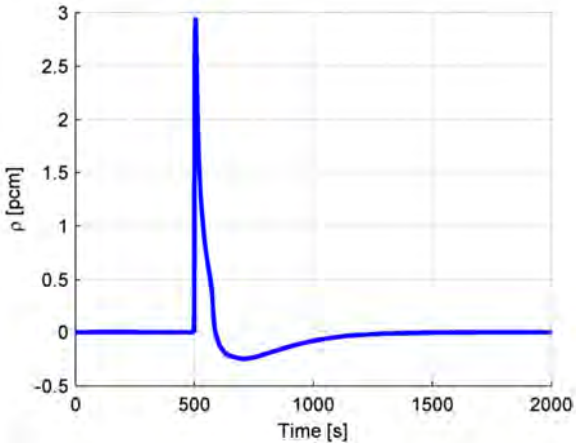


**Figure 196. Global reactivity variation following a 10 % enhancement of lead mass flow rate.**

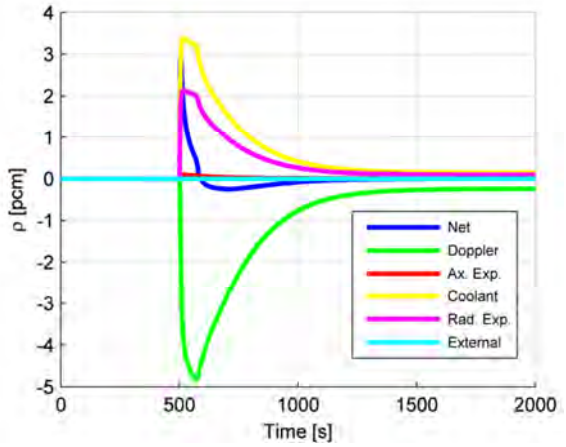


**Figure 197. Reactivity components variation following a 10 % enhancement of lead mass flow rate.**

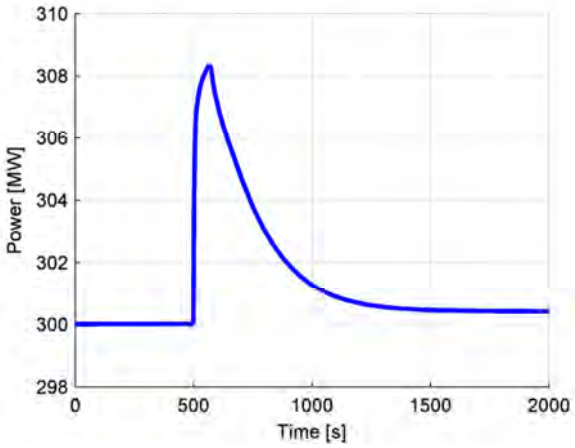


**Figure 198. Core power variation following a 10 % enhancement of lead mass flow rate.**

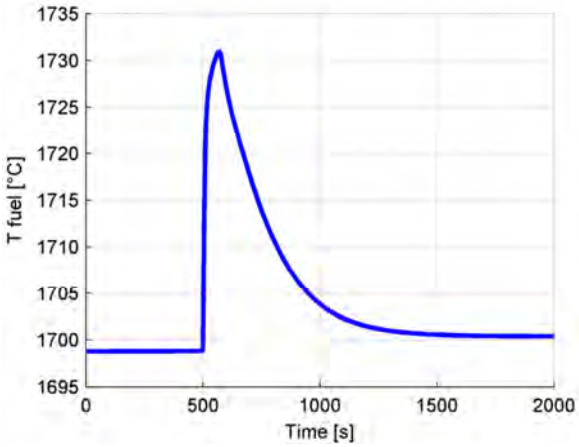


**Figure 199. Fuel temperature variation following a 10 % enhancement of lead mass flow rate.**

Table XLI resumes the main plant variables at the end of the transient.

**Table XLI. Results after lead mass flow rate positive variation.**

| **Lead mass flow rate: +2576 kg $s^{-1}$** | | | |
|---|---|---|---|
| **Core** | | Variation | % Variation |
| Power [MW] | 300.4 | +0.4 | +0.13 % |
| Fuel temperature [°C] | 1700 | +1 | +0.06 % |
| Cladding temperature [°C] | 470.4 | 0 | 0 % |
| Coolant in temperature [°C] | 403.5 | +3.5 | +0.88 % |
| Mean coolant temperature [°C] | 439.9 | -0.1 | -0.02 % |
| Coolant out temperature [°C] | 476.3 | -3.7 | -0.77 % |
| **Steam generator** | | | |
| Sub-cooled length [m] | 6.565 | -0.521 | -7.35 % |
| Two-phase length [m] | 15.31 | -0.69 | -4.31 % |
| Superheated length [m] | 33.13 | +1.22 | +3.91 % |
| *Lead temperature* | | | |
| Inlet [°C] | 476.3 | -3.7 | -0.77 % |
| Superheated region [°C] | 460.8 | -2.2 | -0.48 % |
| Two-phase region [°C] | 429.5 | +0.9 | +0.21 % |
| Sub-cooled region [°C] | 408.6 | +3 | +0.74 % |
| Outlet [°C] | 403.5 | +3.5 | +0.88 % |
| *Wall temperature* | | | |
| Sub-cooled region [°C] | 374.6 | +1.9 | +0.51 % |
| Two-phase region [°C] | 384.9 | +1 | +0.26 % |
| Superheated region [°C] | 440.7 | -0.5 | -0.11 % |
| *Water temperature* | | | |
| Inlet [°C] | 335.0 | 0 | 0 % |
| Sub-cooled region [°C] | 347.9 | 0 | 0 % |
| Two-phase region [°C] | 360.8 | 0 | 0 % |
| Superheated region [°C] | 415.7 | +0.3 | +0.07 % |
| Water outlet temperature [°C] | 470.6 | +0.6 | +0.88 % |
| Pressure [bar] | 188.5 | 0 | 0 % |

***Reactivity variation***

An extraction of control rods corresponding to a 20 pcm (0.06 $) step variation is considered in this transient case.

This is the unique simulation achievable by acting directly on the core inputs: in fact, after coupling the two main systems of the loop, both lead mass flow rate and temperature are defined by the system conditions and cannot act as inputs any longer. The only way to perturb the core is moving the control rods, with the consequent insertion of reactivity, either positive or negative. This core-driven simulation gives an immediate feedback to the SG, due to the coolant core outlet temperature enhancement which rebounds on the SG with an increase of the inlet lead temperature. Thanks to the presence of the pool, the action of the SG on the core, operated by an increase of the core inlet temperature, is delayed and gentled. The steady-state is reached after 1500 seconds.

For the first part of transient, the behavior of the core is the same as the stand-alone model. In fact, after the step-wise insertion of reactivity given by control rods (Figs. 200 and 201) the power suddenly increases with the prompt jump and, after a small decrease, starts reaching the steady-state.

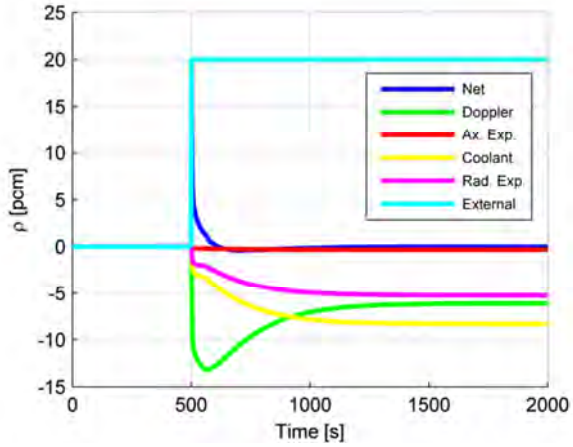


**Figure 200. Reactivity components variation following a 20 pcm reactivity insertion.**

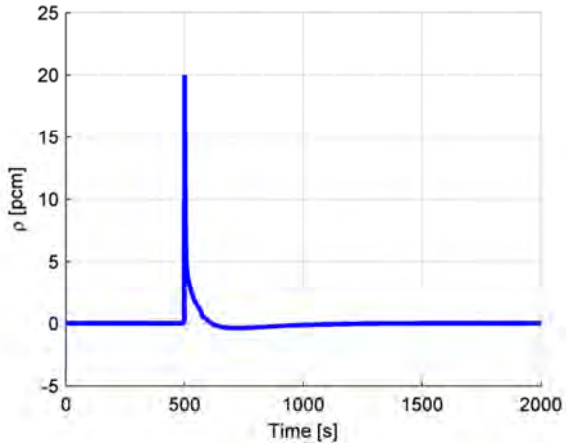


**Figure 201. Global reactivity variation following a 20 pcm reactivity insertion.**

With the power enhancement, fuel, cladding and coolant temperatures increase, giving a negative contribution to reactivity finally reinstating criticality.

Then, the lead core outlet temperature increase initiates the transient on the SG side (Figs. from 203 to 205).

For what regards the SG transient, this component experiences the reactivity insertion in the core as an enhancement of lead temperature at its inlet, very similar to a stepwise perturbation. For this reason many oscillations characterize the beginning of the transient, but after few seconds they are smoothed out and a clear trend is obtained.

As an immediate consequence, a better heat exchange occurs due to the hotter primary fluid, with consequent reduction of both the sub-cooled and two-phase lengths, and corresponding enlargement of the superheated region (Figs. 206 and 207). A change on the primary side of the SG does not affect pressure inside the tubes (neglecting some initial oscillations, Fig. 209).

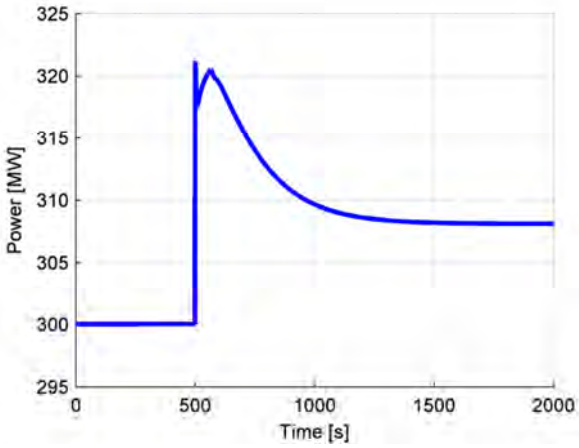


**Figure 202. Core power variation following a 20 pcm reactivity insertion.**

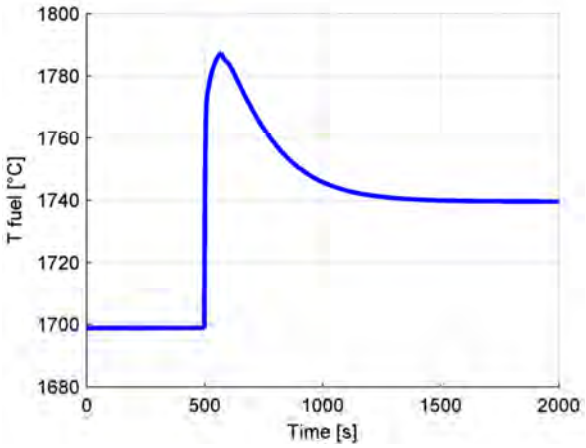


**Figure 203. Fuel temperature variation following a 20 pcm reactivity insertion.**

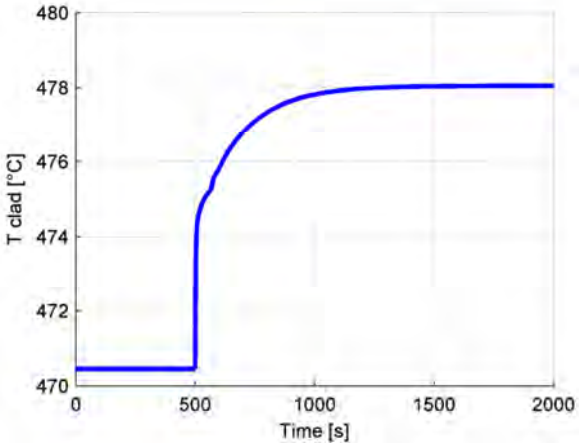


**Figure 204. Cladding temperature variation following a 20 pcm reactivity insertion.**

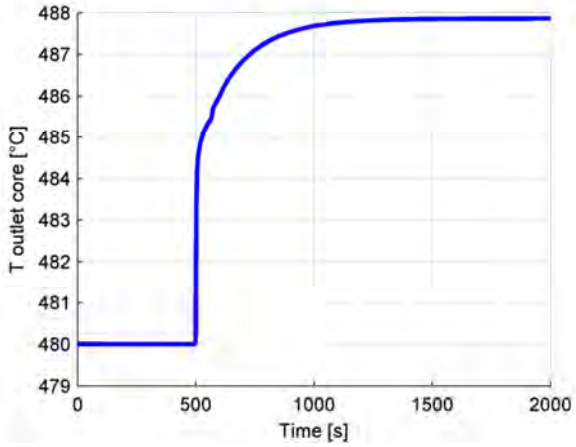


**Figure 205. Coolant core outlet temperature variation following a 20 pcm reactivity insertion.**

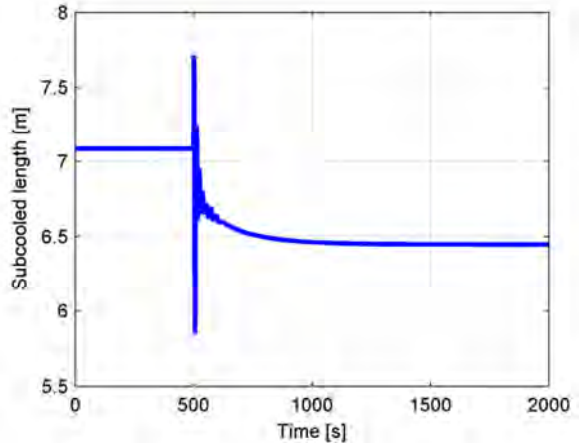


**Figure 206. Sub-cooled length variation in the SG following a 20 pcm reactivity insertion.**

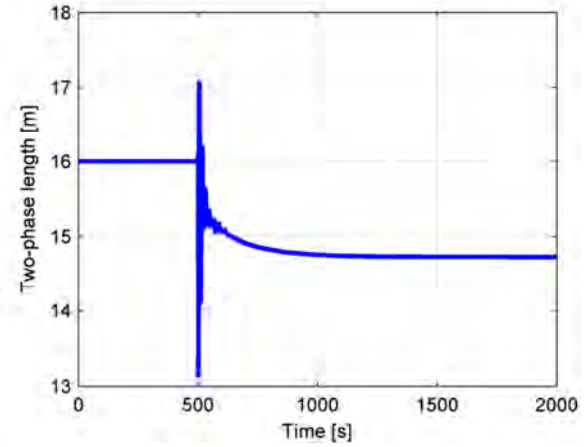


**Figure 207. Two-phase length variation in the SG following a 20 pcm reactivity insertion.**

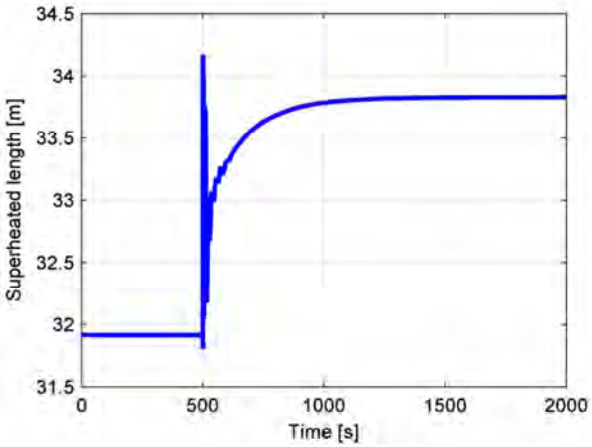


**Figure 208. Superheated length variation in the SG following a 20 pcm reactivity insertion.**

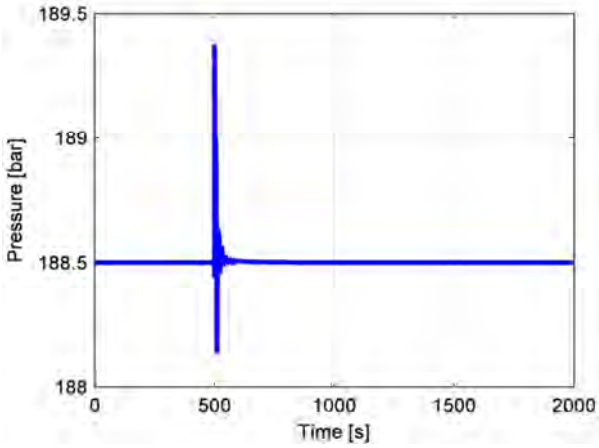


**Figure 209. Pressure variation in the SG following a 20 pcm reactivity insertion.**

The result of this simulation at the SG outlet is represented by an increase of the steam temperature (Fig. 210) ensuing from the exchanged power enhancement (Fig. 211), and by an increase of the lead SG outlet temperature (Fig. 212), only less consistent than the lead SG inlet temperature variation (Fig. 205) because of the improved power exchange .

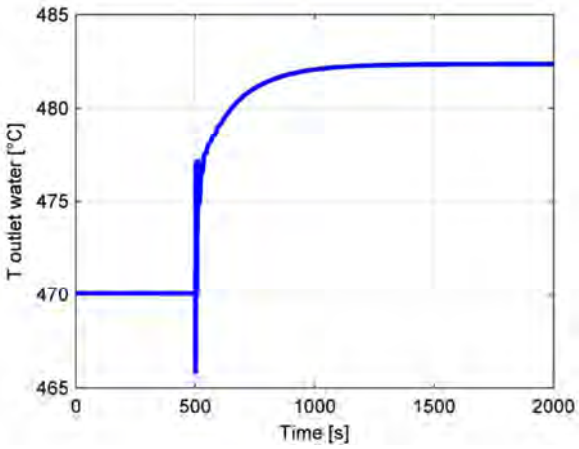


**Figure 210. Steam outlet temperature variation in the SG following a 20 pcm reactivity insertion.**

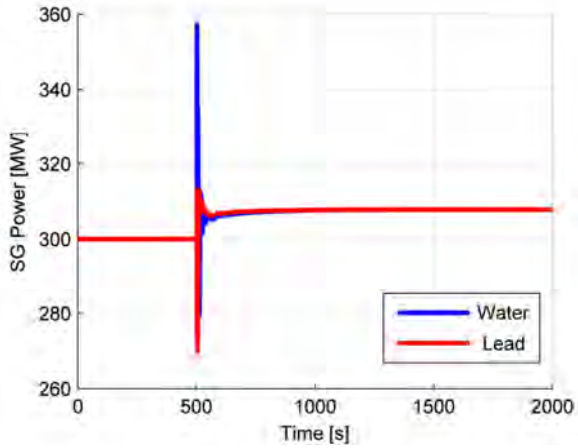


**Figure 211. SG power variation following a 20 pcm reactivity insertion.**

As a result of the pool action, a smooth increase of the core inlet temperature takes place (Fig. 213), whose negative effect influences the core behavior by combining with the previous reactivity insertion. In fact after 70 s a reversal of some variables trends is recognized: the power stops its increase and starts decreasing because of the insertion of negative reactivity due to the coolant density and radial expansion coefficient. The fuel temperature decreases stabilizing at a steady-state higher than the nominal one, as well as cladding and coolant temperatures.

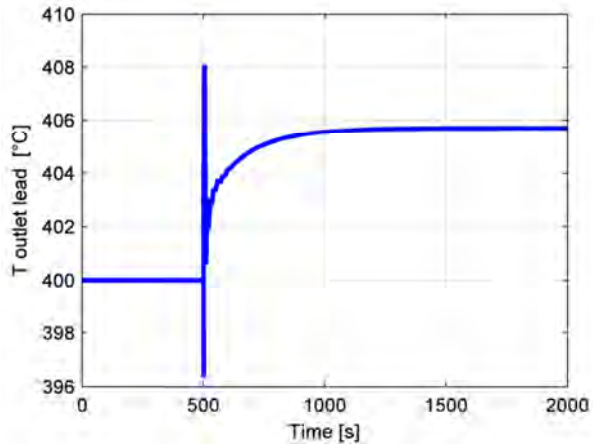


**Figure 212. Lead SG outlet temperature variation following a 20 pcm reactivity insertion.**

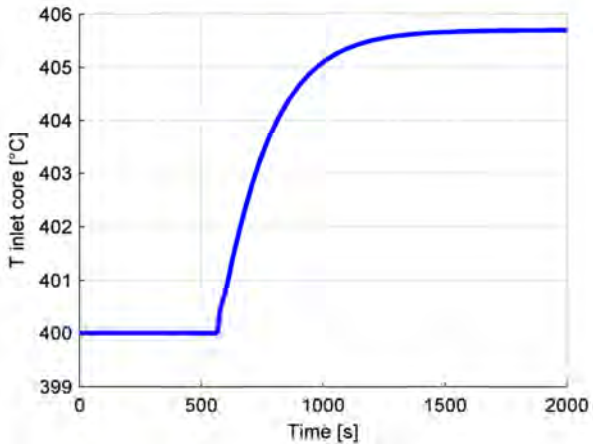


**Figure 213. Coolant core inlet temperature variation following a 20 pcm reactivity insertion.**

Table XLII resumes the main plant variables at the end of the transient.

**Table XLII. Results after a reactivity insertion.**

| **Reactivity insertion: +20 pcm** | | | |
|---|---|---|---|
| **Core** | | Variation | % Variation |
| Power [MW] | 308.1 | +8.1 | +2.7 % |
| Fuel temperature [°C] | 1740 | +41 | +2.41 % |
| Cladding temperature [°C] | 478.0 | +7.6 | +1.62 % |
| Coolant in temperature [°C] | 405.7 | +5.7 | +1.43 % |
| Mean coolant temperature [°C] | 446.8 | +6.8 | +1.55 % |
| Coolant out temperature [°C] | 487.9 | +7.9 | +1.65 % |
| **Steam generator** | | | |
| Sub-cooled length [m] | 6.446 | -0.64 | -9.03 % |
| Two-phase length [m] | 14.72 | -1.28 | -8 % |
| Superheated length [m] | 33.83 | +1.92 | +6.02 % |
| *Lead temperature* | | | |
| Inlet [°C] | 487.9 | +7.9 | +1.65 % |
| Superheated region [°C] | 469.8 | +6.8 | +1.47 % |
| Two-phase region [°C] | 434.4 | +5.8 | +1.35 % |
| Sub-cooled region [°C] | 411.3 | +5.7 | +1.41 % |
| Outlet [°C] | 405.7 | +5.7 | +1.43 % |
| *Wall temperature* | | | |
| Sub-cooled region [°C] | 375.1 | +2.4 | +0.64 % |
| Two-phase region [°C] | 385.7 | +1.8 | +0.47 % |
| Superheated region [°C] | 448.0 | +6.8 | +1.54 % |
| *Water temperature* | | | |
| Inlet [°C] | 335.0 | 0 | 0 % |
| Sub-cooled region [°C] | 347.9 | 0 | 0 % |
| Two-phase region [°C] | 360.8 | 0 | 0 % |
| Superheated region [°C] | 421.6 | +6.2 | +1.49 % |
| Water outlet temperature [°C] | 482.4 | +12.4 | +2.64 % |
| Pressure [bar] | 188.5 | 0 | 0 % |

## 4.1 Influence of the Coolant Reactivity Coefficient Sign on the Control Strategy

In the previous sections, it has been pointed out that a fundamental role in coupling the core and SG sub-systems is played by the coolant density and radial expansion feedback coefficients. In fact, they are correlated with lead temperature, that in the plant influences both SG and core.

For this reason, from a control-oriented point of view, it is interesting to study the dynamic behavior difference between a negative coolant coefficient situation and a positive one, since in a LFR the sign of this effect is not preconceived and depends strongly on the size of the reactor.

As described in this section, the reactor behavior in free dynamics is completely different if a positive coolant coefficient is considered. The following simulation – assumed as an example case - is based on a step-wise enhancement of water mass flow rate (10 % of the nominal value), with the only difference that the negative coolant density coefficient is changed into a positive ($\alpha_l = +1.23$ pcm $K^{-1}$ instead of the actual $\alpha_l = -1.23$ pcm $K^{-1}$). With a positive coolant coefficient, the free dynamics of the system results to be slower, reaching the steady state after four thousand seconds, approximately twice than in the previous simulations.

As in the case of negative coolant density coefficient, the simulation is initiated by the mass flow rate enhancement, causing an enlargement of the sub-cooled (Fig. 214) and two-phase regions and their respective temperatures, besides an increase of pressure in the SG, as depicted in Fig. 215.

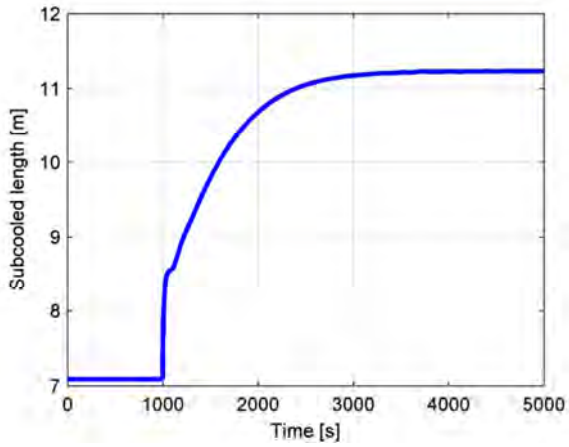


**Figure 214. Sub-cooled length variation in the SG following a 10 % enhancement of water mass flow rate, $\alpha_L > 0$.**

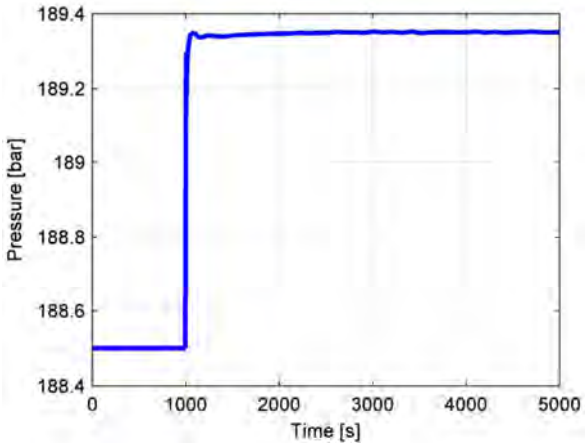


**Figure 215. Pressure variation in the SG following a 10 % enhancement of water mass flow rate, $\alpha_L > 0$.**

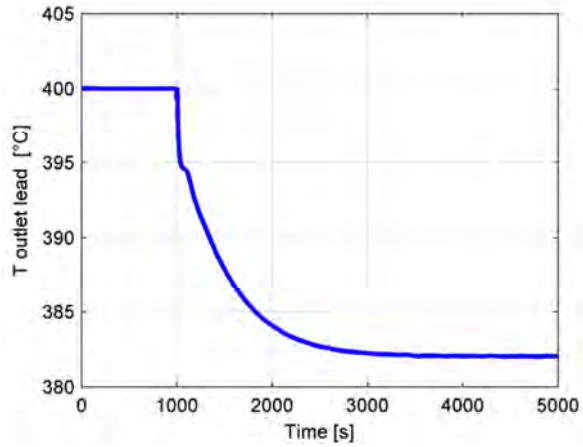


**Figure 216. Lead SG outlet temperature variation following a 10 % enhancement of water mass flow rate, $\alpha_L > 0$.**

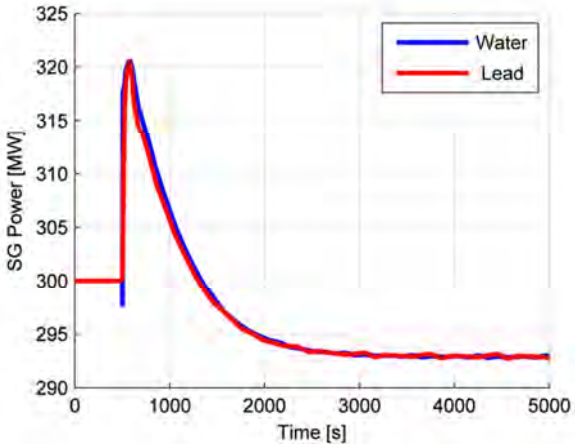


**Figure 217. SG power variation following a 10 % enhancement of water mass flow rate, $\alpha_L > 0$.**

For the first 70 s the simulation develops identically to the analogous one with the reference $\alpha_L$. When colder lead begins to flow into the core, the coolant density coefficient does not react together with the core expansion effects so as to enhance the power in the core (with a positive insertion of reactivity), which would be the best situation for control purposes: in fact, it is desired that, following an increase of water mass flow rate, the SG increases its power (Fig. 217), and, thanks to a negative feedback, the core follows this trend by enhance the power in turn. In this case, the positive lead coefficient leads to a negative insertion of reactivity (the different components are shown in Fig. 219, while net reactivity in Fig. 220) that determines a reduction of power (Fig. 221) since radial and axial contractions are not strong enough to counteract such an effect. Therefore a disparity between core and SG power occurs. This explains the time delay necessary to reach the new steady-state: the system has to equilibrate this situation.

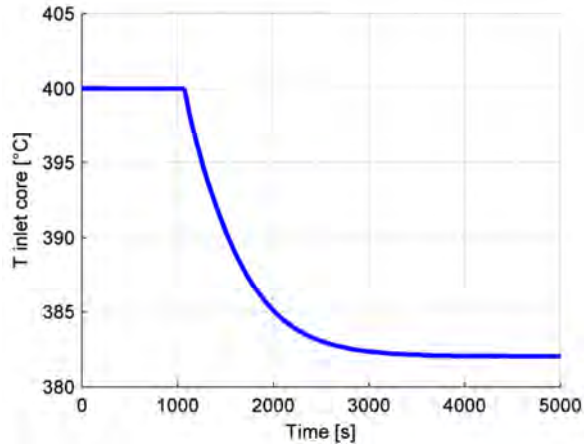


**Figure 218. Coolant inlet temperature variation following a 10 % enhancement of water mass flow rate, $\alpha_L > 0$.**

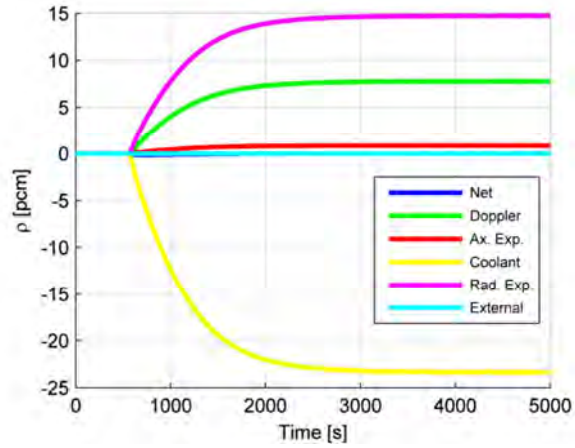


**Figure 219. Reactivity variation following a 10 % enhancement of water mass flow rate $\alpha_L > 0$.**

The system reacts so as to reach equilibrium by favoring the core, which generally turns into a decrease of the plant power level. The insertion of negative reactivity leads to a reduction of fuel, cladding and coolant temperatures, in particular at the core outlet as well.

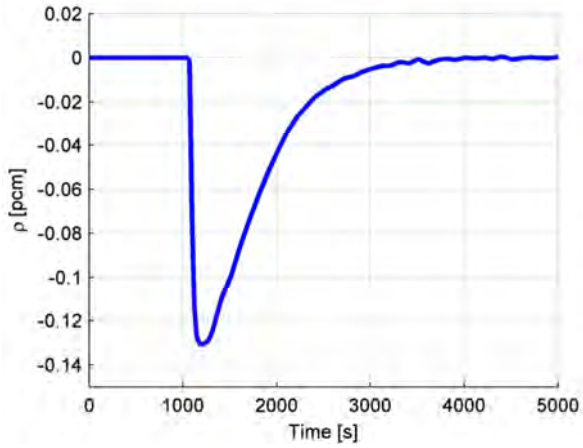


**Figure 220. Global reactivity variation following a 10 % enhancement of water mass flow rate, $\alpha_L > 0$.**

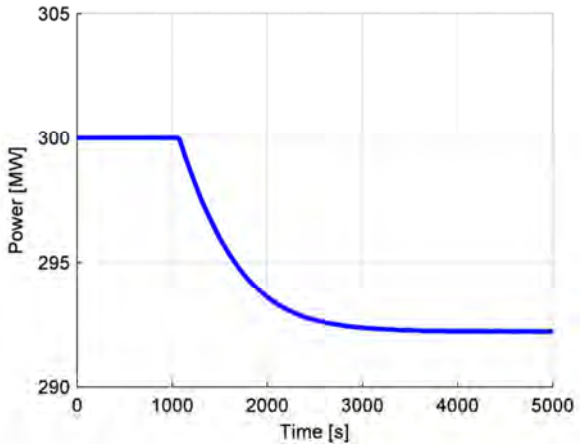


**Figure 221. Core power variation following a 10 % enhancement of water mass flow rate, $\alpha_L > 0$.**

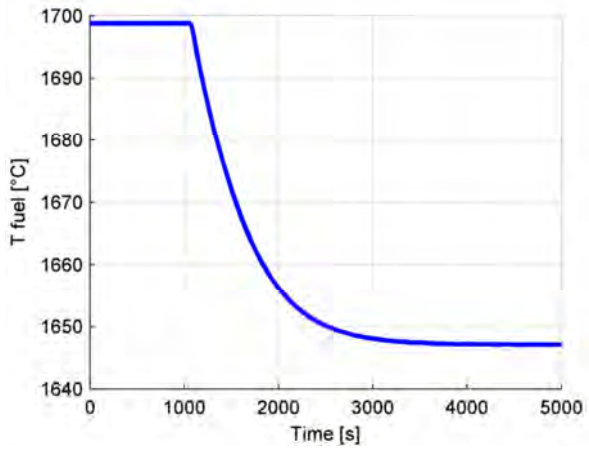


**Figure 222. Fuel temperature variation following a 10 % enhancement of water mass flow rate, $\alpha_L > 0$.**

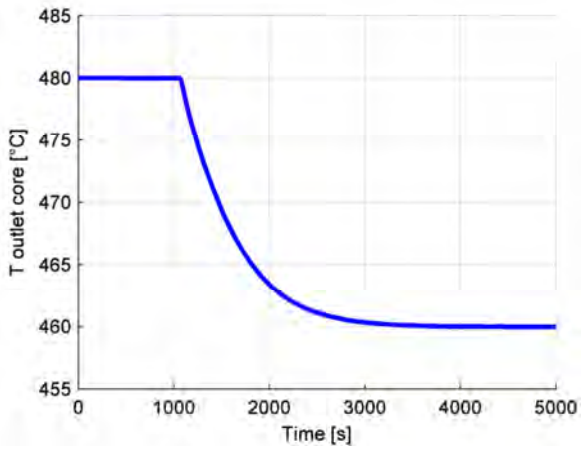


**Figure 223. Coolant core outlet temperature variation following a 10 % enhancement of water mass flow rate, $\alpha_L > 0$.**

The difference between the previous simulations is that the temperature difference between inlet and outlet is decreased. This means that the cooling effect is more marked at the outlet than at the inlet. In this way, at the inlet of the core there is a much colder lead that makes the power decrease under the previous steady-state value. Table XLIII resumes the main plant values at the end of the transient.

**Table XLIII. Results after water mass flow positive variation with positive coolant density coefficient.**

| Water mass flow variation: +18.56 kg $s^{-1}$, $\alpha_l > 0$ | | | |
|---|---|---|---|
| **Core** | | Variation | % Variation |
| Power [MW] | 292.2 | -7.8 | -2.6 % |
| Fuel temperature [°C] | 1647 | -52 | -3.06 % |
| Cladding temperature [°C] | 450.6 | -19.8 | -4.21 % |
| Coolant in temperature [°C] | 382.0 | -18 | -4.5 % |
| Mean coolant temperature [°C] | 421.0 | -19 | -4.32 % |
| Coolant out temperature [°C] | 459.9 | -20.1 | -4.19 % |
| **Steam generator** | | | |
| Sub-cooled length [m] | 11.23 | +4.144 | +58.48 % |
| Two-phase length [m] | 22.59 | +6.59 | +41.19 % |
| Superheated length [m] | 21.17 | -10.74 | -34.41 % |
| *Lead temperature* | | | |
| Inlet [°C] | 459.9 | -20.1 | -4.19 % |
| Superheated region [°C] | 446.1 | -16.9 | -3.65 % |
| Two-phase region [°C] | 413.5 | -15.1 | -3.52 % |
| Sub-cooled region [°C] | 388.3 | -17.3 | -4.27 % |
| Outlet [°C] | 382.0 | -18 | -4.5 % |
| *Wall temperature* | | | |
| Sub-cooled region [°C] | 365.0 | -7.7 | -2.07 % |
| Two-phase region [°C] | 379.0 | -4.9 | -1.27 % |
| Superheated region [°C] | 419.3 | -21.9 | -4.96 % |
| *Water temperature* | | | |
| Inlet [°C] | 335.0 | 0 | 0 % |
| Sub-cooled region [°C] | 348.1 | +0.2 | +0.06 % |
| Two-phase region [°C] | 361.2 | +0.4 | +0.11 % |
| Superheated region [°C] | 392.6 | -22.8 | -5.49 % |
| Water outlet temperature [°C] | 424.0 | -46 | -9.79 % |
| Pressure [bar] | 189.4 | +0.9 | +0.48 % |

## 5. Conclusions

In the present work, a zero-dimensional, control-oriented simulator for a LFR demonstrator with reference to the ELSY-based DEMO design has been developed.

The model is very flexible, simple and fast running: these features are intentionally obtained for the purpose of realizing the dynamic analyses necessary for the conception of a proper control strategy.

The non-linear, analytical lumped-parameter model of DEMO core has been demonstrated to provide reliable results, as the benchmark and validation with SAS4A/SASSYS-1 Liquid Metal Reactor Code System attest. Discrepancies between the two models are very slight, which is impressive if the completely different approach adopted by the two models - a simple zero-dimensional treatment against a more complicated one dimensional description - is reminded.

The validated non linear model has then been compared with its linear approximation: this represents an essential phase of the work, since the control strategy definition is usually based on models linearized around significant power levels, such as in classic control when employing PID controllers. Results show a very good agreement for small perturbations; in particular, satisfactory results are provided by the reactivity and core inlet temperature change simulations, while for a variation of the lead mass flow rate the linear model seems to be less adequate for describing the system dynamic behavior even for very small perturbations. Moreover, the linear model has been employed to assess MOX and metal dynamic performance, as the latter are envisioned as candidate fuel alternative options for DEMO. The outcomes of this analysis highlight a faster dynamics for the ceramic fuel, but a better behavior is found for the metal option, in particular concerning the respect of the cladding-related technological constraints.

In order to finalize a tool simulating the entire primary loop, a Steam Generator model has been developed and implemented. This component is expected to give strong feedbacks to the core dynamics, closing the loop between outlet and inlet coolant.

The SG model has been conceived based on a moving boundary approach, which permits to get the physical behavior of the component while preserving simplicity, flexibility and fast-running characteristics characterizing the zero-dimensional core modeling as well. Despite its straightforwardness, the SG model provides information on both transient behavior and new equilibrium values following a perturbation concerning the main variables involved, namely sub-cooled, two-phase and superheated lengths, both lead and water temperatures in these regions, and controlled parameters, such as pressure and exchanged power. The knowledge of these variables makes possible to assemble the two main models in order to create the primary loop.

Obviously, the presence of the coolant pool cannot be neglected to obtain reliable dynamic responses due to its important delaying and smoothing action on the lead core inlet temperature. In fact, the time needed to reach the steady-state is very long when running the primary loop simulations incorporating the pool, which determines a slower dynamics that must be necessarily taken into account for the control strategy conception.

The possible control variables are evaluated by studying transient simulations. Results confirm the strong coupling between core and SG, besides showing the characteristic time constants of the various components dynamics. All these information are fundamental to establish a proper control strategy and, more important, it has been showed how reactivity coefficients (in particular the coolant density feedback) heavily influence the primary loop dynamics, inducing even opposite behaviors depending on their sign.

As a major achievement of this work, it can be stated that the free dynamics simulation results are very satisfactory and they will constitute the basis and provide the means for conceiving a suitable control strategy for the innovative small-size LFR systems under development.

## AKNOWLEDGEMENTS

The authors are very grateful to Davide Bortot for his valuable contribution to this report.

## REFERENCES


1. A Technology Roadmap for Generation IV Nuclear Energy Systems – GIF 002-00 (2002).

2. Cinotti, L., et al. *The ELSY Project*. Proceeding of the 2008 International Conference on the Physics of Reactors (PHYSOR), Interlaken, Switzerland, September 14-19, 2008.

3. Bortot S. et al., *Preliminary Core Characterization of a Generation IV Lead Fast Reactor DEMO: Goals, Design Rationales and Options*, Energy Conversion and Management, **51**, 9, p.p. 1806-1812 (2010).

4. Bortot S. et al. *Conceptual Core Design of a Generation IV LFR Demonstration Plant*. Proceedings of PHYSOR 2010 – Advances in Reactor Physics to Power the Nuclear Renaissance, Pittsburgh, PN, USA, May 9-14, 2010.

5. Bortot S. et al. *Design Study on a Metallic Fuel Core Option for a GEN-IV LFR DEMO.* Transactions of the American Nuclear Society Winter Meeting, Las Vegas, NV, USA November 7-11, 2010.

6. Cinotti L. et al., "Lead-cooled System Design and Challenges in the Frame of Generation IV International Forum", *Proc. of the 2011 International Congress on Advances in Nuclear Power Plants (ICAPP '11)*, Nice, France, May 2-5, 2011, American Nuclear Society (CD-ROM).

7. Walters L., Wade D., and Hoffman G. *An Innovative Particulate Metallic Fuel for Next Generation Nuclear Energy*. Proceedings of the 2010 International Congress on Advances in Nuclear Power Plants, San Diego, CA, USA, June 13-17, 2010.

8. Sarotto M. et al. *ELSY core design, static dynamic and safety parameters with the open square FA*. Technical Report Deliverable D8, EURATOM, 2009.

9. Cahalan, J.E., Tentner, A.M., Morris, E.E, *Advanced LMR Safety Analysis Capabilities in the SASSYS-1 and SAS4A Computer Codes.* Proceedings of the International Topical Meeting on Advanced Reactors Safety. American Nuclear Society, **2**, 1038-1045, Pittsburgh, Pennsylvania, USA, 1994.

10. Rimpault, G. et al., *The ERANOS code and data system for Fast Reactor neutronic analyses.* Proceedings of the 2002 International Conference on the physics of reactors (PHYSOR 2002), Seoul, Korea, 2002.

11. JEF project, *The JEFF-3.1 Nuclear Data Library.* Technical Report JEFF Report 21, OECD/NEA, 2006.

12. "Handbook on Lead-bismuth Eutectic Alloy and Lead Properties, Materials Compatibility, Thermal-hydraulics and Technologies 2007 Edition", OECD NEA No. 6195, ISBN 978-92-64-99002-9 (2007).

13. Zhukov A. V. et al. *Heat transfer in lead cooled fast reactor (LCFR).* Advanced Reactor Safety: Proceedings of the International Topical Meeting, Pittsburgh, PA, April 17 - 21, 1994, American Nuclear Society, **1**, pp. 66-69 (1994).

14. Pfrang W., Struwe D. *Assessment of Correlation for Heat Transfer to the Coolant for Heavy Liquid Metal Cooled Core Designs.* Forschungszentrum Karlsruhe GmbH, Karlsruhe, 2007.

15. Chandra L. et al. *A stepwise development and validation of a RANS based CFD modeling approach for the hydraulic and thermal-hydraulic analyses of liquid metal flow in a fuel assembly.* Nuclear Engineering and Design, **239**, p.p. 1988–2003 (2009).

16. Duderstadt J. J., Hamilton L. J. Nuclear Reactor Analysis. John Wiley & Sons, 1976.

17. Dwyer O. *Liquid Metals Handbook, Sodium and NaK Supplement.* Washington D.C., U.S. Atomic Energy Commission, Chapter 5.

18. Carbajo J.J. et al. *A review of the thermophysical properties of MOX and $UO_2$ fuels*. Journal of Nuclear Materials, **299**, p.p. 181-198 (2001).

19. Seitz F. *The Modern Theory of Solids*. McGraw-Hill, New York, USA, 1940.

20. W.J. Carmack et al., "Metallic fuels for advanced reactors", *Journal of Nuclear Materials,* **392**, p.p. 139-150 (2009).

21. Yokoo T. *A Design Study on the FBR Metal Fuel and Core for Commercial Applications.* Journal of Nuclear Science and Technology, **37**, p.p. 636-645 (2000).

22. ANL, Private Communication (2010).

23. Jensen J. and Tummescheit H. *Moving boundary models for dynamic simulations of two-phase flows*. Proceedings of the 2nd International Modelica Conference, pp. 235–244 (2002).

24. Cheng, X., Tak N. *Investigation on Turbulent Heat Transfer to Lead-Bismuth Eutectic Flows in Circular Tubes for Nuclear Applications*. Nuclear Engineering and Design, **236**, p.p. 385-393 (2006).

25. Wagner W. et al. *The IAPWS Industrial Formulation 1997 for the Thermodynamic Properties of Water and Steam*. Journal of Engineering for Gas Turbines and Power, **122**, 150-182 (2000).

26. Kandlikar S.G. *A general correlation for saturated two-phase flow boiling heat transfer inside horizontal and vertical tubes*. Journal of Heat Transfer, **1112**, p.p. 219-228 (1990).

27. Bigoni A. *Modellistica e controllo predittivo del reattore di IV generazione Elsy.* Master's degree thesis, Politecnico di Milano, 2009.

28. Blinchikoff, H.J., Zverev A.I. *Filtering in the Time and Frequency Domains*. John Wiley & Sons, New York, 1976.